The City College of New York

NEUP Project 15-8205 – FINAL REPORT

Experimental Investigation of Forced Convection and Natural Circulation Cooling of a VHTR Core under Normal Operation and Accident Scenarios

Project Start Date **10/1/2015**
Project End Date **6/30/2019**

Prepared for:

U.S. Department of Energy - Nuclear Energy University Program
NEUP Integration Office
Center for Advanced Energy Studies
P.O. Box 1625
Idaho Falls, ID 83415

Technical Point of Contact: Jim Wolf
National Technical Director: Gerhard Strydom
Federal Manager: Diana Li

Prepared by:

Masahiro Kawaji
Dinesh Kalaga
Sanjoy Banerjee
City College of New York
Richard R. Schultz
Idaho State University
Hitesh Bindra
Kansas State University
Donald M. McEligot
Idaho National Laboratory

September 30, 2019

EXECUTIVE SUMMARY

This NEUP project #15-8205 entitled "Experimental Investigation of Forced Convection and Natural Circulation Cooling of a VHTR Core under Normal Operation and Accident Scenarios", has investigated important phenomena in the safety of Very High Temperature Reactors (VHTRs) using the experimental facilities at City College of New York (CCNY) and Kansas State University (KSU), in collaboration with the Idaho State University (ISU) and Idaho National Laboratory (INL).

The main objectives of this project were to investigate the forced convection and bypass flow phenomena, natural circulation flow and heat transfer, and graphite oxidation due to air ingress which could occur in a Very High Temperature Reactor (VHTR) with a prismatic core. High pressure/high temperature experiments have been conducted to obtain data that could be used for validation of VHTR design and safety analysis codes. The focus of these experiments was on the generation of benchmark data for design and off-design heat transfer for forced and natural circulation in a VHTR core.

This work has built on the previous NEUP project #11-3218 which investigated forced convection and flow laminarization phenomena in a prismatic core of a VHTR and natural circulation of a pure gas under Pressurized Conduction Cooldown (PCC) and Depressurized Conduction Cooldown (DCC) conditions. Under each Task, extensive literature reviews on natural circulation, bypass flow, air ingress and graphite oxidation phenomena were conducted. In Task 1, scaling analyses were conducted by Idaho State University followed by design and construction of experimental facilities needed to conduct both bypass flow and natural circulation experiments at CCNY. Natural circulation experiments were conducted in Task 2 to investigate the air ingress phenomena, and bypass flow phenomena in Task 3, both at CCNY. In Task 4, radiation heat transfer and graphite oxidation tests were performed at Kansas State University. The experimental data were then analyzed to obtain quantitative results on natural circulation of pure gases and gas mixtures under DCC conditions, bypass flow rates, radiation heat transfer and graphite oxidation. In addition, CFD and Direct Numerical Simulations were conducted by INL and CCNY to investigate the flow laminarization phenomenon in strongly heated gas flows.

The scaling analyses have shown that the key nondimensional numbers and parameters all have acceptable distortion levels principally because the CCNY facility's test sections have representative cooling channel dimensions and are using either helium or a scalable gas such as nitrogen at representative state conditions.

The natural circulation experiments involving helium and nitrogen gas mixtures at CCNY have elucidated the effect of nitrogen (simulating air) ingress into a lower plenum on the onset of natural circulation, mass flow rates and heat transfer coefficients under different power input levels in the riser section. Also, the transport of nitrogen from the lower plenum to upper plenum due to natural circulation was quantified for the first time. Nusselt number correlations for the heat transfer coefficient under natural circulation as a function of Reynolds and Prandtl numbers was also developed. The experiments at KSU revealed that prior to the onset of natural circulation

(ONC), molecular diffusion plays a significant role in air-ingress, however, at higher temperatures convection currents may be influencing air ingress and in-turn ONC times.

Bypass flow experiments faced difficulties in the measurement of gas velocity in the main channel due to the failure of a high temperature Hot Wire Anemometer probe, so an energy balance method was instead employed to estimate the flow distribution between the main and bypass flow channels.

In the graphite oxidation experiments conducted at KSU, oxidation was found to increase the thermal diffusivity of nuclear grade graphite. This change is believed to be driven by oxidation decreasing graphite sample density rather than raising the thermal conductivity. Oxidation was also shown to greatly alter graphite emissivity. If large amounts of impurities have built up within the graphite over time and have significantly increased its effective ash content, then air ingress is likely to severely inhibit the radiative heat transfer abilities of the graphite due to the formation of low emissivity, ash layers on its surface. However, if the purity of the graphite at the time of the air ingress is still close to that of its virgin specifications, the oxidation induced roughening of the graphite's outer surface would have the effect of slightly raising its emissivity.

The flow laminarization phenomenon was investigated by INL by examining the results of Direct Numerical Simulations of previous experiments, and by CCNY conducting its own DNS simulations using DOE's Nek5000 code.

Acknowledgements

All the authors of this Final report would like to thank the Department of Energy for supporting this project through the Nuclear Engineering University Program (NEUP) under Contract No. DE-NE0008412/0002.

Table of Contents

	Page
Executive Summary	i
Acknowledgements	ii
Table of Contents	iii
CHAPTER 1. Introduction	1
1.1 Project Objectives	2
1.2 Review of Natural Circulation and Air Ingress in VHTR's	3
CHAPTER 2: Task 1 Report on Identification of Key Phenomena and Scaling Analysis	7
CHAPTER 3: Task 2 Report on Natural Circulation and Air Ingress Experiments	47
CHAPTER 4: Task 3 Report on Bypass Flow Experiments and Data Analysis	69
CHAPTER 5: Task 4 Report on Radiative Heat Transfer and Air Ingress Effects	90
CHAPTER 6: Numerical Simulations of Flow Laminarization Phenomenon	137
CHAPTER 7: Validation and Verification Database	150
LIST OF PUBLICATIONS PRODUCED FROM THE PROJECT	150
APPENDIX 1. High Pressure - High Temperature Test Facility	154
APPENDIX 2. Constant Property Simulations of Flow Laminarization using Nek5000	200

CHAPTER 1. INTRODUCTION

After the severe accidents at Fukushima Daiichi Nuclear Power Plants, the need for understanding the response of nuclear facilities to externally or environmentally initiated events, such as strong earthquakes, tsunamis, and flooding has become significantly important [1]. The next generation nuclear power plants such as a Very High Temperature Reactor (VHTR) illustrated in Fig. 1.1 have passive safety system designs, but it is not fully clear whether their safety system designs will perform as per design requirements under all accident scenarios.

In a prismatic reactor core (Fig. 1.2) of a VHTR, cylindrical fuel compacts are stacked inside channels drilled along the length of a hexagon graphite block. Cylindrical coolant channels are drilled along the graphite block length between the columns of fuel compacts. A gaseous coolant (helium) at high pressure flows through these channels, which are independent vertical passages through the reactor. If there is bypass flow between the graphite blocks, the helium temperature leaving a block has been predicted to go up by ~60°C, which can lead to heat up of fuel by ~80°C. The bypass flow through the interstitial passages may be ~10-25% of the total core flow [2, 3], and can also increase as a result of block distortion stemming from irradiation.

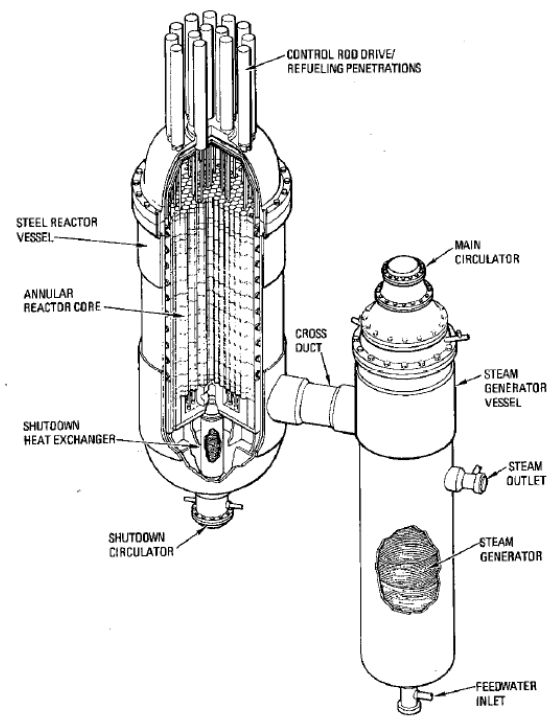

Fig. 1.1 MHTGR module (DOE, 1986)

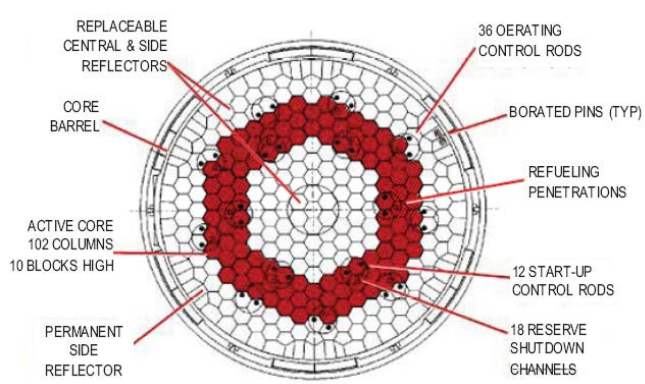

Fig. 1.2 Plan view of VHTR reactor vessel and core region (DOE 1986)

Under accident conditions in a VHTR, the Pressurized Conduction Cooldown (PCC) and Depressurized Conduction Cooldown (DCC) phenomena are expected to occur following a break in the coolant system and in Loss-of-Flow Accident scenarios. The DCC in the case of a break in the coolant system could involve air ingress into the lower plenum at low pressure and

subsequent transport through the core which could lead to graphite oxidation in the core at high temperatures.

1.1 Project Objectives

The objectives of this project were to perform the following three separate and mixed effects experiments to better understand the physical phenomena and yield reliable experimental data useful for validation of VHTR design and safety analysis codes.

1. Natural circulation flow and effect of air ingress (CCNY)

2. Forced-convection and the effect of bypass-coolant flow in a prismatic core (CCNY)

3. Radiative heat transfer and effect of oxidation by air ingress (KSU)

To achieve the above objectives and yield reliable experimental data for validation of VHTR design and safety analysis codes, this project was organized as shown in Fig 1.3. A scaling analysis was performed at ISU based on which a high pressure/high temperature gas heat transfer facility constructed under a previous NEUP project at CCNY was modified and used to experimentally investigate the natural circulation and bypass flow phenomena. A full description of the Test Facility at CCNY is given in Appendix 1.

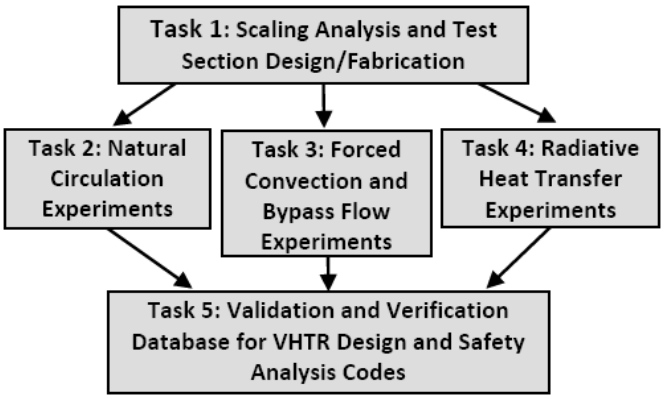

Fig. 1.1 Flow Chart of Tasks

At KSU, new experimental facilities were also developed to investigate the onset of natural circulation in an “h” shaped tube geometry and graphite oxidation phenomena. INL and CCNY also conducted analytical and numerical simulation studies on flow laminarization phenomena in strongly heated gas flows.

As shown in several Phenomena Identification and Ranking Tables (PIRT) for VHTRs [4, 5] under normal operation, transient, and accident scenarios, the key phenomena leading to localized hot spots in the reactor core include degraded heat transfer in coolant channels under forced circulation due to bypass flow and laminarization of flow, natural circulation and effect of air ingress, and non-uniform heat generation across the core. Some of these phenomena have been investigated experimentally at CCNY and KSU, and theoretically by CCNY and INL. The focus

of this project was on the generation of benchmark data for design and off-design heat transfer for forced and natural convection in a VHTR core with prismatic blocks.

1.2 Review of Natural Circulation and Air Ingress in VHTRs

An important accident scenario that needs to be investigated in greater detail is natural circulation under DCC and the effect of air-ingress and subsequent air transport through the core that could cause exothermic graphite oxidation reactions. The potential for air-ingress into the VHTR vessel exists during postulated loss-of-flow accidents (LOFAs) [6-21]. Since the VHTR vessel is located in a reactor cavity filled with ambient air, air could enter the reactor vessel following a double-ended guillotine break of a hot duct, rapid discharge of the coolant (helium) and depressurization of the primary loop. Eventually, the behavior of the flow at the break changes from momentum-driven to density-gradient driven flow with air or helium-air mixture flowing into the lower plenum of the reactor vessel as illustrated in Figure 2.1.

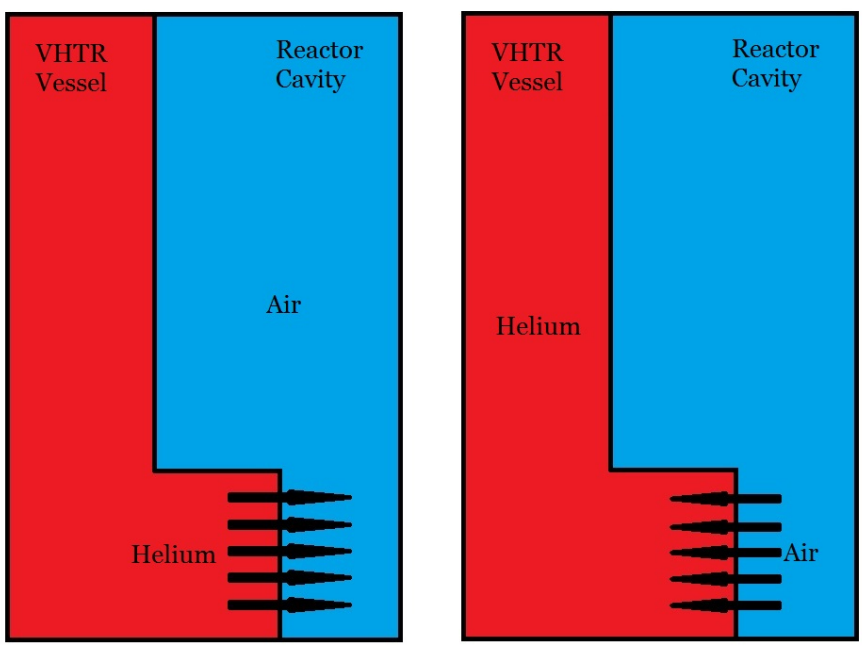

(a) (b)

Fig. 1.2 Air-Ingress Scenario (a) depressurization due to loss of helium, and (b) air entering the vessel after depressurization.

There have been conflicting reports in the literature on what the dominant mechanism is for air transport through the reactor core. While some researchers have suggested that air transport

during air ingress is only driven by molecular diffusion, it was later understood that molecular diffusion is followed by natural circulation which is marked by the Onset of Natural Circulation (ONC) [17-19]. There are also conflicting reports in the literature with regards to the ONC time. Numerical simulations performed by Oh et al. [6, 13, 14] using a FLUENT CFD code suggested that ONC would occur within 100 seconds after the depressurization phase. However, the simulations performed by using a Gamma code [15, 16] suggested that the ONC would occur over several hours rather than several tens or hundreds of seconds after the depressurization event. Thus, our work is aimed at experimentally determining the ONC times for different reactor core temperatures and understanding the air transport phenomena in the reactor core following air ingress into the lower plenum. Also, while numerical investigations have been performed by several authors to study air-ingress [13-20], a limited amount of experimental data has been reported in the literature [21]. Recently, ONC experiments were conducted by Gould et al. [22] using an "h" shaped tube initially filled with helium and open to the atmosphere at both bottom ends. They showed the ONC times to be much greater than several hundred seconds in contrast to the numerical simulations of Oh et al. [6, 13, 14]. Our experiments would add both to the experimental database for the ONC and air transport under the DCC conditions.

References for Chapter 1

1. SCIENCEDAILY, "Fukushima at Increased Earthquake Risk, Scientists Report," (2012) URL <http:/ /www.sciencedaily.com/releases/2012/02/120214100819.htm>.
2. Yoon, S-J, Lee, J-H, Kim, M-H, and Park, G.C., 2012, "The effects of crossflow gap and axial bypass gap distribution on the flow characteristics in prismatic VHTR core", Nucl. Eng. & Design, 250, 465–479.)
3. G. E. MCCREERY, L. J. TEW, B. G. WILLIAMS, R. R. SCHULTZ and D. M. MCELIGOT, "MHTGR Core Bypass Flow Patterns and Pressure Losses," INL/CON-12-27833, Idaho National Laboratory (2013).
4. R. VILIM, W. D. POINTER, and T. Y. WEI, "Prioritization of VHTR System Modleing Needs Based on Phenomena Identification, Ranking and Sensitivity Studies," ANL-GenIV-071, Argonne National Lab (2006).
5. S. J. BALL, M. CORRADNI, S. E. FISHER, R. GAUNTT, G. GEFFRAVE, J. C. GEHIN, Y. HASSAN, D. L. MOSES, J. P. RENIER, R. SCHULTZ and T. Y. WEI, "Next Generation Nuclear Plant Phenomena Identification and Ranking Tables (PIRTs) Volume 2: Accident and Thermal Fluids Analysis PIRTs," ORNL/TM--2007/147/V. 2, Oak Ridge National Laboratory (2008).

6. C. H. OH, S. K. EUNG, S. RICHARD and P. DAVID, “Implications of Air Ingress Induced by Density-Difference Driven Stratified Flow,” Proc. ICAPP ’08, Anaheim, CA, June 8-12 (2008).
7. T. TAKEDA and M. HISHIDA, “Studies on molecular diffusion and natural convection in a multicomponent gas system,” Int. J. Heat Mass Transf. 39 3, 527 (1996); https://doi.org/10.1016/0017-9310(95)00148-3.
8. T. TAKEDA, "Air ingress behavior during a primary-pipe rupture accident of HTGR”, JAERI—1338, Japan Atomic Energy Research Inst. (1997).
9. E. S. KIM, H. C. NO, B. J. KIM and C. H. OH, “Estimation of graphite density and mechanical strength variation of VHTR during air-ingress accident,” Nucl. Eng. Des. 238 4, 837 (2008); https://doi.org/10.1016/j.nucengdes.2007.08.002.
10. M. HISHIDA, M. FUMIZAWA, T. TAKEDA, M. OGAWA and S. TAKENAKA, “Researches on air ingress accidents of the HTTR,” Nucl. Eng. Des. 144 2, 317 (1993).
11. D. J. ARCILESI, T. K. HAM, I. H. KIM, X. SUN, R. N. CHRISTENSEN and C. H. OH, “Scaling and design analyses of a scaled-down, high-temperature test facility for experimental investigation of the initial stages of a VHTR air-ingress accident,” Nucl. Eng. Des. 288, 141 (2015); https://doi.org/10.1016/j.nucengdes.2015.03.007.
12. T. TAKEDA, and M. HISHIDA, "Study on the passive safe technology for the prevention of air ingress during the primary-pipe rupture accident of HTGR." Nucl. Eng. Des. 200 2, 251 (2000).
13. C. H. OH and E. S. KIM, “Air-ingress analysis: Part 1. Theoretical approach,” Nucl. Eng. Des. 241 1, 203 (2011); https://doi.org/10.1016/j.nucengdes.2010.05.064.
14. C. H. OH, H. S. KANG, and E. S. KIM, “Air-ingress analysis: Part 2 - Computational fluid dynamic models,” Nucl. Eng. Des., 241, 1, 213, (2011); https://doi.org/10.1016/j.nucengdes.2010.05.065.
15. H. G. JIN, H. C. NO, and I. H. KIM, “Stratified flow-induced air-ingress accident assessment of the GAMMA code in HTGRs,” Nucl. Eng. Des. 241 8, 3216 (2011); https://doi.org/10.1016/j.nucengdes.2011.04.022.
16. H.S. LIM and H. C. NO, "GAMMA multidimensional multicomponent mixture analysis to predict air ingress phenomena in an HTGR." Nuclear Science and Engineering, 152 1, 87 (2006).
17. T. K. HAM, D. J. ARCILESI, I. H. KIM, X. SUN, R. N. CHRISTENSEN, C. H. OH and E. S. KIM, “Computational fluid dynamics analysis of the initial stages of a VHTR air-ingress accident using a scaled-down model,” Nucl. Eng. Des. 300, 517 (2016); https://doi.org/10.1016/j.nucengdes.2016.02.011.
18. H. HAQUE, W. FELTES, and G. BRINKMANN, “Thermal response of a modular high temperature reactor during passive cooldown under pressurized and depressurized conditions,” Nucl. Eng. Des. 236 5–6, 475 (2006); https://doi.org/10.1016/j.nucengdes.2005.10.027.

19. C. H. OH, E. S. KIM, and H. S. KANG, “Natural circulation patterns in the VHTR air-ingress accident and related issues,” Nucl. Eng. Des. 249, 228 (2012); https://doi.org/10.1016/j.nucengdes.2011.09.031.
20. X. SUN, R. CHRISTENSEN, and C. OH, “Investigation of Countercurrent Helium-air Flows in Air-ingress Accidents for VHTRs,” 09-784, Battelle Energy Alliance, LLC (2013).
21. T. TAKEDA, "Air ingress phenomena in a depressurization accident of the very-high-temperature reactor." Fourth International Topical Meeting on High Temperature Reactor Technology, Washington, DC, September 28–October 1 (2008).
22. D. GOULD, D. FRANKEN, H. BINDRA and M. KAWAJI, “Transition from molecular diffusion to natural circulation mode air-ingress in high temperature helium loop,” Ann. Nucl. Energy, 107, 103 (2017); https://doi.org/10.1016/j.anucene.2017.03.049.

CHAPTER 2

Task 1 Report on Identification of Key Phenomena and Scaling Analysis

Richard R. Schultz

Benjamin McDaniel

September, 2019

Department of Nuclear Engineering

921 S. 8th Ave, MS 8060

Pocatello, ID 83209-8060

EXECUTIVE SUMMARY

The City College of New York's (CCNY) High Pressure and Temperature Test Facilities are comprised of the Natural Circulation Flow Loop (NCFL) and the Forced Circulation Bypass Flow Loop (FCBFL). The geometry, instrumentation, and capabilities of these facilities are described and compared to a single-core cooling channel in the Modular High Temperature Gas-Cooled Reactor (MHTGR). The key phenomena to be investigated in these facilities, including their scaling relationships to the reference MHTGR at operational as well as specific off-normal and accident conditions are described.

The CCNY facilities are designed to provide data for validation of high-fidelity and systems analysis codes at representative conditions for the MHTGR in a single cooling channel. As such the facilities were constructed to obtain representative conditions in a typical cooling channel under forced and natural circulation conditions. The CCNY test facilities have the following characteristics:

- The CCNY test section graphite simulated cooling channel has a diameter of 16.8 mm; thus the CCNY cooling channel differs by only 5% to 6% from a typical MHTGR cooling channel (16.8/15.9 = 1.056). This agreement gives a close match to a typical MHTGR cooling channel and forms the basis for performing experiments that give MHTGR-typical flow and heat transfer characteristics.
- The core bypass for the CCNY FCBFL facility is within the band of bypass flows that are typical for the MHTGR.
- The CCNY facilities are capable of providing conditions in the test section that are typical for the MHTGR including either the same working fluid (helium) or a scalable working fluid (nitrogen)—meaning that the alternate working fluid, in this case nitrogen in the CCNY FCBFL facility, can be delivered to the test section at appropriate scaled values. Therefore, (i) for experiments performed with helium as a working fluid the CCNY test facilities have working fluid properties that match those of the MHTGR and (ii) for experiments performed with nitrogen as the working fluid the gas conditions can be adjusted to give matching key nondimensional quantities representative of the MHTGR, i.e., Reynolds number, Grashof number, and nondimensional heat flux.
- The Prandtl numbers of both helium and nitrogen may be approximated as 0.7.

It is noted that: "… the Reynolds number (Re), Grashof number (Gr and Gr^*) and Prandtl number (Pr) or alternatively Rayleigh number (Ra), and non-dimensional heat flux (q^+) are the main non-dimensional numbers that we should match between the prototypical and test conditions. Other parameters, namely, the Buoyancy parameter (Bo*) and the accelerator parameter (K_v) will be matched automatically as we match Re, Gr, Gr*, Pr and q^+ between the prototype and the model test section."

The key parameters in the form of well-known nondimensional numbers and nondimensional parameters such as the buoyancy parameter and the acceleration parameter all have acceptable distortion levels in the CCNY experiments principally because the CCNY facilities test sections have representative cooling channel dimensions and are using either helium or a scalable gas such as nitrogen at representative state conditions.

CONTENTS

1. INTRODUCTION 14

2. REFERENCE PLANT 14
   2.1 Overview 14
   2.2 Description of MHTGR Core and Typical Cooling Channel 16

3. PHENOMENA RELEVENT TO CCNY EXPERIMENT 17
   3.1 Conditions During Normal Operation 18
   3.2 Off-Normal or Accident Conditions in the Core 18
   3.3 Turbulent Flow at Normal Full Power Operation 19
   3.4 Laminar Flow 23
   3.5 Mixed Convection 27
      3.5.1 Defining the Key Non-Dimensional Numbers Used for MIT Experiments 27
      3.5.2 On the Use of Nitrogen as a Working Fluid 32
   3.6 Summary 33

4. CALCULATION: MHTGR FLOW AND HEAT TRANSFER IN CORE DURING PCC AND DCC SCENARIOS 34
   4.1 PCC Scenario 34
   4.2 DCC Scenario 37
   4.3 Summary 38

5. CCNY EXPERIMENTS: RELEVANCE TO HTTF AND SCALING 38
   5.1 HTTF: Relevance to CCNY Experiments 42
   5.2 Scaling: Forced Circulation Bypass and Natural Circulation Flow Loops 43

6. REFERENCES 43

FIGURES

1. MHTGR design 2
2. Block-type fuel elements 4
3. Effects of buoyancy on convective heat transfer for fully-developed flow in vertical circular tubes [Jackson, Cotton, and Axcell, 1989; Li, 1994] 9
4. Prediction of local heat transfer parameters for air and helium in laminar flow accounting for effects of gas property variation [Worsoe-Schmidt, 1966] 11
5. Effects of buoyancy on heated, fully-established laminar flow in vertical circular tubes with the Boussinesq approximation [Scheele and Hanratty, 1962] 12
6. Operating conditions maps for the NGNP Point Design [MacDonald et al., 2003] during full and reduced power operation, order-of-magnitude estimates 12
7. Estimated flow rate trends furing a hypothetical PCC in a typical NGNP concept 13
8. Estimated heat flux (a) and buoyancy (b) trends during a hypothetical PCC in a typical NGNP concept 14
9. Tentative forced-mixed-free convection boundaries for Pr = 0.7 18
10. Complete Ra vs. Re map generated from experimental loop 20
11. Average Reynolds number of gases moving from core into upper plenum of MHTGR during PCC scenario from the inner, middle, and outer rings 22
12. Average temperature as a function of time (s) of gases moving from core into upper plenum of MHTGR during PCC scenario from the inner, middle, and outer rings 23
13. Average temperature of gases moving from active core region into upper reflector compared to average gas temperature in upper plenum 23
14. Average Reynolds number of gases moving from core into upper plenum of MHTGR during DCC scenario from the inner, middle, and outer rings 24
15. Average temperature of gases moving from core into upper plenum of MHTGR during DCC scenario from inner, middle and outer rings 25
16. CCNY Forced Circulation Bypass Flow Loop test facility 26
17. CCNY Natural Circulation Flow Loop facility 27

TABLES

1. Core parameters and full power operating conditions 4
2. Comparison of CCNY Natural Circulation Flow Loop and Forced Circulation Bypass Flow Loop test facilities core test section to reference MHTGR 28
3. Key nondimensional groups for the core region: HTTF 29
4. Summary of CCNY Test Facility Pi Groups and Estimates of Scaling Distortion 30

NOMENCLATURE

{ }	function of
A_{cs}	flow area
C	empirical coefficient
c_p	specific heat at constant pressure
D	diameter
D_h	hydraulic diameter, 4 A_{cs} / P_w
d	wire diameter
g	acceleration of gravity
g_c	units conversion factor, e.g., 1 kg m / (N s2), 32.1739 lbm ft / (lbf sec2)
G	mean mass flux, $\dot{m}$ / A_{cs}
H	lower plenum height; also height of idealized column of gas
h	convective heat transfer coefficient
k	thermal conductivity, turbulent kinetic energy
$\dot{m}$	mass flow rate
P	perimeter; P_w, wetted; P_h, heated surface
p	pressure, pitch
q"	heat flux; q''_w, wall heat flux
r	radius
T	temperature
U, V	mean velocity
V_b	bulk or mixed-mean streamwise velocity
u_τ	friction velocity, $(g_c\, \tau / \rho)^{1/2}$
$\overline{u\,v}$	Reynolds shear stress
v	velocity fluctuation about mean
x	axial location

Non-dimensional quantities

A_c	general acceleration onset parameter (see text)
Bo	general buoyancy onset parameter (see text)
Bo*	Jackson buoyancy parameter, Gr* / ($Re_{Dh}^{3.425}\, Pr^{0.8}$)
d+	wire diameter, $d\, u_\tau / \nu$
f, f_τ	friction factor, $2\, \rho_b\, g_c\, \tau_w / G^2$
Frj	jet Froude number (see text)
G	Grashof number as used by Scheele and Hanratty [1962], $g\, \beta\, q''_{wall}\, r_w^4 / (k\, \nu^2)$
Gr*	Grashof number based on heat flux, $g\, \beta\, q''_{wall}\, D_h^4 / (k\, \nu^2)$
Gr_{ws}	modified Grashof number of Worsoe-Schmidt [1966], $g\, D^3 / \nu^2$
K_v	acceleration parameter, $(\nu_b / V_b^2)\, (dV_b / dx)$
Nu	Nusselt number, $h\, D_h / k_b$
Pe	Peclet number, RPr
Pr	Prandtl number, $c_p\, \mu/k$
Q+	heat flux for laminar analyses by Worsoe-Schmidt [1966], $r_w\, q''_{wall} / (k\, T)$
q+	heat flux, $\beta\, q''_{wall} / (G\, c_p)$

R Reynolds number as used by Scheele and Hanratty [1962], $V_b\ r_w / \nu$
Re Reynolds number, $4\ \dot{m} / \pi\ D\ \mu$; Re_{Dh}, based on hydraulic diameter, $G\ D_h / \mu$
Ri overall Richardson number, $g\ (\rho 1-\rho 2)\ H / (\rho 1\ V_b^2)$
Ri_{wall} Richardson number defined in terms of wall quantities (see text)

Greek symbols

β volumetric coefficient of expansion, $-(1/\rho)\ (\partial\rho/\partial T)_p$
ε dissipation of turbulence kinetic energy
μ absolute viscosity
ν kinematic viscosity, μ / ρ
ρ density
τ shear stress; τ_w, wall shear stress

Subscripts

b evaluated at bulk or mixed-mean temperature (or enthalpy)
D based on diameter
DB Dittus-Boelter [1930] correlation
Dh evaluated with hydraulic diameter
f, fc forced convection
i, in evaluated at inlet, entry
j jet
max maximum value
p support post
ref evaluated at reference conditions
w, wall wall, evaluated at wall temperature

TASK1. SCALING ANALYSES AND TEST SECTION DESIGN

HIGH PRESSURE & TEMPERATURE TEST FACILITIES: IDENTIFICATION OF KEY PHENOMENA AND SCALING

1. INTRODUCTION

The City College of New York's (CCNY) High Pressure and Temperature Test Facilities are comprised of the Natural Circulation Flow Loop (NCFL) and the Forced Circulation Bypass Flow Loop (FCBFL). The geometry, instrumentation, and capabilities of these facilities are described in Kalaga, Rudra, and Kawaji, 2019. The key phenomena to be investigated in these facilities, including their scaling relationships to the reference Very High Temperature Reactor (VHTR) at operational as well as specific off-normal and accident conditions are described herein. The reference VHTR is the prismatic Modular High Temperature Gas-Cooled Reactor--MHTGR [Stone & Webster, 1986] although the reactor and core designs of the MHTGR are very similar to the Gas Turbine-Modular Helium Reactor—MH-GTR [General Atomics, 1996]

The CCNY facilities are designed to provide data for validation of high-fidelity and systems analysis codes at representative conditions for the VHTR in a single cooling channel. As such the facilities were constructed to obtain representative conditions in a typical cooling channel under forced and natural circulation conditions.

The report is divided into five sections including: (1) this introduction; (2) a description of key dimensions of the MHTGR relevant to the design of the CCNY facilities; (3) a summary of key phenomena for the operational, off-normal (the pressurized conduction cooldown—the PCC—scenario), and accident (the depressurized conduction cooldown—DCC) scenarios; (4) a summary of RELAP5-3D [RELAP5-3D Code Development Team, 2014] calculations of the MHTGR behavior during the PCC and DCC scenarios to illustrate the anticipated magnitudes of key nondimensional quantities; and (5) a summary of the key nondimensional numbers together with their magnitudes relative to the MHTGR to quantify the scaling relationships between the MHTGR and the CCNY facilities. The fifth section also includes a summary of the key nondimensional quantities relevant to the core region at steady-state conditions identified when the Oregon State University High Temperature Test Facility (HTTF), an integral experimental facility scaled to the MHTGR, was designed [Woods et al., 2015].

2. REFERENCE PLANT

The reference gas-cooled VHTR design is based on the MHTGR; [Stone & Webster, 1986].

2.1 Overview

The MHTGR is a 350 MWth indirect cycle gas-cooled reactor with a prismatic core as shown in Figure 1. The reactor operating pressure is 6.38 MPa and the core outlet temperature is 687 °C. Important characteristics of the MHTGR are:

1. The working fluid is helium.

2. The helium:

a. Enters the vessel through a pipe annulus near the bottom of the vessel in a direction that is at right angles to the vertical axis of the reactor vessel.

b. Makes a 90-degree turn upward and is distributed, via a plenum, into riser channels that lead upward to the upper plenum that is over the core itself.

c. Is directed downward from the upper plenum into the core.

d. Moves from the core into a lower plenum and is directed to a single circular cross-section pipe (the hot duct) that is mounted at a right angle to the reactor vessel centerline.

e. As the helium transits the core the gas temperature increases (by ~ 430°C).

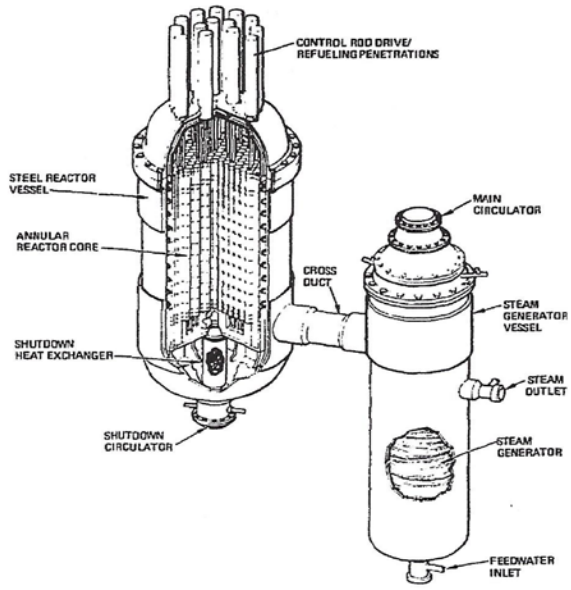

a) System Design Configuration and Helium Flow Path

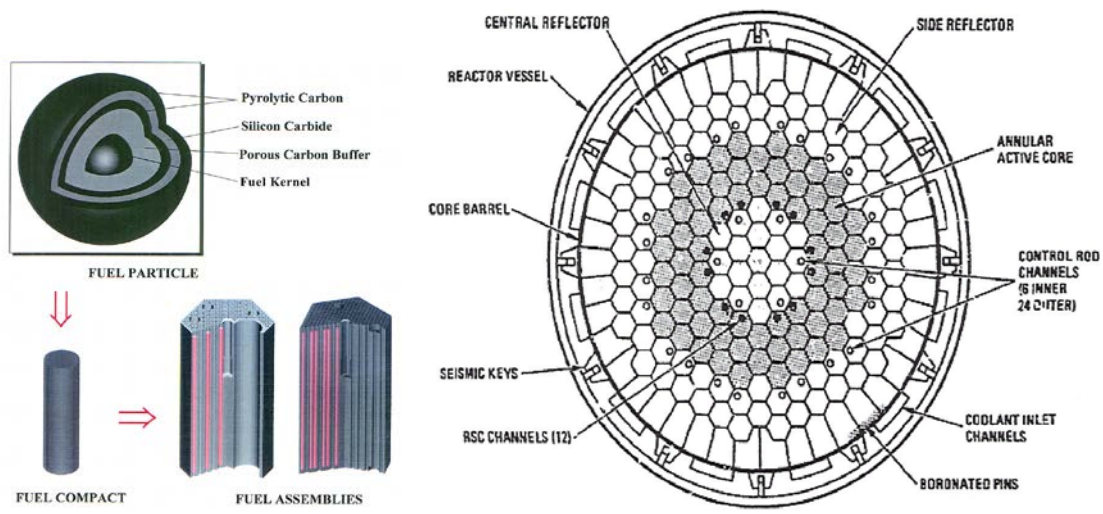

b) Prismatic Core Layout

Figure 1. MHTGR Design

3. The helium coolant flow distribution in the core is governed by the differential pressure between the upper and lower plena, the friction and loss coefficients in the respective flow paths, and the local power generation considering representative peaking factors.

4. The moderator in the reactor core is graphite—there are moderator blocks above, below, in the outer periphery, and in a central cylindrical region about the annular core blocks (see Figure 1). The annular core region itself consists of graphite blocks with TRISO fuel-particles dispersed in a graphite matrix—see Figures 1 and 2.

5. The design relies on forced flow, provided by blowers, of the helium coolant during operation.

6. The design relies on passive cooling during any loss-of-power scenario or loss-of-coolant scenarios.

7. The ultimate heat sink is the environment and all excess heat can be transported to the environment without natural circulation cooling inside the vessel via heat conduction and radiation to the vessel walls. From the vessel walls the heat is transported to the environment via a combination of radiation and natural circulation transport using a reactor cavity cooling system.

8. Air is present in the confinement such that if the reactor depressurizes, stemming from a leak in the primary pressure boundary, air will ingress into the vessel by diffusion and countercurrent density-gradient driven flow.

2.2 Description of MHTGR Core and Typical Cooling Channel

The MHTGR prismatic core design consists of typical block-type fuel elements that are hexagonal cross-section graphite blocks with dimensions of 0.794 m in length and 0.360 m across the flats of the cross-section. There are two types of block elements installed in the core. Figure 2 shows the standard fuel element and the reserve shutdown element respectively. These fuel elements with reflector elements compose the MHTGR core as shown in Figure 2 where a standard fuel element is shown in Figure 2a while a control and/or reserve fuel element is shown in Figure 2b.

The average core parameters and full power operating conditions are shown in Table 1. These parameters were used to design the scaled CCNY test section. To obtain specific conditions applicable to the CCNY single-channel experiments the global average values were applied to a single-channel and bypass passage.

Table 1. Core Parameters and Full Power Operating Conditions.

Parameter	MHTGR
Reactor Power, Q (MWt)	350
Tin/Tout (°C)	259/687
Reactor Pressure (MPa)	6.38
Reactor Mass Flow rate , (kg/s)	157.
Effective Core Height (m)	7.93
Number of Fuel Blocks	660
Diameter of Typical Fuel Element Cooling Channel (mm)	15.9
Design Bypass Flow Fraction (%)	10 ~ 15
Maximum Bypass Flow (%)	20.
Average Core Power per Cooling Channel per unit length (watts/mm)	6.32
Radial Peaking Factor	1.25
Axial Peaking Factor	1.30
Maximum Core Power per Cooling Channel per Unit Length (watts/mm)	10.27
Single-Channel Mass Flux (kg/s-mm^2)—assuming 10% bypass	0.000104
No Coolant Holes to Fuel Holes	2.06

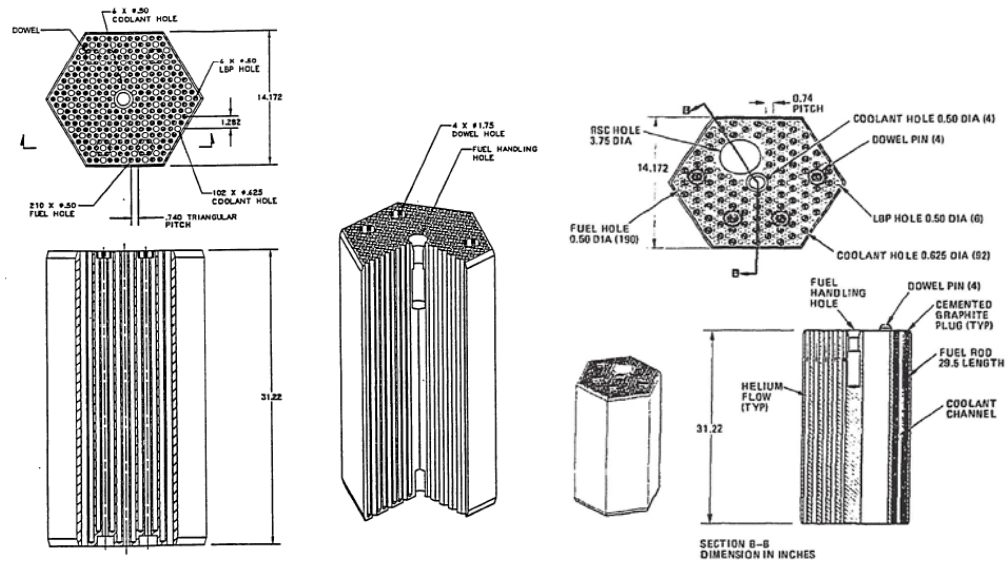

(a) Standard fuel element **(b) Reserve shutdown element**

Figure 2. Block-type fuel elements

3. PHENOMENA RELEVENT TO CCNY EXPERIMENT

The phenomena anticipated at operational conditions, off-normal conditions (the PCC scenario) and an accident condition (the DCC scenario) are summarized. Anticipated conditions for forced turbulent flow as well as both laminar and turbulent natural circulation are described using the work given in McEligot

and McCreery, 2004—pages 4 through 21—in sections 3.1 through 3.4 below with modifications/revisions by the authors of this report. Discussion on mixed convection and also the characteristics of using nitrogen in place of helium as the working fluid are drawn from Cochran et al., 2004—see sections 3.5—also with modifications/revisions by the authors of this report.

The forced flow experiments performed at CCNY were conducted using nitrogen as the working fluid. The natural circulation experiments were performed using helium, nitrogen, and helium-nitrogen mixtures—all representative of the PCC and especially the DCC scenarios. The anticipated phenomena are summarized in section 3.6.

3.1 Conditions During Normal Operation

Conditions of the flow through the lower regions of the core during normal operation are expected to be in the following ranges:

- Helium temperature: 600 - 700 °C
- Helium pressure: 40 – 65 atm
- Flow type: Near stagnant to highly turbulent

The design issue in this case is the need for determining whether degraded heat transfer may occur in the core stemming from laminarization and also predicting the core exit conditions..
.

3.2 Off-Normal or Accident Conditions in the Core

The off-normal scenario under study is the PCC "pressurized cooldown". For this scenario coolant is not lost so helium remains at the high pressure operating condition. Conditions are expected to be:

- Helium temperature: 400 - 1600 °C
- Helium pressure: 40 - 65 atm
- Flow type: Overall natural circulation

Stemming from the high thermal capacitance of the structure, the transient problem is quasi-steady with respect to the fluid physics. That is, fluid residence times in the passages are much shorter than the characteristic thermal response times of the solids forming the passage surfaces and determining the thermal boundary conditions; the convection problem can be treated as instantaneously steady. The flow varies from its initial high Reynolds number to near zero as the temperature differences are reduced, approaching thermal equilibrium. During this transient the flow sequentially passes from the high-Reynolds-number turbulent regime, through the low- Reynolds-number turbulent and laminarizing regimes, to laminar flow both upwards and downwards. For predictions, the most difficult and uncertain conditions are expected to be the low-Reynolds-number turbulent and laminarizing flows, particularly with gas property variation and complex geometries. Also of concern is the mixing of the hot plumes from the core into the upper plenum during this scenario; thus from the perspective of the CCNY facilities, the gas flow conditions at the core exit..

During a PCC scenario the buoyancy-driven flow phenomena that governs the flow between the inner hotter and the outer cooler channels within the core is of interest. The natural circulation is induced by differences in buoyancy forces but within the passages themselves the flow may be expected to be

predominantly forced by the pressure difference between the upper and lower plena (although this forced convection may be modified by buoyancy forces within the passages and thermal radiation across them). In the cooling channels the fluid is typically high pressure helium. Design issues are:

- Prediction of the buoyancy-driven coolant flow between hotter and cooler core channels
- Evaluation of the gas-flow conditions at the core exit from the perspective of determining boundary conditions to perform evaluations of thermal mixing of hot plumes in the core upper plenum before they reach metallic components and
- Need for an accurate prediction of the maximum fuel temperature of the reactor core.

This temperature is directly correlated to a clear understanding of the buoyancy-driven heat transfer within the core and outside the reactor vessel.

Perhaps the most severe accident condition is the depressurized conduction cooldown (DCC) scenario in which a leak in the primary depressurizes the primary and afterward enables containment air to move into the reactor vessel. Under this situation, recirculation in the core occurs but with a mixture of air and helium flowing through the cooling channels. The same design issues, with respect to the flow and heat transfer, are present for the DCC as are stated above for the PCC scenario. In addition the potential exothermic reactions between the oxygen-ladened air and hot graphite in the core also requires evaluation; however the phenomena inherent to this process are not the subject of this discussion.

3.3 Turbulent Flow at Normal Full Power Operation

The "deterioration" of turbulent convective heat transfer observed in some experiments with common gases may stem from radial property variation, acceleration, buoyancy or combinations of these phenomena, depending on the conditions of the applications [Hall and Jackson, 1969; McEligot, Coon and Perkins, 1970; Mikielewicz et al., 2002]. For pure forced convection in turbulent flow through an uninterrupted long duct at constant properties (i.e., low heating rates giving small temperature differences), the convective heat transfer from the fuel rods away from the entrance can typically be predicted by a relation of the form:

$$Nu_{Dh} \approx C\, Re_{Dh}^{0.8}\, Pr^{0.4} \qquad (1)$$

as shown for internal flow in tubes by Dittus and Boelter [1930]. For gas flow in circular tubes this relation becomes:

$$Nu_{D} \approx 0.021\, Re_{D}^{0.8}\, Pr^{0.4} \qquad (2)$$

[Drexel and McAdams, 1945; McAdams, 1954, page 219; McEligot, Ormand and Perkins, 1966; Kawamura, 1979]; for predicting surface temperatures, it is important to recognize that this coefficient is ten per cent lower than the common textbook value (i.e., liquids). Other relations have been recommended for circular tubes, but for Prandtl numbers near unity, most predict approximately the same magnitude [Taylor, Bauer and McEligot, 1988]. If this relation is rearranged to predict the convective heat transfer coefficient explicitly for a given mass flow rate and geometry, the variation with properties as the flow is heated along a duct takes the form:

$$h \sim c_p^{0.4}\, k^{0.6} / \mu^{0.4} \qquad (3)$$

With "strong" heating, the temperature variation leads to fluid property variation which, in turn, can cause several phenomena which may reduce or improve the convective heat transfer parameters. For gases, the property variations may be approximated by non-dimensional power laws as [Perkins, 1975]:

$$(\mu/\mu_{ref}) \approx (T/T_{ref})^a \; (k/k_{ref}) \approx (T/T_{ref})^b \qquad (4)$$

$$(\rho/\rho_{ref}) \approx (p/p_{ref}) \; (T_{ref}/T) \; (c_p/c_{p,ref}) \approx (T/T_{ref})^d \qquad (5)$$

The variation of the properties across the flow will modify the fluid temperature distribution and the relation between the heat flux and the temperature difference, i.e., the convective heat transfer coefficient. This effect can often be accommodated by introducing property ratios such as μ_w/μ_b (or in the case of gases, T_w/T_b) in empirical correlations [Kays, 1966]. For moderate fluid property variation, Gersten and Herwig [Section 16.1.7g, 1992] have derived analytical predictions of the exponents to be applied to the property ratios and, hence, temperature ratio in such correlations. For gases, the modification of the Nusselt number will be less than about five per cent if the temperature ratio is less that about 1.1 [McEligot, 1986].

In addition to the property ratios, a non-dimensional heat flux:

$$q+ = \beta \; q''_{wall} / (G \; c_p) \text{ where } \beta = - (1/\rho) \; (\partial\rho/\partial T)_p \qquad (6)$$

can provide an indication of whether the Nusselt number may be significantly changed. This quantity (or a comparable one) evolves when the mathematical description for cases with specified wall heat flux distributions [Bankston and McEligot, 1970] is nondimensionalized. (The definition becomes $q+ = q''_{wall} / (G \; c_p \; T)$ for fluids satisfying the perfect gas approximation.). For high-Reynolds-number flow without significant buoyancy or acceleration influences, a value of $q+ < \sim 0.0005$ is expected to induce a reduction in Nusselt number of less than five per cent as shown by an empirical correlation of McEligot, Magee and Leppert [1965]. Non-dimensionalization of the governing equations and their boundary conditions plus property variations shows that, in forced convection for a given geometry, the heat transfer coefficient can be represented as:

$$Nu = Nu\{Re_{Dh}, Pr, q+, a, b, d, x/D_h\} \qquad (7)$$

for gases at low Mach numbers satisfying the perfect gas approximation [Bankston and McEligot, 1970]. As noted above, the constants a, b and d are the exponents of the power law approximations for the properties and accommodate their dependencies on temperature. In turbulent flow the dependence on the distance from the thermal entry (x/Dh) becomes negligible after about thirty diameters. For typical gases, d is small and a and b are 0.5 to 1.0 approximately (for helium Worsoe-Schmidt [1966] employed a = b = 0.65 and d = 0.0) and the resulting function is not highly sensitive to small differences in their values. Thus, the same correlation can be used for data with air, nitrogen and helium [McEligot, Magee and Leppert, 1965]. In fact, for many gases the parameters q+, a, b and d can be replaced by a temperature ratio Tw/Tb raised to a fractional power as indicated above [Kays, 1966; Gersten and Herwig, 1992].

A significant variation of fluid properties across the flow makes it important for investigators to identify specifically at what temperature (or enthalpy) the properties are evaluated in their relations. There are many different definitions of the Reynolds number and, therefore, different magnitudes depending on the choices for property evaluation [McEligot, 1967, 1986]. Use of properties evaluated at the bulk enthalpy is usually most convenient for a designer in a case where the wall heat flux distribution is known because the enthalpy can be determined via an energy balance [Ward Smith, 1962]. It is also important to specify clearly the source of the fluid properties employed in the data analysis.

Heating of a fluid in a duct reduces its density so the velocity increases in the streamwise direction. This streamwise acceleration corresponds to a favorable streamwise pressure gradient, which is known to stabilize laminar boundary layers. One may hypothesize that for a turbulent flow, the acceleration would tend to stabilize bursting from the important viscous layer and thereby reduce turbulent transport [Corino and Brodkey, 1969]. With sufficiently large acceleration, a condition called "laminarization" can occur where flows expected to be turbulent show heat transfer parameters as low as in laminar flows [Bankston, 1970]. A measure of this phenomenon is an acceleration parameter K_v defined as (ν_b/V_b^2) (dV_b/dx) [McEligot, Coon and Perkins, 1970]. For an arbitrary cross section with some unheated surfaces, this parameter can be shown to be:

$$K_v \approx 4\ (P_h/Pw)\ q+\ /\ Re_{Dh} \tag{8}$$

which reduces to

$$K_v \approx 4\ q+\ /\ Re_D \tag{9}$$

for circular tubes. Moretti and Kays [1965] suggested that for K_v less than about 3 x 10-6 the flow would remain turbulent while for higher values it is likely to laminarize, giving a substantial reduction in heat transfer parameters. For flows accelerated by lateral convergence, Murphy, Chambers and McEligot [1983] found agreement with turbulent predictions when K_v < ~ 9.5 x 10-7 and agreement with laminar predictions when K_v > ~ 4 x 10-6.

If buoyancy forces become significant in vertical turbulent flow through a heated duct, the convective heat transfer can become inhibited in up-flow while in downflow it could be enhanced; these observations are opposite to those for laminar flow and are not as one might expect [Jackson, Cotton and Axcell, 1989]. With a specified wall heat flux, the Grashof number is usually defined as:

$$Gr^* = g\ \beta\ q''_{wall}\ D_h^4\ /\ (K_v^2) \tag{10}$$

Jackson [Mikielewicz et al., 2002] developed an approximate analysis for the onset of buoyancy influences in fully-established flow in terms of a buoyancy parameter which can be written as:

$$Bo = Gr^*\ \delta M+\ (\nu_w/\nu_b)\ (\rho_w/\rho_b)1/2\ /\ [2\ Nu_{Dh}\ Re_{Dh}^3\ (f\tau/2)^{3/2}\ Pr^{0.4}] \tag{11}$$

for an arbitrary heated surface in a vertical duct. Here $\delta M+$ is a distance near the edge of the viscous layer (Jackson used 26) and the Nusselt number and friction factor correlations are for pure forced convection to fully-established flow in a duct of the appropriate cross section and appropriate heated surface. A value of Bo ≈ 0.1 would correspond to the onset of buoyancy influences. Applying the Dittus-Boelter correlation for gases and the Blasius friction correlation, Jackson rearranged this criterion to:

$$Bo^* = Gr^*\ /\ (Re_{Dh}^{3.425}\ Pr^{0.8}) > \sim 6 \times 10^{-7} \tag{12}$$

for fully-developed flow in circular tubes. As shown in Figure 3, the data of Li [1994] and the semi-empirical model of Jackson and Hall [Jackson, Cotton and Axcell, eqn. 11, 1989] demonstrate that the value of Bo* ≈ 6 x 10-7 provides a reasonable order-of-magnitude estimate of the buoyancy threshold for vertical circular tubes. The relation for Bo above provides a means to extend this approach to non-circular vertical ducts with a heated surface. The treatments above are based primarily on well-developed flow in tubes. For short circular tubes, Cotton and Jackson [1990] predict that the threshold for buoyancy effects will require higher values of Bo* and that the maximum reduction in Nusselt number will be less than for fully-developed flow. These trends have been confirmed by the experiments of Vilemas and Poskas [1999]. One

can expect comparable behavior for non-circular ducts and for acceleration but the magnitudes have not been quantified.

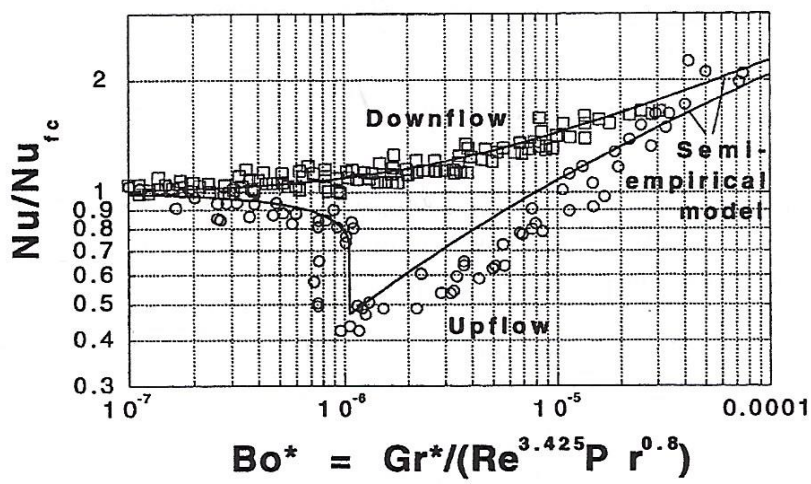

Figure 3. Effects of buoyancy on convective heat transfer for fully-developed flow in vertical circular tubes [Jackson, Cotton, and Axcell, 1989; Li, 1994]

Applying the same reasoning as for buoyancy influences, a comparable approximate criterion may be deduced for the onset of streamwise acceleration effects in pipe flow [Mikielewicz et al., 2002]. The resulting acceleration threshold parameter can be derived to be:

$$A_c = K_v\ \delta M + (\nu_w/\nu_b)\ (\rho_w/\rho_b)^{1/2} / [(f\tau/2)^{3/2}\ Pr^{0.4}] \qquad (13)$$

Again the criterion would be that this parameter should be less than about 0.1 to limit the effect on Nusselt number to less than about five per cent. The friction factor $f\tau$ to be used is the one for the heated surface involved.

For several gas-cooled reactor designs, at full power the Reynolds numbers are "high" and the parameters Bo and Ac will be sufficiently small that buoyancy or acceleration should not cause a reduction in heat transfer parameters. However, at reduced power the situation may change from that at design operating conditions for full power. When the flow rate is reduced to give approximately the same operating temperatures at reduced power, the heat flux and mass flow rate would be reduced approximately proportionately. In that case, q+ remains roughly the same, K_v varies as the reciprocal of the mass flow rate (and Reynolds number) and Bo* varies as $1/Re^{2.5}$ approximately. Consequently, buoyancy and acceleration effects may become important at reduced power. During a transient DCC scenario, the variation of these parameters and the likelihood of the phenomena will depend on the relative rates of decrease of the power and the mass flow rate.

It is recommended that experimentalists and analysts routinely calculate the parameters Re, T_w/T_b (or μ_w/μ_b or $c_{p,w}/c_{pb}$ as appropriate), q+, K_v, Bo and A_c in reducing their data or in predicting behavior when turbulent flow is desired. These quantities can serve as indicators to alert the investigator whether property variation, acceleration and/or buoyancy may have significant influences and, if so, which may be dominant. The discussion to this point has considered nominally turbulent flow at the inlet.

3.4 Laminar Flow

When the flow is laminar, as in a "pressurized cooldown," other non-dimensional parameters are appropriate. Non-dimensionalization of the governing equations for strongly-heated laminar flow in a vertical circular tube, as by Worsoe-Schmidt and Leppert [1965; Worsoe-Schmidt, 1966] yields a different non-dimensional heat flux parameter:

,

$$Q+ = r_w \, q''_{wall} / (k \, T) = D \, q''_{wall} / (2 \, k \, T) \qquad (14)$$

and a buoyancy parameter,

$$(Gr_{ws}/Re) = (g \, D^3 / \nu^2) / (G \, D / \mu) \qquad (15)$$

based on inlet temperature, plus the property-law exponents. The heat transfer predictions for uniform wall heat flux are shown in Figure 4 in terms of the local Nusselt number and local Graetz number (= π Re Pr / (4x)), both evaluated at the local bulk temperature. Flow is from right to left. One sees that for Q+ = 5 and negligible buoyancy there is only a slight influence on Nu and it is constrained to the thermal entry. So we may estimate that for Q+ less than unity or so, the effects of gas property variation on heat transfer parameters would be negligible. The effects on the wall shear stress are approximated by a correlation of the numerical results as:

$$f_{Re} \approx 16 \, (T_w/T_b) \qquad (16)$$

(This value is not the "apparent friction factor" needed for one-dimensional treatments [Bankston and McEligot, 1970].) For axially-varying wall heat fluxes as in a nuclear reactor, one can presumably apply the superposition technique of Bankston and McEligot [1969] with the heat transfer correlation provided by Worsoe-Schmidt. Figure 4 also gives insight into the magnitude of Gr_{ws}/Re needed to induce significant buoyancy influences on the convective heat transfer. Some insights into the complicated buoyancy influences were provided by Scheele and Hanratty [1962, 1963]. For well-developed axi-symmetric laminar flow with constant gas properties, several authors [Hallman, 1956; Hanratty, Rosen and Kabel, 1958; Morton, 1960] have derived analytical predictions via the Boussinesq approximation (i.e., density variation only affecting the gravitational body force). Results may be described in terms of the ratio of two dimensionless numbers:

$$G = g \, \beta \, q''_{wall} \, r_w^4 / (k \, \nu^2) \text{ and } R = Re_r = (V_b \, r_w / \nu) = Re_D/2 \qquad (17)$$

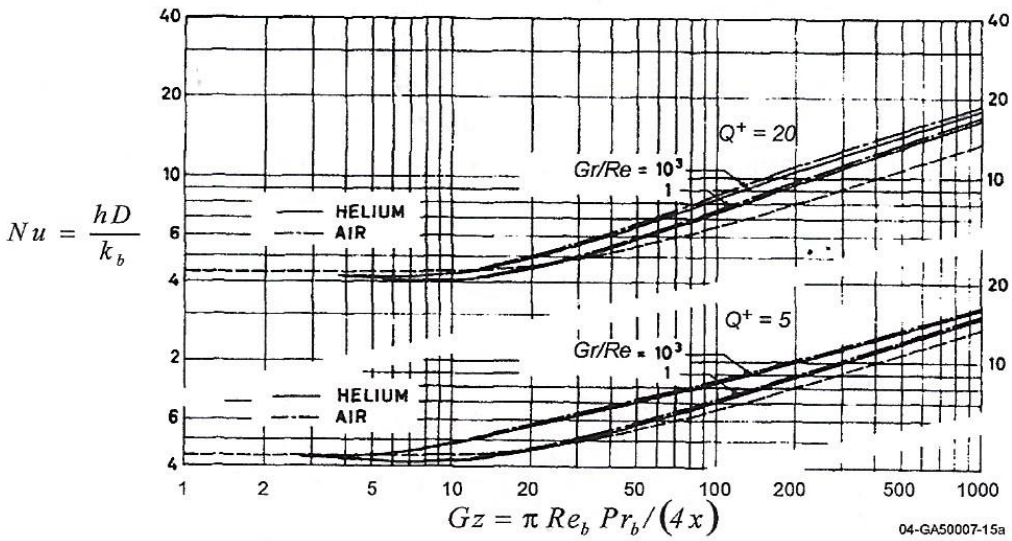

Figure 4. Prediction of local heat transfer parameters for air and helium in laminar flow, accounting for effects of gas property variation [Worsoe-Schmidt, 1966]

for buoyancy and flow rate, respectively. From the definitions, the quantity G/R can be shown to be equivalent to the grouping Gr_{ws} Q+ / (4 ReD). Effects on the velocity profiles are shown in Figure 5. In contrast to turbulent flow, an "aiding" laminar flow (heated upflow or cooled downflow) enhances heat transfer parameters; an "opposing" flow reduces these parameters until it becomes unstable and undergoes transition to a turbulent-like flow. In *aiding* flow the Nusselt number is estimated to be enhanced by about ten per cent when |G/R| is approximately twenty and transition is initiated at |G/R| ≈ 35-40 or more. For *opposing* flow, Scheele and Hanratty suggest that at G/R ≈ 9.87 there is a transition from axi-symmetry to a steady asymmetrical flow with local separation at the wall and then transition to an unsteady and later intermittently turbulent flow begins at about G/R ≈ 52-60.

Estimates of the values of some of the non-dimensional parameters have been made for the NGNP Point Design [MacDonald et al., 2003] at full power and at reduced power for both sizes of coolant channels roposed. In the standard fuel block there are 102 "large" coolant channels of 0.625 inch diameter and six "small" ones of 0.5 inch diameter. The control or shutdown blocks have 92 large channels and four small channels. Of the 66 columns of blocks, 54 have standard blocks and the remaining twelve are either control or shutdown blocks (see Figures 1 and 2). The channel lengths in individual blocks are about 62 and 50 diameters for small and large tubes, respectively; the nominal heated lengths for a core with ten active blocks vertically are therefore about 620 and 500 diameters, Thus, for turbulent flows, fully-developed conditions are expected to be reached. Conceptual designs have been developed for full power from 600 to 840 MWth, average inlet temperature of 491 C, average outlet temperature of 1000 C and corresponding helium flow rates [MacDonald et al., Table 12, 2003]. The estimates allowed a bypass flow fraction of 0.1 with heat fluxes calculated for nominal (average) conditions and for a peaking factor of 1.625 from radial and axial approximations.

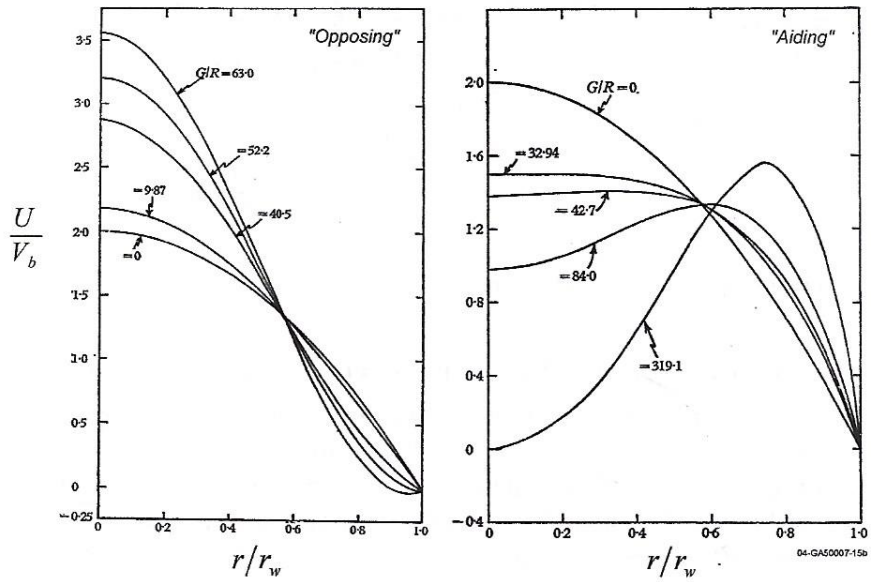

Figure 5. Effects of buoyancy on heated, fully-established laminar flow in vertical circular tubes with the Boussinesq approximation [Scheele and Hanratty, 1962]

The non-dimensional parameters Re, q+, K_v and Bo* were estimated at the entrance, mid-height and exit of the coolant channels for nominal full power and reduced powers of fifteen and ten per cent. The reduced power values were calculated for proportional reductions in gas mass flow rate. These order-of-magnitude estimates are compared to the approximate thresholds for significant effects in Figure 6. Since the viscosity increases with gas temperature, the local Reynolds number decreases along the channels from inlet to outlet. The subfigures in this figure can be considered as "operating conditions maps," comparable to regime maps for a range of experiments.

Highest gas bulk temperatures occur at the outlet from the active core. The range of outlet Reynolds numbers varied from about 57,000 for a high power core to about 2300 at ten per cent power. In all cases calculated, q+, K_v and Bo* were low relative to their thresholds for significant effects. A low value of q+ implies that gas property variation across the channels would have only a slight effect on the local Nusselt number and friction factor. The acceleration parameter K_v provides a measure of the likelihood of laminarization due to streamwise acceleration induced by the reduction in gas density with heating.

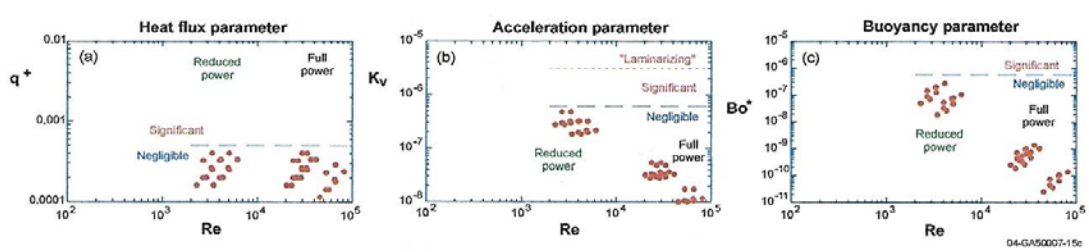

Figure 6. Operating conditions maps for the NGNP Point Design [MacDonald et al., 2003] during normal full and reduced power operations, order-of-magnitude estimates: (a) non-dimensional heat flux showing the significance of property variations, (b) acceleration parameter, and (c) buoyancy parameter.

Likewise, the buoyancy parameter Bo* indicates whether the heat transfer parameters may be enhanced or reduced as a consequence of buoyancy influences. For the proposed diameters of the coolant channels in the NGNP Point Design, neither property variation, acceleration **nor** buoyancy would be expected to have significant effects in normal full-power operations. For estimates of wall and outlet temperatures for the "hot channel" problem in full-power operation, a correlation such as the one of McEligot, Magee and Leppert [1965]:

$$Nu \approx 0.021\ Re^{0.8}\ Pr^{0.4}\ (T_w/T_b)^{-1/2} \tag{18}$$

should be adequate beyond the thermal entry for calculations with an extended systems code for Re > ~ 2500. For accident conditions or for designs with different tube diameters, the nondimensional parameters should be recalculated and these conclusions should be re-assessed.

Since a doubling of diameter will increase the buoyancy parameter by more than an order-of magnitude, mixed convection could become important in operation at reduced power. Estimates of the magnitudes of the governing parameters for a hypothetical PCC were also developed. Paul Bayless, INL provided predictions of this transient from a typical systems code (Athena) and appropriate parameters were calculated from their definitions. Resulting predictions of the Reynolds number variation (non-dimensional flow rate) for three locations each in the inner, middle and outer core rings are shown in Figure 7. In this figure a positive sign corresponds to downflow as in full power operation. One sees that in this scenario the Reynolds number decreases to below 2000 within about sixty seconds and then remains below an absolute value of about 500, indicating that laminar flow would be likely. Flow is predicted to become upwards in the inner and middle rings and to remain downward in the outer ring; heat transfer may be to or from the gas, depending on location and timing. During the initial transient, the turbulent criteria are all predicted to remain below their thresholds for significant effects -- as in normal steady operations.

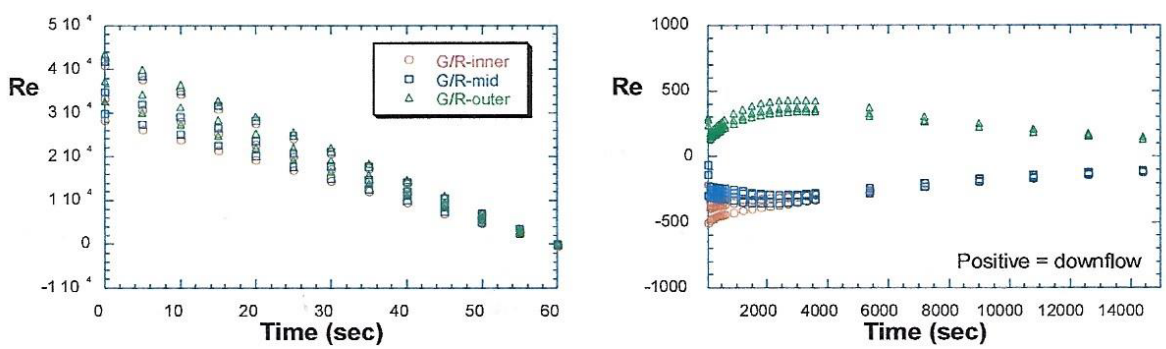

Figure 7. Estimated flow rate trends during a hypothetical PCC in a typical NGNP concept.

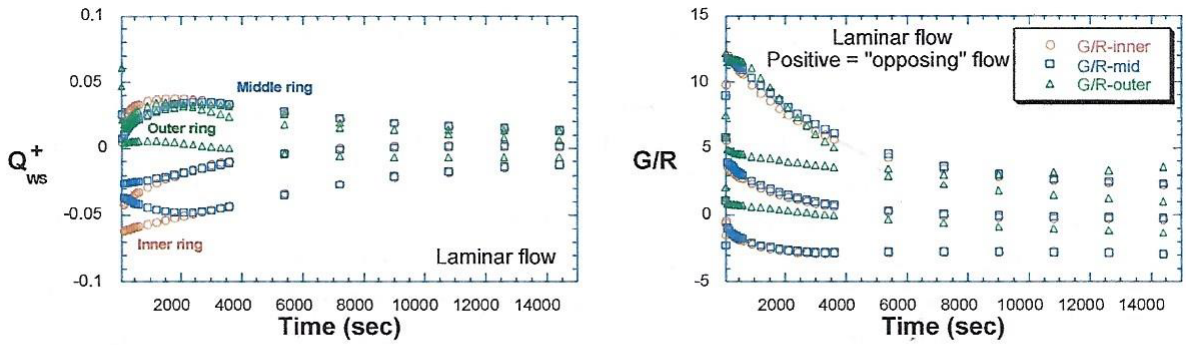

Figure 8. Estimated heat flux (a) and buoyancy (b) trends during a hypothetical PCC in a typical NGNP concept. Definition of G/R from Scheele and Hanratty [1962, 1963]

In the expected laminar flow after sixty seconds, different non-dimensional governing parameters are pertinent than in turbulent flow. As noted above, a quantity Q+ replaces q+ and a Grashof number can be used as G/R to estimate buoyancy effects. Predictions of these quantities are demonstrated in Figure 8. Effects of property variation across the channel are expected to be slight when Q+ is less than five so this scenario with the predicted Q+ < 0.05 can be represented by a constant properties approximation (with the Boussinesq approximation to handle buoyancy). In Figure 8(b) a positive sign corresponds to an opposing flow due to our convention for flow direction. For *opposing* flow, Scheele and Hanratty [1962] suggest that at G/R ≈ 9.87 there is a transition from an axisymmetrical to a steady asymmetrical flow with local separation at the wall and then transition to an unsteady and later intermittently turbulent flow begins at about G/R ≈ 52-60. During the first twenty minutes or so magnitudes are above thefirst criterion, indicating the possibility of asymmetric flow at some locations and a need for a three-dimensional solution allowing for separation. Otherwise, a simple, fast "parabolic" (marching) solution as by Worsoe-Schmidt [1966], Perkins and McEligot [1975] and others would be adequate for CFD approaches provided the flow direction is known.

In summary, for cooling channels of the NGNP concept chosen for the Point Design [MacDonald et al., 2003] and also the reference VHTR (MHTGR), during normal operations at full and reduced power, buoyancy and streamwise acceleration effects are not expected to be significant. During the long-term natural circulation in a pressurized cooldown, property variation is not expected to be significant but buoyancy influences should be observable and the resulting instability might be sufficient to cause an asymmetric, separating low which could be a challenge to predict properly.

3.5 Mixed Convection

Mixed convection studies were performed at a Massachusetts Institute of Technology (MIT) experimental facility consisting of a single cooling channel of 16 mm diameter and 2 m length. The scaling of the facility and results were reported in Cochran et al, 2004 and Lee et al, 2005. The basis for these studies are described below.

3.5.1 Defining the Key Non-Dimensional Numbers Used for MIT Experiments

An analysis for flow in a vertical heated round tube for buoyancy-induced mixed-convection was carried out at MIT by Parlatan in his Ph. D. thesis [Parlatan 1993]. He made the following simplifying assumptions:

1. Steady-state was assumed in macroscopic or time-averaged scale, i.e., turbulent fluctuations were neglected,
2. The Boussinesq approximation was employed, i.e., the density variations were neglected everywhere except in the gravity term of the momentum equation,
3. The energy generation terms due to intrinsic heating, thermal expansion and dissipation were neglected,
4. Flow was assumed to be axisymmetric and fully-developed.

The following characteristic quantities were chosen to non-dimensionalize the governing equations:

V	characteristic velocity,
D	characteristic length (tube inside diameter)
ρ_o	fluid centerline density
T_w	wall inside temperature
T_o	fluid centerline temperature

The following dimensionless variables were defined in terms of the above characteristic quantities:

$$u^* = u/V \tag{19}$$

$$r^* = r/D \tag{20}$$

$$z^* \; z/D \tag{21}$$

$$\widetilde{p^*} = \frac{\tilde{p}}{\rho_0 V^2} \tag{22}$$

$$t^* = t/(D/V) \tag{23}$$

$$T^* = \frac{(T - T_o)}{(T_W - T_o)} \tag{24}$$

The resultant non-dimensional axial momentum and energy equations were:

$$\frac{Gr_{\Delta T}}{Re^2} - \frac{\partial \widetilde{p^*}}{\partial z^*} + \frac{1}{r^*}\frac{\partial}{\partial r^*}\left[\left(\frac{1}{Re} + \frac{\mu_t}{\rho V D}\right) r^* \frac{\partial u^*}{\partial r^*}\right] = 0 \tag{25}$$

$$Re\frac{\partial T^*}{\partial z^*} = \frac{1}{r^*}\frac{\partial}{\partial r^*}\left[\left(\frac{1}{Pr} + \frac{\alpha_t}{\nu}\right) r^* \frac{\partial T^*}{\partial r^*}\right] + \frac{\partial}{\partial z^*}\left[\left(\frac{1}{Pr} + \frac{\alpha_t}{\nu}\right)\frac{\partial T^*}{\partial z^*}\right] \qquad (26)$$

(Equations 2.13 and 2.14 of Parlatan's Ph. D. Thesis (1993))

where

$$Re_D = \rho VD/\mu = VD/\nu \qquad \text{(Reynolds No.)} \qquad (27)$$

$$Pr = \mu c_p/k = \nu/\alpha \qquad \text{(Prandtl No.)} \qquad (28)$$

$$Gr_{\Delta T} = Gr = g\beta(T_w - T_o)D^3/\nu^2 \qquad \text{(Grashof No.)} \qquad (29)$$

It is not surprising that these three non-dimensional parameters are expected to be important during the mixed convection regime since the first two (Reynolds and Prandtl numbers) are known to be important for forced convection and the second two (Prandtl and Grashof numbers) are important for free or natural convection. Various combinations of these parameters have also been used in the heat transfer literature. For developing flow, z* or z/D becomes an additional parameter.

It has been argued by various investigators [e.g., Bejan, 1993] that

$$Ra = Gr \times Pr = g\beta(T_w - T_o)D^3/(\nu\alpha) \qquad \text{(Rayleigh No.)} \qquad (30)$$

is a more appropriate non-dimensional parameter than Grashof No. (Gr) to determine the growth of thermal boundary layer, and therefore the heat transfer coefficient, for free convection. Even the early researchers like Metais and Eckert (1964) proposed Re vs. Ra co-ordinates to plot their data for mixed convection. In our earlier work [Williams et al. 2003], we also used the Re – Ra plot and we would like to continue to use the same plot in the present project.

The demarcation between the forced and mixed convection regimes in turbulent flow is of considerable importance since it determines the onset of significant buoyancy effect which can cause deterioration of heat transfer in the aided mixed convection regime. Several criteria have been suggested in the literature [Aicher and Martin, 1997; Jackson and co-workers, 1989). After a review of the existing criteria, Williams et al (2003) proposed to use the criterion of Aicher and Martin (1997) which was based on the parameter:

$$Ra^{0.333}/(Re^{0.8}\, Pr^{0.4}) \qquad (31)$$

which may be considered as the ratio of heat transfer due to natural or free convection to the heat transfer due to forced convection. The above parameter, let us call it as the Aicher-Martin Parameter, is a plausible candidate for demarcation of boundaries among the forced, mixed and free or natural convection since the

Rayleigh number (Ra) characterizes the strength of the buoyancy forces (or free convection) and Reynolds number (Re) represents the strength of the forced convection. The Aicher-Martin parameter equal to 0.05 denotes the boundary between the forced and the mixed convection regime for turbulent flow. If the Aicher-Martin parameter is greater that 0.05, the buoyancy effects start to become important and the mixed convection regime begins. For common gases, Prandtl number (Pr) may be taken as ~0.7. In that case, the boundary between the forced and the mixed convection for turbulent flow can be expressed by:

$$Ra^{0.333}/Re^{0.8} = 0.04335 \tag{32}$$

Several criteria [Aicher and Martin, 1997] are also available for demarcation of the boundary between the mixed and the free or natural convection for turbulent flow. Burmeister (1993) has suggested the use of Gr/Re^2 for demarcation of the regime boundaries. He argues that Gr/Re^2 represents the ratio of buoyancy to inertial forces and for the free convection heat transfer regime the value of Gr/Re^2 should be greater than unity. However, Williams, et al (2003) found that Gr/Re^2 equal to unity closely represented the criteria of Aicher and Martin (1997), Tanaka, et al (1987) for the boundary between the mixed and the free convection, particularly for the turbulent flow. For Prandtl number of 0.7, the above criterion of Gr/Re^2 equal to unity for the boundary between the mixed and free convection becomes:

$$Ra/Re^2 = 0.7 \tag{33}$$

For laminar flow, the demarcation among the forced, mixed and free or natural convection is of secondary importance since the heat transfer for the aided mixed convection for laminar flow can be expressed as a combination of the forced and natural convection as suggested by Churchill (1998):

For uniform wall temperature:

$$Nu^3_{mc} = Nu^3_{fc} + Nu^3_{nc} \tag{34}$$

For uniform heat flux:

$$Nu^6_{mc} = Nu^6_{fc} + Nu^6_{nc} \tag{35}$$

Based on the above discussion, a tentative map for the various regime boundaries for common gases is shown in Figure 9. One of the objectives of the present experimental program is to generate data to either confirm or improve upon this tentative map.

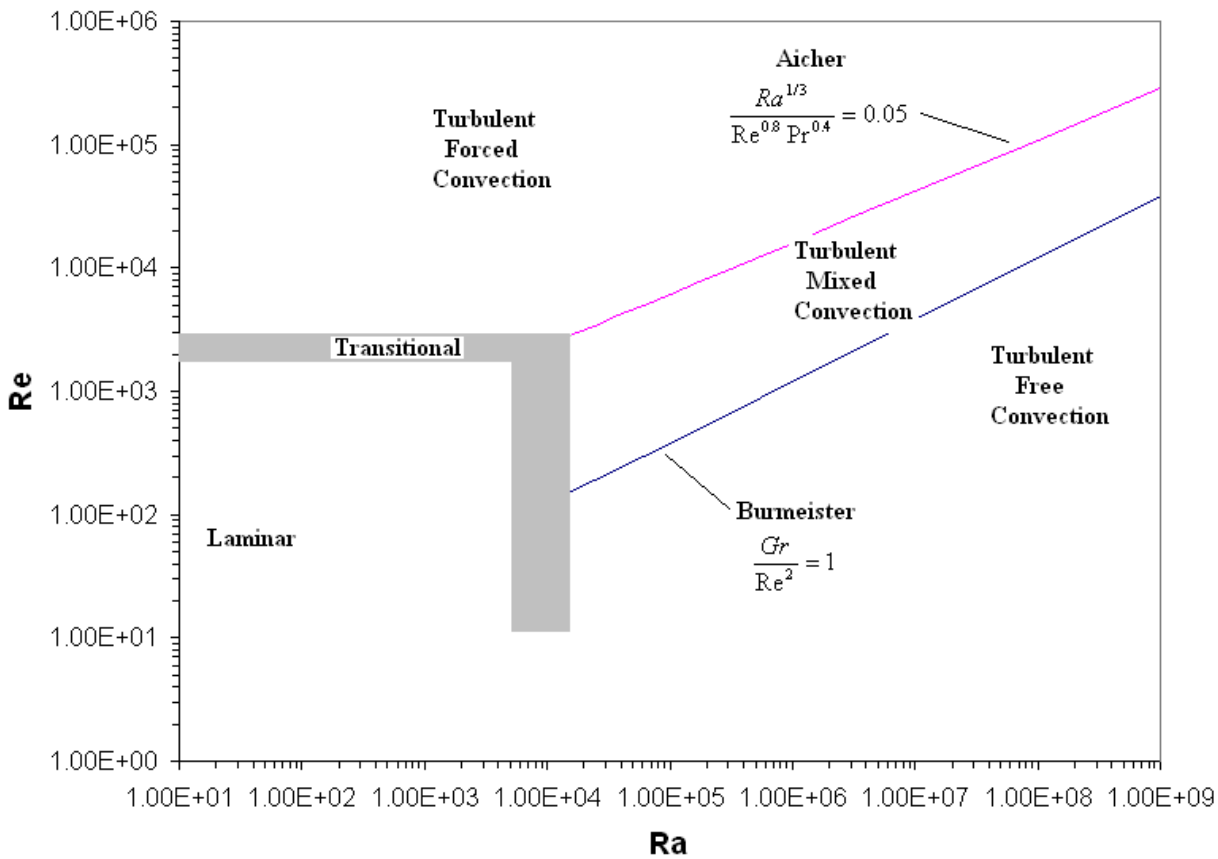

Figure 9. Tentative Forced-mixed-free convection boundaries for Pr = 0.7

Jackson and co-workers (1989) preferred to use Grashof number (Gr*) based on the wall heat flux instead of Grashof number (Gr) based on the wall-to-bulk temperature difference to correlate their data for mixed convection. For turbulent flow, they introduced the Buoyancy Parameter (Bo*) defined Equation (12) and given in section 3.3.

As per Jackson (1998), the onset of buoyancy influence for gas flow in round tubes begins at Bo* > 5 x 10^{-7}. This criterion for forced-to-mixed convection heat transfer boundary for turbulent was examined with the experimental data to collected during the program [Lee et al, 2005].

At low flow rates, expected during the passive decay heat removal phase, the streamwise acceleration effect due to heating of gas and thereby increasing the axial velocity could also be important. With sufficiently large acceleration, a condition called "laminarization" can occur where flows considered being turbulent show lower heat transfer as in laminar flows (Bankston 1970). Following the work of Morretti and Kays (1965) for external flow, Bankston (1970) and McEligot, Coon and Perkins (1970) defined the acceleration parameter, K_v, for internal heated flow as:

$$K_v = (\nu/V_b^2)\,(dV_b/dz) \qquad (36)$$

where V_b is the local bulk velocity, ν is the kinematic viscosity, and z is the axial streamwise distance. For constant-area flow of a perfect gas with negligible change in pressure, the above acceleration parameter can be written as:

$$K_v = (\nu/V_b\, T_b)\, (dT_b/dz), \qquad (37)$$

where T_b is the local bulk temperature. Using the steady-state energy balance for a heated round tube, the above acceleration parameter can finally be written as:

$$K_v = 4\, (q_w''/Gc_pT_b)/(V_bD/\nu) = 4q^+/Re, \qquad (38)$$

where q^+ is the non-dimensional heat flux and Re is the Reynolds number. The result on the far-right of equation (32) is the form given in section 3.3—see equation (9). As per McEligot and Jackson (2004), laminarization is expected to be prominent at $K_v > \sim 4\text{x}10^{-6}$.

Based on the above theoretical considerations, it is clear that the Reynolds number (Re), Grashof number (Gr) and Prandtl number (Pr) or alternatively Rayleigh number (Ra), and non-dimensional heat flux (q^+) are the main non-dimensional numbers that we should match between the prototypical (or GFR) and test conditions. Other parameters, namely, the Buoyancy parameter (Bo*) and the accelerator parameter (K_v) will be matched automatically as we match Re, Gr, Gr*, Pr and q^+ between the prototype and the model test section.

3.5.2 On the Use of Nitrogen as a Working Fluid

Using nitrogen as a working fluid, in place of helium, is sometimes an attractive approach in separate-effects experiments of the sort performed at MIT and CCNY. Reasons leading to the use of nitrogen instead of helium are:

- Incompatibility of existing equipment to pump one of the desired gases at the desired conditions.
- Using to advantage the lesser state requirements for nitrogen as a working fluid (in contrast to helium) to obtain equivalent key parameters such as Reynolds number or the other key nondimensional numbers discussed in previous sections of this chapter.

Studies performed by MIT experimentalists using their LOCA-COLA code [Cochran et al, 2004] showed equivalent Reynolds numbers (e.g., Re = 1200) are achieved for helium and nitrogen in their 16 mm diameter test section at a 1 MPa pressure, average channel temperature of ~430 °C, and a helium mass flow rate of $4.3\text{x}10^{-4}$ kg/s for helium and at a 0.13 MPa pressure, average channel temperature of ~260 °C and a nitrogen mass flow rate of $3.8\text{x}10^{-4}$ kg/s for nitrogen. Thus, the nitrogen state conditions to obtain an equivalent Re number are approximately an order-of-magnitude lower in pressure.

Using such an approach, a Rayleigh number versus Reynolds number map for the MIT facility was produced as shown in Figure 10. Similar approaches may be used in other experimental programs. The data labeled “prototype” were calculated using LOCACOLA while the “Model” data using either carbon dioxide, nitrogen, or helium were obtained in the MIT flow loop.

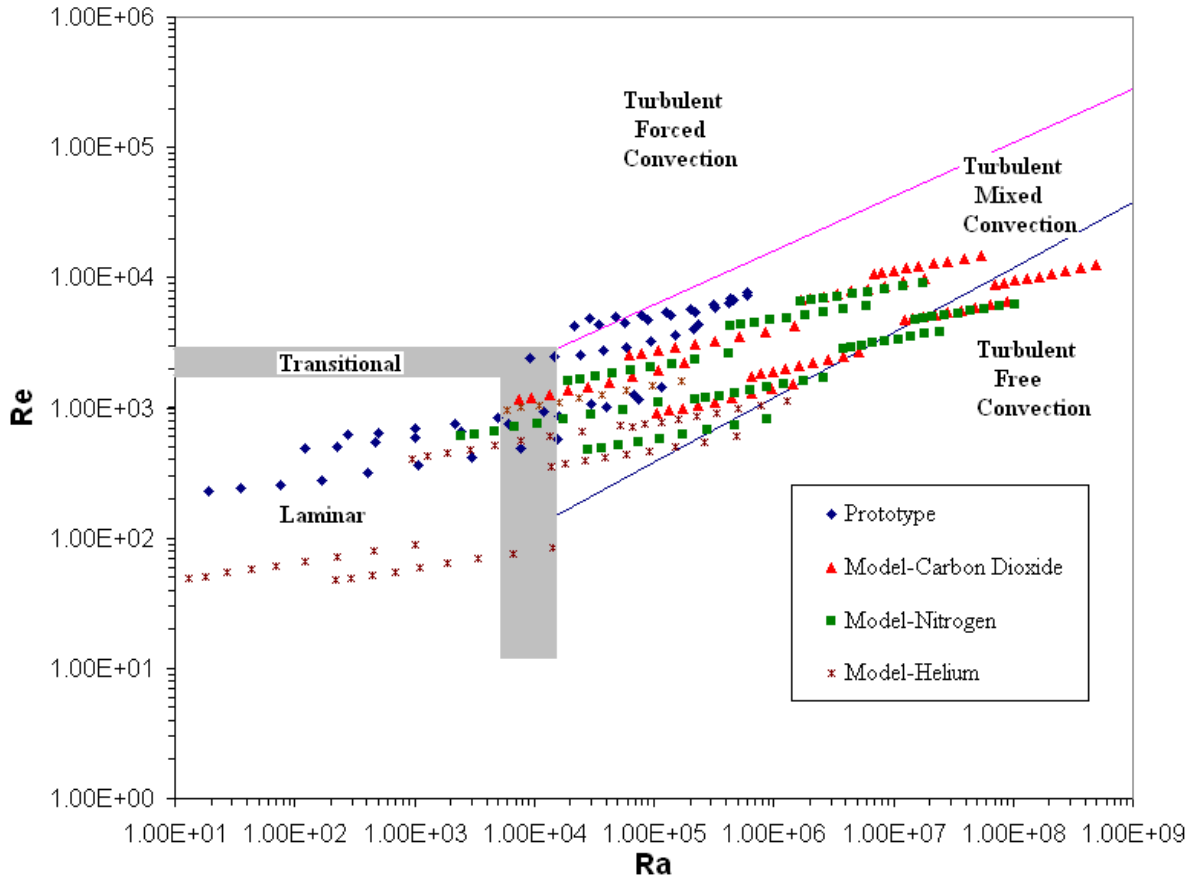

Figure 10. Complete Ra vs. Re map generated from experimental loop

3.6 Summary

Key nondimensional numbers are identified in this chapter. In addition to the Reynolds number and Nusselt number of forced turbulent flow, other nondimensional numbers of importance are:

- Heat flux: q^+--see equation 6
- Acceleration parameter: K_v—see equations 8 and 9
- Grashof number: Gr—see equation 10
- Buoyancy parameters: Bo and Bo^*--see equations 11 and 12
- Acceleration parameter: A_c—see equation 13
- Rayleigh number: Ra—see equations 32 and 33

Of note is the observation that: "…it is clear that the Reynolds number (Re), Grashof number (Gr) and Prandtl number (Pr) or alternatively Rayleigh number (Ra), and non-dimensional heat flux (q^+) are the main non-dimensional numbers that we should match between the prototypical (or GFR) and test conditions. Other parameters, namely, the Buoyancy parameter (Bo*) and the accelerator parameter (K_v) will be matched automatically as we match Re, Gr, Gr*, Pr and q^+ between the prototype and the model test section."

Also, nitrogen is a useful alternative to helium as a working fluid—since it offers advantages leading to operation at less demanding state conditions than helium. This point is discussed in section 3.5.2.

4. CALCULATION: MHTGR FLOW AND HEAT TRANSFER IN CORE DURING PCC AND DCC SCENARIOS

The calculations discussed in this chapter were performed using RELAP5-3D [RELAP5 Code Development Group, 2014] by P. Bayless [Bayless, 2018]. The two calculations were performed using a model of the MHTGR undergoing the PCC scenario and the DCC scenario following operation at 100% power.

Following a loss-of-offsite power, the circulators in a very MHTGR quickly coast down in conjunction with insertion of the control rods. Thereafter, if the VHTR does not have a leak in the primary pressure boundary, the scenario is commonly known as a PCC. On the other hand, if boundary does have a leak in the primary pressure boundary, the scenario is commonly known as a depressurized conduction cooldown (DCC).

In either case, the core flow, normally downward-oriented under operational conditions, reverses and flows upward. The core flow rate is governed by the heat transferred to the gases in the core and is affected by the core geometry, frictional pressure-loss characteristics, and relevant material properties. The core flow in either situation is density-gradient dominated in the core coolant channels. Gases flow from the core region into the upper plenum. Depending upon the flow velocity, either the gas impinges on the upper vessel head as jets or it flows gently upward to merge with gases in the upper regions of the plenum. In some situations, the flow may emerge from the core coolant channels as a jet and then evolve to a plume prior to reaching the nearest structure, as it moves upward.

To investigate the behavior of the helium flow in the cooling channels during these scenarios, Reactor Excursion and Leak Analysis Program (RELAP)5-3D calculations were performed. RELAP5-3D is a systems analysis tool and is generally used to calculate global behavior in large regions of a system. To study the flow in an MHTGR core, the core region was divided into three rings in a plane normal to the coolant channel flow. The inner ring is in the center. The middle ring is an annular region nested between the inner and outer rings while the outer ring is the peripheral region—represented as an annulus.

4.1 PCC Scenario

The average Reynolds number and average temperature of the gas flowing from the core into the upper plenum for the three rings are plotted in Figures 11 and 12. Because the model was constructed to study the capability of the MHTGR to survive a PCC scenario without the availability of external heat sinks, e.g., a heat exchanger located in the balance of plant, natural circulation flow was restricted to the MHTGR vessel.

Figure 11, showing the average Reynolds-number behavior, indicates that throughout the PCC scenario the average exit Reynolds numbers of the gases moving from the core into the upper plenum never exceed 700. Therefore, they are for the most part laminar, with only a low probability of forming a jet capable of impinging on the upper surfaces of the upper plenum. The flow has the following characteristics:

- Flow from the rings with highest power (the inner and outer rings) is upward while flow in the peripheral ring is downward
- The Reynolds number in the inner and middle rings is less than 200 from 8 hours (28800 s) onward.

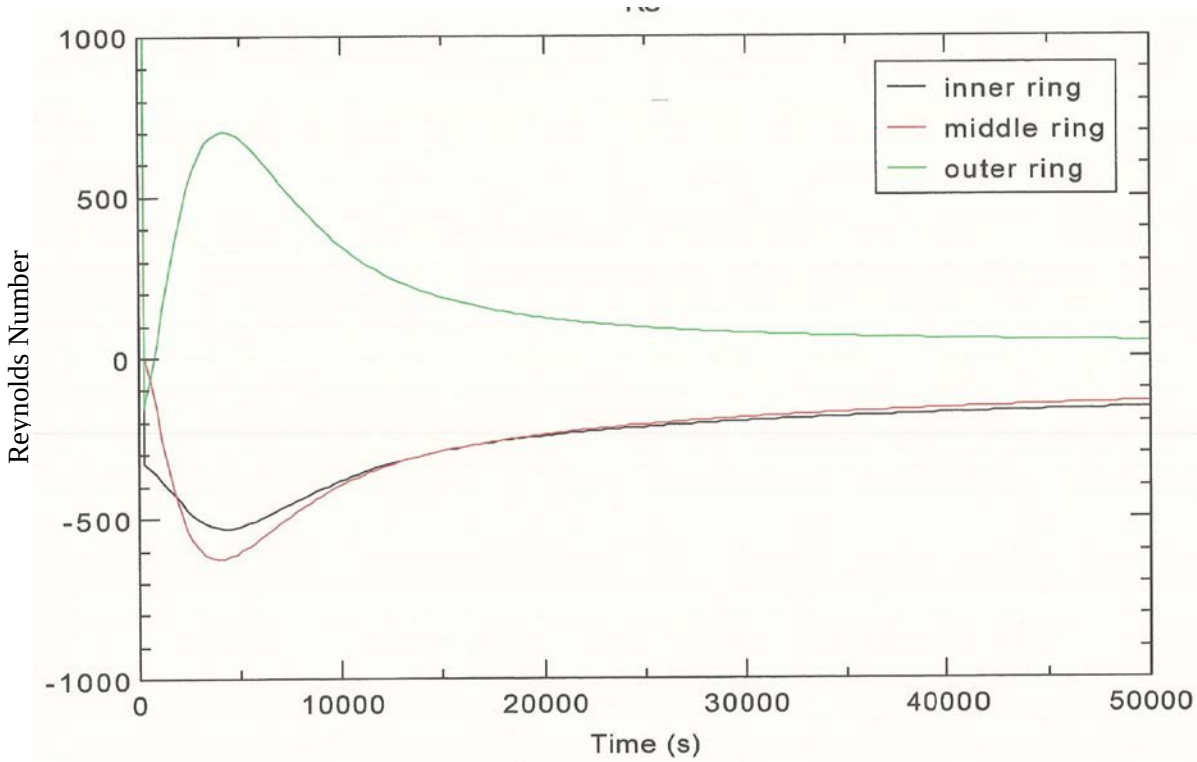

Figure 11. Average Reynolds number of gases moving from core into upper plenum of MHTGR during PCC scenario from the inner, middle and outer rings.

Figure 12 shows the average temperature for the gas moving from the three rings into the upper plenum. The average temperature reaches 900 K in about 3 hours (627°C), but does not reach peak temperature (950 K = 677°C) until 2.8 days (2.4×10^5 s). However, it is instructive to examine the changes in coolant temperature between the top of the active core region and the top of the reflector blocks. Keeping in mind that there are two reflector blocks above the top of the active fuel region and that there are no sources of heat in the reflector blocks, the flow moving from the active core region into the reflector blocks undergoes cooling. Figure 13 shows the average temperature of the coolant flow at the exit of the active core region for the inner and middle rings as the flow enters the reflector blocks. Also shown is the average coolant temperatures in the upper plenum.

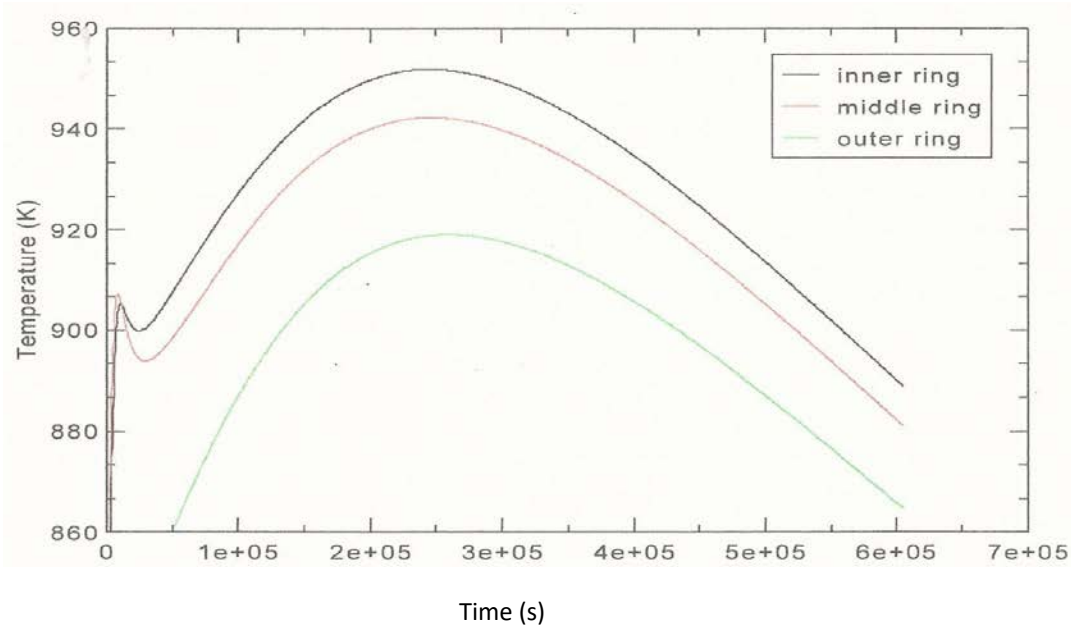

Figure 12. Average temperature as a function of time (s) of gases moving from core into upper plenum of MHTGR during PCC scenario from the inner, middle, and outer rings.

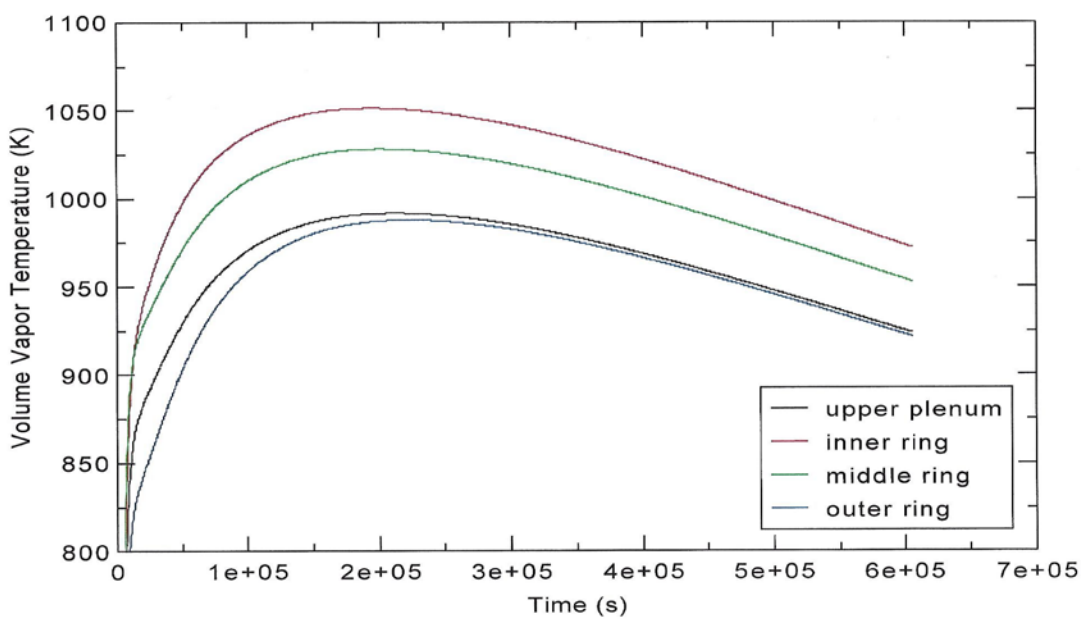

Figure 13. Average temperature of gases moving from active core region into upper reflector compared to average gas temperature in upper plenum.

The difference between the temperatures of the flow entering the reflector blocks and the helium entering the upper plenum is indicative of heat losses sustained by the coolant flow to the reflector blocks; the difference ranges between ~40 and ~70 K. The reflector blocks are initially cooler than the core and as such are a heat-storage repository by design for the MHTGR for the PCC scenario.

The above calculation suggests the following:

- The reflector blocks exert an important influence on the temperature and behavior of the helium coolant prior to moving into the upper plenum.
- Cooling sustained by the helium coolant in the region of the reflector blocks will act to increase the helium density adjacent to the wall in the reflector region and will reduce the gas velocity adjacent to the wall. This effect will show as a marked velocity gradient near the wall, which is more pronounced than would be obtained for isothermal flow.

4.2 DCC Scenario

The average Reynolds number and average temperature of the gas flowing from the core into the upper plenum are shown in Figure 14 and Figure 15. The calculation was performed using the same model for the reactor vessel as for the PCC calculation. The confinement air was allowed to flow into the lower plenum following the depressurization, and the natural circulation flow moving upward from the core into the upper plenum was allowed to flow down the riser and out the hot duct outer annulus into the confinement. Therefore, all three core rings had gas moving upward into the upper plenum. However, the gas in the core moved at very low Reynolds numbers for the DCC scenario, as indicated in Figure 14. Thus, even though the gas temperatures were much higher for the DCC scenario than for the PCC scenario, the gas clearly moved into the upper plenum via very slow moving plumes and created stratified gas layers that would result in uniform heat transfer to the upper plenum structures with a low probability of localized high thermal stresses.

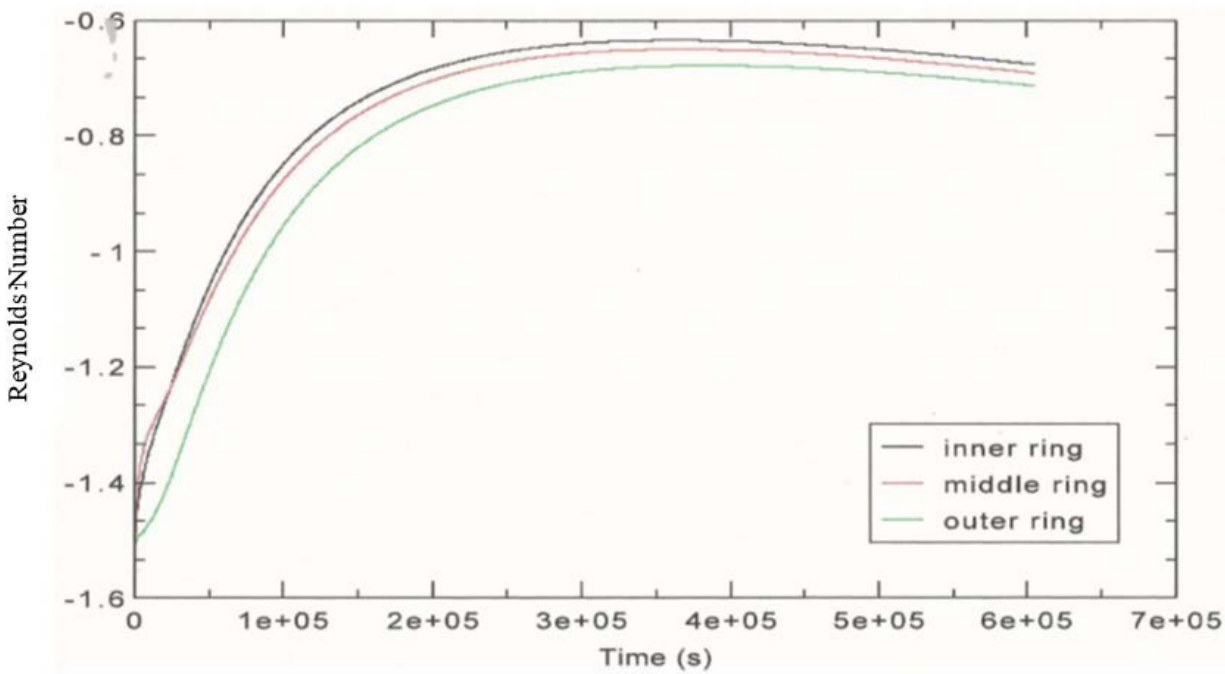

Figure 14. Average Reynolds number of gases moving from core into upper plenum of MHTGR during DCC scenario from the inner, middle, and outer rings.

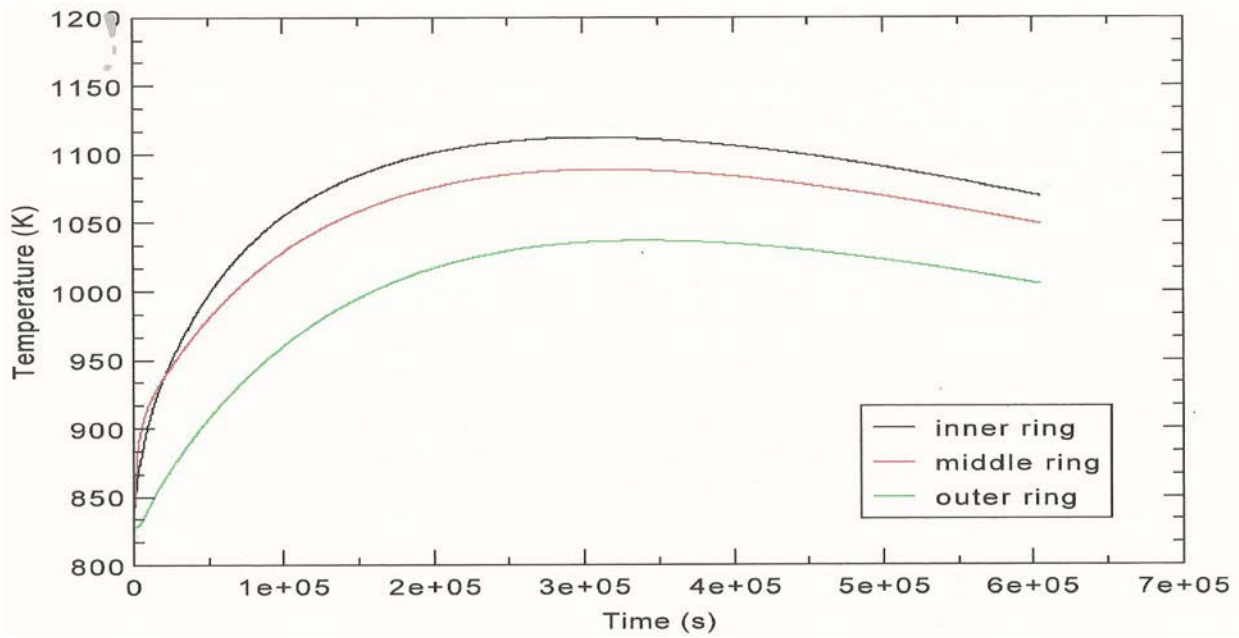

Figure 15. Average temperature of gases moving from core into upper plenum of MHTGR during DCC scenario from the inner, middle, and outer rings where (a) an irradiated active core region will likely have a geometrical mismatch with the upper reflector blocks and (b) the resulting plenum-like region between the active core and reflector blocks results in a flat entrance velocity profile in the reflector block cooling channels.

4.3 Summary

The calculations discussed in Chapter 4 predict:

- Laminar flow conditions in the core region for most of the PCC scenario in the MHTGR for the average cooling channels. However, the behavior in "hot" cooling channels, in combination with fuel peaking factors may result in turbulent or mixed convection conditions—and these conditions should be investigated.
- Very low flow (essentially stagnant) conditions in the core region during the DCC scenario.

5. CCNY EXPERIMENTS: RELEVANCE TO HTTF AND SCALING

The CCNY High Pressure and Temperature Test Facilities (HPTTF) are described in Kalaga, Rudra, and Kawaji, 2019 and were designed to duplicate core cooling channel conditions representative of those in the MHTGR for the operational, PCC, and DCC scenarios. The CCNY Forced Circulation Bypass Flow Loop (FCBFL) facility was used to perform forced flow experiments and the CCNY Natural Circulation Flow Loop (NCFL) facility was used for natural circulation experiments.

The CCNY facilitie are separate effects facilities designed to provide data to validate high-fidelity numerical analysis codes and to complement and supplement the data recorded in the High Temperature Test Facility (HTTF)—Woods et al., 2015. As separate-effect test facilities the CCNY facilities were operated at steady-state conditions while the core channel flow and simulate power levels were adjusted to obtain the desired flow and heat transfer conditions. Insulation on the outer diameter of the graphite test

section minimized energy losses and allow an adiabatic boundary condition at the outer diameter of the graphite section.. The FCBFL facility core test section had a single core cooling channel with an inner diameter of 16.8 mm and a single bypass channel with rectangular dimensions: 3 mm x 40 mm while the NCFL facility had a single core cooling channel with an inner diameter of 16.8 mm. The maximum available power for the FCBFL experiments was 9.2 KW while the maximum available power for the NCFL experiments was 6.9 KW. Schematics of the FCBFL and NCFL test facilities are shown in Figures 16 and 17.

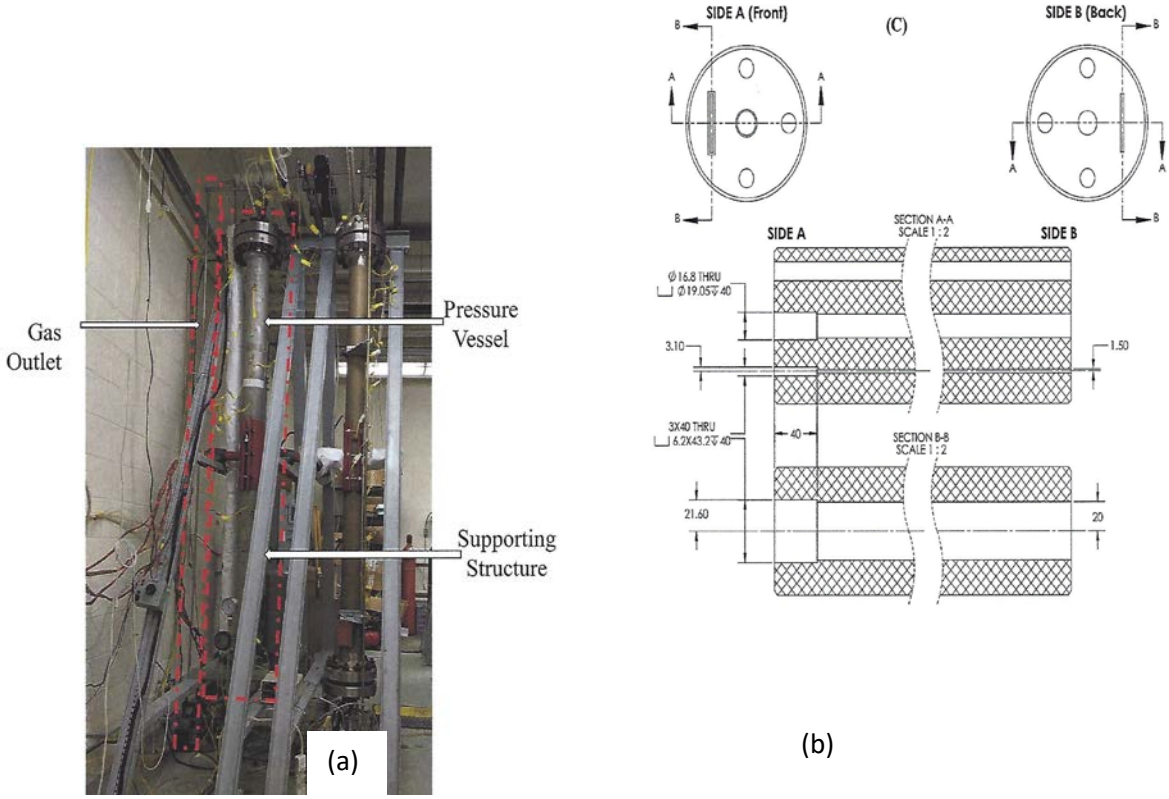

Figure 16. CCNY Forced Circulation Bypass Flow Loop test facility. (a) Photograph of facility. (b) Schematic of core test section.

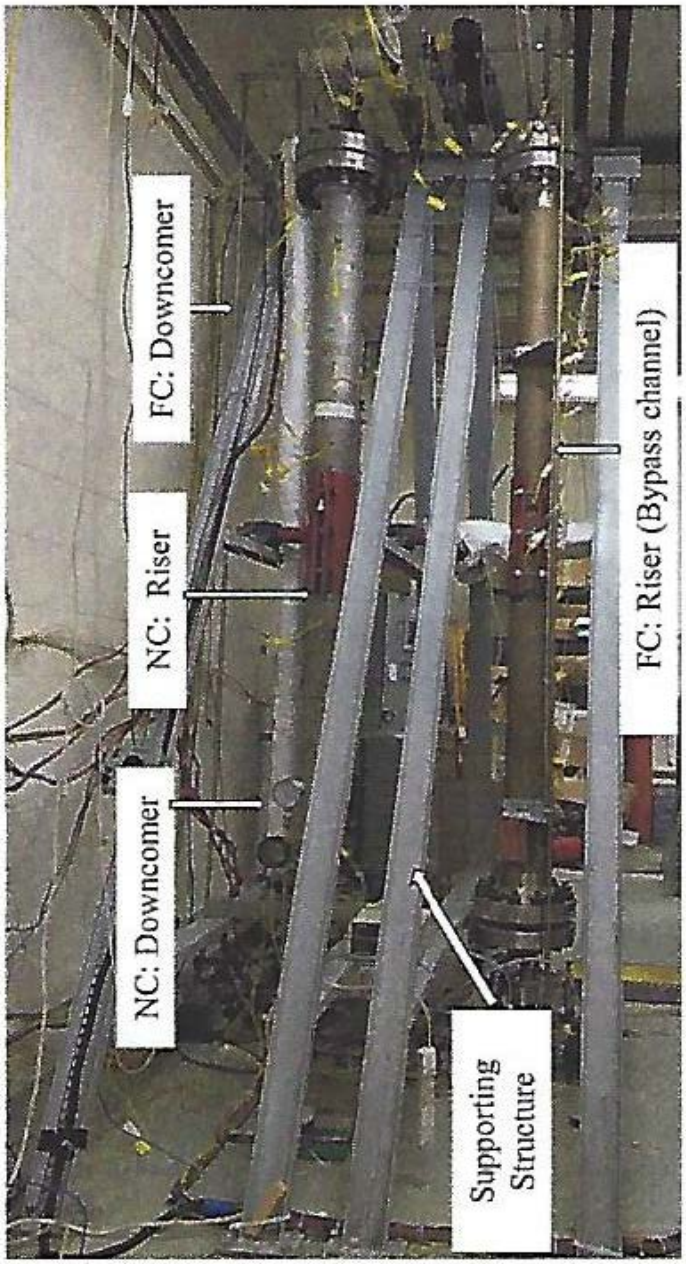

(a)

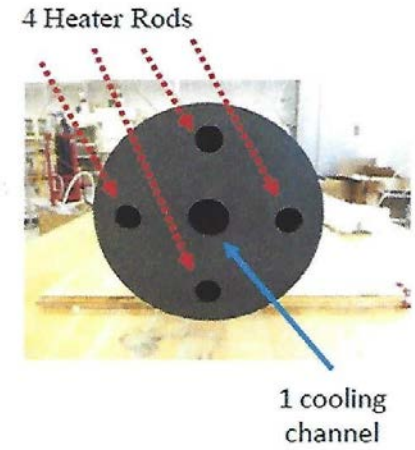

(b)

Figure 17. CCNY Natural Circulation Flow Loop facility. (a) Photograph of facility. (b) Cross-section photograph showing cooling channel and four heater rods.

The characteristics of the natural circulation flow and forced flow facilities are given in Table 2 and compared to those of the MHTGR. It is noted that: "… it is clear that the Reynolds number (Re), Grashof number (Gr) and Prandtl number (Pr) or alternatively Rayleigh number (Ra), and non-dimensional heat flux (q^+) are the main non-dimensional numbers that we should match between the prototypical (or GFR) and test conditions. Other parameters, namely, the Buoyancy parameter (Bo*) and the acceleration parameter

(K_v) will be matched automatically as we match Re, Gr, Gr*, Pr and q^+ between the prototype and the model test section." [Cochran et al, 2004]

Inspection of Table 2 reveals the following:

Table 2. Comparison of CCNY Natural Circulation Flow Loop (NCFL) and Forced Convection Bypass Flow Loop (FCBFL) Test Facilities Core Test Section to reference MHTGR

Parameter	MHTGR	CCNY NCFL	CCNY FCBFL
Working fluid	Helium	Helium,nitrogen & He/N_2 mixture	Nitrogen
Flow direction	Forced: down NC: up	Up	Up or down
Outlet temperature @ operational conditions (°C)	637	650	800
Reactor pressure @ operational conditions (MPa)	6.38	6.38	6.38
Effective core height (m)	7.93	2.45	2.45
Diameter: typ fuel element cooling channel (mm)	15.9	16.8	16.8
Design bypass flow fraction (%)	10 ~ 15	No bypass	>10 & <25
Maximum bypass flow (%)	20 ~ 25	No bypass	NA
Average core power per cooling channel per unit length (watts/mm)	6.32	3.76	2.82
Single-channel mass flux (kg/s-mm^2)—assuming 10% bypass—operational conditions	$1. \times 10^{-4}$	NA	$>1.3 \times 10^{-3}$
Graphite material	H-451	G348	G348

- The CCNY test section graphite simulated cooling channel has a diameter of 16.8 mm; thus the CCNY cooling channel differs by only 5% to 6% from a typical MHTGR cooling channel (16.8/15.9 = 1.056). This agreement gives a close match to a typical MHTGR cooling channel and forms the basis for performing experiments that give MHTGR-typical flow and heat transfer characteristics.
- The core bypass for the CCNY FCBFL facility is within the band of bypass flows that are typical for the MHTGR.
- The CCNY facilities are capable of providing conditions in the test section that are typical for the MHTGR including either the same working fluid (helium) or a scalable working fluid (nitrogen)—meaning that the alternate working fluid, in this case nitrogen in the CCNY FCBFL facility, can be delivered to the test section at appropriate scaled values. Therefore, (i) for experiments performed with helium as a working fluid the CCNY test facilities have working fluid properties that match those of the MHTGR and (ii) for experiments performed with nitrogen as the working fluid the gas conditions can be adjusted to give matching key nondimensional quantities representative of the MHTGR, i.e., Reynolds number, Grashof number, and nondimensional heat flux.
- The Prandtl numbers of both helium and nitrogen may be approximated as 0.7.

5.1 HTTF: Relevance to CCNY Experiments

The experimental matrix designed to provide data to validate high-fidelity and systems analysis codes to be used to calculate the operational, off-normal, and accident scenarios for very high temperature gas-cooled reactors consist of an integral experiment (the High Temperature Test Facility—HTTF) and a number of separate-effects experiments such as the CCNY test facilities. The experimental facilities used to generate the required validation data have all been scaled on the basis of the hierarchical two-tiered scaling methodology.

The CCNY core heat transfer experiments are designed to operate at steady-state conditions and focus on phenomena in the core region indicated as important in the HTTF scaling studies (Woods et al, 2015). These nondimensional scaling parameters are listed in Table 3.

Table 3. Key Nondimensional Groups for the Core Region: HTTF [Woods et al, 2015]

Scenario	Phenomena	Nondimensional Number	Comments
Operational conditions	Ratio of inertial forces to viscous forces	Reynolds	Section 7.2
	Ratio of convective to conductive heat transfer	Nusselt	
DCC	Ratio of buoyancy to flow shear	Richardson	Section 5.2.3
	Equals the product of Grashof number and Prandtl number. Grashof number is the ratio of buoyancy to viscous forces. Prandtl number is the ratio of momentum diffusivity to thermal diffusivity	Rayleigh	
PCC	Same as DCC	Richardson	Section 6.1.3
	Same as DCC	Rayleigh	

5.2 Scaling: Forced Circulation Bypass and Natural Circulation Flow Loops

The nondimensional parameters showing the scaling relationships between the CCNY and the MHTGR are listed in Table 4 in terms of Pi ratios where each Pi ratio is defined as:

$$\prod \frac{[No]_e}{[No]_P} = Distortion \qquad (39)$$

where No refers to the number (nondimensional number or parameter) identified in Table 4 and the subscripts e and P refer respectively to "CCNY experiment" and "MHTGR prototype". A Pi ratio of ~1. identifies the distortion as acceptable.

Table 4. Summary of CCNY Test Facility Pi Groups and Estimates of Scaling Distortion

Key Parameter	No	Distortion	Comments
Reynolds number	Re	~1.	See equation (27)
Grashof number	Gr	~1.	See equation (29)
	Gr^*	~1.	See equation (10)
Heat Flux	q^+	~1.	See equation (6)
Prandtl number	Pr	~1.	See equation (28)
Buoyancy parameter	Bo^*	~1.	See equation (12)
Acceleration parameter	K_v	~1.	See equations (8) and (9)
Nusselt number	Nu	~1.	See equation (18) at . > ~2500

The key parameters in the form of well-known nondimensional numbers and nondimensional parameters such as the buoyancy parameter and the acceleration parameter all have acceptable distortion levels principally because the CCNY facilities test sections have representative cooling channel dimensions and are using either helium or a scalable gas such as nitrogen at representative state conditions.

6. REFERENCES

Aicher, T., and H. Martin, 1997, "New Correlations for Mixed Turbulent Natural and Forced Convection Heat Transfer in Vertical Tubes," *International Journal of Heat and Mass Transfer*, Vol. 40, No. 15, pp. 3617-3626.

Bankston, C. A., 1970, "The Transition from Turbulent to Laminar Gas Flow in a Heated Pipe," *Journal of Heat Transfer*, Vol. 92, pp. 569-579.

Bankston, C. A., and D. M. McEligot, 1970. Turbulent and laminar heat transfer to gases with varying properties in the entry region of circular ducts. *Int. J. Heat Mass Transfer*, 13, pp 319-344.

Bayless, P. 2018, Personal communication to R. Schultz

Bejan, A., 1993, *Convection Heat Transfer*, Chapter 4, John Wiley & Sons

Burmeister, L. C., 1993, *Convective Heat Transfer*, 2nd Edition, Chapter 10, John Wiley & Sons.

Churchill, S. W., 1998, "2.5.10 Combined Free and Forced Convection in Channels," Heat Exchanger Design Handbook, ed. G. F. Hewitt, Begell House.

Cochran, P., P. Saha, P. Hejzlar, D. M. McEligot, G. E. McCreery, and R. R. Schultz, 2004, *Scaling Analysis and Selection of Test Facility for Fundamental Thermal-Hydraulic Studies Related to Advanced Gas-Cooled Reactor*, MIT, MIT-GFR-015, September.

Cotton, M. A., and J. D. Jackson, 1990. Vertical air flows in the turbulent mixed convection regime calculated using a low-Reynolds-number k-ε model. *Int. J. Heat Mass Transfer*, 33, pp. 275-286.

Dittus, F. W., and L. M. K. Boelter, 1930. Heat transfer in automobile radiators of the tubular type. *Univ. Calif. Publ. in Engr.*, 2, pp. 443-461.

Drexel, R. E., and W. H. McAdams, 1945. Heat-transfer coefficients for air flowing in round tubes, rectangular ducts and around finned cylinders. NACA Wartime Report 108, February

General Atomics, 1996, Gas Turbine-Modular Helium Reactor (GT-MHR) Conceptual Description Design Report, 910720, Revision 1, July

Gersten, K., and H. Herwig, 1992. *Strömungsmechanik.* Braunschweig: Friedr. Vieweg und Sohn.

Hall, W. B., and J. D. Jackson, 1969. Laminarization of a pipe flow by buoyancy forces. ASME paper 69-HT-55.

Hallman, T. M., 1956. Combined forced and free-laminar heat transfer in vertical tubes with uniform internal heat generation. *Trans., ASME*, 78, pp. 1832-1841.

Hanratty, T. J., E. M. Rosen and R. L. Kabel, 1958. Effect of heat transfer on flow field at low Reynolds numbers. *Ind. Eng. Chem.*, 50, pp. 815-820

Jackson, J. D., 1998, Personal Communication, April as referenced in D. Mikielewicz, et al, "Temperature, Velocity and Mean Turbulence Structure in Strongly Heated Internal Gas Flows—Comparison of Numerical Predictions with Data," International Journal of Heat and Mass Transfer, Vol. 45, pp. 4333-4352, 2002

Jackson, J. D., M. A. Cotton and B. P. Axcell, 1989. Studies of mixed convection in vertical tubes. *Int. J. Heat and Fluid Flow*, 10, pp. 2-15.

Kalaga, D. V., A. V. Rudra, and M. Kawji, 2019, CCNY—High Pressure/High Temperature Test Facility, City College of New York.

Kawamura, H., 1979. Analysis of laminarization of heated turbulent gas using a two-equation model of turbulence. Proc., 2nd Intl. Symp. Turb. Shear Flow, London, pp. 18.16-18.21.

Kays, W. M., 1966. *Convective heat and mass transfer*. New York: McGraw-Hill.

Lee, J., P. Hejzlar, P. Stable, P. Saha, D. M. McEligot, G. E. McCreery, and R. R. Schultz, 2005, Design of Thermal-Hydraulic Loop Related to Advanced Gas-Cooled Reactor, 2nd Annual Report, MIT, September.

Li, J. K., 1994. Studies of buoyancy-influenced convective heat transfer to air in a vertical tube. Ph.D. thesis, U. Manchester.

MacDonald, P. E., J. W. Sterbentz, R. L. Sant, P. D. Bayless, R. R. Schultz, H. D. Gougar, R. L. Moore, A. M. Ougouag and W. K. Terrry, 2003. NGNP preliminary Point Design -- Results of the initial neutronics and thermalhydraulic assessments. Tech. report INEEL/EXT-03-00870 Rev. 1, INEEL.

McAdams, W. H., 1954. *Heat transmission, 3rd edition.* New York: McGraw-Hill.

McEligot, D. M., 1963. The effect of large temperature gradients on turbulent flow of gases in the downstream region of tubes. Ph.D. thesis, Stanford Univ. Also TID-19446.

McEligot, D. M., 1967. Internal gas flow heat transfer with slight property variation. *Bull., Mech. Engr. Ed.*, 6, pp. 251-263.

McEligot, D. M, 1986. Convective heat transfer in internal gas flows with temperature-dependent properties. *Adv. Transport Processes*, 4, pp 113-200.

McEligot, D. M., C. W. Coon and H. C. Perkins, 1970. Relaminarization in tubes. *Int. J. Heat Mass Transfer*, 13, pp. 431-433.

McEligot, D. M., P. M. Magee and G. Leppert, 1965. Effect of large temperature gradients on convective heat transfer: The downstream region. *J. Heat Transfer*, 87, pp. 67-76.

McEligot, D. M., L. W. Ormand and H. C. Perkins, 1966. Internal low Reynolds number turbulent and transitional gas flow with heat transfer. *J. Heat Transfer*, 88, pp. 239-245.

McEligot, D. M., and J. D. Jackson, 2004, *Deterioration Criteria for Convective Heat Transfer in Gas Flow Through Non-Circular Ducts,* INEEL-JOU-03-01311, INEEL Report, revised 2004

McEligot, D. M. and G. E. McCreery, 2004, *Scaling Studies and Conceptual Experiment Design for NGNP CFD Assessment*, INL/EXT-04-02502. November.

Metais, B. and E. R. G. Eckert, 1964, "Forced, Mixed and Free Convection Regimes," *Journal of Heat Transfer*, Vol. 86, pp. 295-296, May

Mikielewicz, D. P., A. M. Shehata, J. D. Jackson and D. M. McEligot, 2002. Temperature, velocity and mean turbulence structure in strongly-heated internal gas flows. Comparison of numerical predictions with data. *Int. J. Heat Mass Transfer*, 45, pp. 4333-4352.

Moretti, P. M., and W. M. Kays, 1965. Heat transfer to a turbulent boundary layer with varying free-stream velocity and varying surface temperature -- an experimental study. *Int. J. Heat Mass Transfer*, 8, pp. 1187-1202.

Morton, B. R., 1960. Laminar convection in uniformly heated vertical pipes. *J. Fluid Mech.*, 8, pp. 227-240.

Murphy, H. D., F. W. Chambers and D. M. McEligot, 1983. Laterally converging flow. I. Mean flow. *J. Fluid Mech.*, 127, pp. 379-401.

Palatan, Y., 1993, *Friction Factor and Nusselt Number Behavior in Turbulent Mixed Convection in Vertical Pipes*, Ph.D. Thesis, Department of Nuclear Engineering, MIT, June.

Perkins, K. R., 1975. *Turbulence structure in gas flows laminarizing by heating*. Ph.D. thesis, Univ. Arizona.

RELAP5-3D Code Development Team, 2014, *RELAP5-3D Code Manual*, Idaho National Laboratory, June.

Schultz, R. R., P. D. Bayless, R. W. Johnson, W. T. Taitano, J. R. Wolf, G. E. McCreery, 2010, Studies Related to the Oregon State University High Temperature Test Facility: Scaling, the Validation Matrix, and Similarities to the Modular High Temperature Gas-Cooled Reactor, INL/EXT-10-19803.

Stone & Webster Engineering Corp, 1986, Preliminary Safety Information Document for the Standard MHTGR, Volume 1, HTGR-86-024

Taylor, M. F., K. E. Bauer and D. M. McEligot, 1988. Internal forced convection to low-Prandtl-number gas mixtures. *Int. J. Heat Mass Transfer*, 31, pp. 13-25.

Vilemas, J., and P. Poskas, 1999. Effects of body forces on turbulent heat transfer in channels. New York: Begell House.

Ward Smith, A. J., 1962. On the correlation and presentation of information on turbulent variable property heat

Williams, B., R. R. Schultz, D. M. McEligot, G. E. McCreery, 2015, Studies of Deteriorated Heat Transfer in Prismatic Cores Stemming from Irradiation-Induced Geometry Distortion, DOE/NEUP-10-876

Williams, W. C., P. Hejzlar, M. J. Driscoll, W. J. Lee, and P. Saha, "Analysis of a Convection Loop for GFR Post-LOCA Decay-Heat Removal from a Block-Type Core, Topical Report MIT-ANP-.-095, Department of Nuclear Engineering, MIT.

Woods, B. G., R. B. Jackson, B. L. Nelson, S. R. Cadell, J. N. Reyes, 2015, Scaling Analysis for the Very High Temperature Reactor Test Facility at Oregon State University, OSU-HTTF-000000-Tech-001-R0

Worsoe-Schmidt, P. M., 1966. Heat transfer and friction for laminar flow of helium and carbon dioxide in a circular tube at a high heating rate. *Int. J. Heat Mass Transfer*, 9, pp. 1291-1295.

CHAPTER 3: TASK 2 REPORT ON NATURAL CIRCULATION AND AIR INGRESS EXPERIMENTS

One of the VHTR's advantages over other new reactor designs is their capability to passively remove decay heat. This feature will enable long term cooling of these reactors without any forced convection or active cooling mechanisms. Such a capability is due to effective surface cooling from the reactor vessel due to radiative heat transfer and natural convection. In addition, high thermal conductivity of graphite and natural circulation of coolant would help transport the decay heat from the fuel-region to the surface of the reactor vessel. Natural circulation flows are expected to occur in a VHTR under both PCC and DCC conditions due to fluid temperature and density differences between the hot fuel zone and cooler reflector zone in the reactor core, although natural circulation is more important under PCC conditions in transporting the heat generated by fuel rods radially across the core. Air ingress occurs under DCC after the primary system has depressurized and air would enter the reactor vessel from the Reactor Cavity cooling System surrounding the reactor vessel. Therefore, for safety analyses it is essential to study the characteristics of natural circulation and the air ingress into the lower plenum at low pressures, and the transport of air through the core which could cause oxidation and damage the internal graphite structures. To this end, natural circulation experiments have been performed using helium-nitrogen gas mixtures focusing on the mass flow rates, between the hot riser and cold downcomer sections of the rectangular flow loop.

3.1 Test Facility

An existing high-pressure and high temperature gas flow test facility at City College of New York has been modified and used in this work. The schematic of the modified experimental set-up can be seen in Fig. 3.1a. The facility consisted of a stainless steel 304 pressure vessel (rated at 70 bar/923 K) simulating the hot fuel zone in the flow loop (referred to as the riser or hot vessel (HV)), and a downcomer region around the core periphery (referred to as the cold vessel).

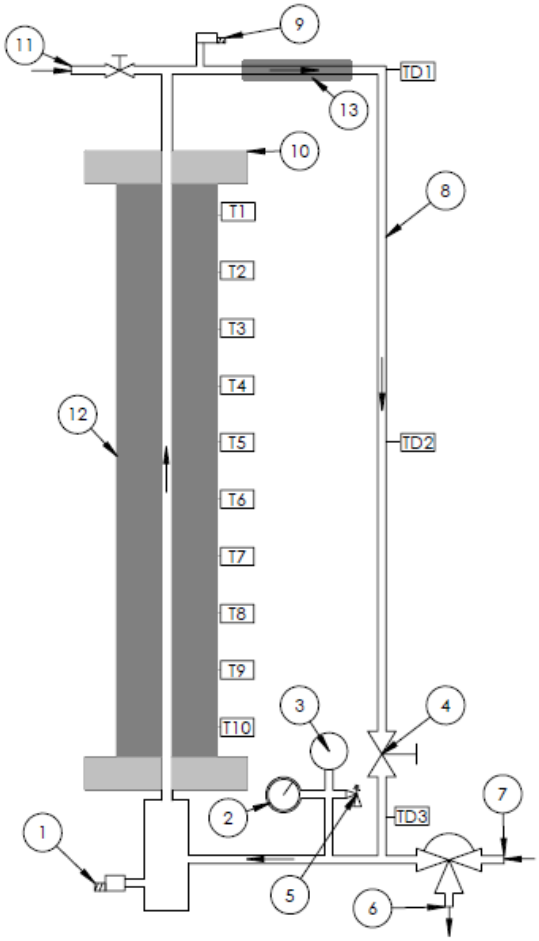

LEGEND

1. Lower plenum sampling port, 2. Pressure gauge, 3. Pressure Transducer, 4. Needle valve, 5. Pressure relief valve 6. vacuum pump line, 7. Nitrogen Injection 8. Cold Vessel (Downcomer), 9. Upper plenum sampling port, 10. Vessel flange, 11. Helium Injection, 12. Hot Vessel (riser) containing a graphite column, 13. Mass flow measurement device, T1-T10: Thermocouples connected to the riser, TD1-TD3: Thermocouples connected to the downcomer.

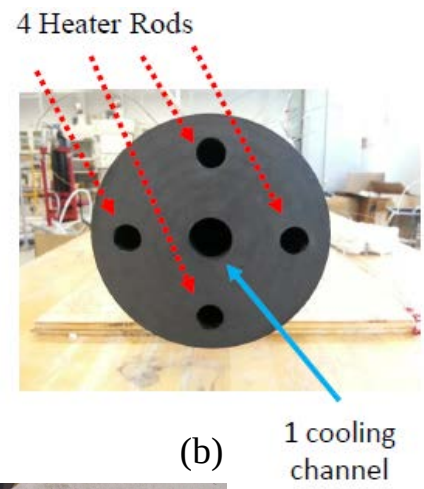

(a) (b)

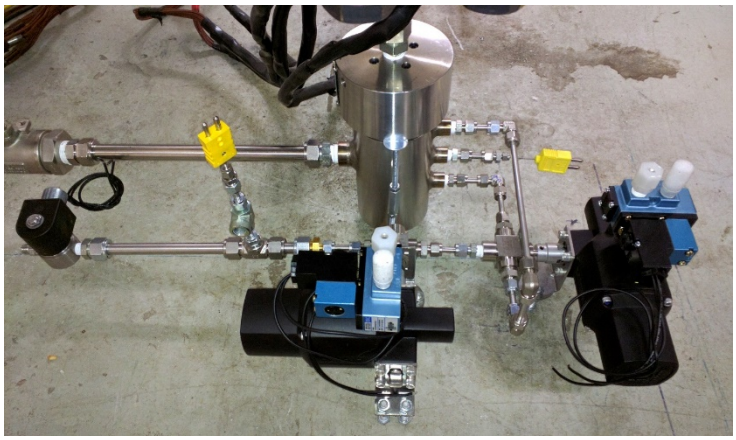

Fig. 3.1 (a) Natural Circulation Experimental Set-up, and (b) Cross-sectional view of the graphite column in HV, (c) lower plenum and gas sampling system.

The hot vessel housed a 2.7 m long graphite column with a 108 mm outer diameter. The graphite column had four 2.3 kW electric heater rods symmetrically placed around a central coolant channel

of 16.8 mm diameter as shown in the cross-sectional view in Fig 3.1b. The temperatures in the graphite were measured using 40 thermocouples imbedded at ten axial locations 25 cm apart. Each plane had four thermocouples at different radial and azimuthal locations. A stainless-steel cylindrical chamber with a 7.0 cm diameter and 17.0 cm height was fabricated to represent the lower plenum and attached to a gas sampling system for measuring the helium concentration as shown in Fig. 3.1c.

A stainless-steel tube of 14.5 mm inner diameter was used to connect the top of the riser and the lower plenum as a downcomer of the flow loop simulating the cooler reflector zone in the VHTR core. A mass flow measurement system was set up in the top horizontal section as described in the next section. The vertical downcomer section was thermally insulated but allowed cooling of the gas by natural convection to the environment. A three-way valve connected a vacuum pump and nitrogen gas cylinder to the bottom of the downcomer. The vacuum pump was used to completely flush out the gases from the flow loop before filling it with helium. A pressure transducer (Omega, PX313) was installed on the inlet piping connected to the pressure vessel for continuous monitoring of the system pressure. The thermocouples and pressure transducer were connected to a National Instruments data acquisition system for continuous monitoring and data acquisition via a LabVIEW program.

3.2 Experimental Procedure

Prior to the actual experiments, the test facility was vacuumed to near vacuum twice and filled with helium. Then, nitrogen was slowly injected into the lower plenum of the riser until the system pressure rose to required values. The gas mixture was allowed to settle for at least 10 minutes so heavier nitrogen would occupy the lowest part of the flow loop including the lower plenum. The needle valve (Fig. 3.1a, legend 4) connecting the riser and downcomer at the bottom was then closed completely to prevent natural circulation by isolating the riser from the downcomer. The electric heater rods in the riser were then turned on and the graphite midpoint temperature (GMT) in the riser was increased to a desired value. An important point to note here is that the system pressures for pure helium, pure nitrogen and gaseous mixture cases were initially set at the same selected values (138, 172 and 207 kPa), however, the system pressure eventually increased with the increase in the GMT. After the steady temperature profiles were reached in the heated riser test section, the needle valve was opened to initiate natural circulation of a helium-nitrogen mixture through the riser and downcomer. Immediately after the opening of the needle valve, the helium-nitrogen mixture began flowing upward in the hot riser and downward in the cold downcomer due to the density difference arising from the temperature difference between the riser and downcomer. From the data, the steady mass flow rates reached after transient periods are analyzed and reported.

The volumetric concentrations of helium and nitrogen in the gaseous mixture were measured by helium analyzers (Divesoft, M12) which were connected to the upper and lower plena through gas sampling ports (1) and (9) as shown in Fig. 3.1a. A helium analyzer could determine the volumetric concentrations of helium in the gaseous mixture. For each measurement, a small volume of gas was sampled from each sampling port at certain time intervals, passed through the

helium analyzer and then discharged to the atmosphere. Data acquisition was continued until steady state conditions were reached after about 5 to 8 hours, and the concentrations of nitrogen and helium (in gaseous mixture) became constant in both the upper and lower plena, respectively.

3.3 Mass Flow Rate Measurement

A mass flow rate measurement device was designed, constructed and installed in the upper plenum in order to measure the natural circulation flow rate. It consisted of two 50 W heating tapes [Chromalox, 121620] powered by a 24V DC source, that were connected and wrapped around the interconnecting tube at the top (upper plenum). This tubing connecting the outlet of the riser (hot vessel) and inlet of the downcomer (cold vessel) was also insulated on the outer surface to minimize heat losses. Thermocouples were installed on the insulation surface (Fig. 3.2) to measure the average temperature difference between the insulation surface and ambient temperature in order to further corroborate any heat loss values.

By adjusting the voltage and current on the power supply, the heater's power was adjusted in the mass flow measurement system to a desired value. Four thermocouples were inserted into the tube to measure the gas temperatures before and after the heated section.

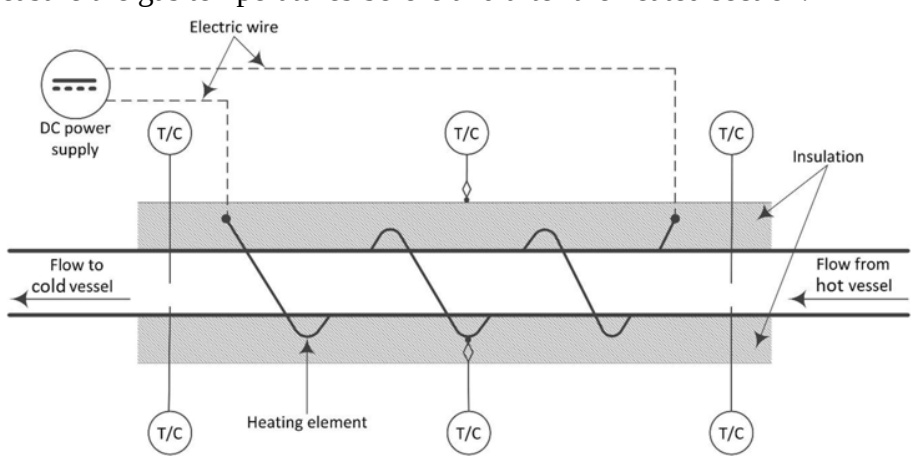

Fig. 3.2 Mass flow rate measurement system.

By applying DC power to the heating tape and measuring the inlet and outlet bulk temperatures at steady state, an energy balance given by Eq. (1) could be solved for two power levels to obtain the mass flow rate. The heat transfer coefficient for natural convection heat loss from the insulation surface was first determined as a function of the outer surface temperature with a stagnant gas inside the tube. The method described by Eq. (3.1) involved at least two experimental conditions to determine the mass flow rate.

$$\dot{m}C_P\left(T_{Out_i} - T_{in_i}\right) - h\left(T_{Insulation_i} - T_{Ambient_i}\right) = Q_{Heater_i} \tag{3.1}$$

3.4 Experimental Results

The mass flow rate results are presented for different graphite midpoint temperatures (GMT) in the riser, different operating pressures and initial concentrations of nitrogen-helium mixtures (in

terms of gas partial pressures). The amount of nitrogen gas initially injected into the lower plenum and thus the overall nitrogen concentration in the flow loop was systematically changed to determine its effect for different graphite midpoint temperatures in the riser. Mass flow measurements were also performed in natural circulation experiments using single gases (pure helium and pure nitrogen) in order to better understand the effect of nitrogen on the mass flow rates for the gas mixture. Table 3.1 shows the different experimental conditions covered during these natural circulation experiments.

Table 3.1 Experimental Conditions

Experimental Parameter	Range/Value
Graphite Midpoint Temperature (GMT) (^{0}C)	100 – 400
Initial Helium Pressure (kPa)	34 – 207
Initial Nitrogen Pressure (kPa)	34 – 207
Initial He-N_2 mixture Pressure (kPa)	34 - 207

3.4.1. Single Gas Mass Flow Measurements

Fig. 3 displays the mass flow rates measured in twelve different experiments performed (Fig. 3a for pure nitrogen and Fig. 3.3b for pure helium, respectively). For both gases, there is a clear dependency of mass flow rate on the working pressure because of the relation between pressure and gas density. Also, the results in Fig. 3.3 show that the mass flow rates for nitrogen are almost an order of magnitude greater than those of helium, and this can be attributed to the density of nitrogen which is ~7 times greater than that of helium thereby resulting in much higher mass flow rates.

It would also be useful to examine the increase in the mass flow rate with the riser (HV) temperature as well, since at higher temperatures, a greater difference in helium density between the riser and downcomer might be expected. As the graphite midpoint temperature (GMT) was increased in the riser, the gas temperature increased and the gas density decreased.

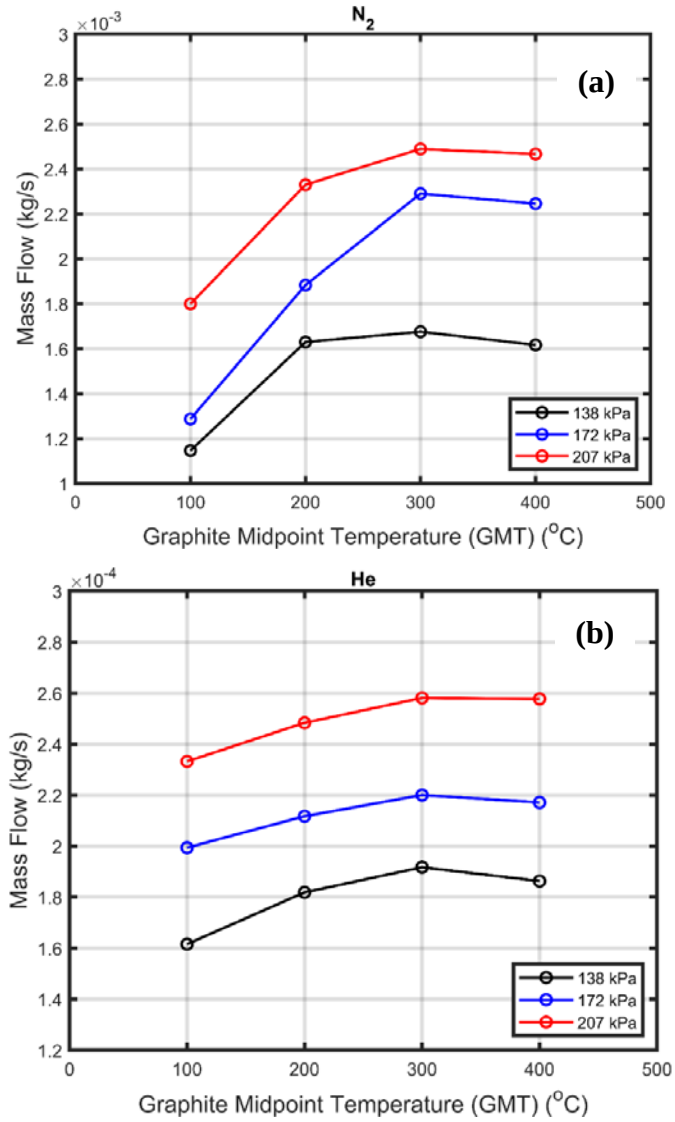

Fig. 3.3 Mass flow rates for (a) pure N_2, and (b) pure Helium for different riser GMTs and initial system pressures.

A less dense gas is also expected to move at a faster velocity. However, the profiles shown in Fig. 3.3 show the effects of two opposing properties: viscosity and density. As the gas temperature increases, its density decreases but the dynamic viscosity increases. Thus, as GMT increases from 300 to 400 ^{o} C, the flow resistance would increase triggering a decrease in mass flow rate as observed in Fig. 3.3. This can be better explained by analytically solving the continuity and Navier-Stokes equations in cylindrical coordinates, considering the following assumptions: a) one-dimensional axisymmetric flow, b) a long tube with no end effects, c) fully developed hydrodynamic conditions, d) Boussinesq's approximation is valid, and e) narrow channel assumption (i.e., the fluid temperature is nearly the same as the wall temperature). Velocity can be

obtained and integrated over the cross section to obtain the mass flow rate solution presented in Eq. (3.2),

$$\dot{m} = \left(\frac{\pi R^4 g}{8}\right)\left(\frac{\rho^2}{\mu}\right)\left(1 - \frac{1}{\tau}\right) \tag{3.2}$$

where μ represents the dynamic viscosity and $\tau = Tw/Tb$. As can be seen, Eq. (3.2) highlights the strong dependency of flow rate on pressure (through ρ^2), and the opposing effect of temperature (through μ).

3.4.2 Gaseous Mixture Mass Flow Measurements

Figure 3.4a presents the variations in mass flow rates for different concentrations of helium-nitrogen with different GMTs. It can be seen that as the concentration of nitrogen increases in the gaseous mixture due to different initial concentrations, the mass flow rate is found to increase. As mentioned earlier, this is owing to the high density of nitrogen in comparison to helium.

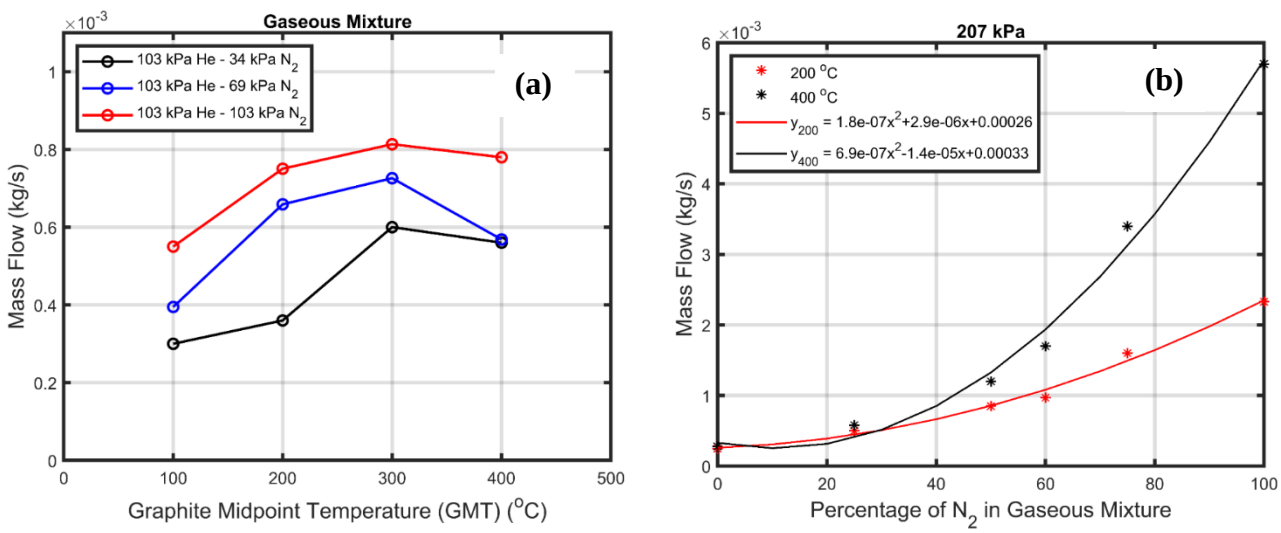

Fig. 3.4 Natural circulation mass flow rates for (a) different gas mixture concentrations at different GMTs and (b) Effect of nitrogen concentrations on mass flow rates at GMT's of 200° C and 400° C and initial system pressure of 207 kPa.

The effect of nitrogen on the mass flow rates and eventually air ingress can be better understood from Fig. 3.4b where the initial pressure of the gaseous mixture was kept constant at 207 kPa and the ratio of the nitrogen to helium concentration was varied for two different GMTs (200° C and 400° C). The mass flow rate can be seen to increase as a quadratic function of the nitrogen concentration in the mixture. Table 3.2 shows a comparison of mass flow rates with respect to the nitrogen concentration in the gaseous mixture keeping the initial gas mixture pressure the same for 200° C GMT.

Table 3.2 Variations of mass flow rates with N_2 concentration in the gas mixture at 200 ^oC GMT.

Initial Gaseous Mixture Concentrations (kPa)	He Concentration (%)	N_2 Concentration (%)	Mass Flow Rates (MFR) x 10^{-3} (kg/s)	$\frac{MFR_{He+N_2}}{MFR_{He}}$
207 kPa He - 0 kPa N_2	100	0	0.248	1
155 kPa He - 52 kPa N_2	75	25	0.500	2
103.5 kPa He - 103.5 kPa N_2	50	50	0.850	3.43
83 kPa He - 124 kPa N_2	40	60	0.970	3.91
52 kPa He - 155 kPa N_2	25	75	1.600	6.45
0 kPa He - 207 kPa N_2	0	100	2.330	9.34

It can be observed from Table 3.2 that when there is no nitrogen present in the system (pure helium), the mass flow rate is very low. But, as the concentration of nitrogen is increased with decreasing concentration of helium, the mass flow rate increases significantly and becomes 6.45 times greater at 75% nitrogen and almost 10 times when there is pure nitrogen in the system. The increment in the mass flow rate is almost quadratic as can be seen from Fig. 3.4b. This signifies the importance of nitrogen on the gas transport during air ingress and implies that more nitrogen (air in the actual situation) will lead to faster mass flow rates and eventually faster oxidation of the graphite core in the VHTR.

The effects of the graphite midpoint temperature (GMT) on the mass flow rates are shown in Table 3. It can be clearly observed from Table 3.3 that as GMT increased from 200 to 400 ^{0} C, the mass flow rate increased by as much as ~2.45 times for pure nitrogen compared to pure helium. Also, as mentioned earlier, the mass flow rates were found to decrease after a certain GMT thus showing the dominance of viscosity over density as can be seen in Fig. 3.4a.

Table 3.3 Comparison of mass flow rates for different graphite midpoint temperatures (GMT).

Initial Gaseous Mixture Concentration (kPa)	Mass Flow Rate (MFR) at 200° C x 10^{-3} (kg/s)	Mass Flow Rate (MFR) at 400° C x 10^{-3} (kg/s)	$\frac{MFR_{400^o\,c}}{MFR_{200^o\,c}}$
207 kPa He - 0 kPa N_2	0.248	0.278	1.13
155 kPa He - 52 kPa N_2	0.500	0.580	1.16
103.5 kPa He - 103.5 kPa N_2	0.850	1.200	1.41
83 kPa He - 124 kPa N_2	0.970	1.700	1.75
52 kPa He - 155 kPa N_2	1.600	3.400	2.13
0 kPa He - 207 kPa N_2	2.330	5.700	2.45

3.5 Effect of Mean Temperature difference between Riser and Downcomer

In this section, we look at the effect of the mean temperature difference between the riser (hot vessel) and downcomer (cold vessel) which is the main driving force for natural circulation of gases. As mentioned earlier, the riser is the only component that is heated during the experiments. This led to a temperature difference between the riser and the downcomer and once the valve connecting them was opened, this temperature difference induced natural circulation. The experimental results displayed almost a linear variation of the mean temperature difference between the riser and downcomer with GMT in the riser as shown in Fig. 3.5 for different cases including pure nitrogen, pure helium, and He-N_2 mixtures at different initial system pressures.

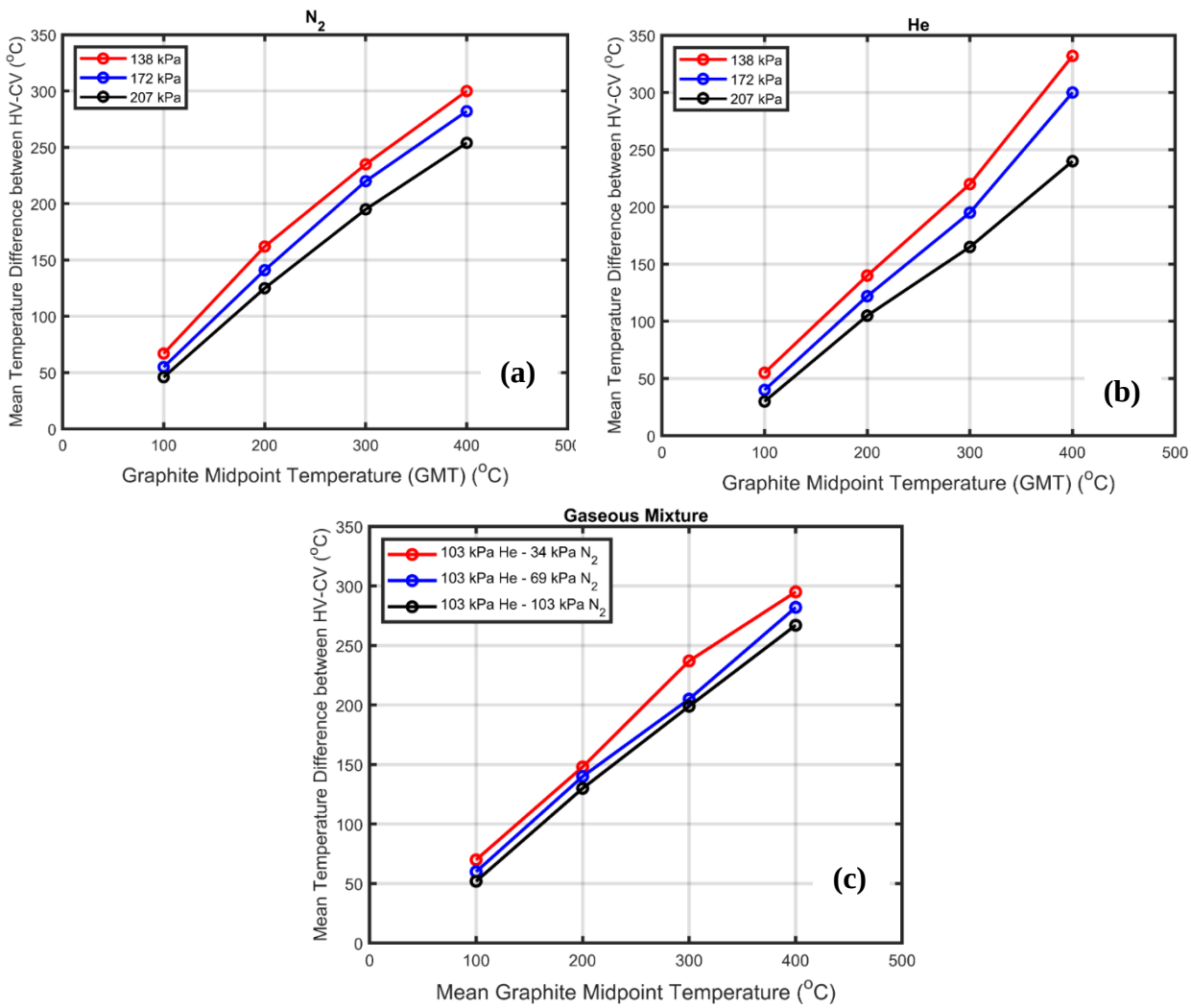

Fig. 3.5 Mean temperature difference between the riser and downcomer as a function of GMT for (a) pure N_2, (b) pure He and (c) He-N_2 mixture.

The effect of the mean graphite temperature difference between the riser and downcomer on the mass flow rates can be seen in Fig. 3.6. As mentioned earlier, after a certain temperature difference, a drop in the mass flow rates can be seen owing to the dominance of viscosity leading to greater flow resistance.

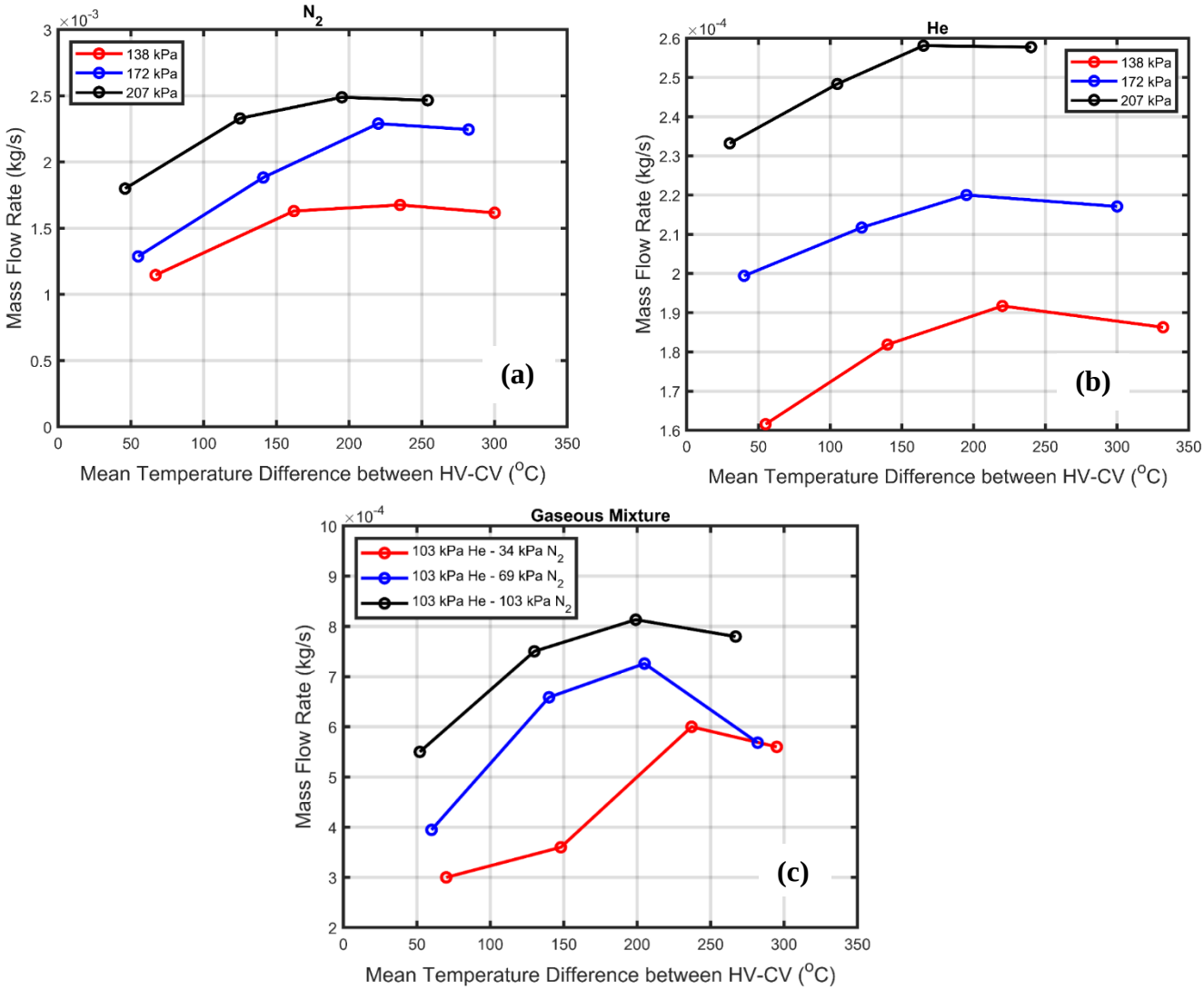

Fig. 3.6 Variations of mass flow rate with mean temperature difference between riser and downcomer for (a) pure N_2, (b) pure He and (c) He-N_2 mixture.

3.6 Effect on Reynolds number (Re)

Using the mass flow rates that have been obtained using the mass flow measurement system, other parameters such as velocity, density, local Reynolds numbers (Re) and steady state mean Reynolds numbers are examined next.

First, the effects of GMT in the riser on the average gas density and velocity are shown in Fig. 3.7. The average gas density in the riser decreases and the velocity increases with an increase in GMT which are similar for all the cases (pure helium, pure nitrogen and He-N_2 mixtures). However, if we look at the average Reynolds numbers (Re) in the riser at steady state (Fig. 3.8), the values of Re for pure nitrogen (Fig. 3.8b) were nearly an order of magnitude higher in comparison to the pure helium case (Fig. 3.8a) owing to the higher density of nitrogen in comparison to helium (almost 7 times).

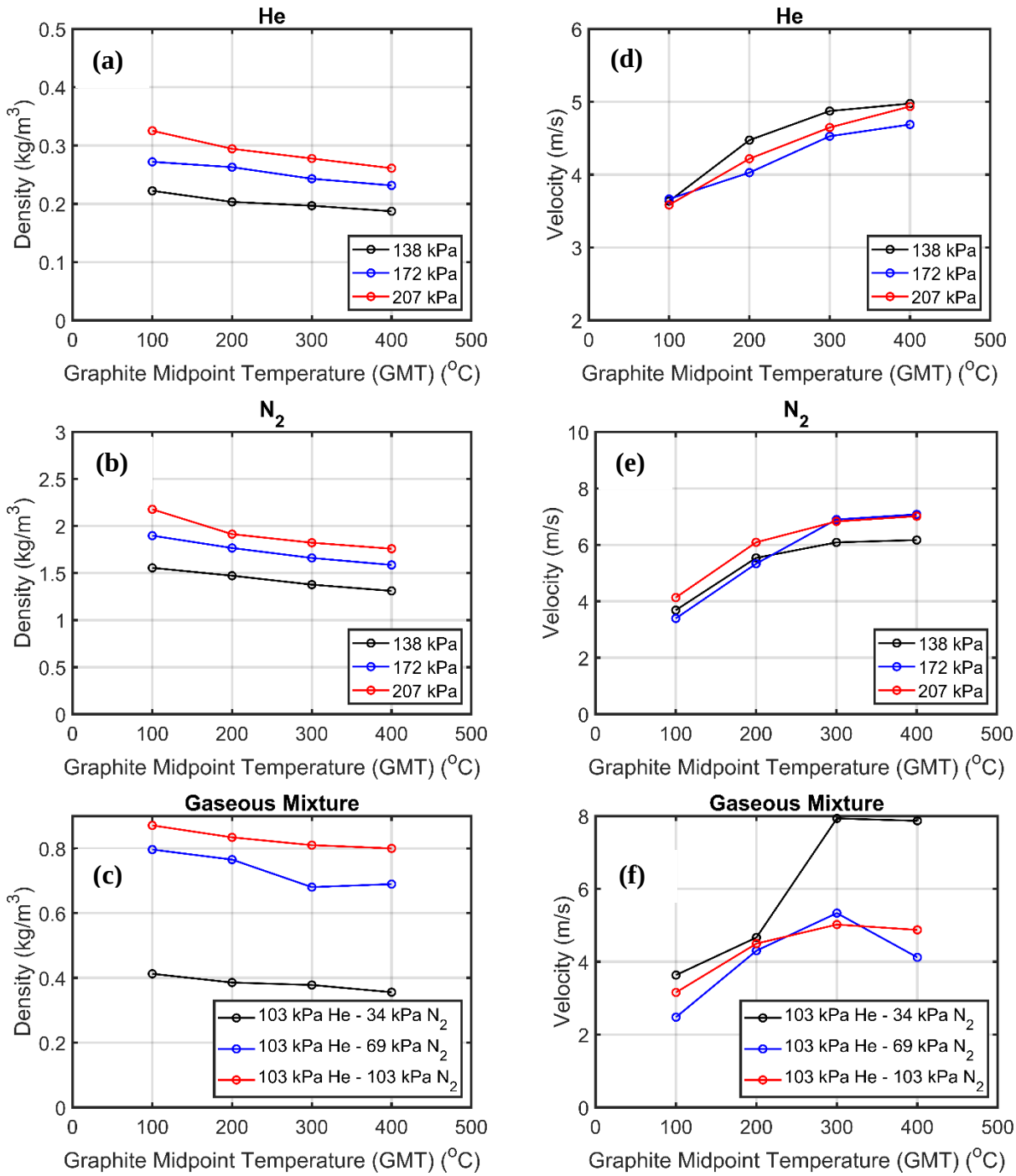

Fig. 3.7 Variations of average densities of (a) pure He, (b) pure N_2, and (c) He-N_2 mixtures, and average velocities for (d) pure He, (e) pure N_2, (f) He-N_2 mixtures with graphite midpoint temperature (GMT).

Different behaviors are observed in the variations of mean Re with GMT between pure helium and pure nitrogen results. For pure helium, the mean Re (= $\rho UD/\mu$) calculated using the

(c) **(f)**

average density, velocity and viscosity in the riser, is found to continuously decrease with GMT. Although the mass flow rate of helium increased continuously with GMT (Fig. 3.3b), the mean Re continuously decreased (Fig. 3.8a) due to the falling density and increasing viscosity. However, for pure nitrogen, mean Re increased first, reached a peak at 200 or 300 ^{o} C and then decreased. The mass flow rate of nitrogen shows a similar variation (Fig. 3.3a), indicating that the effect of viscosity eventually becomes dominant and causes Re to decrease at higher values of GMT.

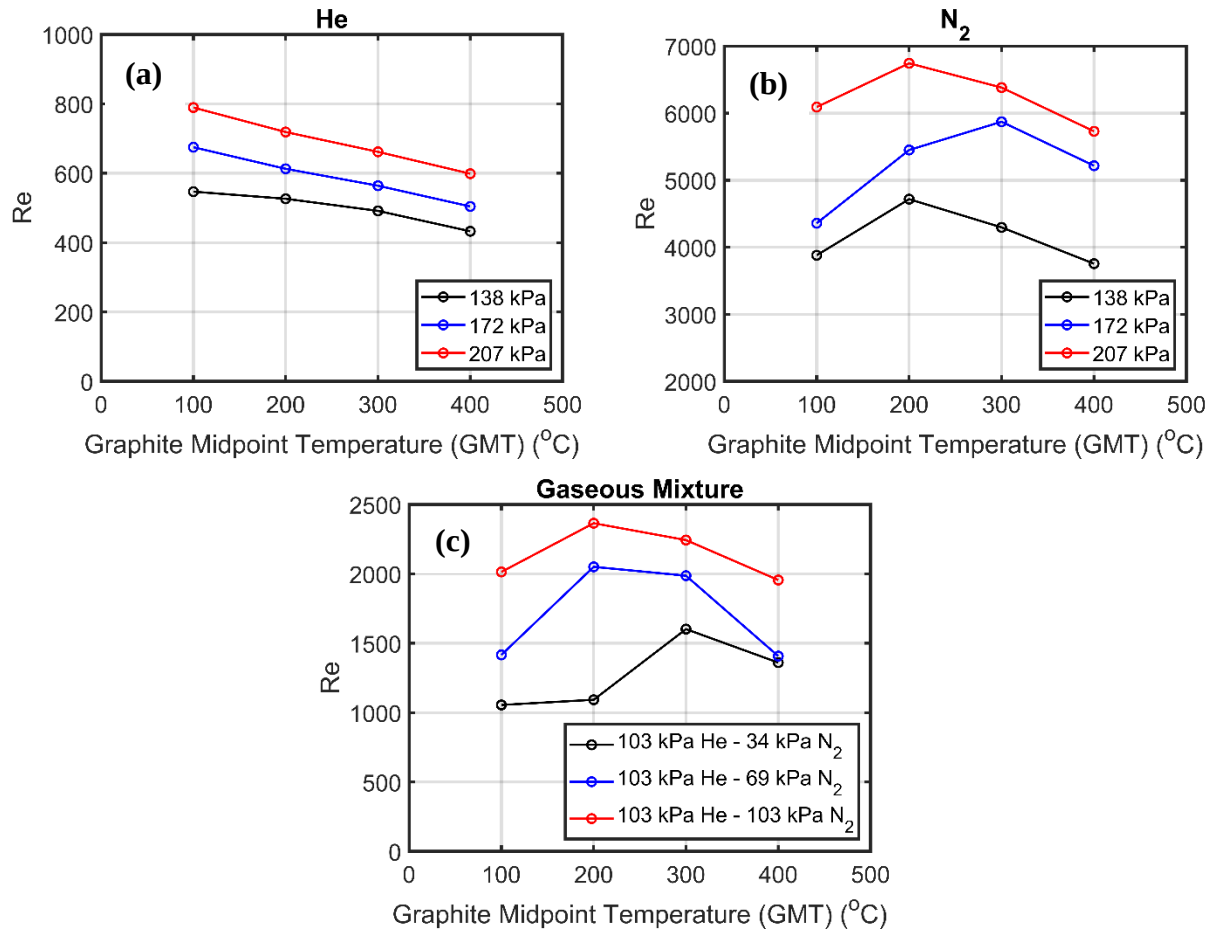

Fig. 3.8 Average Re in the riser at steady state for (a) pure He, (b) pure N_2 and (c) He-N_2 mixtures as a function of GMT.

The influence of nitrogen is felt in the gaseous mixture cases as well where Re shows trends similar to those of the pure nitrogen case. The Re values for gaseous mixtures are found to be in between the values for pure helium and pure nitrogen cases with the trends resembling those of nitrogen at increasing nitrogen concentration in the gaseous mixture.

Having measured the mass flow rate of the gas through the system, it was possible to calculate the local bulk temperature from an energy balance and the local Reynolds number at any axial location in the riser [34-35] by using Eq. (3.3),

$$\mathrm{Re}_i = \frac{2\dot{m}}{\pi \mu_i r} \tag{3}$$

where r is the tube radius and the local dynamic viscosity μ_i is evaluated at the local bulk temperature, T_i. Viscosity was calculated from Sutherland's formula, which could be used to obtain the dynamic viscosity of an ideal gas as a function of the temperature [37]. The bulk temperature profile of the gas was determined by dividing the graphite test section in the riser into 11 segments and carrying out an energy balance for each segment [34-36]. The inlet and outlet bulk temperatures for each segment were then determined using Eq. (3.4),

$$T_{i+1} = T_i + \frac{\Delta Q}{C_p \dot{m}} \tag{3.4}$$

where, T_i and T_{i+1} denote the inlet and outlet bulk temperatures in each segment. ΔQ refers to the total heat transferred to the fluid given by,

$$\Delta Q = Q_{in} - Q_{out} \tag{3.5}$$

where, Q_{in} is the total heat generated in each segment by the electric heater rods and Q_{out} is the total heat loss from the PV surface and via axial conduction [35-36].

Figure 3.9a shows the variations of the local Reynolds numbers in the riser for different concentrations of nitrogen in the gaseous mixture in one of the cases (207 kPa initial system pressure and 400° C). The maximum local Re occurs at the inlet and increases with the concentration of nitrogen. Furthermore, the local Re decreases axially as the bulk temperature increases. As the concentration of nitrogen increases in the gaseous mixture, the reduction in the local Re between the inlet and outlet of the riser, represented by ΔRe, increases nearly linearly by as much as 2,500 for pure nitrogen as shown in Fig. 3.9b. This can be explained with the help of Eq. (3.6) which is a subset of Eq. (3.3),

$$\Delta Re = \frac{2\dot{m}}{\pi r} . [\frac{1}{\mu_{initial}} - \frac{1}{\mu_{final}}] \tag{3.6}$$

where $\mu_{initial}$ and μ_{final} are the local dynamic viscosities at the first and eleventh segment of the riser respectively. The variations in the local bulk temperatures are quite similar for pure helium, pure nitrogen and gaseous mixture cases (Fig. 3.9c), hence leading to similar magnitudes of local dynamic viscosities in all the cases. The local Re is directly proportional to the mass flow rate. As mentioned earlier, the mass flow rate of pure nitrogen is much higher in comparison to that of pure helium (almost 10 times more) as shown in Fig. 3.3. Hence, the increasing mass flow rate with increasing nitrogen concentration is the primary reason for this large Re reduction between the riser inlet and outlet.

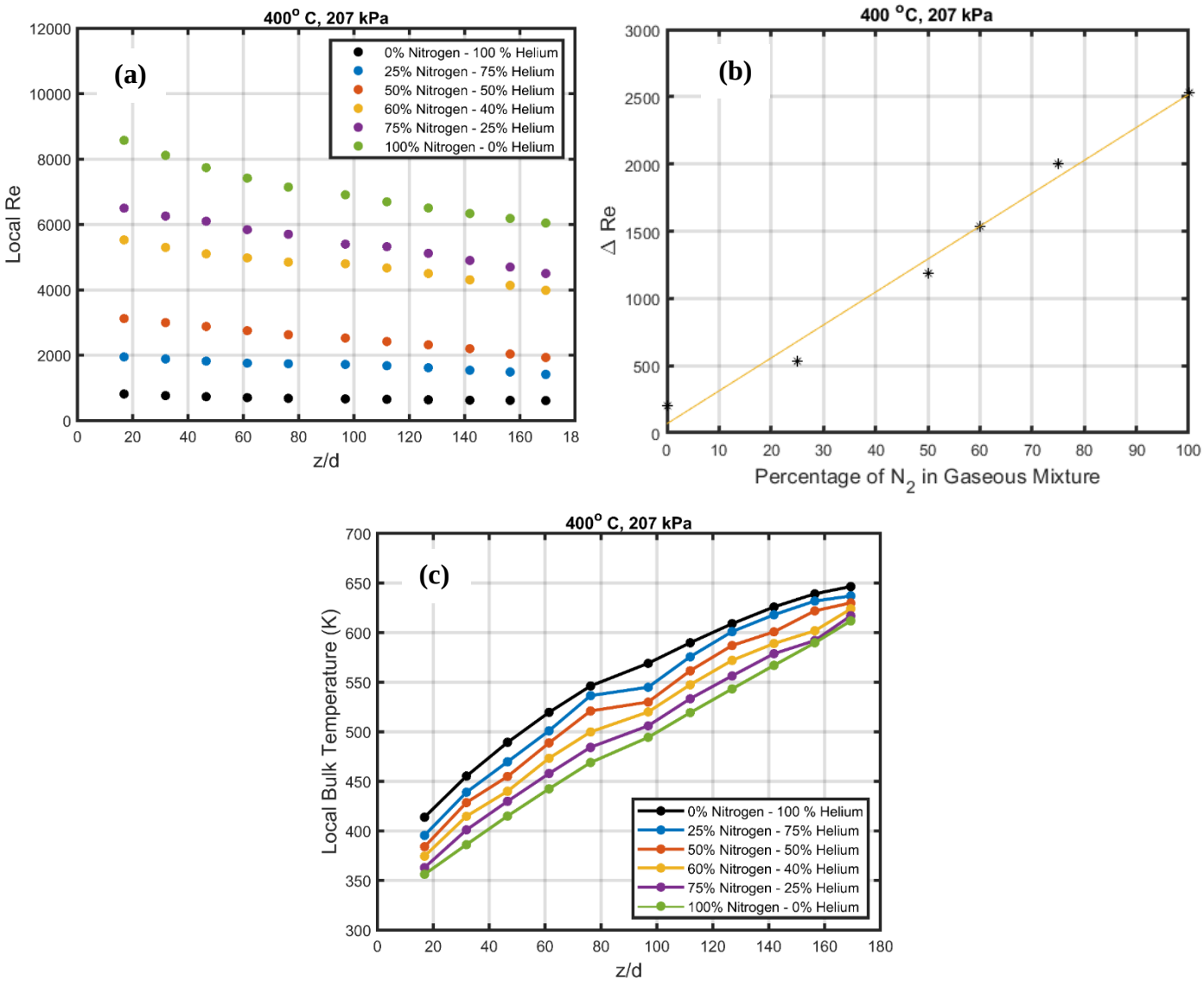

Fig. 3.9 Variations of (a) local Reynolds numbers, (b) reductions in mean Re, and (c) local bulk temperatures in the riser for different nitrogen concentrations (GMT of 400° C and initial system pressure of 207 kPa).

1.7 Heat Transfer in Natural Circulation

From the natural circulation flow data, heat transfer results were obtained in the form of various dimensionless numbers and other parameters for different graphite midpoint temperatures (GMT) in the riser, different operating pressures and initial concentrations of nitrogen-helium mixtures (in terms of gas partial pressures). The amount of nitrogen gas initially injected into the lower plenum and thus the overall nitrogen concentration in the flow loop was systematically changed to determine its effect on graphite midpoint temperatures in the riser. Heat transfer measurements were performed in natural circulation experiments using pure gases (helium and nitrogen) and

helium-nitrogen gas mixtures in order to better understand the effect of nitrogen on the heat transfer rates for the gas mixture. Table 3.4 shows the different experimental conditions covered during the natural circulation heat transfer experiments.

Table 3.4 Experimental Conditions

Experimental Parameter	Range/Value
Graphite Midpoint Temperature (GMT)	100 – 400 ^{o}C
Initial Helium Pressure	34 – 207 kPa
Initial Nitrogen Pressure	34 – 207 kPa

3.7.1 Effect of Heater Power on GMT

The heater power required to heat the graphite core in the riser is presented in Fig. 3.10a. As expected, higher heater power increases the graphite midpoint temperature. Also, as the concentration of nitrogen in the gas mixture increases, less heater power is required to achieve the required GMT. This can be better understood with the help of Fig. 3.10b where a comparison of the heater power applied for pure helium and pure nitrogen cases at an initial gas mixture pressure of 207 kPa is shown. The heater power applied for helium is much higher in comparison to nitrogen showing the effect nitrogen in the gaseous mixture has on heat transfer.

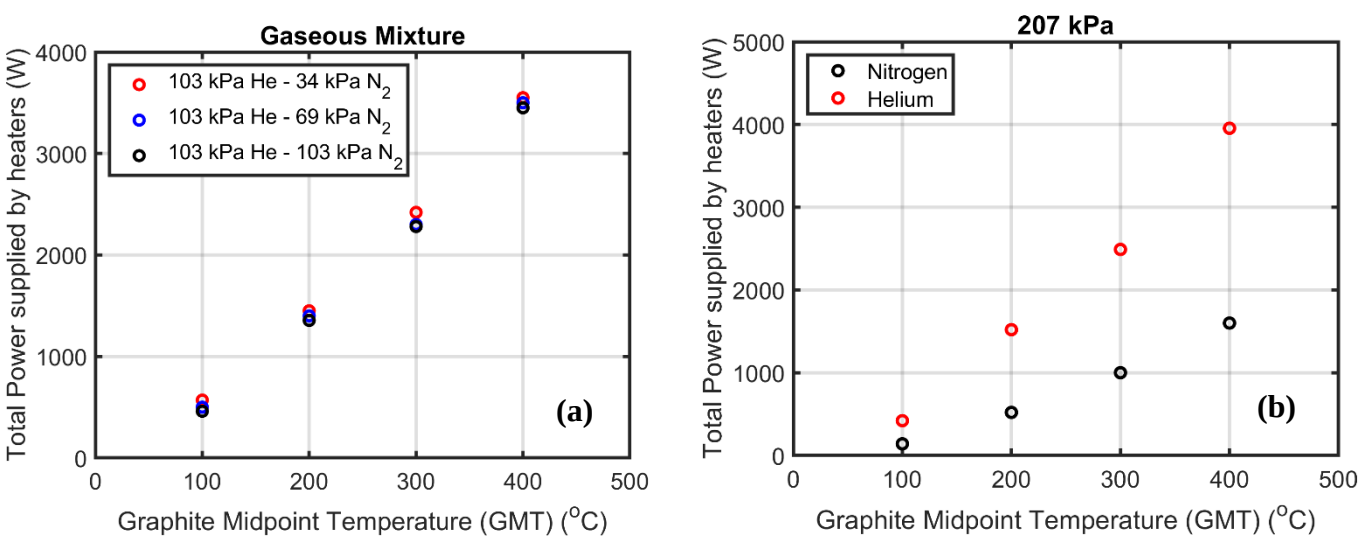

Fig. 3.10 (a) Total heater power applied as a function of GMT and (b) Total heater power applied for pure helium and pure nitrogen for initial system pressure of 207 kPa as a function of GMT.

An important point to note is that most of the power supplied by the heaters is lost to the atmosphere in the form of radial and axial heat losses. The actual heat going to the fluid is much less in comparison to the total heater power applied in the riser. Almost 90 percent of the total heat supplied is lost and does not reach the fluid (Fig. 3.11). These heat losses are taken into account in order to calculate the heat transfer parameters in the following sections.

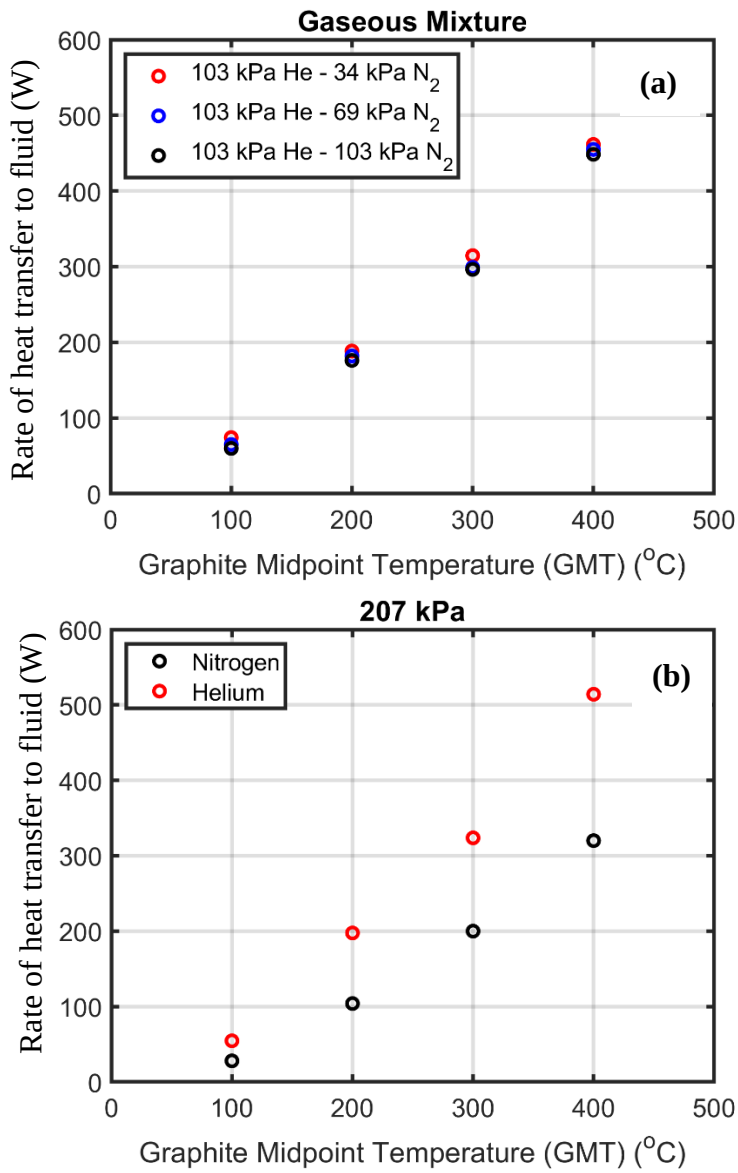

Fig. 3.11 Rate of heat transfer to fluid (a) as a function of GMT and (b) pure helium and pure nitrogen for initial system pressure of 207 kPa as a function of GMT.

3.7.2 Heat Transfer Coefficient (HTC) in the Riser

The heat transfer coefficient (HTC) in the riser (heated section) is calculated using,

$$\mathrm{HTC} = \frac{Q''}{\Delta T} \tag{3.6}$$

where Q'' is the average wall heat flux (equal to the total heater power per inner heat transfer area) in the riser, and . The values of heat transfer coefficient calculated from Eq. 3.6 are plotted for

different gas mixture concentrations in Fig. 3.12a. As the concentration of nitrogen increases, the heat transfer coefficient is seen to decrease. This can be further examined with the help of the equation for the overall convection heat transfer rate, Q_f, given by Eq. 3.7,

$$Q_f = \dot{m}\, C_p\, \Delta T_f = \rho\, V\, A\, C_p\, \Delta T_f \tag{3.7}$$

where $\dot{m}$ is the mass flow rate, ΔT_f is the temperature difference between the inlet and outlet of the riser, ρ is the gas density, V is the bulk velocity, and A is the flow channel area, respectively. The only parameters changing are the graphite midpoint temperatures (GMTs) and the nitrogen concentration. We can quantify the differences in the rate of heat transfer to the fluid with the help of ΔT_f.

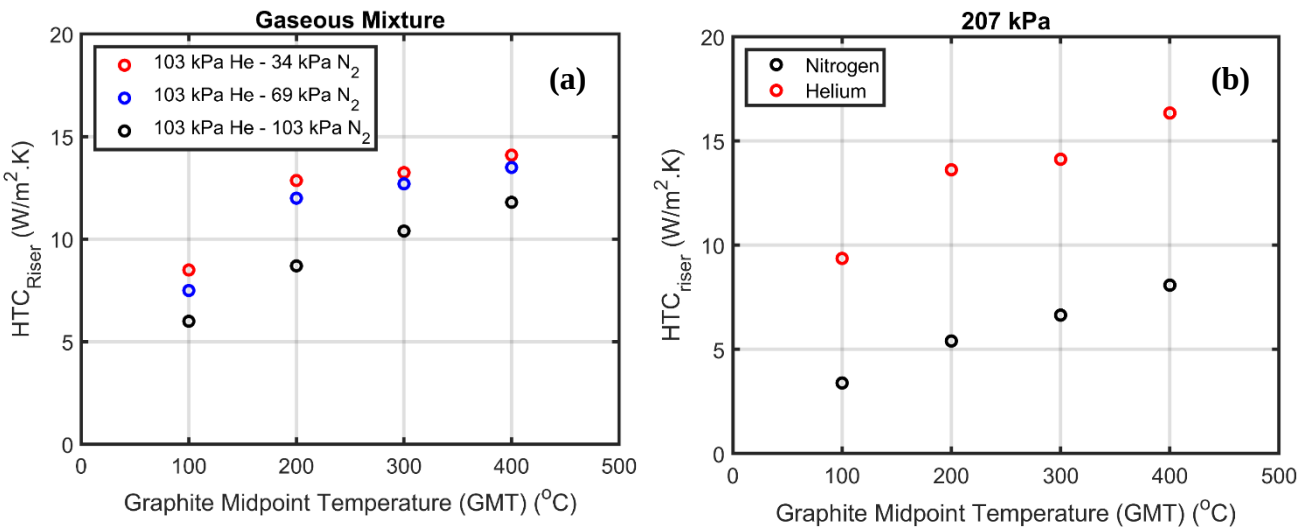

Fig. 3.12 (a) HTC in the riser for (a) different gas mixture concentrations, (b) pure helium and pure nitrogen for initial system pressure of 207 kPa

Fig. 3.12b shows that the HTC for helium is much higher in comparison to nitrogen owing to the large amount of heat carried by nitrogen thereby requiring less heater power and hence resulting in a lower HTC.

Conclusions

Natural circulation experiments have been carried out in order to quantitatively analyze the mass flow rates during the natural circulation of a helium-nitrogen mixture in a high temperature gas flow loop. The flow loop was initially filled with helium and nitrogen was slowly introduced into the lower plenum, prior to heating of the riser until steady temperatures were reached. Then a valve between the riser and downcomer was opened to initiate natural circulation. A mass flow rate measurement system was designed and installed in the upper plenum of the experimental setup in order to measure the natural circulation flow rate. The mass flow rates were determined for gaseous mixtures of different concentrations of helium and nitrogen and for pure helium and pure

nitrogen as well, in order to better understand the effect of nitrogen in the gaseous mixture on the natural circulation mass flow rates.

For both pure gases, helium and nitrogen, there was a clear dependency of mass flow rate on the working pressure because of the relation between pressure and gas density. Furthermore, the mass flow rates for nitrogen were found to be almost an order of magnitude greater than those for pure helium owing to the density of nitrogen being ~7 times greater than helium at the same pressure and temperature. Another interesting result in the mass flow rate data was due to the effect of two opposing properties: viscosity and density. The mass flow rates were found to initially increase and then eventually decrease with the increasing riser temperature (GMT) which is different from what is expected from a decrease in density and an increase in viscosity of gases with increasing gas temperature. The decrease in the mass flow rate was attributed to the increasing dominance of viscosity over density. At higher temperatures, the flow resistance would increase triggering a decrease in mass flow rate.

The effect of nitrogen concentration on the mass flow rates was studied as well. With an increase in nitrogen concentration in the gaseous mixture, the mass flow rates increased. The results imply that more ingress of nitrogen (air in actual air ingress situations) would lead to faster natural circulation flow rates and eventually faster oxidation of the graphite core in the flow loop. The effect of nitrogen concentration in the gaseous mixture on local Reynolds numbers at steady state was also investigated. The local Reynolds numbers were found to decrease along the riser flow channel due to the increase in the local bulk temperatures and the local gas viscosities. The present data on natural circulation of helium-nitrogen mixtures and the quantification of mass flow rates can be used to validate computational models used in safety analyses of high temperature gas reactors in accident situations.

Nomenclature

Cp	specific Heat Capacity, J/(kg·K)
d	channel diameter, m
g	gravitational acceleration, m/s^2
$\dot{m}$	mass flow rate, kg/s
Q_{Heater}	heater power going to mass flow rate measurement system, W
Q_{in}	total heat generated in each segment by the heaters, W
Q_{out}	total heat lost from PV surface and via axial conduction, W
r	radius of coolant channel, m
R	channel radius, m
Re	Reynolds number
$T_{Ambient}$	ambient temperature, K
Tb	bulk temperature
T_{in}	inlet temperature of mass flow rate measurement system, K
$T_{Insulation}$	insulation temperature of mass flow rate measurement system, K
T_{out}	outlet temperature of mass flow rate measurement system, K
Tw	wall temperature

U	velocity, m/s
z	channel length, m

Greek Symbols

ΔQ	total heat transferred to fluid, W
ΔRe	Reduction in local Re in the riser
μ	dynamic Viscosity, Pa.s
ρ	density, kg/m^3
τ	wall to bulk temperature ratio

Subscripts

He	Helium
$He + N_2$	Helium and Nitrogen Mixture
i	index number signifying local value for each segment
in	inlet
initial	first segment
final	eleventh segment
out	outlet

Abbreviations

CV	Cold Vessel
GMT	Graphite Midpoint Temperature
HV	Hot Vessel
MFR	Mass Flow Rate
PV	Pressure Vessel
T/C	Thermocouples connected to the mass flow rate measurement system
TD1-TD3	Thermocouples connected to the downcomer
T1-T10	Thermocouples connected to the riser
VHTR	Very High Temperature Reactor

REFERENCES (for Chapter 3)

[1] T. Takeda, M. Hishida, Studies on molecular diffusion and natural convection in a multicomponent gas system. Int. J. of Heat Mass Transf. 39 (1996), 527-36, https://doi.org/10.1016/0017-9310(95)00148-3.

[2] T. Takeda, M. Hishida, Study on the passive safe technology for the prevention of air ingress during the primary-pipe rupture accident of HTGR. Nucl. Eng. Des. 200 (2000), 251-259, https://doi.org/10.1016/S0029-5493(99)00338-6.

[3] G.E. McCreery, K.G. Condie, Experimental modeling of vhtr plenum flows during normal operation and pressurized conduction cooldown. Idaho National Laboratory (INL), 2006, https://inldigitallibrary.inl.gov/sites/sti/sti/3480271.pdf.

[4] X.L. Yan, T. Takeda, T. Nishihara, K. Ohashi, K. Kunitomi, N. Tsuji, A study of air ingress and its prevention in HTGR. Nuclear Technology. 163 (2008), 401-415, https://doi.org/10.13182/NT08-A3998

[5] C. Oh, E.S. Kim, R. Schultz, D. Petti, C.P. Liou, Implications of Air Ingress Induced by Density-Difference Driven Stratified Flow. Idaho National Laboratory (INL), 2008, https://inldigitallibrary.inl.gov/sites/sti/sti/3984774.pdf
[6] T. Takeda, Air ingress phenomena in a depressurization accident of the very-high-temperature reactor. Nucl. Eng. Des. 240 (2010), 2443-2450, https://doi.org/10.1016/j.nucengdes.2010.01.026.
[7] S. Kim, M.S. Yadav, J.D. Talley, A. Ireland, S.M. Bajorek, Separate effects experiments for air-ingress in helium filled vessel. Exp Therm Fluid Sci. 49 (2013), 1-13, https://doi.org/10.1016/j.expthermflusci.2013.02.022.
[8] D. J. Jr. Arcilesi, T.K. Ham, I.H. Kim, X. Sun, R.N. Christensen, C.H. Oh, Scaling and design analyses of a scaled-down, high-temperature test facility for experimental investigation of the initial stages of a VHTR air-ingress accident. Nucl. Eng. Des. 288 (2015) 141-62, https://doi.org/10.1016/j.nucengdes.2015.03.007.
[9] J.S. Kim, J.S. Hwang, E.S. Kim, B.J. Kim, C.H. Oh, Experimental study on fundamental phenomena in HTGR small break air-ingress accident. Ann Nucl. Energy. 87 (2016), 145-156, https://doi.org/10.1016/j.anucene.2015.08.012.
[10] I.A. Said, M.M. Taha, S. Usman, B.G. Woods, M.H Al-Dahhan, Investigation of natural convection heat transfer in a unique scaled-down dual-channel facility. AIChE J. 63 (2017), 387-396, https://doi.org/10.1002/aic.15583.
[11] S.M. Alshehri, I.A. Said, M.H. Al-Dahhan, S. Usman, Plenum-to-plenum natural convection heat transfer within a scaled-down prismatic modular reactor facility. Therm. Sci. Eng. Prog. 7 (2018), 288-301, https://doi.org/10.1016/j.tsep.2018.06.011.
[12] I.A. Said, M.M. Taha, S. Usman, M.H. Al-Dahhan, Effect of helium pressure on natural convection heat transfer in a prismatic dual-channel circulation loop. Int. J. Therm. Sci. 124(2018), 162-173, https://doi.org/10.1016/j.ijthermalsci.2017.10.004.
[13] I.A. Said, M.M. Taha, S. Usman, M.H. Al-Dahhan, Experimental investigation of the helium natural circulation heat transfer in two channels facility using varying riser channel heat fluxes. Exp. Therm. Fluid Sci. 93(2018), 195-209, https://doi.org/10.1016/j.expthermflusci.2017.12.027
[14] J.J. Lee, T.K. Ghosh, S.K. Loyalka, Oxidation rate of nuclear-grade graphite IG-110 in the kinetic regime for VHTR air ingress accident scenarios. J. Nucl. Mater. 446 (2014), 38-48, https://doi.org/10.1016/j.jnucmat.2013.11.032.
[15] S. Alshehri, I.A. Said, M.H. Al-Dahhan, S. Usman, Experimental Investigation of Plenum-to-Plenum Natural Circulation Heat Transfer in a Prismatic Very-High-Temperature Reactor. Amer. Nucl. Soc. Annual Meeting 2018.
[16] C.H. Oh, E.S. Kim, C.H. No, N.Z. Cho, Final report on experimental validation of stratified flow phenomena, graphite oxidation, and mitigation strategies of air ingress accidents. Idaho National Laboratory (INL); 2011. https://www.osti.gov/servlets/purl/1023463.
[17] M. Hishida, M. Fumizawa, T. Takeda, M. Ogawa, S. Takenaka, Researches on air ingress accidents of the HTTR. Nucl. Eng. Design. 144 (1993), 317-325, https://doi.org/10.1016/0029-5493(93)90147-2.

[18] D. Gould, D. Franken, H. Bindra, M. Kawaji, Transition from molecular diffusion to natural circulation mode air-ingress in high temperature helium loop. Annal. Nucl. Energy. 107 (2017), 103-109, https://doi.org/10.1016/j.anucene.2017.03.049.
[19] A.V. Rudra, D.V. Kalaga, M. Kawaji, Experimental Investigation of Natural Circulation During Air-Ingress Scenario in a Very High Temperature Reactor. Nucl. Sci. Eng. (2019), https://doi.org/10.1080/00295639.2019.1595311.
[20] X. Sun, R. Christensen, C. Oh, Investigation of countercurrent helium-air flows in air-ingress accidents for VHTRs. Final Report on NEUP Project No. 09-784, Battelle Energy Alliance, LLC; (2013), https://www.osti.gov/servlets/purl/1128529
[21] H. Haque, W. Feltes, G. Brinkmann, Thermal response of a modular high temperature reactor during passive cooldown under pressurized and depressurized conditions. Nucl. Eng. Des. 236 (2006), 475-484, https://doi.org/10.1016/j.nucengdes.2005.10.027.
[22] C.H. Oh, E.S. Kim, H.S. Kang, Natural circulation patterns in the VHTR air-ingress accident and related issues. Nucl. Eng. Des. 249 (2012), 228-236, https://doi.org/10.1016/j.nucengdes.2011.09.031.
[23] C.H. Oh, H.S. Kang, E.S. Kim, Air-ingress analysis: Part 2—Computational fluid dynamic models. Nucl. Eng. Des. 241 (2011), 213-225, https://doi.org/10.1016/j.nucengdes.2010.05.065.
[24] H.G. Jin, H.C. No, H.I. Kim, Stratified flow induced air-ingress accident assessment of GAMMA code. In Proceedings of the 2010 International Congress on Advances in Nuclear Power Plants-ICAPP'10 2010, https://www.sciencedirect.com/science/article/pii/S0029549311003281
[25] H.G. Jin, H.C. No, B.H. Park, Effects of the onset time of natural circulation on safety in an air ingress accident involving a HTGR. Nucl. Eng. Des. 250(2012), 626-632, https://doi.org/10.1016/j.nucengdes.2012.06.028.
[26] T.K. Ham, D.J. Jr. Arcilesi, I.H. Kim, X. Sun, R.N. Christensen, C.H. Oh, E.S. Kim, Computational fluid dynamics analysis of the initial stages of a VHTR air-ingress accident using a scaled-down model. Nucl. Eng. Des. 300(2016), 517-529.
https://doi.org/10.1016/j.nucengdes.2016.02.011.
[27] W. Xu, Y. Zheng, L. Shi, P. Liu, Oxidation analyses of massive air ingress accident of HTR-PM. Sci. Technol. Nucl. Installations. 2016, 1-9, http://dx.doi.org/10.1155/2016/6419124.
[28] E.S. Kim, H.C. No, B.J. Kim, C.H. Oh, Estimation of graphite density and mechanical strength variation of VHTR during air-ingress accident. Nucl. Eng. Des. 238(2008), 837-847, https://doi.org/10.1016/j.nucengdes.2007.08.002.
[29] Y.H. Tung, R.W. Johnson, Y.M. Ferng, C.C. Chieng, Modeling strategies to compute natural circulation using CFD in a VHTR after a LOFA. Nucl. Eng. Des. 275(2014), 80-90, https://doi.org/10.1016/j.nucengdes.2014.04.012
[30] H.S. Lim, H.C. No, GAMMA multidimensional multicomponent mixture analysis to predict air ingress phenomena in an HTGR. Nucl. Sci. Eng. 152(2006) 87-97, https://doi.org/10.13182/NSE06-5.

[31] D. Franken, D. Gould, P.K. Jain, H. Bindra, Numerical study of air ingress transition to natural circulation in a high temperature helium loop. Annal. Nucl. Energy. 111(2018), 371-378, https://doi.org/10.1016/j.anucene.2017.09.007.
[32] C.H. Oh, E.S. Kim, Air-ingress analysis: Part 1. Theoretical approach. Nucl. Eng. Des. 241 (2011), 203-212, https://doi.org/10.1016/j.nucengdes.2010.05.064.
[33] F.I. Valentín, N. Artoun, R. Anderson, M. Kawaji, D.M. McEligot, Study of convection heat transfer in a very high temperature reactor flow channel: Numerical and experimental results. Nucl. Technol. 196 (2016), 661-673, https://doi.org/10.13182/NT16-46.
[34] F.I. Valentín, R. Anderson, M. Kawaji, Experimental Investigation of Convection Heat Transfer in High Pressure and High Temperature Gas Flows. J. Heat Trans. 139 (2017), 091704, doi: 10.1115/1.4036524.
[35] F.I. Valentín, N. Artoun, M. Kawaji, Experimental Investigation of Flow Laminarization in a Graphite Flow Channel at High Pressure and High Temperature. J. Heat Trans. 140 (2018), 112004, doi:10.1115/HT2017-4818.
[36] F.I. Valentín, N. Artoun, M. Kawaji, D.M. McEligot, Forced and Mixed Convection Heat Transfer at High Pressure and High Temperature in a Graphite Flow Channel. J. Heat Trans. 140 (2018), 122502, doi: 10.1115/1.4039585.
[37] J.P. Holman, Heat Transfer, 9th ed., McGraw-Hill, New York (2002).

CHAPTER 4: Task 3 Report on Bypass Flow Experiments and Data Analysis

This Chapter discusses the bypass flow experiment facility utilizing nitrogen and experimental procedure used to collect bypass flow data in a circular channel and rectangular bypass channel. The method of data analysis and results are also described. Since the inlet and outlet gas temperatures in VHTR designs are expected to be 450 and 950°C, giving rise to a ~500°C increase, the present experiments are consistent with the coolant temperature increase in the VHTR reactor core, although the current flow channel length is about 1/3 of that of the VHTR.

4.1 Bypass Flow Test Facility

An existing high temperature/high pressure forced convection test facility constructed at CCNY in the preceding NEUP project was modified to conduct the bypass flow experiments. This flow loop was rated at maximum operating pressure and temperature of 68 bar (1000 psi) and 600°C, respectively. As explained in Appendix 1, the bypass flow test facility includes a pressure vessel, graphite test section with a rectangular bypass flow channel, high pressure compressor, coil heat exchanger, and thermocouple assembly. Figure 4.1 shows a photograph of the bypass flow test facility. A cross section of the bypass flow test section is shown in Fig. 4.2.

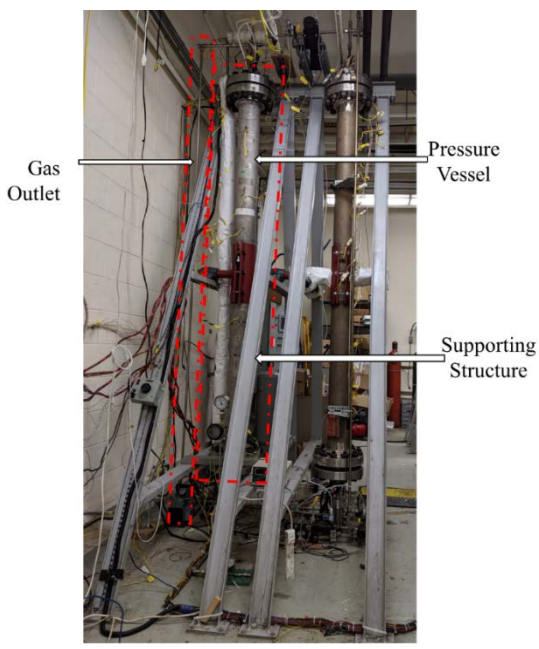

Figure 4.1 Photograph of the bypass flow test facility at CCNY

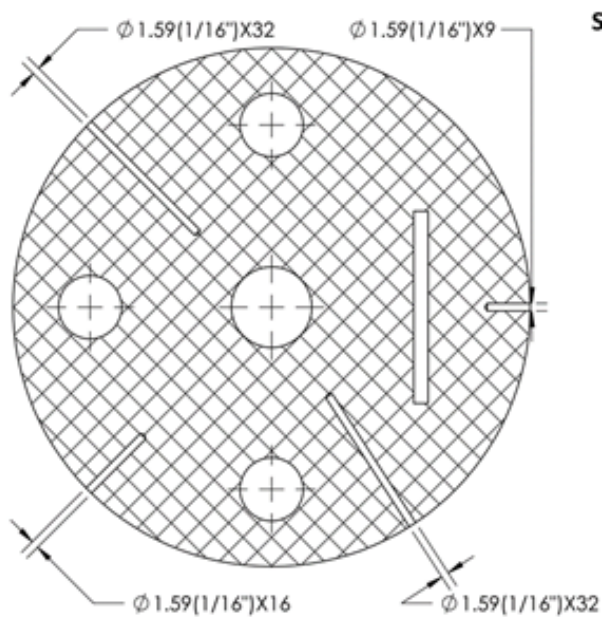

Figure 4.2 Graphite test section for bypass flow tests

A process flow diagram is shown in Fig. 4.3. A 3D drawing of the entire test facility is shown in Fig. 4.4, while individual components in the 3-D drawing are shown in Figs. 4.5 and 4.6.

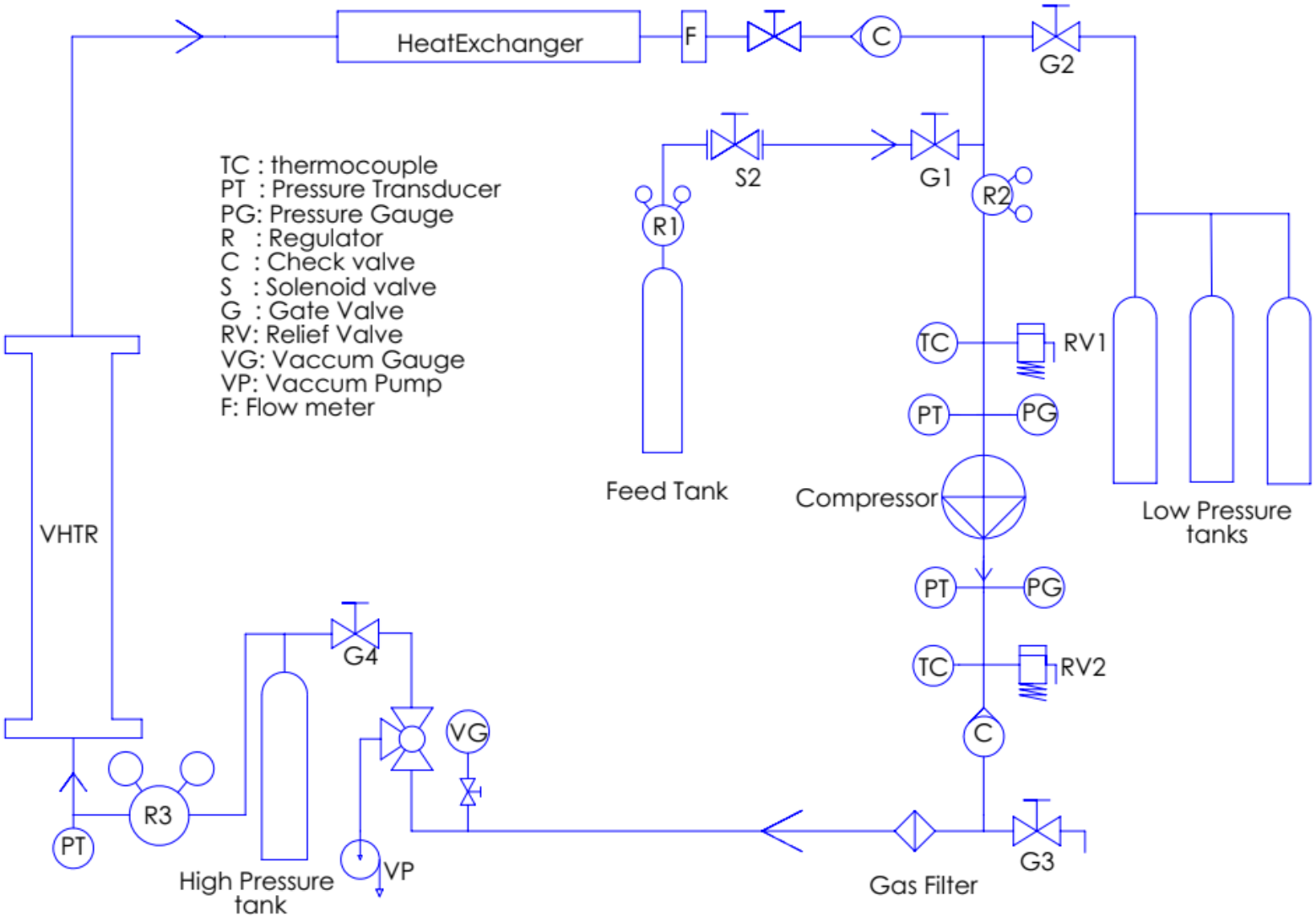

Figure 4.3 Process Flow Diagram of the Bypass Flow test facility.

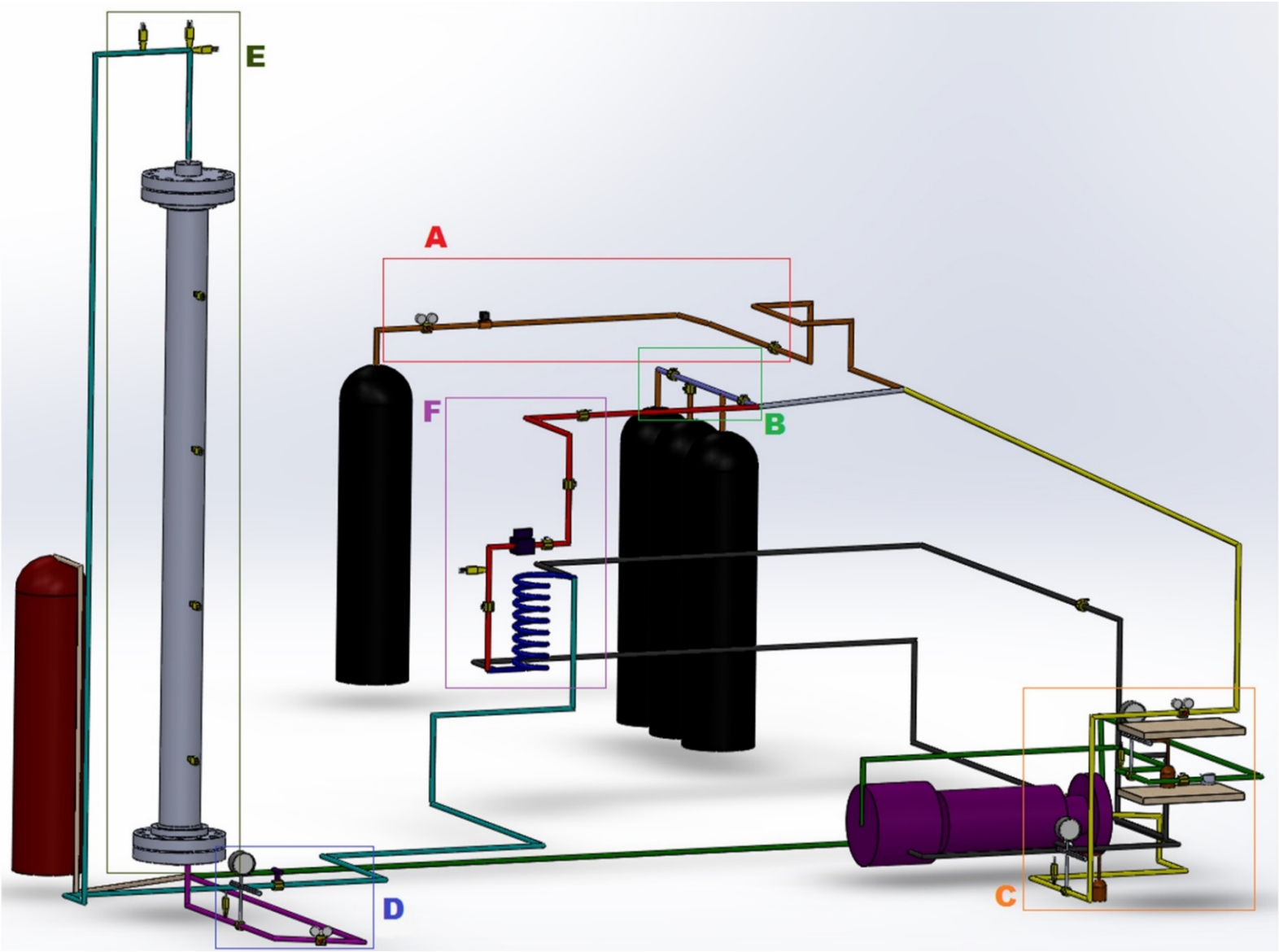

Figure 4.4 A 3D drawing of the Bypass Flow test facility.

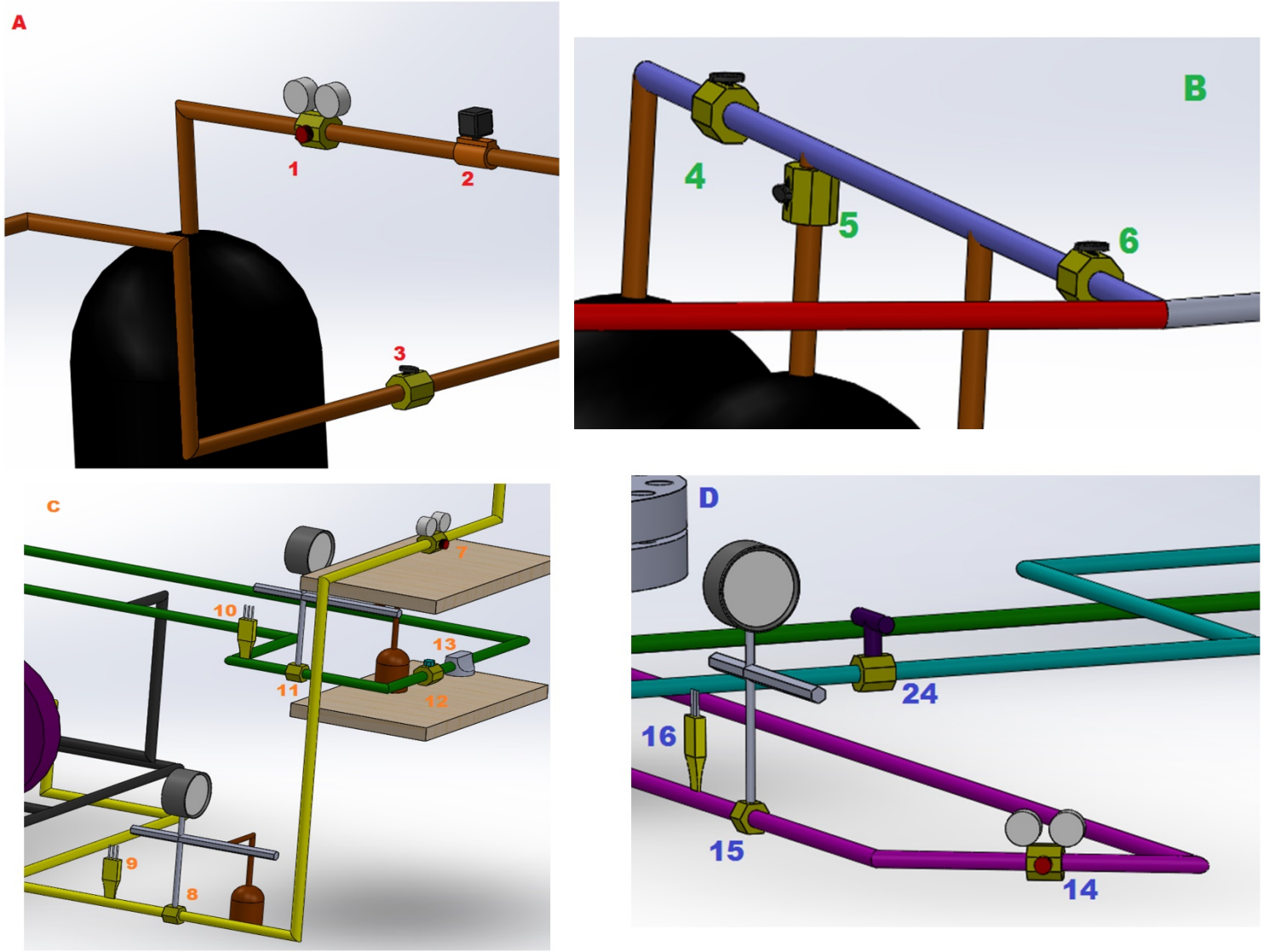

Figure 4.5 Magnified view of the sub sections A to D of the flow diagram.

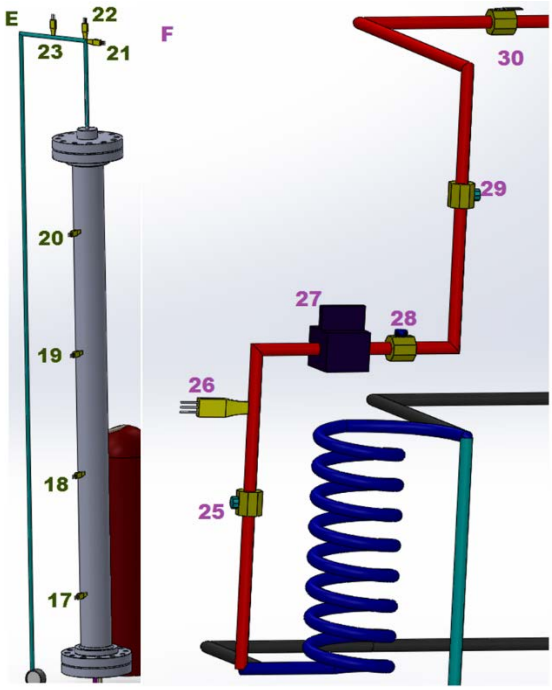

Figure 4.6 Magnified view of the sub sections E and F of the flow diagram

The bypass flow test section was designed and fabricated to accommodate a circular main flow channel of 16.8 mm diameter in the middle, a rectangular bypass flow channel (3.0 mm x 40.0 mm) and three holes for heater rods in a graphite column as shown in Table 4.1 and Fig. 4.2. The heater input power could be varied to maintain different mean graphite temperature in the graphite test section.

Table 4.1 Dimensions of the graphite test section

Material	Graphite G348	
Length	2,750 mm	108.0” (2 x 54.5”)
Outer Diameter	108.0 mm	4.25”
Flow Channel Diameter	16.8 mm	0.66”
Bypass flow Channel	40 × 3 mm	1.58” × 0.12”
Heater Channel Diameter	12.7 mm	0.5”

A legend of components shown in Figs. 4.4 and 4.5 is listed in Table 4.2.

Table 4.2 Legend of components in sections of Bypass Flow test loop (Figs. 4.4 and 4.5)

Label Number	Component Name	Section of Loop
1	Regulator	High Pressure Feed Tank
2	Solenoid Valve	
3	Ball Valve (ON/OFF)	
4	Ball Valve (ON/OFF)	Low Pressure Tanks
5	Ball Valve (ON/OFF)	
6	Ball Valve (ON/OFF)	
7	Gas Regulator	Compressor Inlet
8	T-joint (PT, RV, PG)	
9	Thermocouple	
10	Thermocouple	Compressor Outlet
11	T-joint (PT, RV, PG)	
12	Check Valve	
13	Gas Filter	
14	Gas Regulator	VHTR Inlet
15	T-Joint (PT, Vaccum Gauge, PG)	
16	Thermocouple	
17	Thermocouple	VHTR Surface
18	Thermocouple	
19	Thermocouple	
20	Thermocouple	
21	Thermocouple	VHTR Outlet
22	Hot Wire Probe	
23	Thermocouple	
24	Flow Control valve	
25	Check Valve	Coil Heat Exchanger
26	Thermocouple	
27	Mass Flow Meter	
28	Needle Valve	
29	Check Valve	
30	Ball valve (ON/OFF)	

The main components of the Bypass Flow test facility included: 1) a stainless steel pressure vessel, 2) Insulation layer, 3) electrically heated graphite test section with two (circular and rectangular) flow channels, 4) three electric heater rods. The graphite test section was housed in a stainless steel 304 pressure vessel (PV), which was ASME certified at 70 bar (1,015 psi) at 350°C, and had ANSI Class 900 flanges welded at the top and bottom. An inner insulation layer protected the PV wall from the high graphite temperatures, and directed heat flux into the coolant channel. This layer consisted of a 19.2 mm (0.756 in) thick fiberglass thermal insulation [Great Lakes Textiles Inc., GB1BLTMAT] and was placed between the graphite test section surface and inner wall of the PV. The graphite test section was a 108.0 mm (4.25 in) diameter cylindrical column made of thermally isotropic graphite G348 [Graphite Store] with a thermal conductivity of 128 W/mK at 298 K. This graphite test section consisted of two 1250.0 mm (49.2 in) long sections joined in the middle with a short piece of a stainless steel tube (ID:16.8 mm, OD: 19.05 mm and length: 80mm) and a piece of a stainless steel rectangular channel (5 mm x 40 mm, length: 80 mm).

A sketch of the flow channels in the graphite test section is shown in Fig. 4.7. CAD drawings of the pressure vessel, flanges and internal components are shown in Fig. 4.8. The graphite column has a circular flow channel of 16.8 mm at the center and a rectangular flow channel of 3 mm × 40 mm along which the compressed gas flowed. The circular channel radius and the rectangular slit were chosen based on the HTTF design, for which a scaling analysis had been performed (Woods and Jackson, 2010; Schultz et al., 2008, 2010). The HTTF is a scaled model of the General Atomics' MHTGR, scaled ¼ by height and ¼ by diameter.

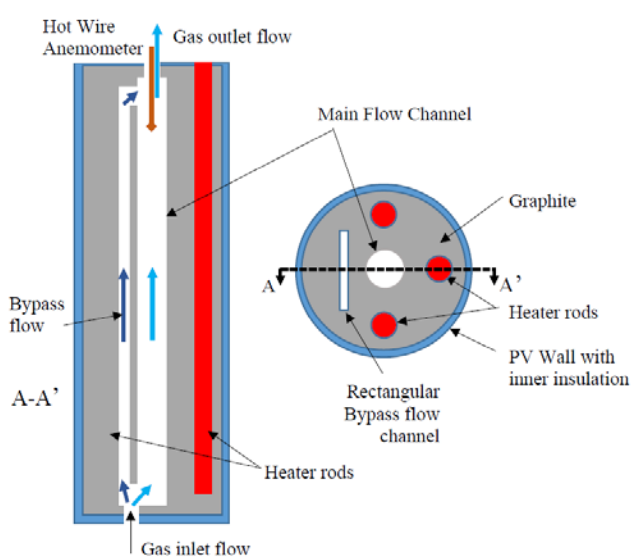

Fig. 4.7 Main Circular and Rectangular Bypass Flow Channels in the Graphite Test section

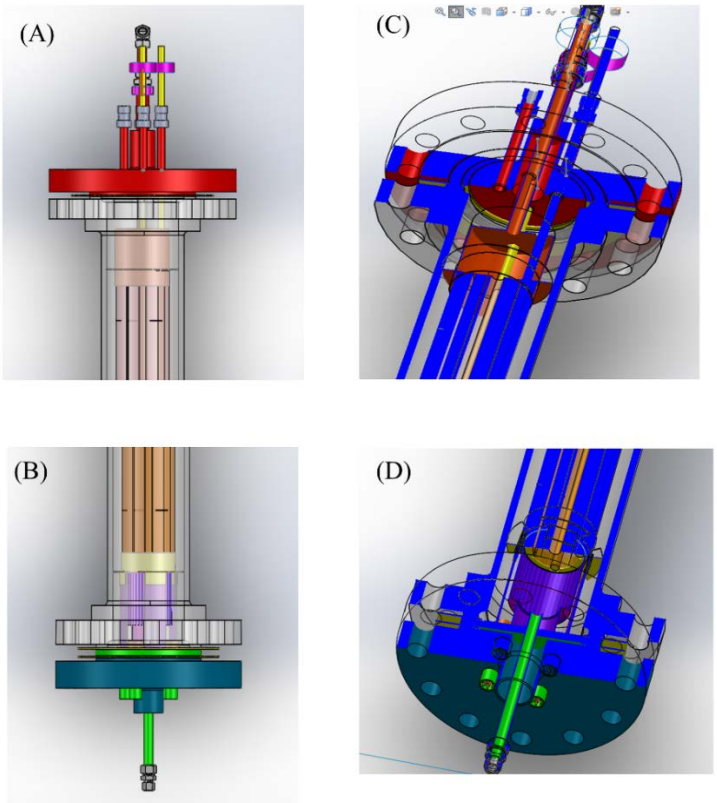

Fig. 4.8 (A) Front view of the top flange. (B) Front view of the bottom flange (C) Sectional view of the top flange showing the gas exit. (D) Sectional view of the bottom flange showing the gas injection, bypass and main flow channels in graphite.

After examining in detail the scaling issues involved in the design of MHTGR and HTTF, the circular flow channel and rectangular flow channel geometries and parameters in the present facility were finalized including the graphite length, gas pressure and temperature, the gas properties and flow rate, in order to best match the dimensionless parameters (Reynolds, Grashoff, and Prandtl numbers) among our tests, prototype, and HTTF. The graphite test section contains three holes symmetrically placed around the circular flow channel for insertion of heater rods (D_{Heater} = 12.7 mm). These heaters rods were 2.3kW, 240 V AC, 12.6 mm diameter [Watlow] and 3,048 mm (120”) long. The top 300 mm (12 in) was an unheated section for penetration through the top flange. Each heater rod was connected to an AC power source through a controller, a 0-240 V AC variable transformer, and circuit breaker, so that the heater power could be individually controlled and recorded.

A total of 40 type K thermocouples were installed at 10 axial locations to measure the axial and radial temperature profiles in the graphite test section. At each axial location, four thermocouples were installed at four diagonal positions and three different radial distances from the axis. Their azimuthal locations were rotated counterclockwise by 90° in each successive axial plane. Six additional thermocouples were spot welded onto the PV's outer surface at 6 different elevations to monitor and record the PV's outer surface temperature profile. A pressure transducer [Omega, PX313] was installed at the inlet piping connected to the pressure vessel. A gas flow meter [Omega, FMA-878A-V] was located on the outlet piping of the open loop to measure the total gas flow rate through the main circular and rectangular bypass flow channels.

To ensure a uniform gas distribution before the gas enters both circular and rectangular by-pass flow channels, the high-pressure gas, which is at room temperature, flows through a stainless-steel tube into an inlet chamber equipped with a porous disk (thickness: 2.3mm O.D: 92.2mm, pore size 100μm) to ensure uniform gas velocity distribution before entering the graphite test section (Fig. 4.9).

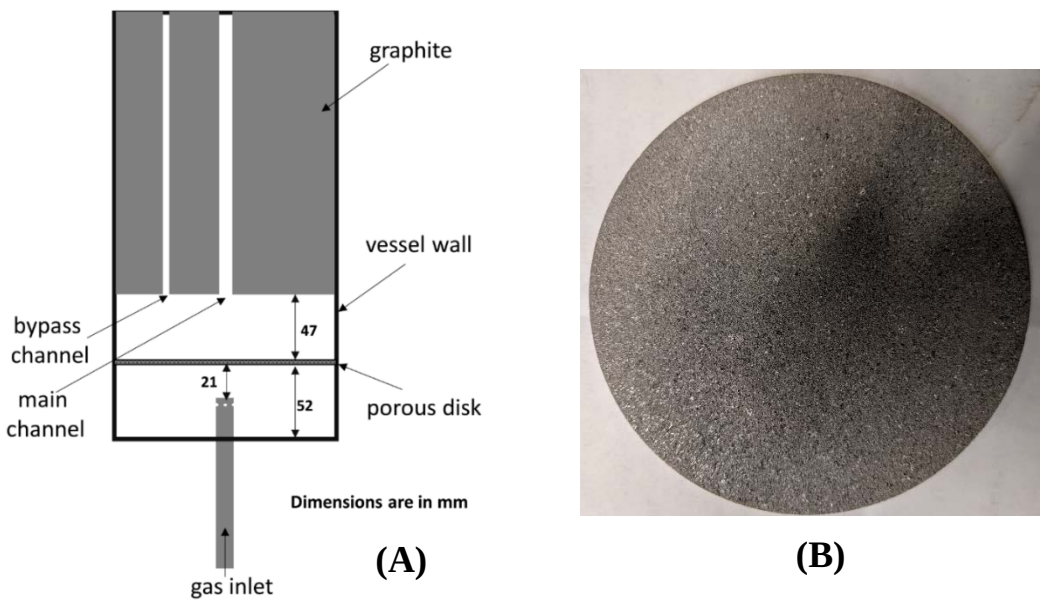

Figure 4.9 Gas injection system for the bypass flow test facility (A) Schematic of the gas injection chamber and (B) a porous disk gas distributor

4.2 Forced Gas Circulation System

In order to carry out bypass flow experiments with nitrogen at high flow rates at a constant operating pressure and operating temperature, a gas circulation system was constructed. A high-

pressure compressor (Hydro-Pac Inc. Model No: C01.5-10-1300LX) was used to compress the low-pressure gas coming from the feed tanks (for initial filling of the flow loop) and low-pressure tanks (while operating in a closed loop). The gas temperature increased in the process of compression and hence the gas coming from the compressor was hot. The compressor was equipped with a shell and tube heat exchanger, and chilled water (< 10 ^{o}C) is circulated through the shell side at a minimum volumetric flow rate of 2.0 GPM. A high pressure gas cylinder was installed just before the pressure vessel inlet, to dampen the fluctuations in the gas flow rate.

To achieve a constant gas flow rate, the test facility was initially (above 200 psi) filled with the nitrogen gas from a high-pressure feed tank. Then the compressor was turned on and the flow loop pressure was maintained at the desired operating pressure. To avoid pressure and flow fluctuations, the high-pressure gas coming out of the compressor was sent to a high-pressure tank before going to the test section. The gas exiting the test section then flowed into a bank of three low pressure receiver tanks. These three low pressure receiver tanks also acted as gas supply tanks to maintain steady gas flow rates.

The gas flow rate entering and leaving the test section was controlled by a gas regulator and needle valve (components 14 in Fig. 4.5 and 28 in Fig. 4.6). The hot gas coming out of the test section was cooled down in a coil heat exchanger. The gas circulation rate was measured by a mass flow meter (OMEGA MODEL: FMA-878A-V) installed downstream of the coil heat exchanger. Eventually the high-pressure gas exiting the graphite test section is depressurized by a valve and flows into low pressure tanks consists of three gas cylinders (see Fig. 4.3). These low-pressure gas cylinders serve as feed tanks when the flow loop is in a continuous operation. To avoid excessive pressure buildup and back flow, two check valves are installed in the compressor outlet line and in the pressure vessel outlet line after the coil heat exchanger. For safety reasons, the flow loop was also equipped with two pressure relief valves set at a relief pressure of 65 bar (950 psi).

4.3 Hot Wire Anemometer Measurement

Preliminary bypass flow measurements were conducted using a high temperature hot wire anemometer (HWA) probe from Dantec Dynamics. The X-wire HWA probe equipped with a thermocouple (Fig. 4.9) was inserted into the main flow channel at the top of the graphite test section as shown in Figure 4.10.

Fig. 4.10 High Temperature Hot Wire Anemometer X-wire probe equipped with a thermocouple

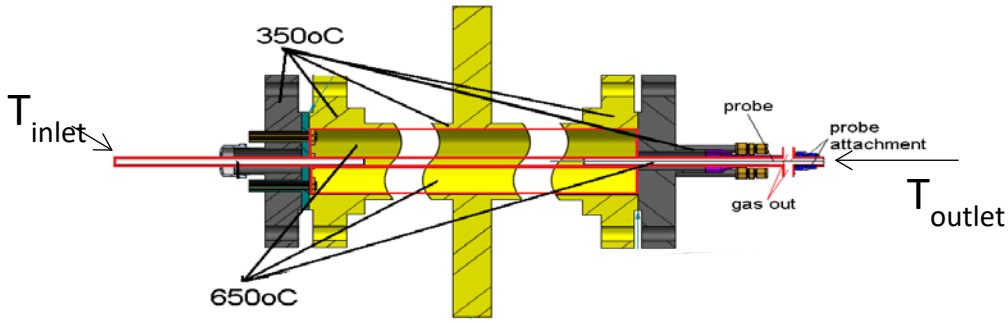

Fig. 4.11 Placement of a hot wire anemometer probe and thermocouple probe for turbulence measurements.

All instruments were connected to a National Instruments' Data Acquisition System [NI-cDAQ-9188], containing eight data acquisition cards. One analog voltage input module (NI 9205) for controlling the compressor outlet pressure, three NI-9213 modules, one NI-9211 and one NI-9263 module were used for recording the thermocouple data. Another module NI-9247 was used to record the pressure data coming from Pressure Transducers. Finally, one NI-9215 BNC module was used to record the Hot Wire Anemometer data. The data monitoring and acquisition was performed on a PC via a LabVIEW program. Additional safety systems included: relief valves set at 950 psi for avoiding overpressure, hater rod temperature controllers, and a water-cooled heat exchanger added to cool the hot gas coming out of pressure vessel and compressor.

4.3 Experimental procedure

Prior to the bypass flow experiments, the test facility was thoroughly tested to check the gas leakage rate. The bypass flow test facility was found to lose its pressure at a rate of 5psi per hour for nitrogen gas as the working fluid. The pressure regulator installed near the high-pressure feed tank (~2500 psi) was slowly opened to fill the entire loop with ~ 20.4 bar or ~300 psi (this

pressure varies proportionally with the operating pressure). The compressor was turned on after ensuring all the valves installed in the flow loop had been fully opened. The compressor was ramped up to achieve the working pressure, by increasing the voltage signal of the compressor motor controller. The compressor was allowed to run for at least 15 mins to achieve the steady working pressure. The AC power for the three heaters was turned on and variacs were adjusted to maintain the prescribed mean graphite temperature in the bypass flow test section. After reaching steady state conditions, the velocity and temperature of the gas flowing out of the main circular graphite channel were measured, over a long time, using a hot wire probe and k-type thermocouple. Further, the total gas circulation rate and the bulk temperature of the gas at the pressure vessel outlet were measured simultaneously using OMEGA mass flow meter and thermocouple, and recorded. Bypass flow experiments have been performed with pure nitrogen over a wide range of temperature and pressure.

After some preliminary testing, however, the hot wire probe was damaged and returned to the manufacturer's repair facility in Denmark for repair in early 2019. The repaired probe was received after two months but the probe tip was again damaged during the shipment and the signals were still unsatisfactory. The hot wire probe was again returned to Denmark, but the repair could not be completed in time before this project ended in June. Thus, an alternative method of determining the flow rates in the main and bypass flow channels was developed based on bulk gas temperature measurements in the main channel and after the gas streams merge above the graphite test section. Energy balance equations for the gas streams between the inlet and outlet of the main and bypass channels could be solved with measured graphite temperatures to obtain respective flow rates.

4.3 Data Analysis Procedure

This section presents the methodology involved in calculating the gas circulation rates and heat transfer parameters from the obtained gas temperature measurements. Having measured the mass flow rate through the system, it was possible to determine the local Reynolds number at any axial location, by knowing the local bulk temperature and using Eq. (4.1)

$$Re = \frac{2\dot{m}}{\pi \mu r} \qquad (4.1)$$

where the local dynamic viscosity, μ, is evaluated at the local bulk temperature. The axial bulk temperature profile of the gas was determined by dividing the graphite test section into 10

segments and carrying out an energy balance for each segment. The inlet and outlet bulk temperatures for each segment were then determined using Eq. 4.2,

$$T_{i+1} = T_i + \frac{\Delta Q}{\dot{m}C_p} \tag{4.2}$$

where T_i and T_{i+1} respectively denote the inlet and outlet bulk temperatures in each segment, and ΔQ is the heat removed by the gas with the specific heat capacity of Cp = 1,089 J/kg·K flowing at a mass flow rate of $\dot{m}$. For Eq. (4.3), ΔQ was calculated per segment as follows,

$$Q_{loss} = Q_{input/segment} - \left(Q_{G_cond} + Q_{PV_cond}\right) \tag{4.3a}$$

$$\Delta Q = Q_{in} - Q_{out,tot} = \frac{\sum_1^3 P_n}{10} - Q_{HL} - Q_{axial} \tag{4.3b}$$

where Q_{in} for each segment was constant and equal to the sum of the heat generated, P_n, by three heater rods in each segment, and $Q_{out,tot}$ included heat losses from the PV surface and net axial conduction for each segment. The rate of heat loss from the PV surface, Q_{HL}, was correlated to the average value of the PV surface and the graphite temperatures at each elevation. This correlation was obtained from stagnant gas tests. A simple diagram of this methodology is illustrated in Fig. 4.5. By performing stagnant gas tests, one could correlate surface heat losses, and then apply this correlation to forced convection tests per segment as presented in Figure 4.5. The axial conduction term, Q_{axial}, was the sum of the net axial heat conduction in both the stainless-steel PV wall and graphite test section, which could be obtained from the axial temperature gradients measured. Equation (4.4) gives the correlation used to determine the local graphite thermal conductivity in the axial heat loss calculations. This correlation was derived from measurements conducted at the Idaho National Laboratory (INL). The data were obtained by using a sample of the same graphite used in our experiments, and measuring the thermal conductivity at temperature, T, ranging from 295 K to 1,274 K.

$$k_{G348} = 134.0 - 0.1074T + 3.749\times10^{-5}T^2 \tag{4.4}$$

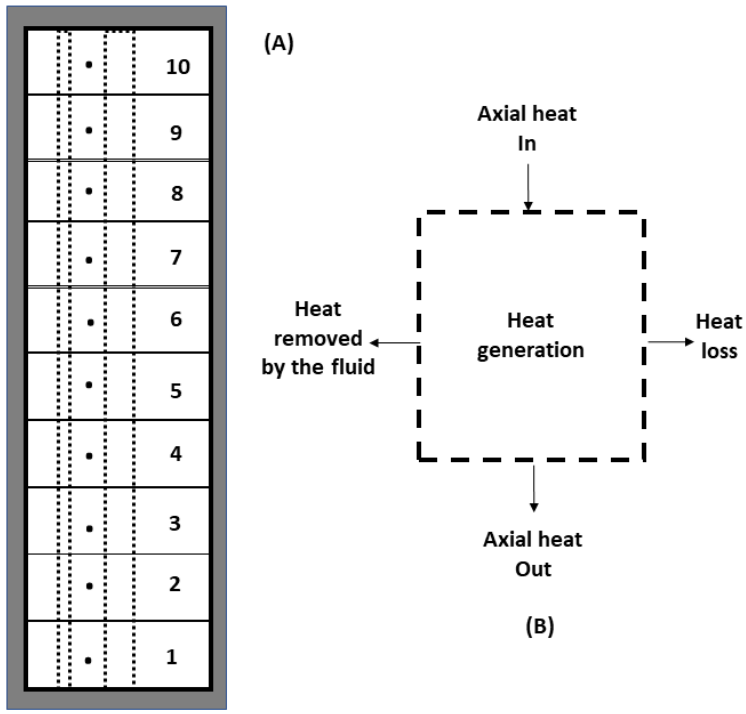

Fig. 4.12 Heat balance diagram for forced circulation tests (a) graphite segments to perform the gas heat balance and (b) heat balance diagram over each segment.

Having measured the graphite temperatures at three different radial positions at any axial elevation, the radial temperature profile was extrapolated to obtain the inner wall temperature, T_{wi}, and calculate the heat transfer to the fluid using Equation 4.5,

$$\Delta Q = hAh(T_{wi} - T_i) \tag{4.5}$$

where h_i is the local heat transfer coefficient, A_h is the heat transfer area (= heated perimeter x segment length). The total mass circulation rate (m_{total}) is measured by the mass flow meter which includes the flows in both the circular ($m_{circular}$) and rectangular bypass (m_{bypass}) channels.

$$m_{total} = m_{circular} + m_{bypass} \tag{4.6}$$

Further, the heat balance for each of the two channels can be performed using the following equations:

$$\Delta Q = m_{circular} C_p \left(T_{gi+1} - T_{gi}\right) \tag{4.7}$$

$$m_{total} C_p T_{g_total} = m_{circular} C_p T_{g_circular} + m_{bypass} C_p T_{g_bypass} \tag{4.8}$$

where *m* denotes the mass circulation rate and *T* denotes the gas temperature. Nitrogen gas density and specific heat capacity were evaluated at the locally calculated bulk gas temperature. The

unknown variables are the individual mass flow rates through circular channel and rectangular bypass channel were obtained by a trial and error method.

4.4 Bypass Flow Experiment Results

Each experiment involved independent selection and control of three parameters: graphite mid-point temperature, gas pressure and flow rate. While the graphite mid-point temperature was controlled by the heater power, pressure and flow rate were set by the controller of the motor attached to the compressor. Experiments were begun by turning on the power for three electric heater rods. The heater power settings were individually controlled with AC variable transformers.

The high-pressure compressor was turned on and the manual flow control valve was adjusted to vary the flow rate from 10-700 SLPM. The low gas flow rate was initially used so that the axial temperature profile in the graphite would reach close to the final temperature profiles more quickly. After the desired mid-point graphite temperature was achieved, the heater input power was adjusted, and the total mass flow rate was set to a desired value. Data acquisition was continued until near steady state values were reached in all parameters. Steady state was declared when the change in any of the graphite temperature readings was less than 3 ^{o}C/hour. The data were then analyzed for this specific time period. A total of 60 experiments were carried out. The average percentage differences in the mass flow rate, pressure and heater power under the same experimental conditions were 1.3, 0.6, and 1.2 %, respectively.

Prior to the actual experiments, stagnant gas experiments were performed to quantify the heat loss for each operating condition. Figure 4.13 shows the typical graphite (accommodating both circular and bypass flow channels) temperature profiles for the operating pressure of 700 psi and the midpoint temperatures of 100, 200, 300 and 400°C. The label B1 denotes the thermocouple located at the lowest axial location and B10 denotes the top axial location. It is clear that the temperature variation in the graphite block is very small at low midpoint temperature (100°C) but is large at high midpoint temperature (400°C). In this report, the data corresponding to the 200 ^{o}C case are extracted and used for the axial conduction heat transfer calculations in the graphite.

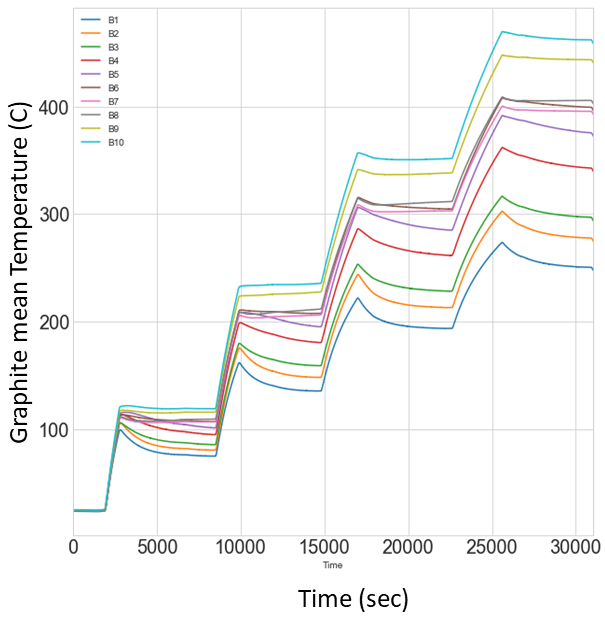

Fig. 4.13 Typical graphite temperature profiles for operation at 700 psi and 100 to 400°C.

The surface temperatures of the pressure vessel, top flange and bottom flange are shown in Fig. 4.14. The data corresponding to the 200 °C are extracted and further used in the analysis of the axial heat transfer among each graphite block segment.

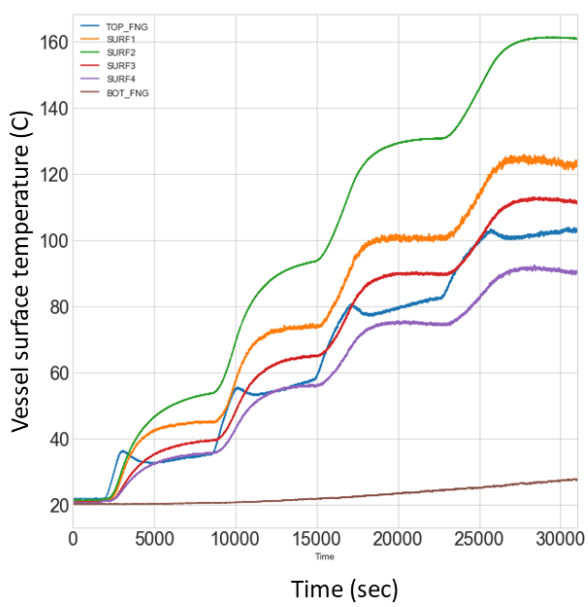

Figure 4.14 Surface temperature profile for the operating pressure (700 psi) and midpoint temperatures of 100, 200, 300 and 400 °C.

Once the graphite midpoint temperature attained the steady state temperature, the compressor was turned on and the required circulation rate was maintained for 10 to 15 mins. Figure 4.15A shows the typical volumetric flow rate profile for the operating pressure at 700 PSI, and operating temperatures of 200 to 400^{0}C. As shown in Fig. 4.15A, three sets correspond to the three temperatures and each set contains steady values of the total volumetric flow rate. The corresponding pressure values at the test section inlet, and compressor inlet and outlet are shown in Fig. 4.15B. As shown, though the pressures are fluctuating at the inlet and outlet of the compressor, the flow is steady.

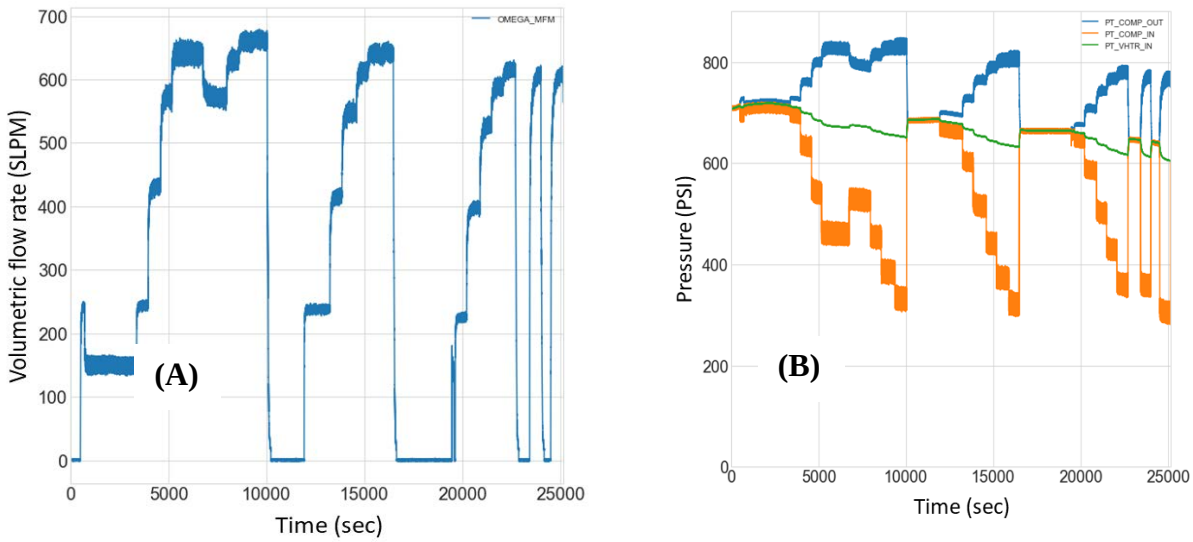

Figure 4.15 (A) Volumetric flow rate of the nitrogen in the entire loop and (B) Pressure for the operating pressure (700 psi) and temperatures of 200, 300 and 400°C.

Figure 4.16 shows the gas temperatures measured at several locations in the bypass flow test facility. The temperatures of the gas leaving the main circular channel, and in the Pressure Vessel (PV) outlet, are high compared to the gas temperatures at all other locations. This confirms that the gas heating is only due to the heater rods in the graphite test section. It is important to note that the nitrogen gas in the circular channel is always high compared to the gas existing the Pressure Vessel, which is the combined gas temperature of the gas leaving both bypass and circular channels.

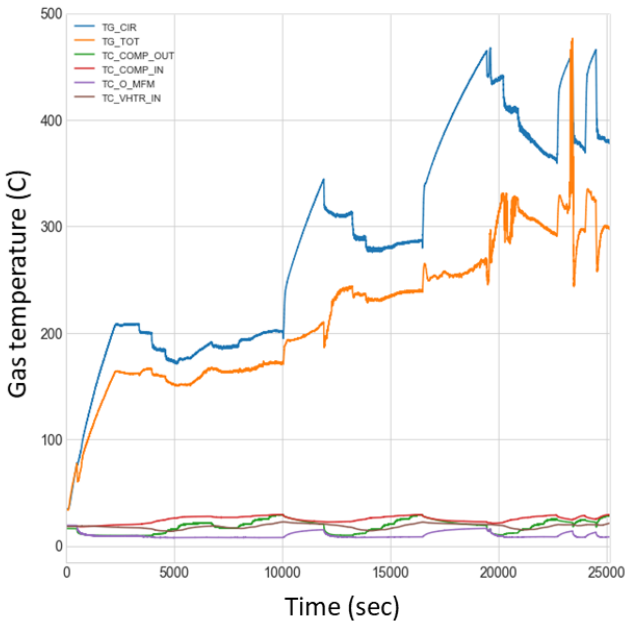

Fig. 4.16 The gas temperatures measured at different locations in the flow loop for the operating pressure (700 psi) and temperatures of 200, 300 and 400°C.

Figure 4.17 shows the heater power, gas inlet and outlet bulk temperatures, and graphite temperature data for 700 psi and 200 °C graphite mean temperature. The data are then used in the heat balance analysis to determine the mass flow rates in the bypass and main flow channels.

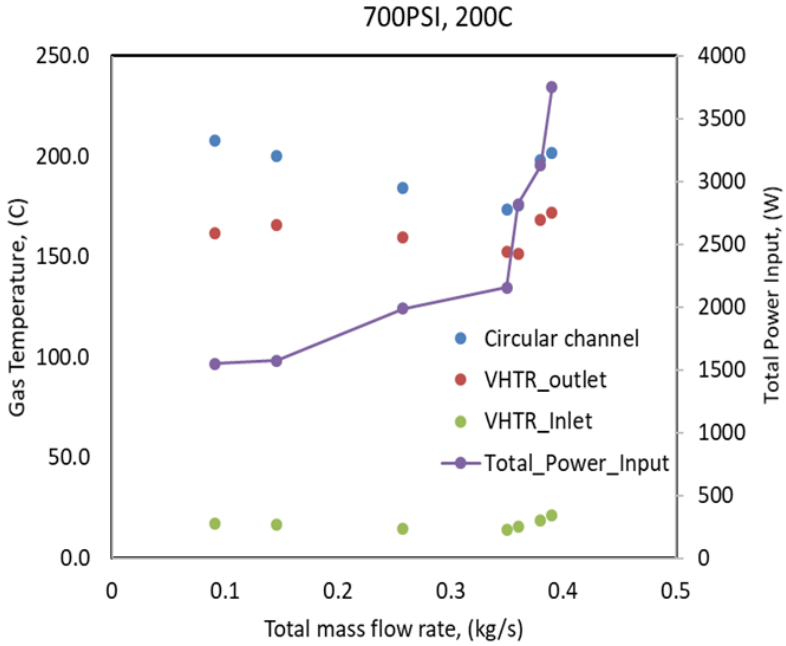

Figure 4.17 Plot showing the gas temperature and power input with respect to the total mass flow rate in the entire loop for the loop pressure of 700 psi and Temperature of 200 °C.

Figure 4.19 shows the pressure of the gas entering the PV and also the pressure at the compressor inlet and outlet for all the temperatures (200, 300 and 400 ^{o}C) for the system pressure of 700 psi. The pressure at the inlet of the PV is maintained at 700 psi throughout the experiment. As the total mass flow rate increases, the pressure at the outlet of the compressor also increases and the pressure at the inlet of the compressor decreases. This can be explained by the mass continuity of the gas in the entire flow loop.

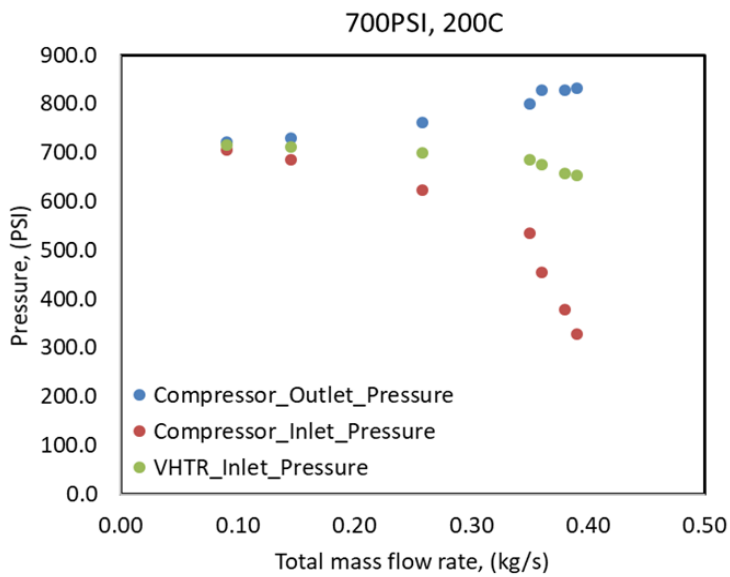

Fig. 4.19 Plot showing the gas temperature and power input with respect to the total mass flow rate in the entire loop for the loop pressure of 700 psi and Temperature of 200 ^{o}C.

For the case of 700 psi and 200 ^{o}C graphite midpoint temperature, Fig. 4.20 shows that more gas flows through the bypass channel at low mass flow rates, but as the total mass flow rate is increased beyond a certain value (0.2 kg/s), the gas flowing through the main circular flow channel is much higher compared to the bypass flow channel. The difference in the mas flow rates continues to increase rapidly with the total mass flow rate.

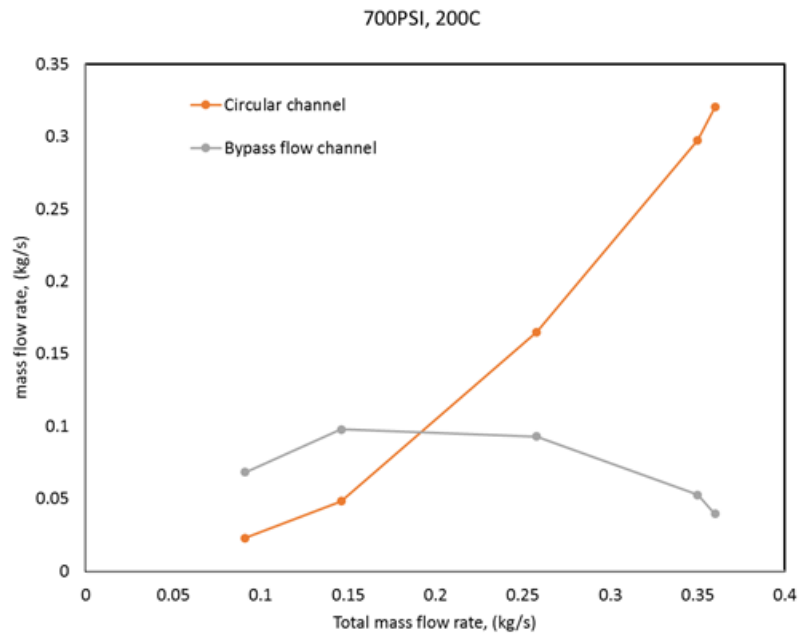

Fig. 4.20 Variations of gas mass flow rates in the bypass and main flow channels with the total mass flow rate.

Although the above results and other sets of data need to be further analyzed, the following factors need to be considered in understanding the relative flow rates. The bypass flow channel has a wetted perimeter, P_w = 86 mm, which is 1.63 times greater than that of the main circular channel (P_w = 52.8 mm). On the other hand, the hydraulic diameter, D_h, of the bypass flow channel is 5.6 mm, which is 1/3 of the main channel diameter of 16.8 mm. Thus, for the same gas velocity, V, and properties (ρ and μ), the Reynolds number ($Re = \rho V D_h/\mu$) would be 3 times smaller, and the turbulent friction factor given by Blasius correlation, $f = 0.316/Re^{0.25}$, would be 30% higher for the bypass flow channel than the circular main channel.

Since the friction pressure drop must be equal between the two parallel channels, the velocity in the main channel would be 14% greater than that in the bypass flow channel. Also, since the cross sectional area of the main channel (221.7 mm^2) is 85% greater than that of the bypass flow channel (120 mm^2), the mass flow rate in the main channel would be twice as large as the flow rate in the bypass flow channel, which is consistent with the results for large total mass flow rates shown in Fig. 4.20.

4.5 CFD analysis of Bypass flow (INL)

Available computational fluid dynamics (CFD) predictions of pressure distributions in the vertical bypass flow between blocks in a prismatic gas-cooled reactor (GCR) were analyzed to deduce apparent friction factors and loss coefficients for nuclear engineering systems and network codes. Calculations were performed for vertical gap spacings “s” of 2, 6 and 10 mm --- representing one, three and five mm in a GCR design, horizontal gaps between the blocks of 2 mm and two flow rates, giving a range of vertical gap Reynolds numbers Re_{Dh} of about 40 to 5300. The focus was on examination of the flow in the vertical gaps. Horizontal gaps are treated in the CFD calculations but their flows are not examined. Laminar predictions of the fully-developed friction factor f_{fd} were about three to ten per cent lower than the classical infinitely-wide channel. In the entry region, the local apparent friction factor was slightly higher than the classic idealized case but the hydraulic entry length L_{hy} was approximately the same. The per cent reduction in flow resistance was greater than the per cent increase in flow area at the vertical corners of the blocks. The standard k-ε turbulence model was employed for flows expected to be turbulent. Its predictions of f_{fd} and flow resistance were significantly higher than direct numerical simulations for the classic case; the value of L_{hy} was about thirty gap spacings. Initial quantitative information for entry coefficients and loss coefficients for the expansion-contraction junctions between blocks was also presented. The study demonstrated how CFD predictions can be employed to provide integral quantities needed in systems and network codes.

CHAPTER 5

Task 4: Radiative Heat Transfer and Air Ingress effects

Hitesh Bindra, Daniel Gould
Kansas State University

Note: This task is divided into 3 parts– (Task 4.1) Quantifying the radiative and conductive heat transfer in HTGRs; (Task 4.2) Experimental report on onset of natural convection under air ingress scenarios; (Task 4.3) Effects of air ingress on graphite oxidation and thermal properties

Part I

Task 4.1: Radiative and Conductive Heat Transfer: Passive Heat Removal

Summary Passive decay heat removal is one of the prime passive safety features of HTGRs and the heat conduction through the internal core region, graphite matrix, to the periphery is one of the prime mechanisms of passive safety in HTGRs. The conduction and radiation heat transfer provide long-term heat removal and natural circulation provides immediate heat removal mechanism during a pressurized or depressurized loss of forced circulation of Helium coolant. For long term coolability and safety analyses, it is important to quantify radiative and conductive heat transfer. Considering the X-Energy HTGR, which is a pebble-bed modular reactor design, to be one of the upcoming reactor designs in U.S. this work focused on computational analysis and experimental validation of radiation and conduction heat transfer in pebble beds. The most common way of conducting thermal analysis on a Pebble Bed Reactor (PBR) geometry has always been to treat the reactor core as homogeneous or semi-homogeneous domain, through which heat conducts at a rate defined by an effective thermal conductivity. Unfortunately, for this method to be effective at predicting the temperature distribution within the reactor core, the combined effects of numerous complicated physical phenomenon (e.g. point thermal contacts, thermal radiation, packing geometry, and heat generation) must be accurately and fully encapsulated in this effective thermal conductivity. Recently, computational power has increased to where it has become possible to perform some CFD simulations on spatially-resolved PBR core geometries. However, validation of these models is challenging, especially for accident conditions and at locations near the bed wall. In this work, a simple Discrete Element Method (DEM) code was written and used to create several different geometries of randomly packed spheres and cylinders. Heat transfer within these geometries was then modeled using both a numerical Finite Element Method (FEM) and an idealized homogeneous method. After validating the DEM code and analysis methods using temperature data obtained from cooling experiments featuring cylindrical geometry, the methods were extended to a PBR type geometry. A conduction cool down scenario was modeled and the results from the FEM model were compared to best possible results obtainable from a more traditional, homogeneous 1–D approximation. It was found that even the best possible homogeneous model was unable to match the FEM results under post-accident conditions.

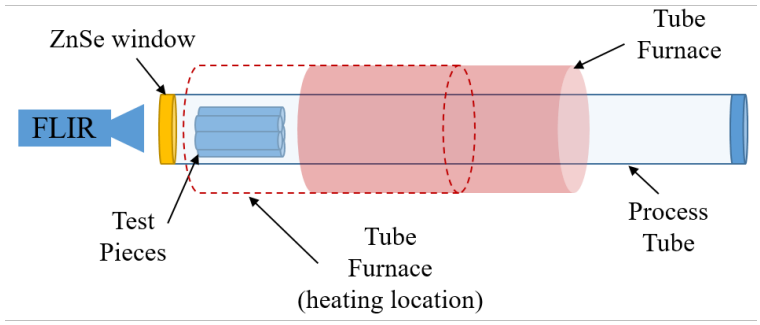

Figure 1: Schematic of the experimental setup

1. INTRODUCTION

Although blessed with the potential of high core power densities, simplified refueling, and a high level of passive safety, modeling the heat transfer within Pebble Bed Reactor (PBR) designs has proven difficult due to the complex flow paths and numerous point to point contacts that exist between the fuel elements. A common method of analysis for such beds is to represent the entire bed as a single, homogeneous domain with modified material and thermal properties. In particular, the thermal conductivity of the representative homogeneous domain is defined as the effective thermal conductivity, k_{eff}, of the packed bed, as opposed to the bulk thermal conductivity value of the bed's constituent material. Several thermal contact conductance models are detailed in the literature [1, 2, 3, 4], but most are simplified models that use assumptions – e.g. all contact spots are circular with identical radii – that are likely not to be valid in a post accident scenario. Some extraordinarily thorough models have been proposed for modeling thermal contact resistance in a pebble bed reactor core, such as Van Antwerpen et al.'s [5] Multi Cell Unit model. However, even if using an optimum value of effective thermal conductivity, homogeneous models are likely to be limited in their accuracy and applicability due to the complexities of the pebble bed core – especially if the core were to undergo an air ingress accident [6].

Recently, computational power has increased to where it has become possible to perform some Computational Fluid Dynamics (CFD) and heat transfer simulations on spatially-resolved PBR core geometries. However, validation of these models is challenging, especially for accident conditions and at locations near the bed wall.

The remainder of this work is separated into 3 different sections: first, experimental results from cooling experiments performed with assemblies of graphite cylinders are used to validate a 2-D combined Discrete Element Method (DEM) and Finite Element Method (FEM) model of a packed bed. Next, the validated 2-D DEM code was improved to allow the creation of 3-D packed bed geometries. Heat transfer within one of the DEM created geometries was then modeled using both an FEM and an idealized 1-D effective thermal conductivity method. Finally, several conclusions from this work are presented.

2. 2-D MODEL AND EXPERIMENTAL VALIDATION

2.1. Conduction Cool Down Experiments

Conduction cool down experiments were performed on two different assemblies of graphite cylinders. The cylindrical geometry enabled the temperature data obtained from the experiments to be used in conjunction with lower dimension (i.e., 1-D and 2-D) models. Details of each assembly are provided in Table 1. Each assembly was tested within a quartz tube featuring an ZnSe window through which the temperature of

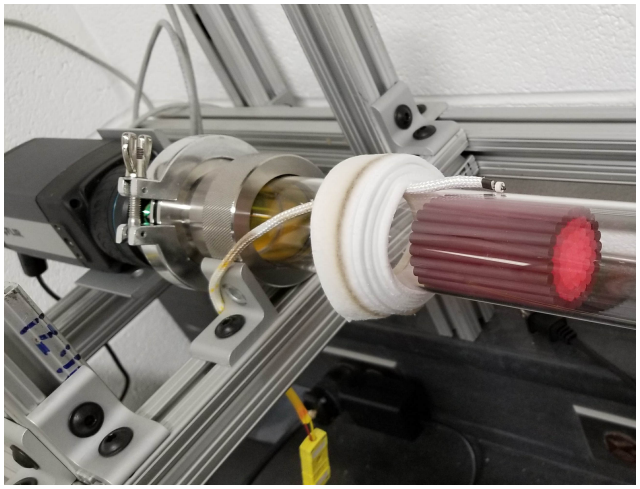

Figure 2: Graphite rod assembly beginning to cool. Assembly without shell is shown for visual clarity.

1	2
G-348 Graphite	G-348 Graphite
30 Rods	18 Rods
2.5 mm Radius	2.5 mm Radius
72 mm Length	72 mm Length
Thin Shell	Thick Shell

Table 1: Details of tested rod assemblies.

each rod could be continuously measured using an infrared (IR) camera. A diagram of the experimental apparatus – based on that previously used by Gould et al.[7, 8] – is shown in Figure 1. Once the assembly was placed inside the process tube, the process tube was sealed, evacuated to a rough vacuum, and an electric furnace surrounding the portion of the tube with the graphite rods was turned on. The assembly was heated until all rods reached the desired steady state temperature.

To initiate the cooling experiment, the radiative heater was switched off and quickly moved away from its original location surrounding the assembly. Figure 2 shows a cooling assembly of graphite rods. Once the heater is removed from its initial position surrounding the assembly, the temperature of the graphite rods begins to drop as the heat being conducted out of and radiated away from the assembly is no longer balanced by the energy input from the furnace. An IR camera was used to both measure the change in temperature of each rod as the assembly cooled and provide geometric information regarding the structure of the assembly. The temperature profiles observed from these experiments were then used to validate a 2-D combined DEM/FEM model.

2.2. Discrete Element Method Simulation

Finite element models require very precise geometric information to accurately simulate the effects of point contacts on inter particle heat transfer. The geometry of the assembly must be defined with a sufficient level of precision for a mesh to be created in which nodes from adjoining rods can be properly connected. Geometry defined using only the images from the IR camera was found to be insufficiently accurate for proper mesh connections to be made between adjoining rods. However, this problem was solved by using an N-body algorithm to improve the accuracy of the geometry data given from the analysis of the IR images. This approach not only allowed for a 2–D finite element model of the rod assembly to be created, but also provided an opportunity to validate a method an algorithm that could then be used to create other, more complicated geometries.

Therefore, a 2–D Discrete Element Method (DEM) simulation was used to modify the rough rod geometry information provided by the IR camera. For the DEM simulation, each rod is modeled as a 2-D circular particle in a single plane. The approximate rod centroid locations found from the IR image analysis were used as initial conditions for the simulation. Due to the initial rod centroid locations not being precisely accurate, some rods will initially overlap. These overlapping regions result in forces – and thus accelerations – being applied to the offending particles. In this 2-D simulation, inter-particle forces are calculated by modeling any pair of overlapping particles as springs – with the repulsion force applied to each particle being a linear function of their overlap distance. This process is repeated over a large number of time steps, during which each particle's acceleration and velocity are tracked, calculated, and integrated to provide new position data each time step. The newest position data is then again analyzed for overlaps, following which new forces are applied. This process repeats until particles are deemed to be moving sufficiently slowly.

In addition to the inter-particle spring forces, two other sources of force are used in the DEM simulation to constrain the assembly. First, gravity is accounted for by applying a small, constant force to each particle in the vertically downward direction. Second, in the same way that repulsion forces are applied to any particles deemed to overlap with each other, similar forces are applied to any particle who's position would have it overlapping with the graphite shell surround the assembly. These "wall forces" are applied to the offending particle in the direction normal to the shell wall at the point of overlap and are again a linear function of the overlap distance.

Because centroid locations obtained from IR images were used as initial conditions for this process – as opposed to random starting locations – few overlaps are seen in the initial geometry and the system is quickly able to converge to a low energy, low velocity state. At this point, its absolute rod positioning will be almost identical to those of the actually assembly and the relative rod locations will be sufficiently accurate to use in a finite elements simulation.

2.3. FEM Model

A commercial multi-physics software, COMSOL, was used to create an FEM of the experimental assemblies. Due to the very high aspect ratios of the objects within assemblies, a 2-D model was used [9]. Precise geometry information, i.e. the location of each rod's centroid in relation to the outer graphite shell, was obtained from the DEM simulation as discussed in Section 2.2. This process resulted in the geometry shown in Figure 3. The contact locations of adjoining – as opposed to merely nearby – objects in the geometry can be visibly identified in Figure 3 from the high density regions of the overlain mesh. The inner boundary of the outer shell is highlighted in blue. Matching the conditions of the experimental setup, the empty areas surrounding the rods within the shell were modeled in COMSOL as a vacuum. Thus no material is seen in between the rods in Figure 3.

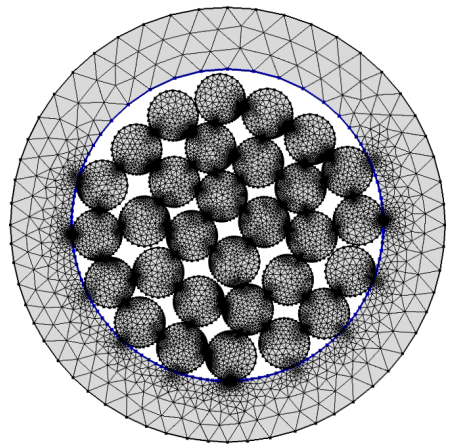

Figure 3: Geometry and mesh of thin-shell FEM model.

For the solid domains, heat capacity was defined as a function of temperature, while a constant value was used for the bulk thermal conductivity of the material.

The boundary conditions used in the model were surface-to-surface radiation, thermal contact resistance, and prescribed temperature. The outer and inner shell boundaries were given time dependent, prescribed temperature boundary conditions. Specifically, the temperatures of these boundaries were set to be equal to the median temperature of the shell face. Analysis of the IR images taken during the cooling process confirmed that the face of the graphite shell experienced negiligable spacial temperature variation.

Any portion of a rod or shell boundary that was in contact with a portion of the shell or another rod was subjected to thermal contact resistance boundary condition. This boundary condition modified the heat flux passing through the boundary by incorporating a resistance term at the boundary. A parametric sweep of resistance values was used to find a near-optimal value of thermal contact resistance for Assembly 1. This value, $8 \times 10^{-5}\,\mathrm{K\,W^{-1}\,m^{-2}}$, was then also used for the COMSOL model of Assembly 2 as well.

Finally, all interior boundaries not in physical contact with another boundary were set to be gray, diffuse surfaces with emissivity values of 0.86.

The COMSOL model was a 570 second transient simulation. The model start time, t_0, was defined as the moment when, following the removal of the surrounding tube furnace, the median shell temperature fell below the lowest measured rod face temperature.

Initial temperatures of the shell and rod faces were obtained from the IR camera measurements at the time t_0 and input into the COMSOL model as a spatial interpolation function. As the simulation marches through time from t_0, the thermal energy initially stored within the rods is diffused and radiated outwards towards the to the shell, which, due to its lower, prescribed temperature, acts as a sink.

2.4. 2-D Results

A comparison between the the measured rod temperatures for Assemblies 1 and 2 and the temperatures given by the COMSOL finite element model is plotted in Figures 4a and 4b, respectively. The plotted shell temperature is the average temperature of the graphite shell surrounding each rod and was also the temperature boundary condition applied to the blue boundary shown in Figure 3. The FEM model predicted the temperatures of both assemblies with a mean error of less than 3 percent in each case.

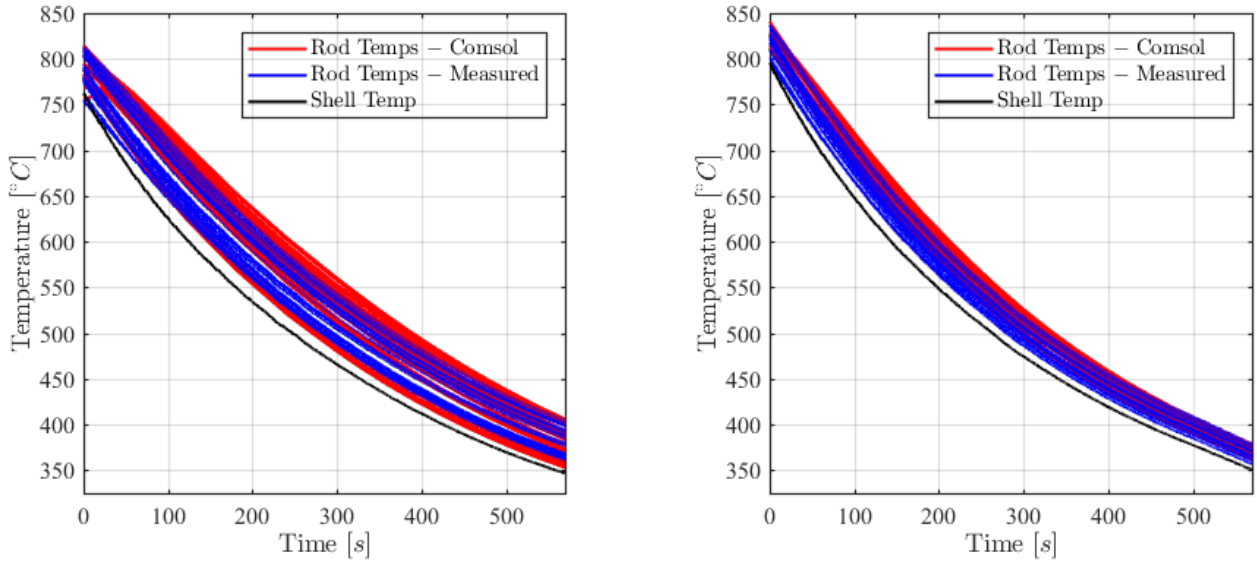

(a) Thin shell **(b) Thick shell**

Figure 4: Comparison of measured vs. FEM generated temperatures.

3. 3-D PACKED BED AND COMPARISON TO 1-D MODEL

3.1. 3-D Discrete Elements Method

The discrete elements method is widely used for generating packed bed geometries [4, 5] and was used here to create the geometry for the 3–D numerical heat transfer simulation. Although the method cannot easily produce periodic geometries and is not as precise as some overlap removal methods [10], it is far more computationally efficient and thus can be used to create far larger beds. To create the packed bed geometry that would be used by the 3–D FEM package, a discrete elements method code was written in MATLAB to determine 500 fuel-pebble centroid locations that would form a stable packing structure within a 240 mm radius cylinder.

Although a custom Matlab DEM code was used in this work, several commercial DEM packages do exist and would allow for much larger simulations to be made. However, while powerful, these codes tend to also be both very complex and expensive. Such power was not needed in this study as the study focus was on the near wall region of the packed bed and thus only a low number of particles needed to be modeled. It was decided that, due to the limited aims of the present study, simply modifying the previously used 2-D Matlab code would be the most efficient option. An additional benefit of this decision is that the geometry generated by the Matlab DEM code could theoretically be used with any available FEM package.

Although based on the code used in Section 2.2, several improvements were made to the code in two different areas. First, although MATLAB provided a very simple and straightforward environment for the creation and visualization of a simple DEM code, its (relatively speaking) slow speed required that several performance optimizations be applied to the previous code to enable the computation of a larger number of particles in a higher dimensional space with reasonable computation times. These improvements included the vectorization of computations within each time step, using integer and single precision data types where appropriate, and using initial conditions that slowly added more particles to the system over time.

This last improvement ended up being the most beneficial. For the 3-D code, the simulation began with each particle being “dropped” into the container from random locations rather than prescribing random

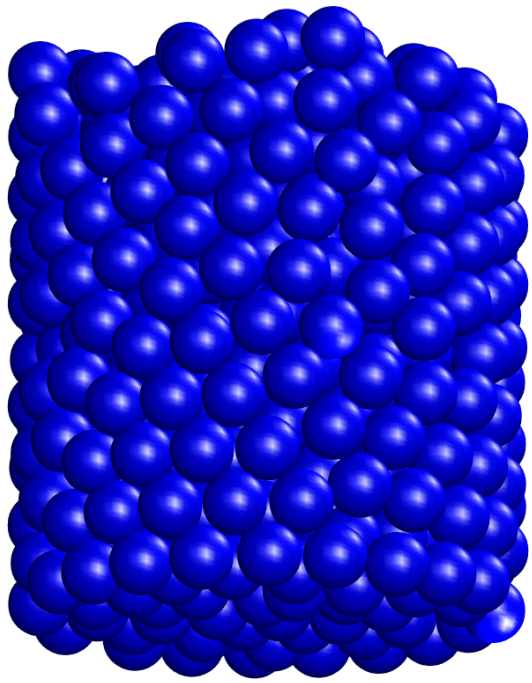

Figure 5: Packed bed of 500, 60 mm diameter spheres.

initial locations for each particle throughout the container's volume. By slowly adding each particle to the system over time the code is able to avoid having to perform calculations on the entire assembly while the particles are in a high energy state and smaller time steps are required.

The second major area of improvement to the 2-D code was the use of Lenard Jones potentials rather than linear spring forces to compute particle-particle interactions. Using the exponential potentials resulted in both a greater accuracy and precision in the calculation of each particle's location, and a decrease in the number of time steps required to resolve severely overlapping particles. The target overlap distance – i.e., the arithmetic difference between the displacement of two particle centroids and the particle's diameter – was 0.35 mm. The simulation was able to achieve a mean overlap distance of 0.3976 mm with a standard deviation of 0.229 mm. The finalized geometry produced by the DEM code is shown in Figure 5.

3.2. Bed Porosity

Overall, the DEM generated packed bed possessed an average porosity of 39%, matching the values achieved by both Pavlidis and Lathouwers [11] using the overlap removal method and Du Toit [12] using a DEM method. This average value was obtained from calculations performed over the middle 80% of the bed's length, where the effects of the top and bottom of the packed bed were minimal.

The relative porosity function plotted in Figure 6a was computed using a Monte Carlo method. A large number of rays running radially outward from the center of the packed bed were defined. Examples of such test rays can be seen in Figure 6b. A set of radial locations along each ray was tested to determine whether or not the individual locations were located within the domain of a solid particle. The tallies for each ray were then recorded as a function of the radial location of each test point. As shown in Figure 6a, the relative porosity of the bed continues to oscillate all the way through the bed center. This continued oscillation confirms that the entire packed bed can be considered in the "near-wall" region. Because of this, many previously developed empirical correlations for packed beds are not valid for this particular geometry.

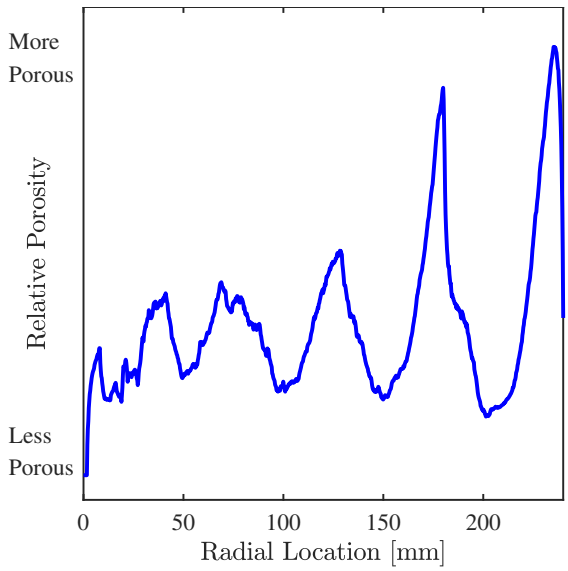

(a) Relative porosity of 500 sphere geometry; calculated using 500 thousand rays.

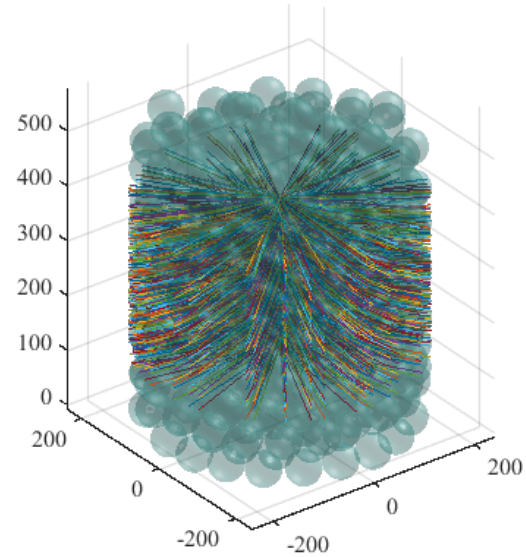

(b) Graphical depictions of example rays for relative porosity calculation.

Figure 6: Relative porosity of packed bed

Table 2: Geometric parameters of individual particles and packed bed.

Sphere Radius	25 mm
Shell Thickness	5 mm
Number of Particles	500
Bed Radius	240 mm
Bed Height	582 mm
Mean Contact Area	28.2 mm^2

3.3. Geometry and Boundary Conditions

Each spherical particle was modeled as a 25 mm radius sphere surrounded by a 5 mm thick shell. These dimensions match those of the fuel particles produced by the NUKEM company for the Thorium High-Temperature Reactor. The splitting of the fuel pebbles into the two separate domains was required as only the inner 25 mm regions (the 'Spheres' domains) of the NUKEM fuel pebbles contained fissile material; the outer 5 mm layer of each pebble (the 'Spherical Shells' domains) was made of graphite alone.

These shapes were created in the SOLIDWORKS CAD program and placed in an assembly at the centroid locations previously determined by the DEM model. This geometry was then exported into the ANSYS Design Modeler program for final processing. Using the Design Modeler software, two additional domains (in addition to the 'Spherical Shells' and 'Spheres' domains imported from the CAD software) were created using Boolean operations. Additionally, the overlapping areas within the 'Spherical Shells' domain were sliced as to implement the "capped" method described by Ferng and Lin [13].

A domain referred to as the 'Solid Air' region was created in the volume between the particles within the packed bed and was defined to be a solid domain possessing the material properties of air. As buoyancy forces, fluid flow, and radiative heat transfer are not considered by this model, modeling this region as a solid material was acceptable.

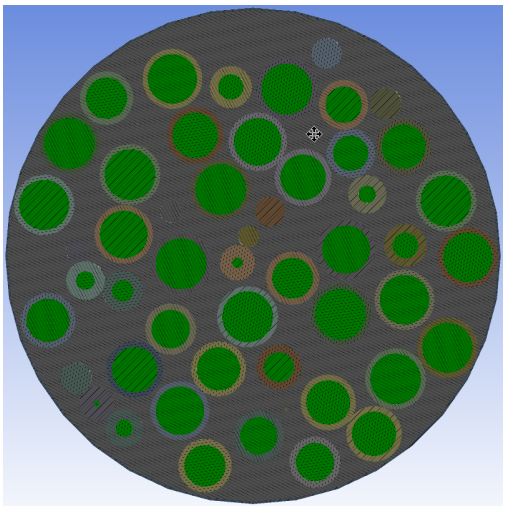

(a) Spheres

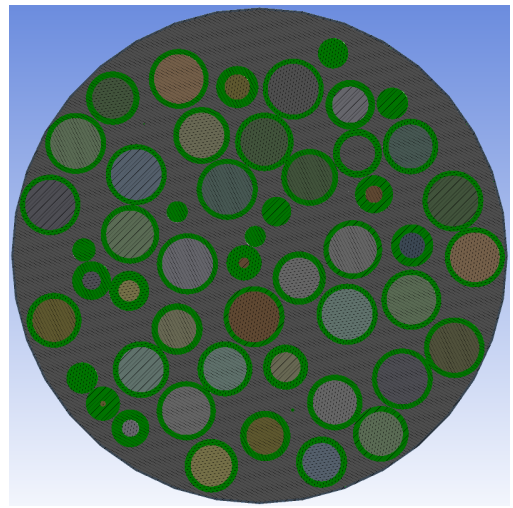

(b) Spherical Shells

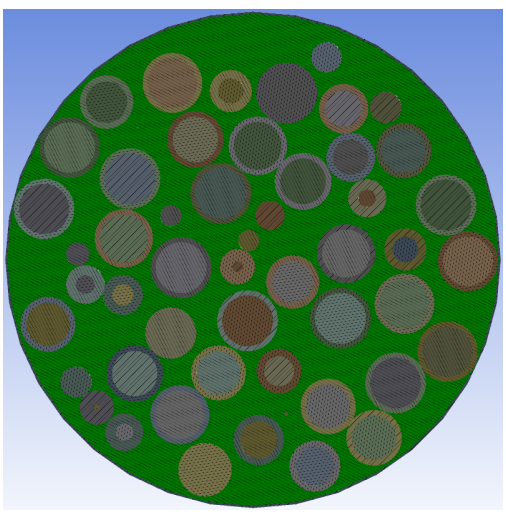

(c) Solid Air

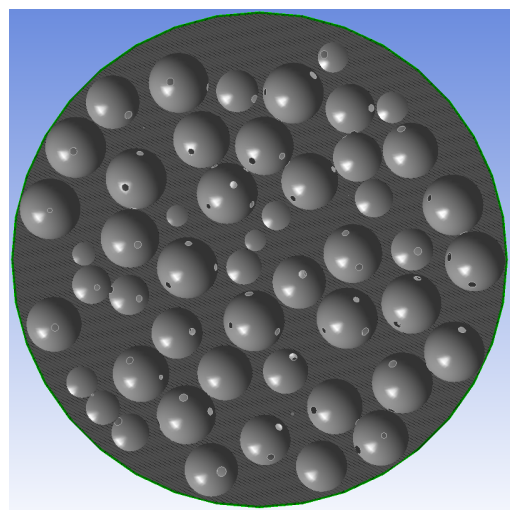

(d) Cylindrical Shell

Figure 7: Cross section of meshed geometry with individual domains identified in green.

Table 3: 1–D homogeneous model data

	(1)	(2)	(3)
	Unoxidized, Perfect Contact [9a]	**Unoxidized, Contact Resistance** [9b]	**Oxidized and Irradiated** [9c]
$k_{eff}\left[\frac{\mathrm{W}}{\mathrm{m\,K}}\right]$	6.6665	2.5469	2.1744

Surrounding the air, sphere, and shell domains is the 'Cylindrical Shell' domain. This domain is a 2.5 mm thick cylindrical shell. A cross section of this shell is shown highlighted in green in Figure 7d. The top and bottom faces of the cylindrical shell – i.e. the domain's exterior faces that are parallel to the cross section shown in Figure 7d – were defined as insulated surfaces while a constant temperature boundary condition of 300 K was applied to the outermost wall of the cylindrical shell.

Perfect thermal contact was assumed to exist between the Spherical Shell domains and the Sphere domains, as well as between the Solid Air domain and the Cylindrical Shell domains. The thermal contacts between individual shells were not assumed to be perfect. Rather, the thermal contact conductance between individual fuel particles was input as a function of their surface roughness. Finally, the bottom and top faces of both the Solid Air and Cylindrical Shell domains were defined to be insulated surfaces.

To represent the decay heat generated within each particle following an air-ingress accident, a time-dependent generation function was applied to each of the 'Spheres' domains. The time-dependent decay heat generation rate reported by Teuchert et. al for pebble bed reactors as a function of steady state power was used [14]. For the NUKEM pebbles, the average total generation rate for each pebble under steady state conditions was specified to be 1.4 kW under steady state operation [15].

3.4. 1–D Model

A 1–D radial model was created to provide a comparison with the results from the 3–D packed bed model. The system was modeled as a homogeneous domain with modified material properties. The density and heat capacity of the representative domain were defined to be porosity-weighted average of that used for the solid particles in the 3–D simulation.

For thermal conductivity, an inverse heat transfer method was used to find the optimal k_{eff} for the packed bed. After computing the direct solution to the heat equation for 1-D homogeneous model, an optimization process was performed with the goal of minimizing the error between both the maximum and mean sphere temperature reported by the 1–D and 3–D models. The thermal conductivity value found by the optimization process to minimize this error was defined to be the k_{eff} of the 1-D model. Results obtained from the 1–D model using this optimized k_{eff} are also compared to those given by the value of k_{eff} provided by Teuchert, Haas, and Van Heek [14] for a pebble bed reactor core.

3.5. 3-D Results

Data sets from three different simulations were analyzed: unoxidized graphite spheres in perfect thermal contact with one another (Case 1), unoxidized graphite spheres with contract resistance (Case 2), and oxidized and irradiated graphite spheres with contact resistance (Case 3). Case 1 is used as a limiting case example in which the graphite still possesses its full density and thermal conductivity and in which any thermal contact resistance between individual spheres is negligible. In Case 2, the graphite spheres were assumed to have an unoxidized, smooth surface and the effects of thermal contact resistance were added to the model. Finally, in Case 3, both the effects of oxidation and irradiation were included in the analysis.

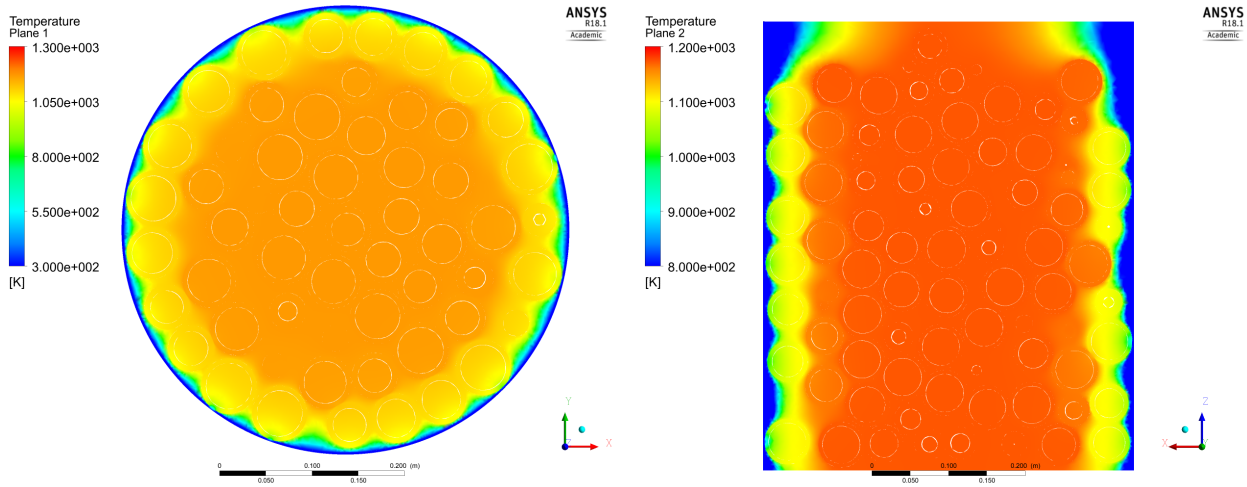

(a) Cross section of bed 0.3 m above bed base. **(b) Axial slice through mid-plane of packed bed.**

Figure 8: Temperature of unoxidized packed bed with no contact resistance at 100 s.

Following irradiation, the thermal conductivity of the NUKEM particles has previously been shown to decrease drastically [15]. And, as any fuel particles that would be involved in an air ingress accident are almost certain to have undergone significant irradiation, for Case 3, in addition to modeling the effects of thermal contact resistance between individual oxidized fuel spheres, the bulk thermal conductivity value of the spheres and shells domains was lowered to the 30 $\frac{\mathrm{W}}{\mathrm{m\,K}}$ value reported by Harms and Trauger[15].

In Figure 8, pseudo-color temperature plots of two different planes are shown from the Case 1 CFD model, 100 seconds into the run. Table 3 presents the results of the effective thermal conductivity optimization algorithm are shown for each case. In each case, the optimal value of thermal conductivity to best match the 3–D CFD results was significantly lower than the10 $\frac{\mathrm{W}}{\mathrm{m\,K}}$ previously suggested by Teuchert, Haas, and Van Heek [14] for an entire pebble bed reactor core at similar bed temperatures. This difference is likely a result of the packed bed geometry simulated in the 3–D CFD model not being large enough for wall effects to become negligible.

Figure 9 plots mean and maximum bed temperatures for each of the three analyzed cases as calculated by both the 3–D CFD and 1–D homogeneous models. The 1–D code over predicted the bed maximum temperature by 39 K, 97 K, and 108 K for cases 1, 2, and 3, respectively. It should be remembered that the 1–D results shown in Figure 9 represent the accuracy of the best possible 1-D, homogeneous model. In the real world, the accuracy of any such model is likely to be far worse.

4. CONCLUSIONS

Although it is obviously not ideal for full core, large scale simulations, the MATLAB computational environment proved readily capable of performing smaller DEM simulations.

By definition, 1-D homogeneous models cannot model the effects of individual point thermal contacts on heat transfer. At best, in a sufficiently uniform packed bed in which the aggregate effects of all point contacts will be both consistent and linear, 1-D homogeneous models can provide reasonable estimates of bulk heat transfer. However, previous reported values of effective thermal conductivity for PBR cores should not be taken as gospel in the near-wall region. Given the temperature over–predictions seen even when using the best possible k_{eff} values, any 1–D homogeneous model claiming to accurately represent the

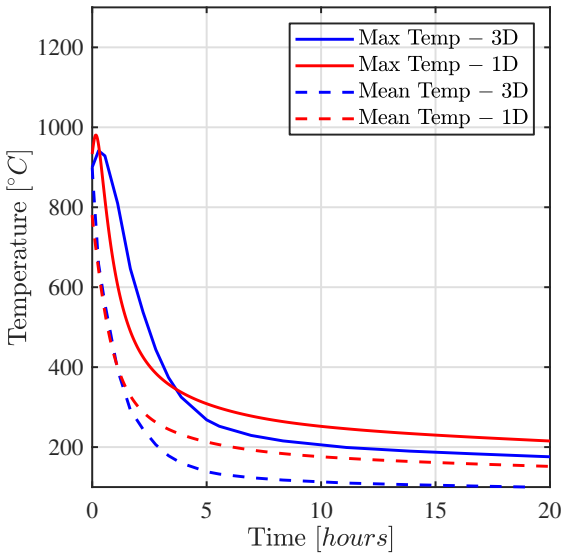

(a) Unoxidized graphite in perfect thermal contact.

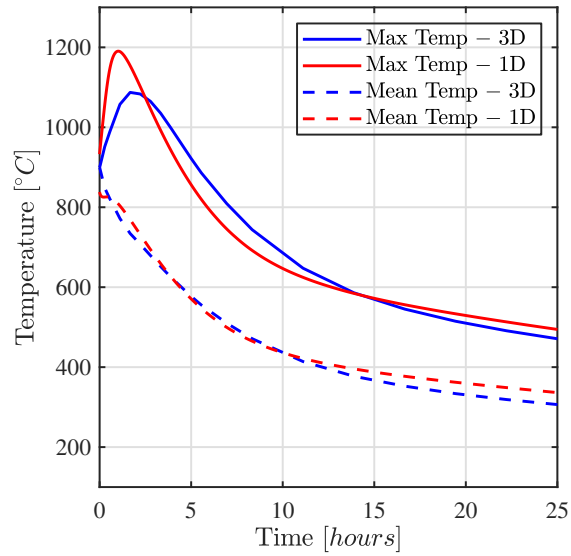

(b) Unoxidized graphite with contact resistance.

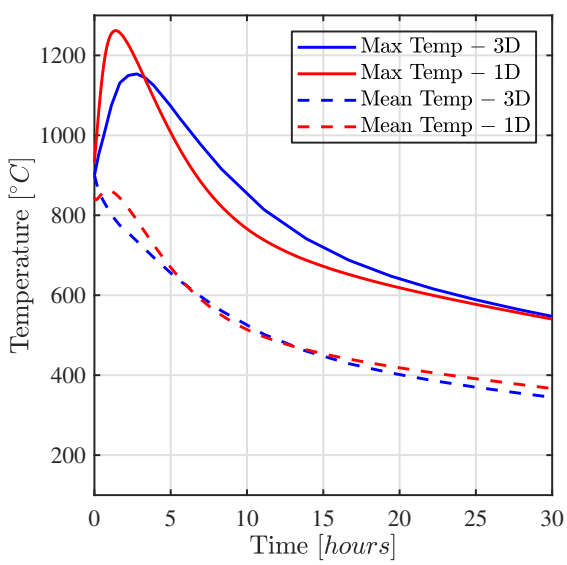

(c) Irradiated and oxidized graphite with contact resistance.

Figure 9: Plots of bed maximum and mean temperatures over time as determined by both 3–D CFD and the 1–D homogeneous code with an optimal k_{eff}.

near-wall region of a PBR bed should be viewed skeptically if precise temperature values are needed in this region. At the very least, any attempt to produce such a model should take into account the both the irradiation and oxidation history of the graphite fuel particles under consideration.

Part II

Task 4.2: Air ingress mechanism: Molecular Diffusion to Natural Circulation

Summary High Temperature Gas-cooled Reactors (HTGRs) have significantly robust passive heat removal capabilities owing largely to conduction and radiation heat transfer through graphite-fuel matrix and reactor vessel wall respectively. However, these capabilities may be significantly impacted if air was to replace Helium in the high temperature graphite under accident scenarios. In case of break in the coolant system high pressure Helium will escape into the reactor cavity leading to depressurization of the reactor. This will allow air from reactor cavity to enter the plenum or core of HTGRs via different mechanisms – diffusion, gravity currents, or natural circulation. Experimental studies were conducted in a geometrically scaled set-up with a shape of small English letter 'h', to depict the role of upper plenum in this process. Main focus of these studies was to understand and observe the transition time from diffusion to natural circulation. Thermal camera is used to identify this transition and flow transducer is used to measure the flow rates. The experimental results on incipience time of natural convection after a chamber pre-filled with Helium is opened to atmosphere are qualitatively similar to observations reported in literature using 'inverse U' shaped experimental setup, but also show distinct quantitative effect of extended leg on the transition times. Prior to onset of natural circulation (ONC), molecular diffusion plays the significant role in air-ingress. However, at higher temperatures convection currents may be influencing air ingress and in-turn ONC times.

NOMENCLATURE

Ω_D	Temperature-dependent collision integral
σ_{A-B}	Average Collision diameter (Å)
τ	Diffusion time constant (s)
D	Diffusivity (cm^2/s)
L	Length (cm)
M	Molar mass (g/mol)
P	Pressure (atm)
T	Temperature (K)
t	ONC time (s)
y	Mole fraction

1. INTRODUCTION

The next generation of nuclear power plants, such as HTGRs, have passive safety design features during off-normal operation, however it is unproven whether their safety systems will perform as per design requirements. The optimal approach to gain this understanding is to computationally model relevant phenomena using either system level or detailed 3D multiphysics codes, and then conduct HTGR related separate effects experiments using scaled models. These models can provide validation data and complement computational efforts to identify critical issues related to passive safety design. Several Phenomena Identification and Ranking Tables (PIRT) for HTGRs show that under normal steady-state, transient, and accident scenarios, the key phenomena leading to localized hot spots in the reactor core include air ingress, water-steam ingress, natural convection, degraded heat transfer in coolant channels, flow laminarization, effects of bypass flow, and non-uniform heat generation across the core [16, 17, 18, 19]. Some of these phenomena have been understood in-depth in recent years but air-ingress is one of the less understood topics till now.

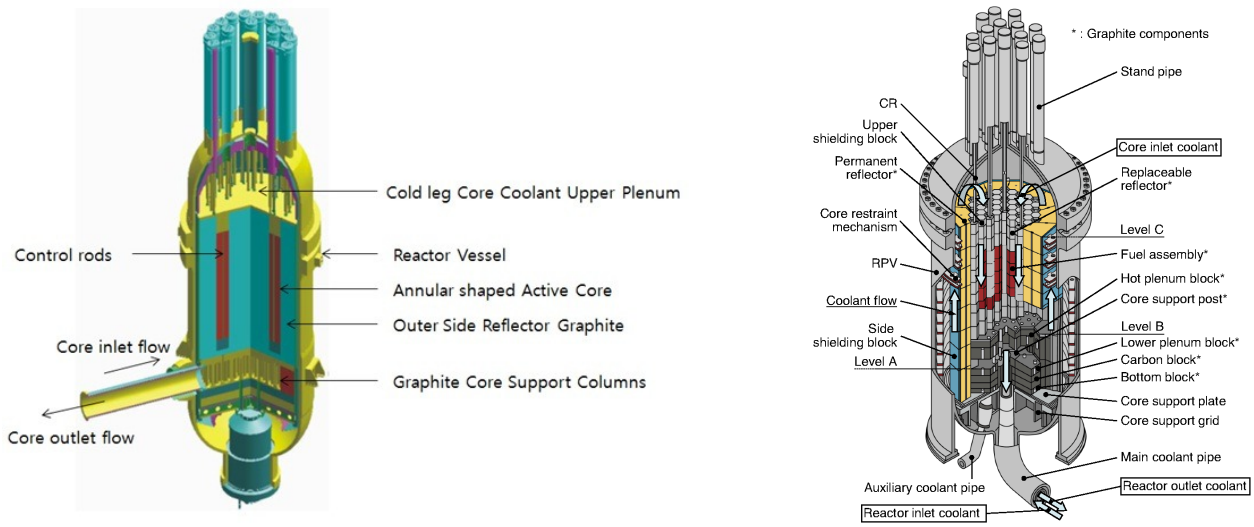

(a) GT-MHR **(b) HTTR**

Figure 10: Two gas-cooled graphite moderated reactor designs: GT-MHR and HTTR

A common feature of HTGRs with a passive safety design is that under certain accident conditions the decay heat is dissipated passively from the core by radiation–conduction–convection heat transport to the surrounding environment. Conduction and radiation heat transfer are expected to provide long-term heat removal. However, during a Depressurized Loss of Forced Coolant (DLOFC) accident, a break in the coolant system will allow air ingress into the high temperature reactor and can lead to graphite oxidation, which will negatively impact the core thermal behavior. Air ingress in the HTGR plena and core regions is a complex process and highly dependent upon the specific geometry of both the reactor and the break. While there have been several analytical or computational studies to estimate air ingress rates in HTGRs, most previous studies have been based on hypothetical scenarios of break-size and orientation.

The High Temperature Test Facility (HTTF)[20] at Oregon Sate University is a 1/3 scale model of Gas turbine Modular Helium Reactor (GT-MHR) – the American HTGR design – and will be used in the future to perform air-ingress experimental studies[21]. Additionally, a 1/8th scaled model for lower plenum has been designed at Ohio State University to study air ingress experiments[22, 23].

One of the goals of the proposed experiments in each of these facilities is to investigate mechanisms for air

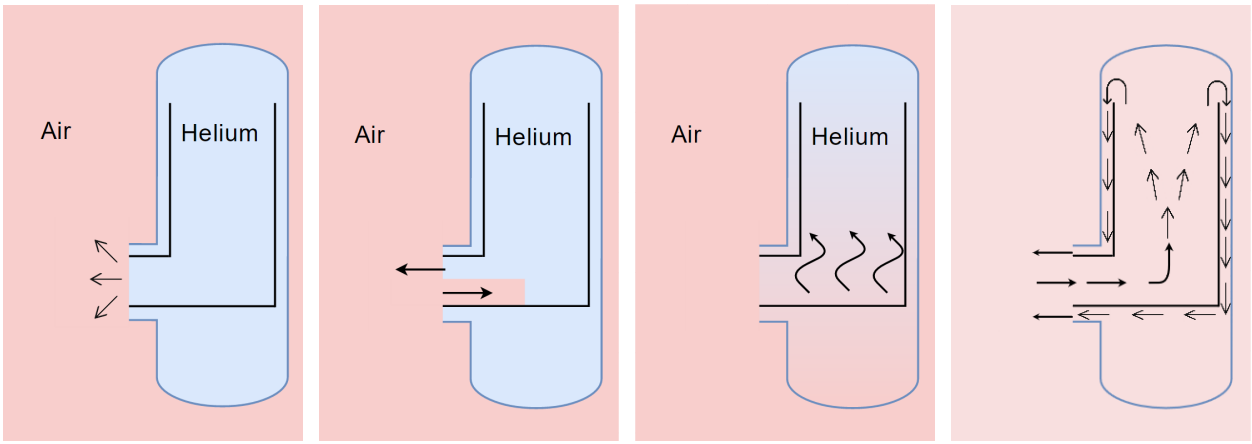

(a) Depressurization **(b) Stratified Flow** **(c) Diffusion** **(d) Natural Convection**

Figure 11: Air ingress scenario with helium-air stratification and diffusionOh2006

ingress from the containment or reactor cavity into the lower plenum and core after a double-guillotine break of the main inlet-outlet co-axial header of GT-MHRs. There are three different possible modes of air-ingress: molecular diffusion due to a concentration gradient of helium-air, convective transport of air, and natural convection due to a thermally driven upward draft in the core. If the dominating mechanism is molecular diffusion, the rate of air-ingress is quite slow, whereas if the driving mode is convective transport, air circulation can start within few minutes. The analytical or computational studies performed on these hypothetical accidents in GT-MHRs suggest that due to gravity currents (lock-exchange) the convective air-ingress mode is reached instantaneously [24, 25]. This air flow into the lower plenum and core with high temperature graphite can lead to adverse consequences such as oxidation of graphite and can negatively impact the passive heat removal capabilities of the reactor. Therefore, it is highly desired to know accurately when this natural convection would begin. It has been suggested by Oh and others[26, 27, 28] that the sequence of events during an air ingress accident involve : (1) depressurization, (2) density-driven stratified flow, (3) diffusion into the reactor core, and (4) global natural circulation (Fig. 11). The potential formation and effect of stratified flow is highly dependent on a given reactor design. The nature of this stratified flow after depressurization determines the initiation time and rate of air ingress into the reactor vessel. At some point after the development of the stratification regime and the filling of the lower plenum with air global natural circulation will begin. However, there are conflicting reports in the literature on the onset of natural convection time.

According to simulation results obtained by Oh et al.[24] using a CFD code, FLUENT, showed that the onset of natural convection time is expected within 100 secs of depressurization. However, simulations performed using the previously validated, 2D Gamma code[29, 30] reveal that the onset of natural circulation within an HTGR is anticipated to occur several hours – rather than several seconds – after the depressurization event. Unfortunately, there is currently a very limited amount of experimental data in the established literature that can be used to understand this transition from diffusion to natural circulation and validate numerical models. In a separate-effects experimental study on isothermal air ingress through horizontal ports in a helium filled scaled-vessel[31], it was found that it would take several minutes to fill the entire test chamber – a result that differs from the numerical predictions by Oh et al. [24, 25].

The predictive modeling of this process is quite challenging because the CFD codes don't have appropriate models for properties such as molecular diffusion in binary mixtures. The thermophysical properties such as thermal conductivity, viscosity and specific heat capacity of helium-air mixtures strongly vary with the air concentration or with the presence of any heavier gas [32, 33], and are difficult to model. At

intermediate concentrations, the Prandtl number of these binary mixtures reduces to values well below those of common gasses. This reduction increases the uncertainty in the applicability of the conventional heat transfer correlations and turbulence models. Taylor et al.[34] showed that some of the most popular correlations over-predicted convective heat transfer for binary gas mixtures in forced convection. The uncertainty would be even greater at low Reynolds numbers and for natural convection flows. Therefore, despite the large volume of work that has been done on this subject, the computational models may require further improvements before they can be reliably used for design basis studies.

The underlying physics for the transition from molecular diffusion to natural circulation is highly dependent upon the concentration of Helium within the core. If the overall Helium concentration is high, the difference in average fluid density between the hot core region and gap region (the space between core barrel and vessel wall) is insufficient to initiate natural circulation. Only when the air concentration in the core reaches a certain value will the density difference between the hot and cold legs be sufficient for the natural circulation of cavity air through the core to begin. Most of the experimental high temperature studies on understanding this transition were conducted by JAERI[35, 36, 37] with an 'inverted U' shaped experimental facility based on the HTTR. Although there are coolant inlet-outlet process design differences between HTTR and GT-MHR, the central physics of depressurization and air-ingress are expected to be governed by similar fundamental mechanisms. These experimental results were also later modeled using the CFD code, FLUENT, by Zhai et al. ZhaiThesisCFD,Kadak2006. While the experimental studies from JAERI do indeed help in understanding the transition, the 'inverted U' design does not take into account the possible effect of the upper plenum on molecular diffusion and air ingress rate.

First, as one can see in Figure 10a, the upper plenum of the proposed GT-MHR reactor design resides directly above the entrance to the coolant inlet channel. After a break, the helium contained within the upper plenum of the reactor will diffuse downward. This process will have the effect of slowing the rise in air concentration in the upper part of the reactor and thus potentially changing the time at which ONC would occur. Thus, a new 'h' shaped experimental facility designed to represent the effect of unmixed helium in the upper plenum was developed and used for the experimental studies presented in this work.

The experimental studies presented here have two goals: a) Experimentally study diffusion to natural circulation transition process with air-ingress into the helium filled chamber. b) Examine the effect of upper unheated helium-filled plenum or chamber on the ONC. The remainder of this paper is organized into three sections: experimental setup design and procedure, results and analysis, and conclusions.

2. EXPERIMENTAL SETUP AND PROCEDURE

To experimentally determine the effect that helium diffusion from the upper plenum might have on the ONC time, a new experimental setup was designed, based on the 'inverted U' design of experimental setups from literature [35, 36, 37]. The 'h' shaped experimental setup developed for this study is made of quartz tubing welded together as shown in Figure 12a. Tube diameters for all the legs in the set-up were selected to be similar to those in the 'inverted U' shaped setup used in previous studies [37]. While visually very similar to setups developed by JAERI, such as the example shown in Figure 12b, the additional vertical tube seen on the upper left side of the apparatus provides several advantages.

First, the extended upper leg of the "h" allows a mass of helium to be present above the 'inverted U' flow loop, modeling the effect that the helium within the upper plenum of the GT-MHR would have on the time duration experienced from the initial coolant pipe rupture and depressurization until ONC. Secondly, the extended upper leg allows for the insertion of instrumentation and test specimens into the left leg of the

assembly. In future studies, this upper leg and the flange will be used to create a scenario of 'control drive nozzle break' postulated accident listed as one of the tests in the matrix provided by Schulz et al. [20].

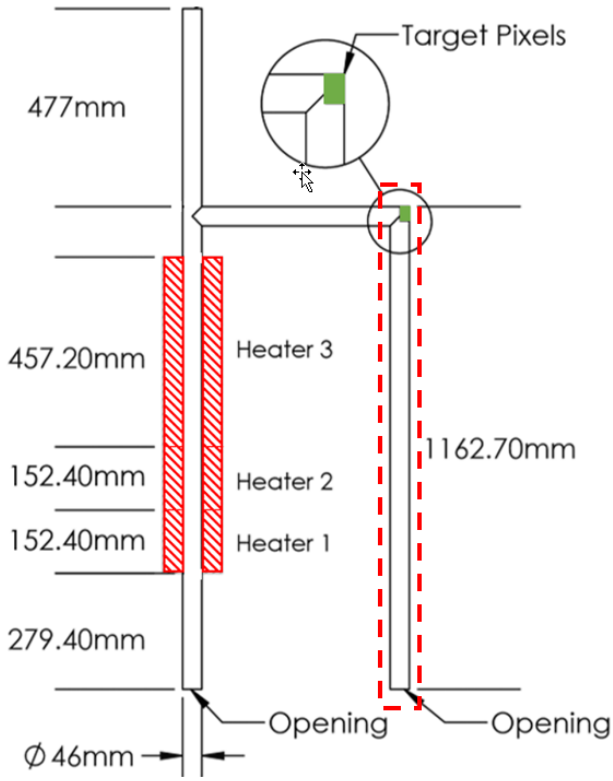

(a) Diagram of 'h' shaped experimental apparatus developed for this study. Dashed red box highlights the observation window for ONC detection.

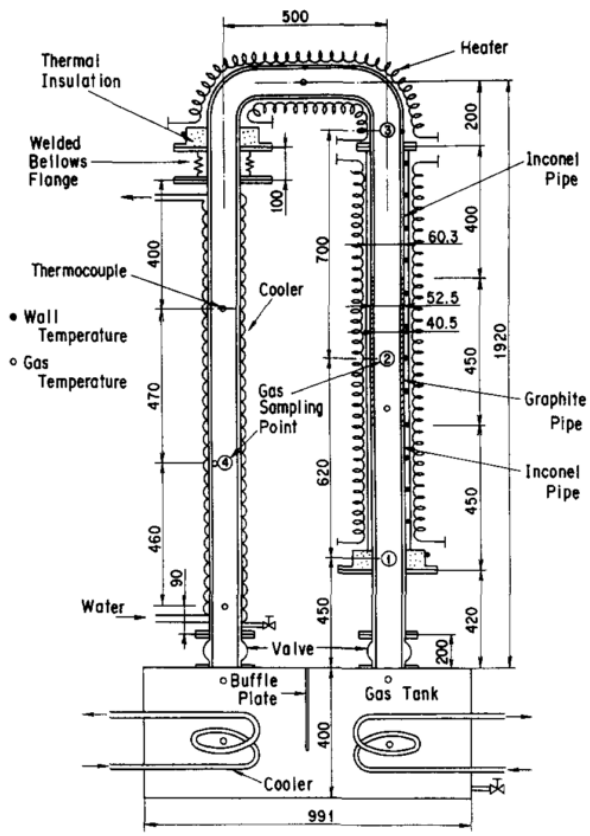

(b) Diagram of 'inverse U' shaped experimental apparatus from JAERI. shown dimensions in mm. Takeda1996

Figure 12: Experimental Setups for studying transition or Onset to Natural Circulation

As presented in Figure 12a, the three legs in the apparatus were made of 46mm ID by 50mm OD quartz tube. It should be noted here that 'inverted U' facility at JAERI had ID of all the tube legs about 40.5mm, but this small variation in the tube area is not expected to play any major in the governing physics. The length of each legs was designed based on the geometric scaling with GT-MHR, i.e., the ratio of upper unheated leg to the heated leg was designed to be 1.5 which is close to the ratio of height of upper plenum to core in the GT-MHR. The heights of GT-MHR core and upper plenum regions were obtained from literature [38, 39]. Low thermal conductivity of quartz eliminated the need for a cooling system on the cold leg of the assembly. Radiative tube furnaces were used to heat the lower portion of the left leg of the 'h' shaped test section.

The manufactured quartz 'h' is originally open to atmosphere at each of its three ends. Before initiating the experiments, all three openings were sealed using KF50 flange connections. For this ONC study, the two lower fittings were opened to simulate a sudden double guillotine break of the main coolant pipe. The third, upper opening remained sealed throughout the experiments performed for this work.

A FLIR A655sc LWIR camera was used to monitor the temperature of the setup before and during experiments. Before each experimental run, the LWIR camera was used to determine when the apparatus

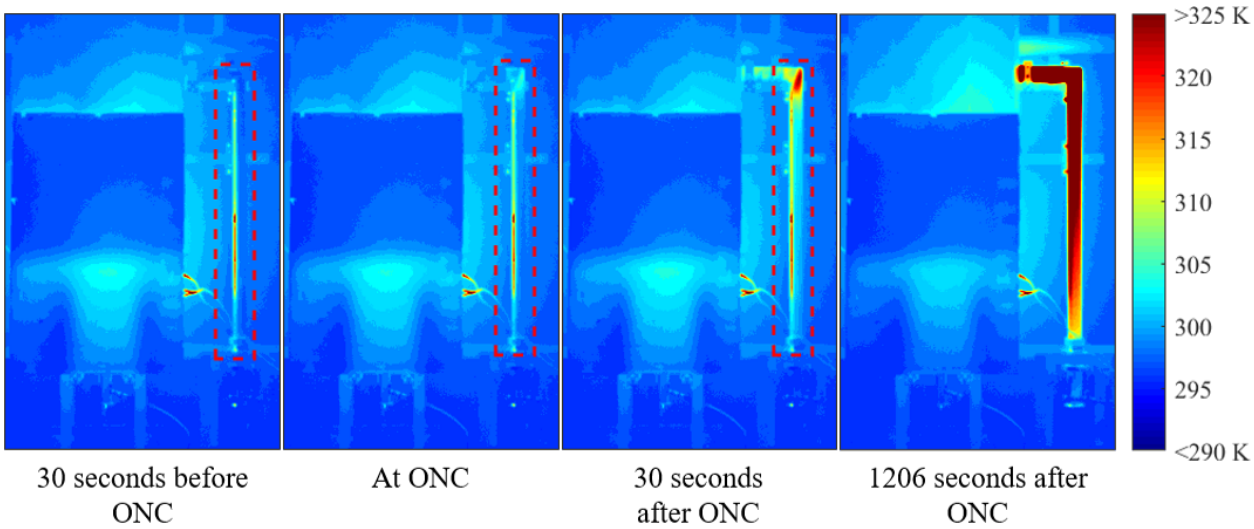

Figure 13: (Color Online) Images from FLIR camera before and after ONC. Observation window is identified by dashed red box.

had reached steady state conditions. In Figure 12a, the portion of the apparatus that can be directly observed with the LWIR camera is marked with a red dashed box.

During each experimental run, the LWIR camera was also used to detect the precise moment that the ONC occurred. This was done by continuously monitoring the values of the pixels making up the upper right corner of the quartz assembly. The approximate location of these pixels is also shown in Figure 12a. It was found that, after ONC, the upper-right corner of the quartz 'h' would be the first area to experience any measurable temperature change as shown in Figure 13. By tracking the average value of 40 pixels in this area denoted as "Target Pixels" in Figure 12a), ONC could be identified within seconds of it occurring. For example, the histories of the average temperatures in the targeted pixels plotted in Figure 14 clearly show the ONC during the experimental runs performed with a hot leg temperature of 375 C.

The measurement of ONC by the LWIR camera was also confirmed using a TSI 8475 flow transducer that was placed directly under the lower left opening of the assembly. Both of these measurement methods generally agreed on the ONC time to within 10 seconds of one another.

The following steps were followed for each run of the ONC experiments.

1. Air is evacuated from the chamber with the help of vacuum pump and a rough vacuum is achieved.
2. Helium is filled into the chamber until pressure inside the chamber is almost equal to atmospheric pressure.
3. The left leg of the chamber is heated to the desired temperature.
4. Any excess helium is removed to ensure chamber pressure equal to atmospheric pressure.
5. Both of the lower ends of the chamber are opened simultaneously.
6. The flow measurement probe is moved into place under the left hand side chamber opening.
7. Chamber wall temperature and system flow rate are monitored to determine ONC.

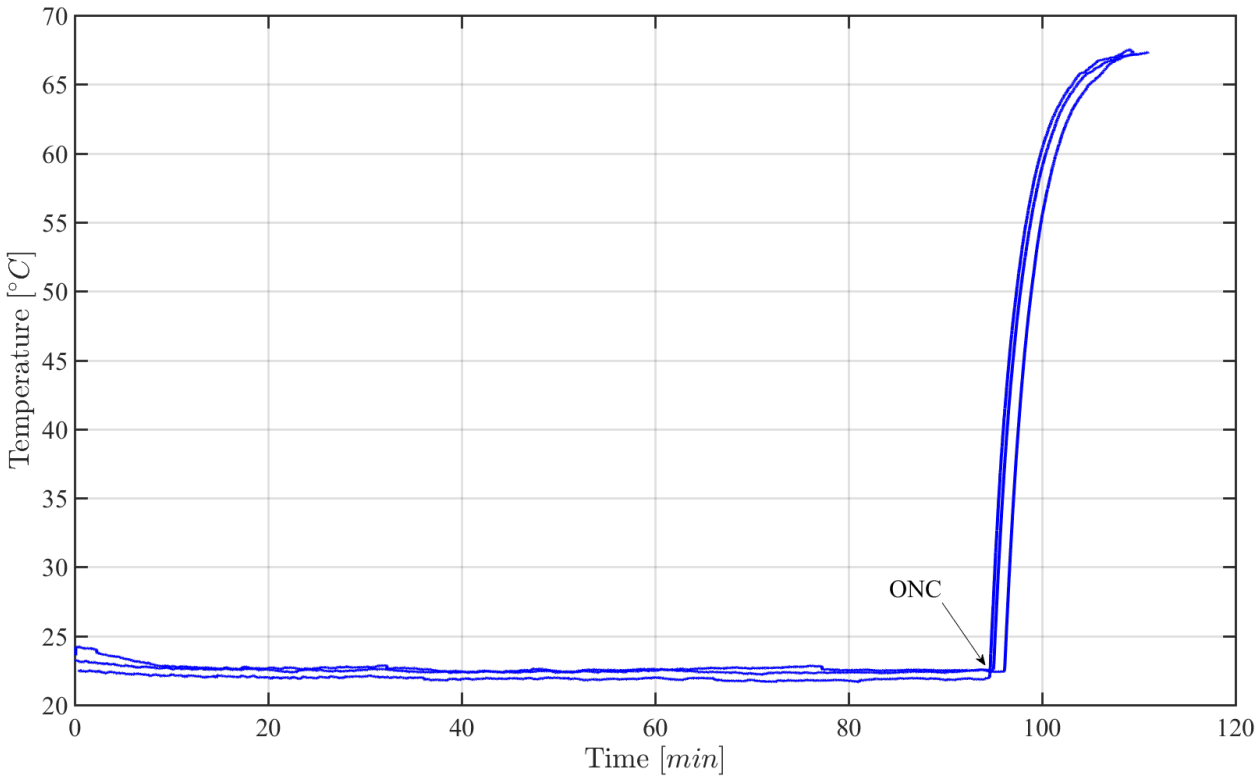

Figure 14: Average temperatures of target pixels

3. RESULTS AND ANALYSIS

As described in the previous section, ONC was detected when the instantaneous average value of the pixels identified in Figure 12a underwent a sudden, steep change. This ”steep change” can be seen in Figure 14. The time histories of the three test runs at the same hot leg temperature also show the consistency of the experimental results.

The ONC times experienced by the setup were measured for five different hot-leg temperatures. For each tested hot-leg temperature, several experimental runs were performed both to ensure experimental repeatability and to obtain data with uncertainties. The particular hot-leg temperatures used in this work were picked to closely match the hot-leg temperatures used in previous work reported by JAERITakeda1996. Experimentally measured ONC times from both the present work and JAERI’s previous study[37] are plotted in Figure 15. Results from both studies show that as the temperature of the hot-leg is increased, the ONC time is reduced. This behavior is expected and can be explained by increase in molecular diffusion and increased density difference driven convection currents with increase in temperature of the hot-leg.

3.1. Calculation of Diffusion Coefficient and Experimental Time Constant

In order for valid comparisons to be made between the results of the present work with those of JAERI, several small differences between the two setups had to be accounted for (see Table 4). First, and most significantly, while the horizontal tube connecting the two long legs of both experimental setups are

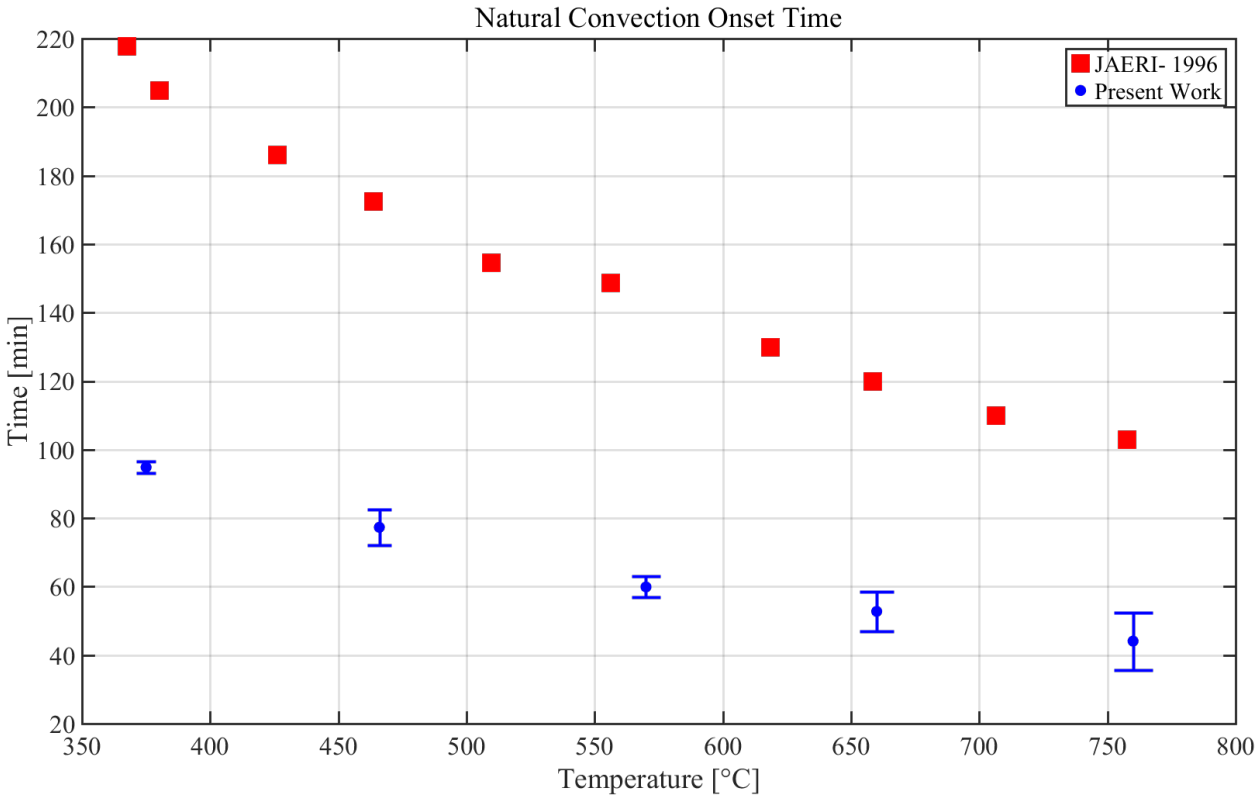

Figure 15: ONC time (*t*) vs hot leg Temperature

identical in length, the vertical legs used in the 'inverted U' setup are longer than the lower portions – that is, the portions of the legs below the horizontal connecting tube – of the vertical legs that were used in the experiments described here. Additionally, slightly different fractions of the hot legs were actually heated to the specified temperature. Additionally, some of the most relevant or comparable results from JAERI [35, 36], were obtained using helium and nitrogen rather than helium and air.

Therefore, to take into account these variations, the time constant τ was defined to better understand and scale the processes in the two different facilities. This time constant was derived based on the assumption that, prior to ONC, molecular diffusion is the dominating mechanism for increasing the air concentration within the test chambers.

When calculating τ, the hot vertical leg – i.e. the lower portion of the left vertical leg in the current work, (see Figure 12a) and the right vertical leg in the previous work by JAERI (see Figure 12b) – were, for analytical purposes, split into a number of segments. Each segment was defined in such a way as to approximate that, under steady-state conditions prior to ONC, the temperature – and therefore diffusion coefficient – of each segment was constant over its length. This constraint resulted in dividing the hot leg of the JAERI setup into two segments. The hot leg of 'h' shaped setup, developed and used in this present study, was divided into three segments.

The time constant of the entire hot leg was then defined as the sum of the time constants of the individual segments within the analyzed leg. In Equation 1, L_j is defined as the length of segment j and D_j as the diffusion coefficient in segment j.

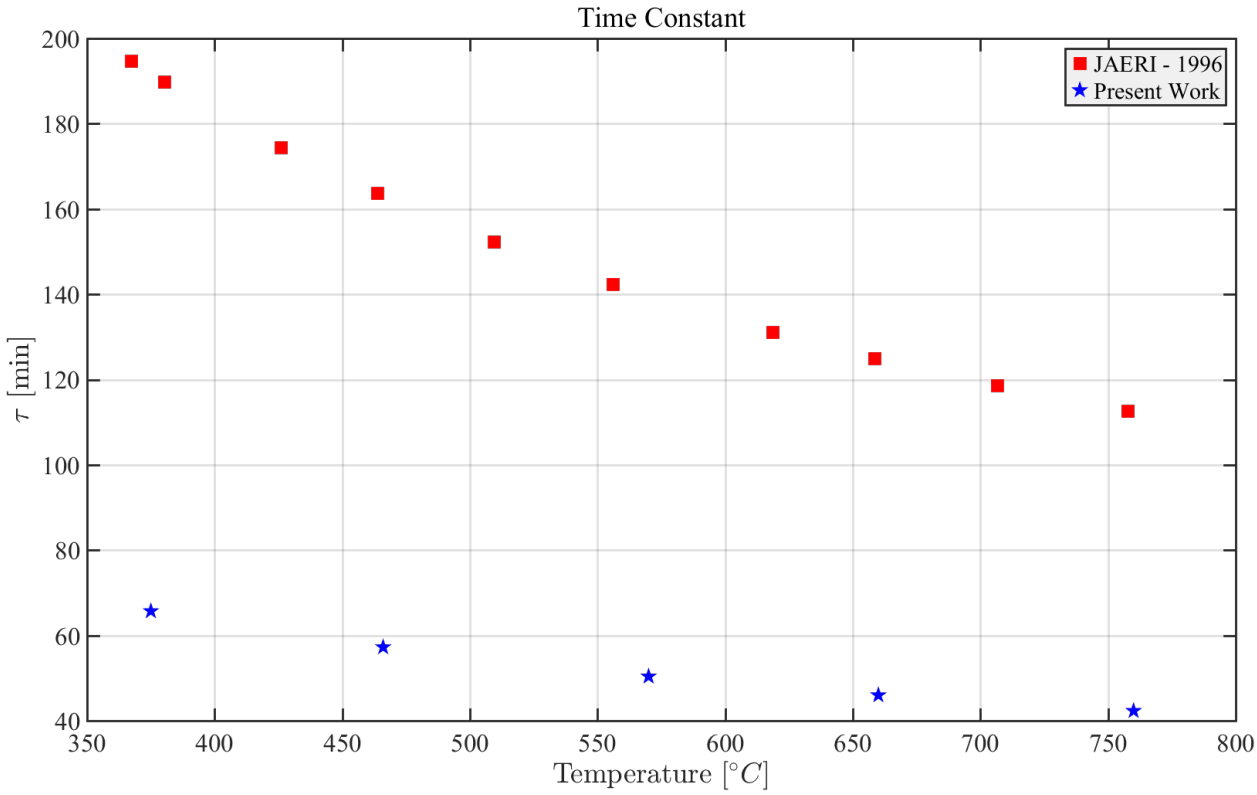

Figure 16: Diffusion time constant (τ) vs hot leg Temperature

	Present Work	**JAERI -1996Takeda1996**
Leg Length [m]	1.216	1.92
Heated Length [m]	0.82	1.50
Interior Diameter [mm]	46	40.5
Exterior Fluid	Air	N_2

Table 4: Experimental Setup Comparison

$$\tau = \sum_j \left[\frac{L_j^2}{D_j}\right] \tag{1}$$

Equation 2 is used to calculate the diffusion coefficient for gas pairs $(D_i)$of non-polar, non-reacting molecules Welty1984 within a segment of the hot leg. Subscript i denotes a particular gas pair such as Helium-Nitrogen. In case of Helium-Air, the diffusion coefficient was modeled with Helium-Nitrogen and Helium-Oxygen pairs. Wilke's approximation (Equation 3) was used to calculate the overall diffusion coefficient of helium into air (D_j) from the diffusion coefficients of binary mixtures of its major components Wilke1950.

$$D_i = \frac{.001858\, T^{32} \left[\frac{1}{M_A} + \frac{1}{M_B}\right]^{12}}{P\sigma_{A-B}^2 \Omega_D} \tag{2}$$

$$D_j = \left[\sum_i \frac{y_i}{D_i} \right]^{-1} \tag{3}$$

In Figure 16, the values of τ calculated for the experimental conditions reported by JAERI [37] and the present study are plotted as a function of the temperature of the heated segment of the hot leg. The large variation in *tau* values as a function of temperature is expected as higher temperature leads to higher diffusion coefficient which implies the diffusion process is expected to be faster. The differences in the τ values for the two facilities is attributed to the differences in the length of the heated segments which strongly govern the diffusion process.

3.2. Effect of Extended Leg

The effect of extended leg on the ONC transition phenomenon is illustrated by the ratio of $\frac{\tau}{t}$ as calculated for each specific test temperature. This ratio is plotted in Figure 17. It can be clearly seen from the plots that for all hot-leg temperatures tested, the ratio of $\frac{\tau}{t}$ calculated using the data generated in this work is lower than that calculated using the data from equivalent temperatures reported by JAERITakeda1996. This observation can be explained by the extra helium in the upper, extended portion of the left leg in the present setup. During the experiment, the helium initially present in the portion of the left leg above the horizontal cross diffuses downward into the lower portion of the apparatus – reducing the average air concentration in the lower leg and thus delaying ONC.

In both studies, the value of the ratio $\frac{\tau}{t}$ is directly proportional to the temperature. This behavior is due to the reduced dominance of molecular diffusion as the cause of increasing air concentration at higher temperatures. At higher temperatures, intra-leg natural convection also begins to play a role as predicted in the literature Takeda1992,Takeda1993a. It should be noted that although the value of the ratio $\frac{\tau}{t}$ seen in the present work is uniformly lower than than respective values generated from the JAERI experiments, the difference between the two respective ratios is not constant for all tested temperatures. Rather, the magnitude of the overall difference between the respective ratios plotted in Figure 17 appears to decrease with the hot leg temperature. This result can be partly attributed to 'natural convection' Takeda1992 that occurs within each leg of the experimental apparatus before ONC. As the temperature of the hot leg will be directly proportional to the flow rate of the intra-leg convection currents, at higher temperatures these currents will be much more effective at introducing air into the hot leg of the setup. Correspondingly, the relative importance of diffusion in determining the air concentration within the hot leg will decrease as the temperature of the hot leg is increased. Thus, at higher temperatures the relative effect of the downward-diffusing helium on the ONC time decreases and the ratio of $\frac{\tau}{t}$ for the 'h' shaped experimental setup will approach the respective values obtained from the 'inverted U' shaped apparatus.

3.3. Flow Velocity

A flow transducer, described in experimental section, was placed under the lower opening of the left leg of the "h" shaped apparatus to provide corroboration of the ONC times identified by the LWIR camera. This flow instrument additionally helped in obtaining measurements of the average flow velocities at the tube entrance post-ONC. Due to both the extremely low flow rates and the close proximity of the heater to the flow transducer, flow rate measurements were associated with a high degree of uncertainties and were not sufficient to obtain a meaningful correlation between flow rates and the hot leg temperature. However, the

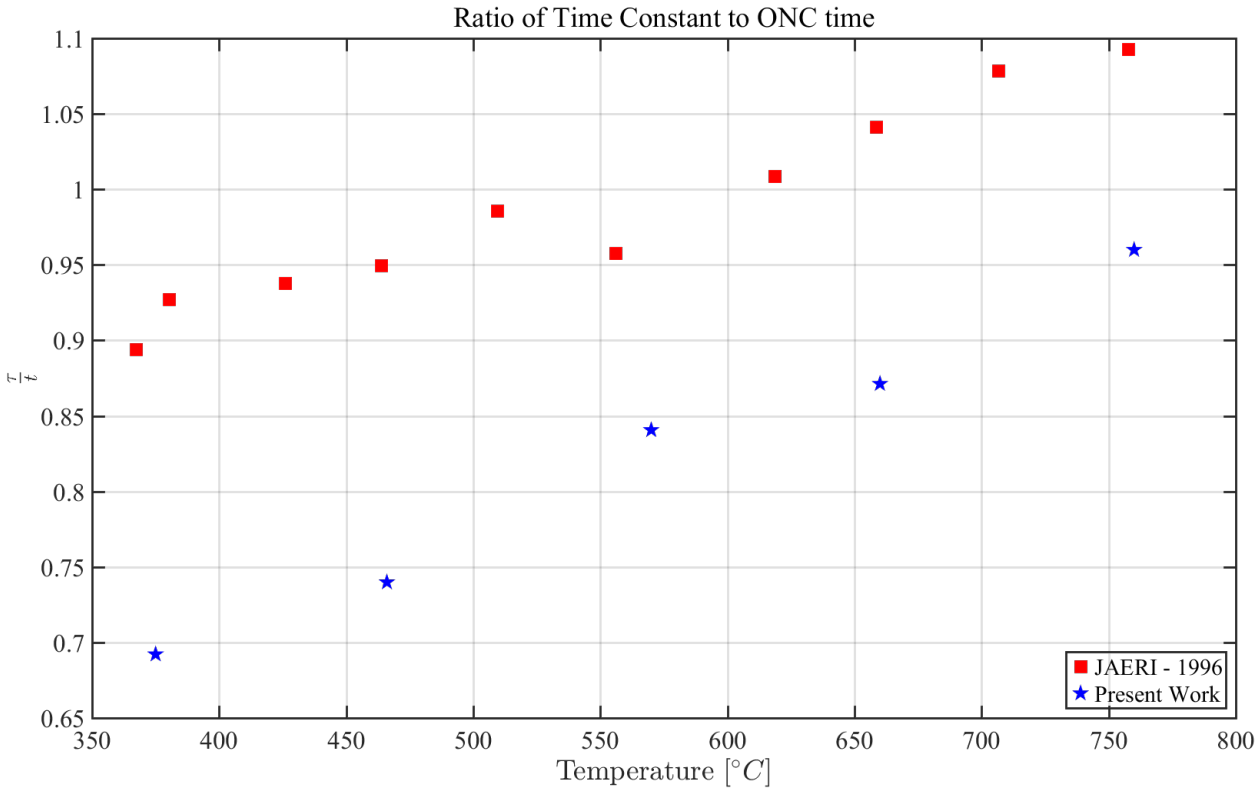

Figure 17: Ratio ($\frac{\tau}{t}$) vs hot leg Temperature

flow velocity measurements that were obtained do agree very well with the approximate $[0.2]ms$ value reported in earlier reports [36]. The obtained velocity measurements are plotted in Figure 18 with error bars showing $\pm$ 2 SD of the measured values for each hot leg temperature. The accuracy level of the velocity probe was not sufficient to measure velocities prior to ONC or to quantify the role of intra-leg natural convection currents – an unsurprising fact given that these currents are expected to be on the order of 1E-6 $[]ms$ to 1E-4 $[]ms$.

4. CONCLUSIONS

Air-ingress after depressurization under inlet-outlet duct break is one of significantly important postulated scenarios under safety analysis of HTGRs. Previous experimental tests conducted at JAERI used 'inverse U' shaped setup to study transition from molecular diffusion to natural circulation. A new 'h' shaped setup was designed and developed in this study to understand the effect of upper unheated leg. In contrast to previous non-oxidizing studies, where Nitrogen was used as the gas present in external cavity, the present study was conducted with ambient air. Although both experimental studies have consistently shown that high temperature leads to earlier ONC, there were some clear differences in quantitative comparisons. Ratio of the diffusion time constant to ONC time, $\frac{\tau}{t}$, for the current study is found to be consistently lower than previous reports for the same corresponding test temperatures. This behavior can be attributed to the presence of this extended leg which increases the ONC time as it acts as an additional source of helium reservoir which leads to downward diffusion of helium.

As the hot leg test temperature was increased the ratio $\frac{\tau}{t}$ increased because of the increased role of natural convection currents. The experimental data on ONC times reported here will be useful for understanding

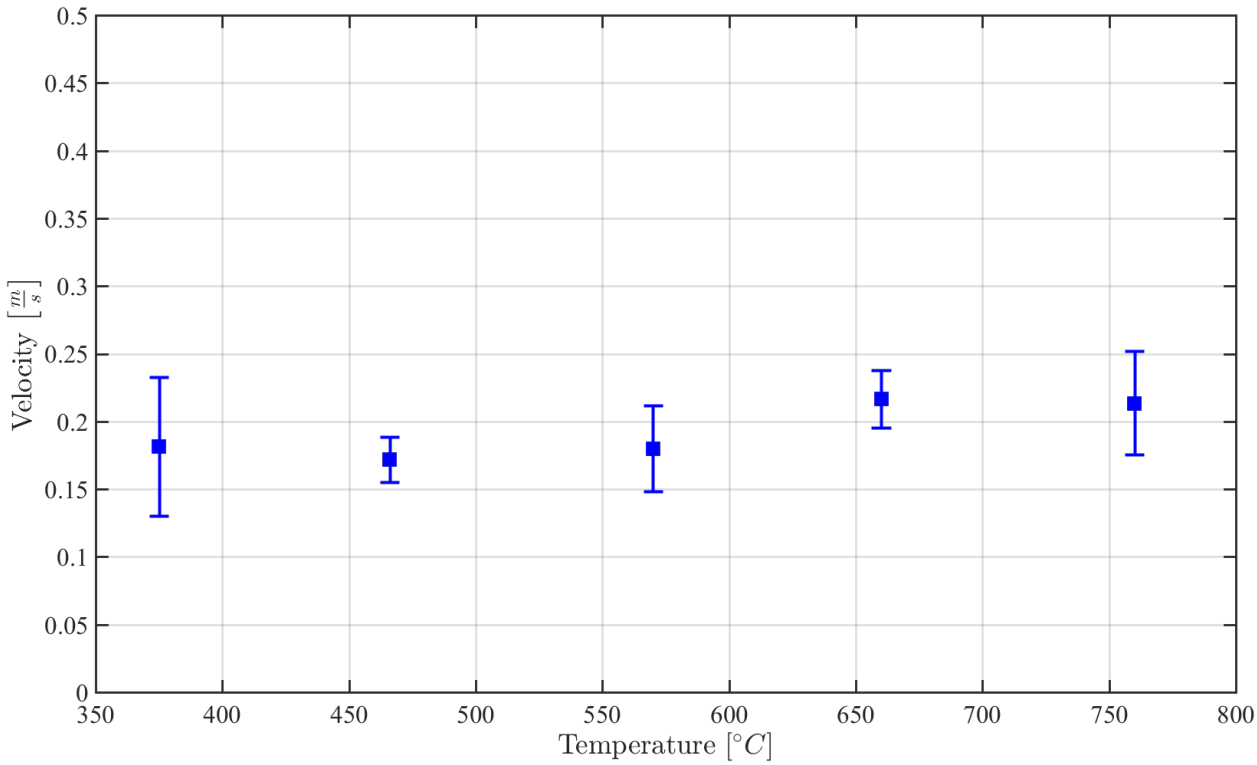

Figure 18: Flow velocity at hot leg inlet after ONC

and validating computer models. In the future, graphite test blocks will be placed in the high temperature helium tube to understand the effect of gaseous products from graphite oxidation on ONC behavior. Next steps will also involve the effect of opening or break orientation, such as horizontal opening and the break or leak at the top end of hot leg, on the ONC times.

Part III

Task 4.3: Effects of air ingress: Graphite oxidation and thermal property changes

Summary Mixed-effects experimental studies were performed to determine the changes induced in nuclear grade graphite exposed to high-temperature, oxidizing flow of varying flow rates and types. Annular and cylindrical graphite specimens were exposed to high temperature, oxidizing environments and continuous, in-situ measurements of the environmental conditions surrounding annular graphite cylinders were taken. Changes in thermal diffusivity, thermal conductivity, density, emissivity, and surface roughness were then calculated using samples taken from the oxidized test pieces. Under all scenarios, the thermal diffusivity of the graphite test samples was shown to increase. This increase was concluded to be driven by changes in sample density rather than thermal conductivity or heat capacity. Oxidation was also found to increase the graphite's surface roughness. The total effect of oxidation on the emissivity of nuclear grade graphite was shown to be highly dependent on the ash content of the tested graphite.

1. INTRODUCTION

The potential of graphite – even nuclear grade graphite – to undergo oxidation if exposed to atmospheric air at high temperatures has long been a concern for graphite moderated reactors[40]. Schweitzer and Singer first experimentally investigated the effects of air flow and temperature on the oxidation process of nuclear graphite and determined reaction rates and equilibrium temperatures for an early reactor-grade graphite in an attempt to determine the conditions required for a self-sustaining oxidation reaction to occur [41, 42, 43]. Since then, a great deal of work has been done characterizing the oxidation rate and kinetic parameters of numerous different grades of graphite, under a wide range of temperatures and air flow rates. Lee et. al [44] experimentally characterized the oxidation behavior of two modern grades of nuclear graphite thermogravimetrically. The transient oxidation behavior demonstrated by several grades of nuclear graphite when exposed a smooth flow of highly purified, dry air of was reported by Chi et. al [45]. A comprehensive model for the oxidation of graphite oxidation was proposed by El-Genk et. al [46] and validated for several different grades of nuclear graphite.

However, all of this work has been done in laboratory environments with single-effects experiments. There has been far less work done on whether the conditions and flow patterns present in a reactor both before and after the Onset of Natural Convection (ONC) can be fully represented by the previous oxidation experiments conducted with forced convective flows. For example, although Takeda and Hishida [37] found that the ONC time was not substantially influenced when the effects of graphite oxidation were included in the system, they also found that the flow rate of oxidizing gas into the system varied over time prior to ONC. As part of an effort to develop and validate computer codes for future HTGR designs, Oh et. al performed a comprehensive analysis of the ONC phenomenon and graphite oxidation [26]. Again however, the ONC and oxidation physics were analyzed separately and only the effects of fully developed, constant flow rate, forced convective flows were examined.

Additionally, potential changes to the thermal properties of any graphite left behind following an oxidizing flow have not been thoroughly examined. Although it has been shown by researchers such as Snead et. al [47] that neutron irradiation, which also causes damage to the graphite crystalline structure [48], can

significantly change graphite's thermal conductivity and structural strength, the effect that oxidation has on graphite's thermal properties – and in particular its thermal diffusivity and emissivity – has not been well established.

Thus, the goals of this work are twofold. First, to capture the mixed effects of air ingress and graphite oxidation to investigate any role played by varied flow conditions on reaction kinetics. And second, to identify and measure any changes in nuclear graphite's thermal properties that are induced by the oxidation process. The remainder of this paper provides details of two sets of experimental studies that were were performed to accomplish these goals, as well as analysis of the results from said experiments.

2. AXIAL FLOW EXPERIMENTS 16

Experiments in which an air flow was induced through a heated, representative graphite flow channel were performed with both forced and natural convection driven flows. For the forced convection tests, air flow rates of 15, 25, and 30 SLM were used. In the natural convection tests, volumetric flow rates of approximately 20 SLM air were observed. After the test pieces were oxidized, samples from each piece were also used to measure the effect of oxidation on the thermal diffusivity and emissivity of graphite.

2.1. Experimental Design

The aforementioned experiments were designed to obtain measurements of thermal diffusivity, crystal structure, and surface roughness form samples of annular graphite test pieces that were exposed to defined environmental conditions and experienced a quantifiable amount of oxidation. The samples were analyzed after the experiment was finished and thus the measurements performed on each sample were representative of the total integrated effect that the oxidation had on a specific annular graphite test piece. Environmental conditions, on the other hand, were measured using in-situ methods and were obtained throughout the entire course of each experiment.

2.1.1. Environmental Measurements

Throughout each experiment, measurements of the furnace temperature, room humidity, fluid flow rate, and oxygen content of exiting flow were taken. Furnace temperature was measured with 3 k-type thermocouples. The temperatures reported from the thermocouples were both recorded and used as inputs for the PID controllers controlling the power to each of the three furnaces used to heat the sample. In each of the forced flow experiments, flow rate was measured and controlled using a thermal mass flow controller. To quantify the amount of oxidation experienced by each test piece, the flow exiting each annular test piece was sampled and tested for oxygen content during all periods of bulk flow. In the cases of the forced flow experiments, the data from this measurement allowed for the total amount of oxygen consumed by the oxidation reaction to be calculated. Further information on each of these measurements can be found in Section 2.2.

2.1.2. Post Experiment Measurements

After each experiment was preformed, several further measurements were taken on the tested cylinders and their representative samples. First, the total mass of each cylinder was measured post-run and recorded to allow better quantification of the oxidation endured by each test piece. Second, samples from each tested annular graphite cylinder were subjected to tests to determine the change in the graphite's thermal properties. Thermal diffusivity was measured using the laser flash method. This state of the art method is detailed in Section 2.4.2. To provide better understanding of the causes of any change in a sample's thermal properties, each sample was also subjected to a X-ray diffraction test to determine if any significant changes to the graphite's crystal structure had occurred.

Finally, the surface roughness of selected samples was tested using a needle profilometer. Surface roughness is a major factor in the emissivity of an object. The magnitude of the change in roughness caused by oxidation was used in the analyses performed in Section **??**. Once again, although other, possibly more exacting methods of measuring surface roughness parameters exist, the needle profilometer was of sufficient resolution and accuracy to achieve our goals while also being readily available for use.

2.2. Experimental Setup

A diagram of the setup is shown in Figure 19a. Annular test pieces were inserted into the apparatus from below the left leg and supported via a smaller 42mm OD by 45mm ID quartz tube. This tube in turn was supported by a custom flange assembly. This flange assembly, that can be seen at the bottom of Figure 19b, was created by welding a steel washer with a 40mm ID between 2 KF 50 flanges.

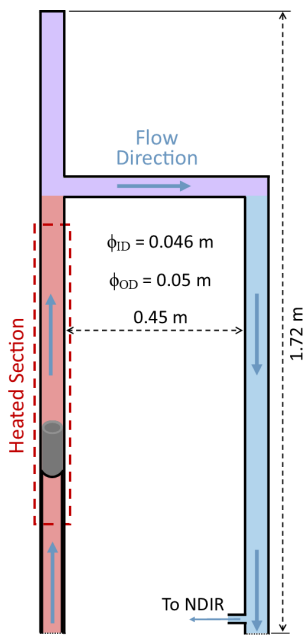

(a) Diagram of experimental setup.

(b) The test piece on the supporting quartz tube and its supporting flange assembly.

Figure 19: Experimental setup for oxidation testing

After the test piece and the supporting quartz tube were inserted into the assembly, the KF 50 flange nearest the test piece was clamped to another such flange at the base of the left leg of the quartz h-tube, while the other end of the welded assembly was attached to other KF style parts that allowed flow connections to be made. Below all this was either a steel blank flange, or a custom made, LWIR transparent, window that also acted as a cover for the final KF 50 connection below the left leg. The zinc-selenide window was used for the experiments detailed later in **??**. This addition both sealed the apparatus and allowed for an IR camera to be used to view the test piece's lower face during an experiment.

Connections for fluid flow were placed at the lowest regions of both legs, below the quartz h-tube. These KF50-NPT tees were placed below the left and right legs and used to inject and remove gasses, respectively. Depending on the experiment, a combination of air, helium and oxygen were connected to the left leg. The helium and oxygen gasses used in the experiments were of the Matheson Ultra High Purity grade. Air injected into the assembly consisted of atmospheric air, pressurized using an oil free compressor. During air injection experiments, the injected air had a relative humidity of about 50%.

For the forced convection experiments, flow control was maintained using thermal mass flow controllers. The mass flow controllers were controlled and read using standard analog 0 V to 5 V signals. These signals were generated and read by a LabJack T7 data acquisition device using its Matlab API.

On the lower right leg of the experimental setup were connections for exhausting, evacuating, and sampling the gas with the system. One opening was connected to a ball valve and was used both to control the system pressure before an experiment, and as an exit for the flow during forced convection experiments. Gas samples were extracted from the setup's right leg using a small, brushless diaphragm pump. The sample flow rate was controlled via another thermal mass flow controller. Extracted sample gas was provided to the inlet of a Thermo-Fisher model 60i Non-Dispersive InfraRed (NDIR) analyzer at atmospheric pressure and a rate between 1.5–3.0 SLM. This unit was used to calculate the remaining oxygen content present in the gas flow after it had passed through the test piece.

The test pieces placed in this experimental apparatus consisted of annular cylinders of G-348 graphite. These cylinders had an inner diameter of 32.3 mm, an outer diameter of 45 mm, and lengths of 152.4 mm. G-348 is an fine grain isotropic graphite fabricated by cold hydro static pressure molding by Tokai Carbon. It is coal tar pitch coke – rather than petroleum – based and possess and average grain size of approximately 30 micron. It is most similar to the IG-430 grade of nuclear graphite. Both grades have similar grain sizes, use coal as their source coke, and are isostatically rather than vibration molded [45].

2.3. Experimental Procedure

For the forced convection experiments, the procedure was as follows:

1. The G-348 test piece was inserted into the left leg of the quartz apparatus.
2. Valves were closed and covering flanges were attached to seal the system.
3. The system was evacuated to a rough vacuum and then back filled with helium.
4. The tube furnaces surrounding the test piece were turned on and the sample was heated to a steady state temperature of 900 °C. System pressure was maintained at close to atmospheric throughout this process by using an exhaust valve to let excess helium escape as needed.

5. After steady state conditions had been achieved, the ball valve attached to the lower right leg was opened. Immediately following this, the DAQ was commanded to send the proper voltage signals to the mass flow controllers and power supply, beginning bulk flow and providing power to the sampling pump.
6. Flow was continued for 90 minutes. During this time, temperature, mass flow rate, and oxygen content data were continuously collected.
7. At 90 minutes, bulk flow was stopped and the system was sealed, evacuated, and cooled.

For the tests involving natural convection driven flow, several steps of the procedure were modified. Steps 1 through 4 from the forced convection experiments were again performed. After this, however, additional steps were required to account for the fact that, unlike the forced convection experiments, bulk flow would not immediately begin due to the buoyancy effects discussed by Takeda and Hishida [35]. Due to the quantity of fluid needed by the NDIR, gas sampling could not begin until after ONC without affecting the results. Therefore, an IR camera was used in the manner previously described by Gould et. al[49] to detect the moment of ONC. The new steps taken for the natural convection oxidation experiments are as follows.

5a After steady state conditions were achieved, the flanges covering the lower openings of both the right and left legs of the apparatus were removed. An IR camera is used to monitor the quartz apparatus and detect specific temperatures changes indicative of ONC.

6a When ONC was detected, signals were sent to the sample pump's power supply and the sample line mass flow controller to begin extracting gas.

7a Sampling was continued for 90 minutes. During this time, temperature and oxygen content data were continuously collected.

8a At 90 minutes past ONC, the flanges were reattached to the openings of the lower legs and the system was sealed, evacuated, and let cool.

2.4. Results and Analysis - Axial Flow Experiments

Before and after images of the entrance and exit regions, respectively, of the graphite cylinders used in the 15 SLM forced convection test are shown in Figures 20a and 20b. The amount of mass lost to oxidation was large enough to measurably reduce both the length and thickness of the tested cylinder with the thickness of the exit region deceasing less than that of the entrance region in all cases. As the temperature of the exit region of a test piece during oxidizing flow will always be higher than that of the entrance region due to the spatial differences in fluid temperature, the reduced erosion seen at the exit regions of the tested graphite samples indicates that the oxidation rate throughout the cylinder is impacted by spatial variations in fluid flow. The reaction rate for each test was calculated as an average for the entire sample per unit of exposed surface area. The surface area value used to calculate the reaction rate of the G-348 graphite was obtained by averaging the before and after oxidation dimensions of the test piece.

The ratio of carbon monoxide to carbon dioxide produced, $P_{CO}P_{CO_2}$, by the oxidation process was calculated by comparing the amount of oxygen consumed by the process with the amount of mass lost from the graphite sample. The total quantity of O_2 used was found by comparing the amount of oxygen leaving the system with the amount put in. The volumetric percentage of oxygen leaving the system was measured continuously using the electro-chemical sensor attached to the NDIR throughout the duration of

(a) Exit **(b) Entrance**

Figure 20: 15 SLM test piece next to untested sample

	Flow Rate			
	15 SLM	**25 SLM**	**30 SLM**	**NC**
Initial Mass [g]	221	220.1	220.5	220.3
Mass Change [g]	55.6	65.7	73.2	69.2
Mean $P_{CO}P_{CO_2}$	0.226	0.227	0.221	~
Entrance Re_D	529	881	1058	~

Table 5: Data from oxidation tests. Each flow rate corresponds to a specific experiment and test piece.

bulk flow in each experiment. This measurement is plotted in Figure 21b for each test. It should be noted that, in the case of the natural convection curve, the first 43.07 minutes of the test prior to ONC were excluded from the plot as no sampling was preformed during that time.

For each forced convection run, the total amount of O_2 leaving the system was found by multiplying the oxygen percent measurement with the flow rate measured by the MFC and then integrating the result over the duration of the experiment. For the natural convection run, no precise measurement of flow rate was available, and thus neither the entrance Reynolds number nor the average $P_{CO}P_{CO_2}$ are reported for this run in Table 5. However, as the total mass lost during the natural convection run was found to be between that lost during the 25 SLM and 30 SLM tests, it is expected that the $P_{CO}P_{CO_2}$ for this run would fall in a similar range to those forced convection tests.

Oxidation rates per unit area are plotted in Figure 21a for each experiment. Due to the limited supply of graphite test pieces that were available to be used, experiments were conducted at only one temperature point, 900 °C. This temperature was chosen as it was high enough to induce significant amounts of oxidation and was close to the temperatures for which other experimental data was available. The values obtained in this work are plotted against values previously reported for NBG-18 [50] and IG-110 graphites [51] and show reasonable agreement with Lee's results.

Importantly however, in the natural convection test there is some indication that either the pre-ONC environment conditions or the post-ONC buoyancy driven flow might be acting to enhance the oxidation

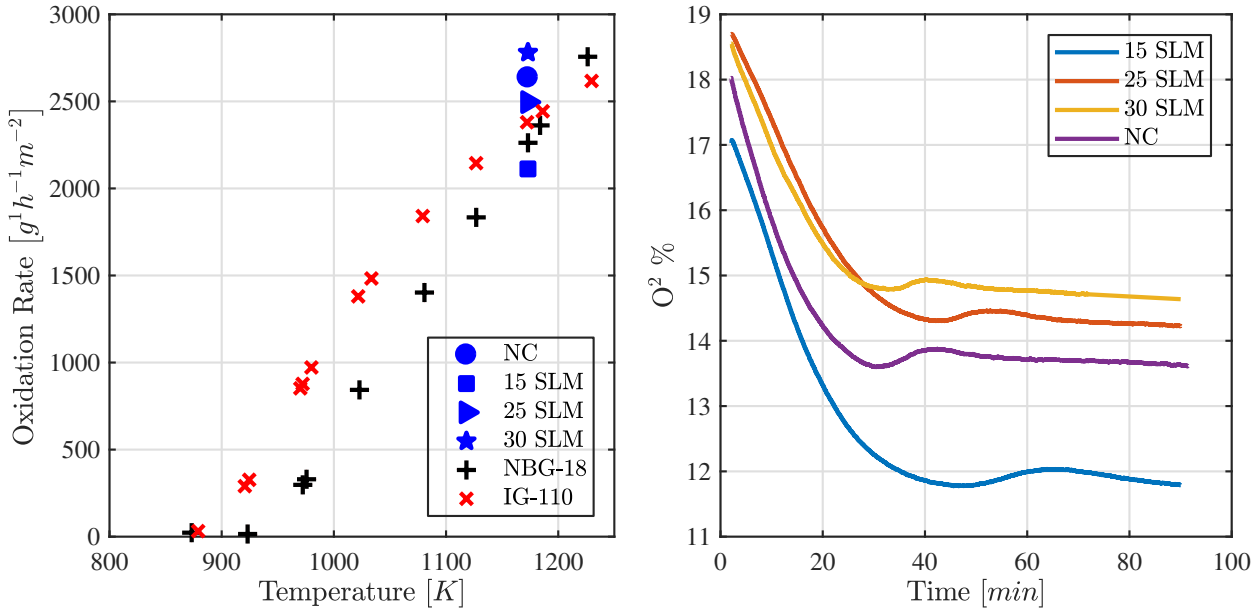

(a) Oxidation rates per unit exposed area. Data plotted for NBG-18 and IG-110 graphite are obtained from Ref. [50] and Ref. [51], respectively.

(b) Percent O_2 remaining in flow.

Figure 21: Comparison of oxidation results

rate beyond what would be expected for its (expected) 20 SLM-equivalent flow rate; the test piece from the natural convection test lost approximately 14% more mass than would have been predicted from the forced convection experimental data. However, better measurements of the precise post-ONC flow rate are likely needed before it can be conclusively said that that such effects are indeed occurring.

Further analysis of the oxidized graphite was performed using samples from the oxidized test pieces. Samples from both the natural convection test, as well as the 15, 25, 30 SLM forced convection experiments, were obtained from their corresponding test cylinders. The entrance regions of the graphite cylinders from each of these tests is shown next to that of an untested sample in Figure 22. In the figure, the locations from which the samples were removed can be identified from the holes seen in each of the tested cylinders. The extracted samples were 12.7 mm in diameter and machined to be less than 6 mm thick at their thickest point. Each sample was extracted using a plugging bit to drill into the side of the test cylinder before being milled on their un-oxidized, outer face to both provide a flat surface and to meat thickness requirements.

2.4.1. XRD

X-ray diffraction (XRD) analysis has been previously shown to be able to identify details a graphite's crystal structure, including details such as the degree of graphitization, crystalline size, inter-layer spacing, and anisotropy [52, 48, 53]. Several works have used this method for both virgin graphite and that which has been damaged by either irradiation or oxidation [54] [48]. The XRD analyses performed on the samples generated in this work (Figure 24), however, did not detect any crystal structure differences.

Figure 22: Entrance region of G-348 test pieces. From left to right: un-oxidized sample, 15 SLM, 25 SLM, NC, 30 SLM

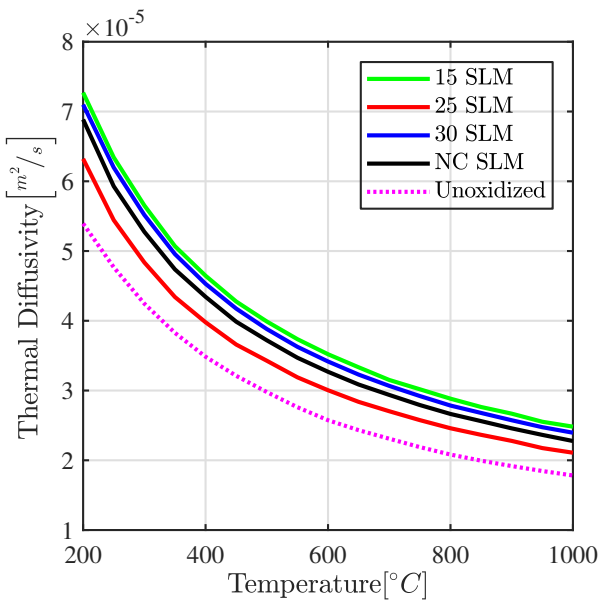

Figure 23: Thermal diffusivity of samples from each test.

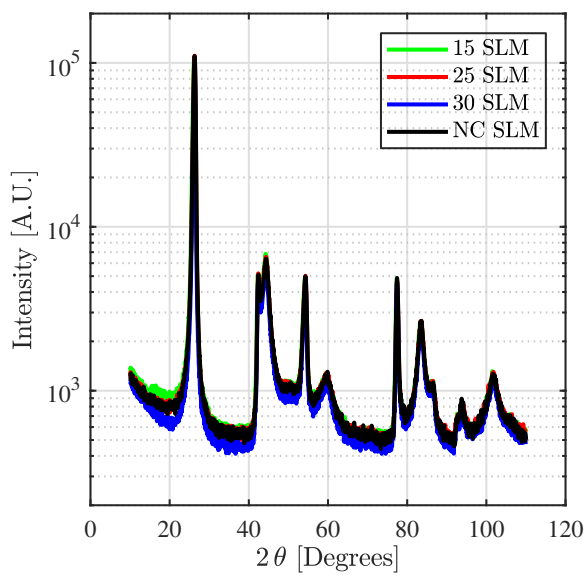

Figure 24: XRD data from each tested sample.

2.4.2. Laser Flash Analysis

The flash method was developed by Parker et. al [55] as a method to quickly and accurately measure the thermal diffusivity of materials that would work at both moderate and high temperatures. The method has been previously used in the study of TRISO nuclear fuel particles by Bari et al [56]. For this work, the LFA 467 laser flash system was used to measure the thermal diffusivity of each the samples taken from the tested graphite cylinders over a wide range of temperatures. Figure 23 shows the results obtained for each sample's thermal diffusivity over a temperature range of 200 °C to 1000 °C. In each case, the thermal diffusivity of the oxidized samples were shown to be greater than that of an un-oxidized control sample over the entire tested temperature range. This increase is assumed to be caused by the existence of an oxidation-induced porous layer on the face of the sample that originally faced the interior of the annular test piece.

Although the graphite sample's density will be directly affected by any porous layer formation, thermal conductivity is not expected to be significantly affected by the porous layer. Although the thermal conductivity of graphite is known to slightly decrease with increasing porosity, the density of the samples tested in this study did not decrease enough for this effect to be appreciable; only a surface layer of our test pieces showed significant oxidation, and even for the least oxidation resistant graphite tested by J.J Lee[44], the average porosity of the oxidized layers only ever reached 25%, and for most grades was significantly less than this. In contrast, the thermal conductivity of 90 percent porous graphite foams is known to drop only 30% below that of solid graphite. Given the lack of any changes in the graphite sample's crystal structure as measured by the XRD analysis, nor is any change in thermal conductivity or heat capacity likely to have occurred to due to changes in the graphite's structure. Thus, for the particular graphite samples tested in this study, it can be safely assumed that the oxidation process affected no significant change in their thermal conductivity or heat capacity. With this assumption, the average density of the porous layers of each test piece can be calculated by assuming that the oxidation layer thickness is similar to that found by J.J. Lee for NBG-18 graphite.

Surprisingly, the sample from the G-348 cylinder that underwent air flow of 15 SLM shows a higher increase in thermal diffusivity than observed for the 25 SLM, 30 SLM and NC samples despite the latter three samples being obtained from test pieces that lost far more mass due to oxidation. However, the interior furnace temperature – measured with a thermocouple placed between the furnace and quartz tube – during the 15 SLM test was measured to be 10 °C to 15 °C lower than that of the other three tests. It is also highly likely that the relative temperature difference between the graphite cylinder in the 15 SLM run and those used with the higher flow rates is even greater than the 10 °C to 15 °C difference measured by the furnace thermocouple. In certain temperature ranges, the rate and effect of graphite oxidation is known to be highly temperature dependent [57]. At lower temperatures, oxidation occurs at a relatively low rate and has the effect of increasing the porosity affected graphite without changing the graphite's outer dimensions. At higher temperatures, oxidation begins to occur only on the graphite surface. This results in little, if any, changes to the porosity of the graphite, but quite possibly in large changes to a graphite sample's outer dimensions.

The transition temperature at which the oxidation process can be said to move from regime to regime is very difficult to define and is known to vary between individual grades of graphite [50]. While no in-depth study has been done on the transition points of G-348, Se-Hwan Chi and Gen-Chan Kim found large, temperature-dependent differences in the transient oxidation kinetics between 808 °C to 911 °C for several different grades of graphite – including the similar IG-430 grade [45]. This indicates that at these temperatures the reaction is not immediately, fully Mode C (see Figure 25) and some amount of temperature dependence in the oxygen penetration depth still exists. Therefore, it is theorized that the lower temperature of the graphite cylinder during the 15 SLM test run enabled deeper penetration of

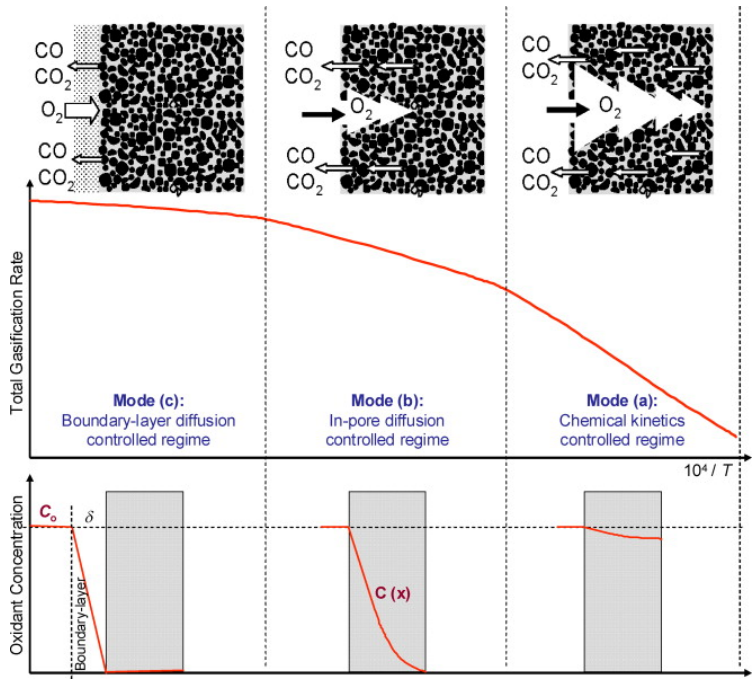

Figure 25: Oxidation modes of porous nuclear graphite. Figure from Ref.[58].

oxygen into the cylindrical test piece and resulted in the sample taken from that test piece possessing a thicker porous layer than that from the higher flow rate tests.

2.4.3. Surface Roughness Changes

The effects of the oxidation process on the surface roughness of the tested graphite were examined by using a profilometer to quantify the surface roughness of several graphite samples cut from the test cylinders. The measured roughness of those samples that were analyzed with the profilometer are shown in Figure 26. Clockwise from top left, the samples in Figure 26 are denoted Control, Saw Cut, Oxidized 1, and Oxidized 2. The 'Control' and 'Saw Cut' samples are un-oxidized samples with differently machined surfaces, while the Oxidized 1 and Oxidized 2 pieces are taken from the entrance and exit of a test piece that had undergone significant oxidation. The measured surface of the 'Control' sample was faced with a 4 flute carbide end mill turning at approximately 3000 rpm. In contrast, the face of the large annular piece denoted 'Saw Cut' resulted from an annular cylinder being cut with a large band saw. This type of surface is the most representative of the average surface conditions present on the portions of un-oxidized graphite viewed by the IR camera. Finally, the two oxidized samples are representative of the damaged surfaces seen in Figures 32b, 22, and 20.

The roughness of each surface is quantitatively defined by the surface's average roughness, R_a and average slope, Δ_a. These values were calculated as defined in ASME B46.1 [59] and are shown in Table 6.

Previous work done analyzing graphite emissivity has indicated that the emissivity of certain grades graphite will rise as surface roughness, such as that caused by oxidation, in the SWIR and MWIR wavelengths [60]. This is also likely what caused the increase in emissivity in the LWIR region reported in Section 3.4. The increased roughness of the oxidized samples shown in Figure 32 is highly apparent compared to the 'Control' and 'Saw Cut' samples shown in Figure 26.

Figure 26: Surface profile samples. Clockwise from top left: NC SLM 1, Control, Saw Cut, NC SLM 2

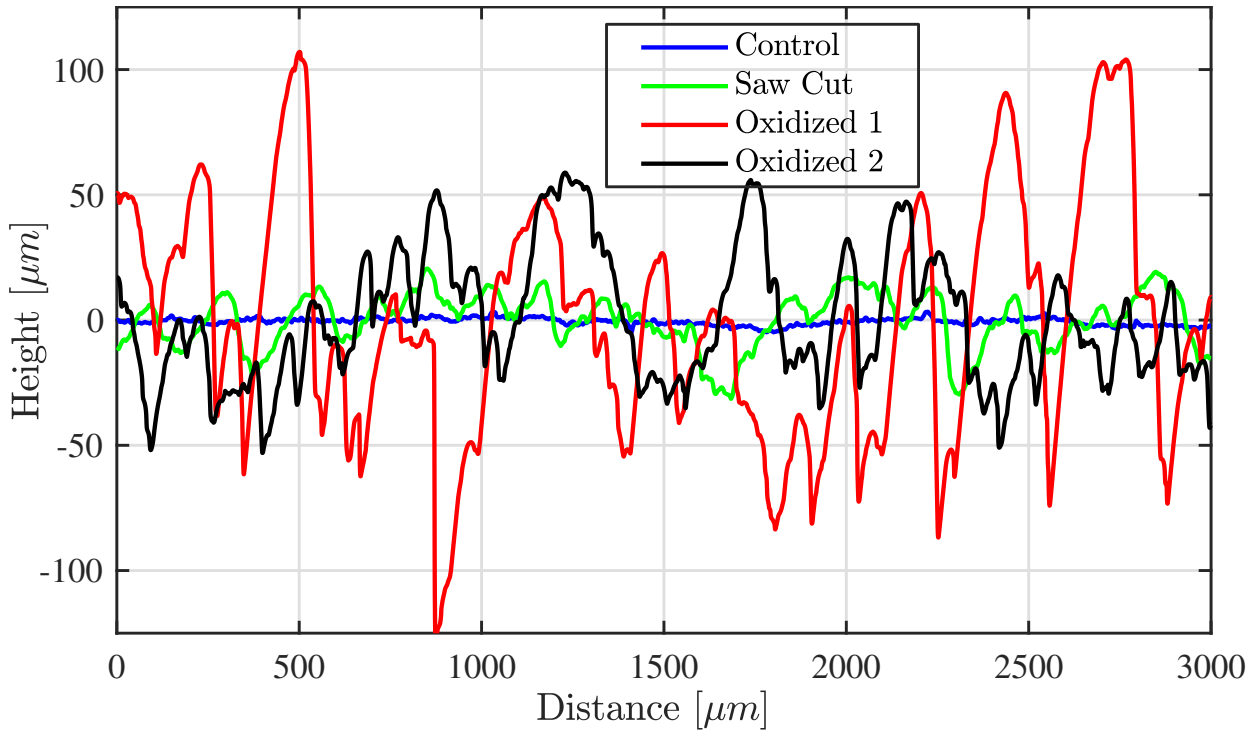

Figure 27: Surface profiles of representative graphite samples

	$\mathbf{R_a}$ [m]	$\mathbf{\Delta}_a$
Control	1.56×10^{-6}	94.0×10^{-3}
Saw Cut	10.89×10^{-6}	263.2×10^{-3}
Oxidized 1	47.55×10^{-6}	1.024
Oxidized 2	25.84×10^{-6}	687.5×10^{-3}

Table 6: Roughness parameters for each of the samples tested.

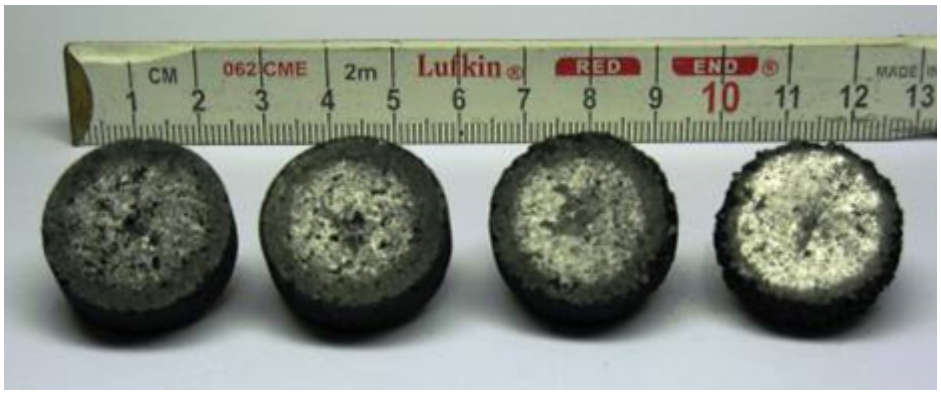

Figure 28: Surface of graphite coupons exposed to a high temperature, oxidizing environment. The outer edges were not exposed due to the ceramic clamps used to hold the coupons. Figure from Ref.[61]

3. EMISSIVITY EXPERIMENTS 24

3.1. Changes to Emissivity

Due to the HTGR's high operating temperatures and gas filled core, radiative heat transfer is likely to be significant in any accident scenario. Helium's low (in comparison to water) thermal conductivity and high transmissivity result in the potential for large amounts of excess heat present during an accident scenario to be transported to the outer walls of the reactor structure via radiation. However, if such a method of heat dispersal is to be depended on, an accurate estimate for the emissivity of the graphite within the core at the time of the accident is needed. Additionally, if the accident itself, such as in the case of an air ingress, has the potential to alter the graphite's emissivity, the phenomenon must be fully understood as well.

If the ash content of the graphite is high enough that an ash layer forms on the graphite surface, the emissivity of the graphite can be greatly reduced. Although nuclear graphite is purified to total impurity levels below 300ppm, it is anticipated that over the lifetime of the reactor some of these impurities will eventually be oxidized and can form a light ash deposit on the outer surface of the graphite components. These oxidized impurities often exhibit a light gray color, and are associated with reduced emissivity and heat transfer efficiency from the purely black carbon-only surface of the graphite components. Figure 28 is provided as an example of some of the potential changes in surface properties which can be attributed to oxidation. Here, the oxidation is shown to radically change the appearance – and therefore likely also the emissivity – of a typical graphite sample that suffers from an above average level of impurities.

If the ash content of the graphite is high enough that an ash layer forms on the graphite surface, the emissivity of the graphite can be greatly reduced. To demonstrate this effect an assembly of 7 graphite

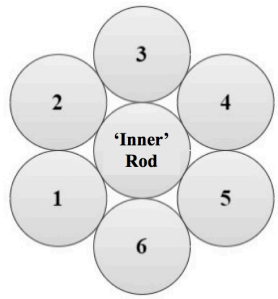

Figure 29: Diagram of 7 graphite rod test assembly.

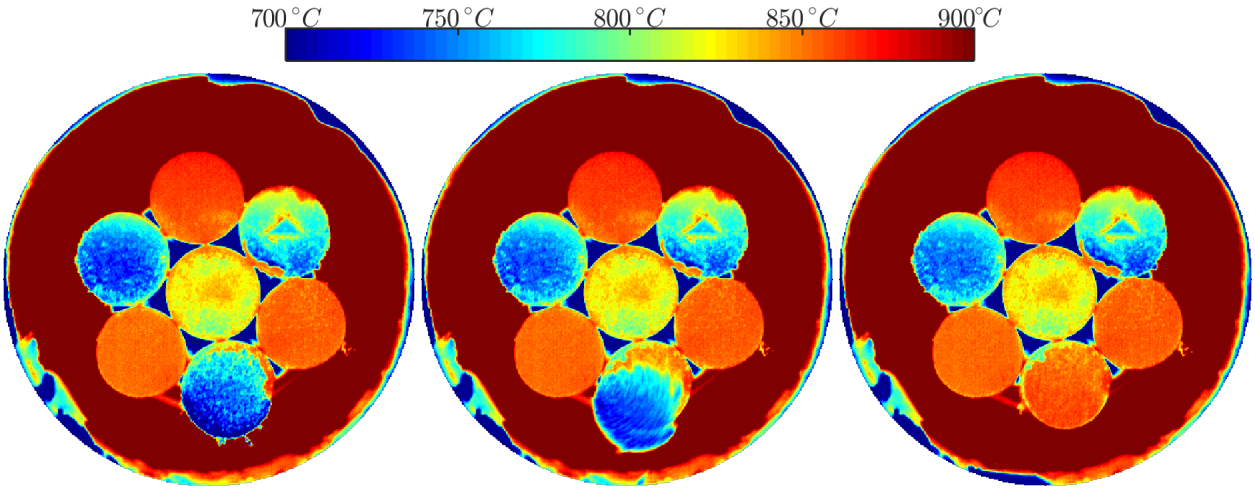

(a) Attached ash layer **(b) Detached ash layer** **(c) Clear surface**

Figure 30: Emissivity change due to ash layer forming and leaving graphite face

rods with an ash content of less than 500 ppm were packed in a manner similar to that shown in Figure 29 and heated to 900 °C in the open atmosphere. During the test, large apparent inter-rod temperature variations began to appear. However, these variations in apparent temperature were identified as being solely caused by oxide layers that built up on the faces of different rods at different rates. In reality, the average temperature of each rod in the assembly were almost identical, however, as can be seen in Figure 30, the amount of thermal energy they emitted was very different.

In Figure 30, three pseudo-colored images are shown from the aforementioned test. The data with which these images were made were obtained from IR camera images taken immediately before, during, and immediately after the detachment of a flake of the ash layer that had grown on the surface of the graphite. The rods on which a complete ash layer has formed can be identified in Figure 30 by their blue – rather than orange – appearance.

The plot shown in Figure 31 is an approximate calculation for the ratio of the average emissivities between the outer rods identified in Figure 29 as numbers 1 and 2. This value is plotted over a chosen time period of interest during the initial heating of the graphite test pieces while they were exposed to the atmosphere. The x-axis reference point $t_0 = 0$ seconds was set to be equal to the time of the frame shown in Figure 30b, at which the flake detached from the rod. At this point in time, the ratio of emissivities plotted in Figure 31 suddenly increases by about 50%. The timing of this jump perfectly coincides with the detachment of the oxide layer from the face of the rod as shown in Figure 30b. Therefore, it can be safely

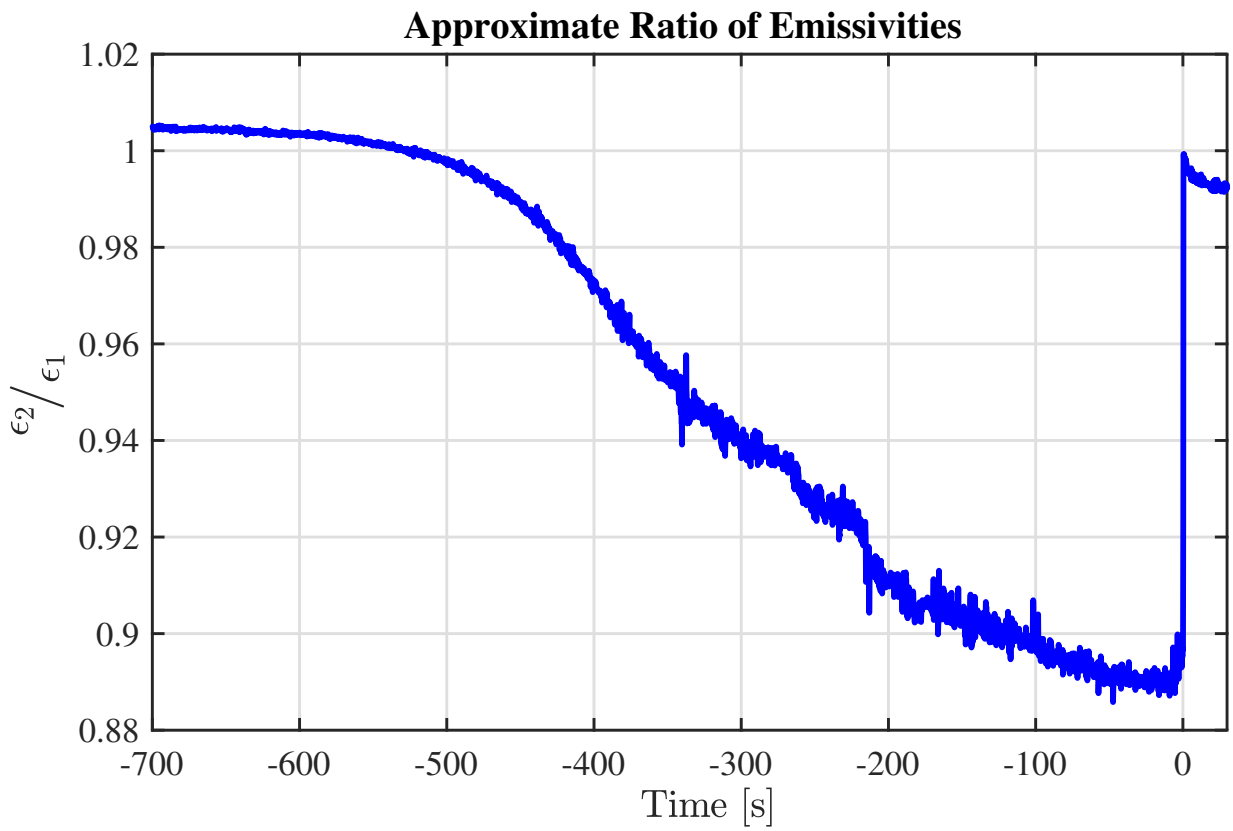

Figure 31: Change in relative emissivity due to an ash layer first building, and then leaving a graphite surface. Figure from Ref. [7]

concluded that the variation in rod temperature seen by the camera and shown in Figure 30 is indeed due to the spatially and temporally varying emissivity caused by the formation of oxide layers on the surface of the graphite rods. Each of the rods in the assembly exhibited similar behavior throughout the experiment; their emissivities would slowly drop as an ash layer formed on the surface of the rod, the layer would fall way, and then the emissivity of the rod would return to it's initial state. The effect of the ash layer on emissivity was seen to be equal for all of the rods in the assembly.

For this calculation, it was assumed that both the average temperature and cross-sectional area of each rod were identical and did not vary temporally during the specified time period during which the measurement was taken. The IR camera was set to record 6.25 frames per second, which resulted in a measurement time of .16 seconds. With these assumptions, any temperature differences observed between these two rods would therefore be the direct result of differing emissivities. Indeed, analysis of Figures 30 and 31 provides confirmation that, in an oxidizing environment, variations in emissivity far and away become the dominating factor in apparent temperature differences between outer rods.

In contrast, oxidation – which, as demonstrated in Section 2.4.3 can substantially increase surface roughness – has been previously shown to increase the emissivity of graphite over certain wavelengths [62]. Thus, the total change in the emissivity of graphite within an HTGR will be a function of several different variables, and combined effects experiments will be required for a meaningful understanding of the phenomenon.

3.2. LWIR Emissivity Measurements

The FLIR A655sc thermal imaging camera was used characterize the emission properties of the G-348 graphite in the long wave domain. The camera has a spectral range of about 7.5 - 14 micron. Although the specific spectral response of the sensor is proprietary, the camera's calibration curve is programmed into the camera itself and can be used in FLIR's proprietary software, allowing for approximate values for average normal Emissivity in the spectral region to be backed out. To do this, a high-temperature paint known to have a constant emissivity in the region of interest was applied to a small portion of the observable face of a graphite test piece and the entire test piece was heated to a constant, uniform temperature - usually 1173 K. Once the G-348 test piece was brought to steady state conditions, it could be assumed that any apparent temperature differences reported by the thermal camera between the pixels of the painted surface and those immediate surroundings was due solely to emissivity differences between the paint and the G-348. As the spectral emission of the paint is well characterized and known to be constant in the long wave domain [63], knowledge of the FLIR camera's specific spectral response is not needed for an accurate and relevant emissivity parameter to be specified for input into the FLIR software. Given the known emissivity of the painted region and specifying the mean temperature of the painted region as the true temperature of the pixels closely surrounding the painted region, the FLIR software will report the an average normal emissivity of bare G-348 surface in the 7.5-14 micron wavelength range. This process resulted in an un-oxidized, long wave normal emissivity value of 0.86 for bare, un-oxidized G-348 graphite with surface roughness similar to that of the 'Saw Cut' sample of Figure 26.

3.3. Experimental Procedure for Emissivity Experiments

To determine the effects of the the oxidation process on the emissivity of G-348, several experiments were carried out in which the IR camera was used to monitor the lower face of the graphite test piece as it was impacted by oxidizing flow. For these tests, the vast majority of the G-348 test piece was coated with a material known to inhibit oxidation. The only uncoated areas on the test pieces were found on the lower – i.e. in terms of its positioning in the furnace – face of the test cylinders, a portion of which was left bare to interact with the flow. Additionally, on some test pieces part of the uncoated region on the lower face was painted with the known emissivity paint. As this painted section was placed directly next to the bare portion of the lower face, any observed differences in the steady state temperatures on a virgin test piece between bare and painted regions could be attributed to emissivity. The cylinders used in these tests possessed the same I.D and O.D as those discussed in Section 2.2, but were 76.2 mm long. The following procedure was used for these experiments:

1. The G-348 test piece was inserted into the left leg of the quartz apparatus.
2. Valves were closed and covering flanges attached to seal the system.
3. The system was evacuated to a rough vacuum and then back filled with helium.
4. The tube furnaces surrounding the test piece were turned on and the sample was heated to a steady state temperature of 900 °C. System pressure was maintained at close to atmospheric throughout this process by using an exhaust valve to let excess helium escape as needed.
5. The power output of the furnace was constrained to a narrow range around the output value that resulted in the steady state conditions. The allowed variation in output was large enough to allow the temperature controller within the furnace to maintain a steady state temperature before the initiation of flow, but small enough that the system could be accurately described as under constant flux

6. After steady state conditions had been achieved, the ball valve attached to the lower right leg was opened. Immediately following this, the DAQ was commanded to send the proper voltage signal to the mass flow controller, beginning bulk flow through the system.
7. Flow was continued for a predetermined amount of time, during which the spatial temperature distribution of the lower face of the test piece was recorded by the IR camera.
8. Bulk flow was stopped and the system was sealed, evacuated, and either cooled or brought back to steady state conditions for another experiment.

3.4. Results and Analysis - Emissivity Experiments

The state of the G-348 test cylinders after being tested is shown in Figure 32. In Figure 32a, the three different sections of the visible, or lower, face are identified. The 'Coated' section is covered with the anti-oxidation coating, the 'Bare' section is bare G-348, and the 'Painted' section is the area that was originally covered with the known-emissivity paint. Although remnants of the paint can still be identified in this last section, most of the paint disintegrated midway through the second test. The sample shown in Figure 32a was tested at 900 °C with 15 SLM air flowing through it.

Even greater damage is seen in 32b which shows the sample that was tested at 1000 °C in 6.8 SLM of pure oxygen. Half of the visible face of this test piece was coated and half was left bare. After being exposed to the oxygen flow for a total of 15 minutes, the oxidation reaction had removed the top 4 mm of graphite from the bare section of the visible face.

In Figure 33, the temperature response of the face of the graphite test pieces to the oxidizing flow is plotted for several experimental runs. For each of the runs shown in Figure 33a, 33b, the average temperatures of the 'Bare' and 'Painted' sections are plotted. Air flow was begun 30 seconds into Figure 33a and 20 seconds into 33b. At each of these points, a sharp jump in the temperatures of both sections identifies the moment that the oxidation reaction began. 6 minutes later, each plot shows another sudden temperature spike. This spike indicates the moment that air flow was stopped in each experiment. At that moment, excess oxygen is still present in the area surrounding the test pieces and thus the oxidation reaction continues relatively unabated for another few seconds before the remaining oxygen is used up. However, as the bulk flow of air has already stopped, the amount of convective cooling felt by the test piece is already greatly reduced. This combination of events leads to the temperature spikes shown at approximately 400 seconds in Figure 33.

Despite enduring the same rate and duration of oxidizing flow, the temperature histories shown in Figure 33b appear very different from those in Figure 33a. This is due to the disintegration of the known-emissivity paint that occurred during the second run. Even at the beginning of the 2nd run, the paint – which is specified only for "intermittent" use at 900 °C – had begun to be removed by the combination of high temperatures and oxidizing flow. This increased the amount of reactive surface area available to the oxidation process and leads to the higher overall temperature of the 'Bare' section seen in Figure 33b compared to Figure 33a. Eventually however, as more paint is lost and the visible surface of that section approaches what is seen in Figure 32a, the average emissivity of the 'Painted' section begins to approach that of the 'Bare' surface, resulting in the apparent – but not actual – temperature drop seen for mean temperature of the 'Painted' section in Figure 33b.

As each sample was brought to a steady state, uniform temperature before each of the runs began, the apparent variance in the steady state temperatures of the bare and painted surfaces shown over the first 20 seconds of data plotted in Figure 33b indicates that the emissivity of the bare graphite surface has

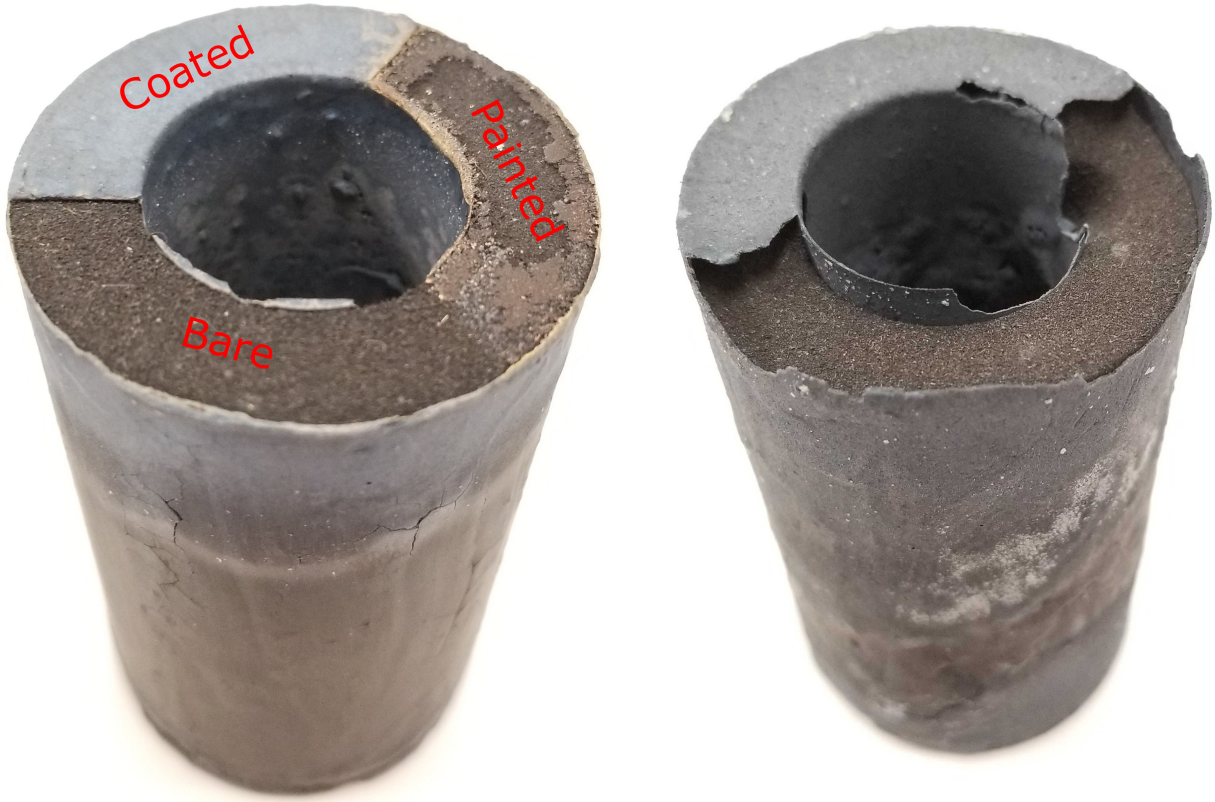

(a) Damage resulting from a total of 12 minutes of 15 SLM air flow.

(b) Damage resulting from a total of 15 minutes of 6.8 SLM O_2 flow.

Figure 32: Condition of the G-348 cylinders that were partially coated with the anti-oxidation coating after testing.

increased since the start of the first run. This 25 °C jump indicates an approximate emissivity change of 3.5%. This is less than the 5 - 15 percent increase seen by Plunkett and Kingery [60], but as the graphite they used was not nuclear grade graphite [64], it is likely that their sample was simply more affected by the oxidation.

4. CONCLUSIONS

Three main conclusions can be drawn from this work. First, it was experimentally demonstrated that oxidation will affect the thermal diffusivity of nuclear grade graphite. Unfortunately, in the transition region between the diffusion controlled and boundary layer controlled regimes, the magnitude of the change in thermal diffusivity was found to be difficult to precisely predict. However, the effect direction was identical for all tested samples – oxidation caused the thermal diffusivity of each test piece to increase. This change is believed to be driven by oxidation decreasing graphite sample density rather than raising sample thermal conductivity.

Second, although oxidation was shown to greatly alter graphite emissivity, both the magnitude and direction of such changes to graphite emissivity are difficult to predict. If an air ingress were to occur

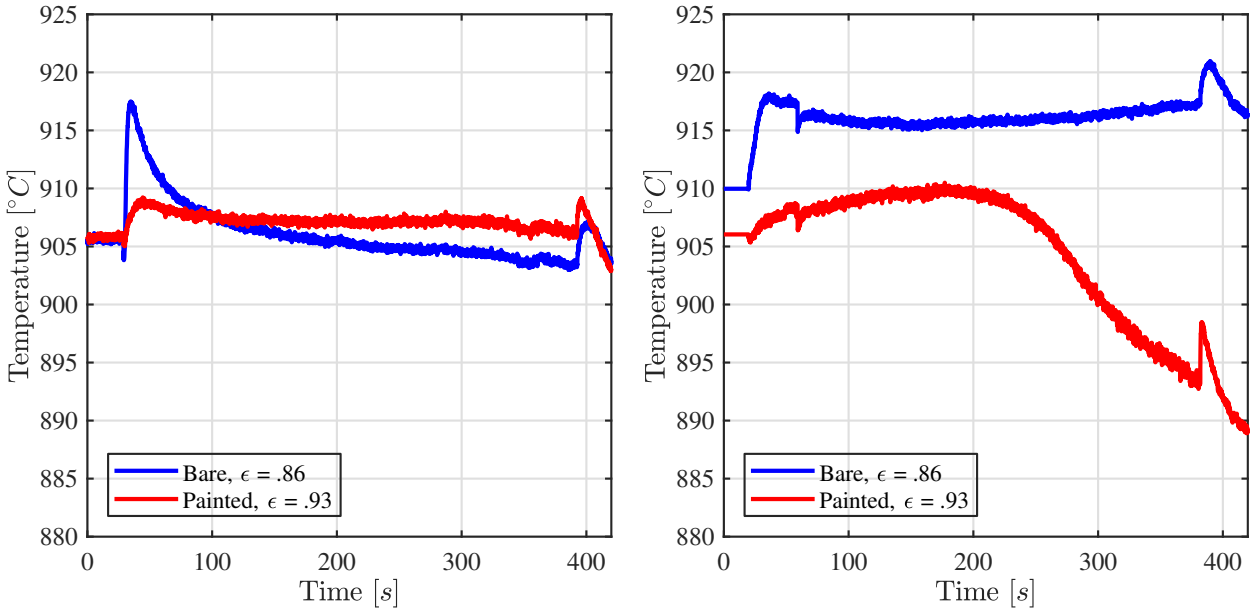

(a) 15 SLM air – 1st run **(b) 15 SLM air – 2nd run**

Figure 33: Effect of oxidation on LWIR emissivity.

within an HTGR, changes to both the macroscopic and the microscopic variables known to affect graphite emissivity are likely to occur. If large amounts of impurities have built up within the graphite over time and have significantly elevated its effective ash content, then an air ingress is likely to severely inhibit the radiative heat transfer abilities of the graphite due to the formation of low emissivity, ash layers on its surface. However, if, at the time of the air ingress, the purity of the graphite is still close to that of its virgin specifications, the oxidation induced roughening of the graphite's outer surface would have the effect of slightly raising its emissivity.

Finally, although the lack of precise velocity measurements makes it impossible to conclusively state the exact reasons for the difference, the in-situ oxidation experiments performed with natural convection resulted in more oxidation occurring than was predicted from the results of the forced flow experiments. Further research into the precise causes of the unexpectedly high oxidation rate observed in buoyancy driven flow is therefore suggested.

REFERENCES

[1] M. G. Cooper, B. B. Mikic, and M. M. Yovanovich. Thermal contact conductance. 12(3):279–300.

[2] B B Mikić. Thermal contact conductance; theoretical considerations. 17(2):205–214.

[3] C.V. Madhusudana. *Thermal Contact Conductance*. Springer.

[4] W. Van Antwerpen, C. G. Du Toit, and P. G. Rousseau. A review of correlations to model the packing structure and effective thermal conductivity in packed beds of mono-sized spherical particles. *Nuclear Engineering and Design*, 240(7):1803–1818, 2010.

[5] W. Van Antwerpen, P. G. Rousseau, and C. G. Du Toit. Multi-sphere Unit Cell model to calculate the effective thermal conductivity in packed pebble beds of mono-sized spheres. *Nuclear Engineering and Design*, 247:183–201, 2012.

[6] Daniel Gould, Daniel Franken, Hitesh Bindra, and Masahiro Kawaji. Transition from molecular diffusion to natural circulation mode air-ingress in high temperature helium loop. *Annals of Nuclear Energy*, 107:103–109, 2017.

[7] Dan Gould, Hanwen Liu, and Hitesh Bindra. Thermographic Studies on the Impact of Material Discontinuities and Oxidation on the Thermal Behavior of a Graphite Matrix. In *NURETH-16*.

[8] Daniel Gould. *Air Ingress in HTGRs: The process, effects, and experimental methods relating to its investigation and consequences*. Dissertation, Kansas State University, 2018.

[9] Daniel W. Gould, Hitesh Bindra, and Sanjoy Das. Thermal response construction in randomly packed solids with graph theoretic support vector regression. *International Journal of Heat and Mass Transfer*, 115:421–429, 2017.

[10] Alexander Z. Zinchenko. Algorithm for random close packing of spheres with periodic boundary conditions. *Journal of Computational Physics*, 114(2):298–307, 1994.

[11] D. Pavlidis and D. Lathouwers. Realistic packed bed generation using small numbers of spheres. *Nuclear Engineering and Design*, 263:172–178, 2013.

[12] Charl G. Du Toit. Radial variation in porosity in annular packed beds. *Nuclear engineering and design*, 238(11):3073–3079, 2008.

[13] Y. M. Ferng and K. Y. Lin. CFD investigation of thermal-hydraulic characteristics in a PBR core using different contact treatments between pebbles. *Annals of Nuclear Energy*, 72:156–165, 2014.

[14] E. Teuchert, K. A. Haas, A. Van Heek, and P. R. Kasten. Distribution of the decay heat in various modul htrs and influence on peak fuel temperatures. In *Decay heat removal and heat transfer under normal and accident conditions in gas cooled reactors*, number IAEA-TECDOC-757, page 53, 1992.

[15] W. O. Harms and D. B. Trauger. Fabrication variables, performance and cost considerations for htgr coated-particle fuels. pages 27–49, 1965.

[16] Won Jae Lee, Thomas YC Wei, and Richard R Schultz. Generation of a preliminary pirt (phenomena identification and ranking table) for very high temperature gas-cooled reactors. Technical report, Korea Atomic Energy Research Institute, 2005.

[17] Hugh M McIlroy, Donald M McEligot, and Robert J Pink. Measurement of turbulent flow phenomena for the lower plenum of a prismatic gas-cooled reactor. *Nuclear Engineering and Design*, 240(2):416–428, 2010.

[18] Ibrahim A Said, Mahmoud M Taha, Shoaib Usman, Brian G Woods, and Muthanna H Al-Dahhan. Investigation of natural convection heat transfer in a unique scaled-down dual-channel facility. *AIChE Journal*, 63(1):387–396, 2017.

[19] Francisco I Valentín, Narbeh Artoun, Ryan Anderson, Masahiro Kawaji, and Donald M McEligot. Study of convection heat transfer in a very high temperature reactor flow channel: Numerical and experimental results. *Nuclear Technology*, 196(3):661–673, 2016.

[20] Richard R Schultz, Paul D Bayless, Richard W Johnson, James R Wolf, and Brian Woods. Scaling studies for high temperature test facility and modular high temperature gas-cooled reactor. Technical report, Idaho National Laboratory (INL), 2012.

[21] Richard R Schultz, Paul D Bayless, Richard W Johnson, William T Taitano, James R Wolf, and Glenn E McCreery. Studies related to the oregon state university high temperature test facility: Scaling, the validation matrix, and similarities to the modular high temperature gas-cooled reactor. Technical report, Idaho National Laboratory (INL), 2010.

[22] Xiaodong Sun, Richard Christensen, and Chang Oh. Investigation of countercurrent helium-air flows in air-ingress accidents for vhtrs. Technical report, Battelle Energy ALliance, LLC, 2013.

[23] David J. Arcilesi. *Developmental Analysis and Design of a Scaled-down Test Facility for a VHTR Air-ingress Accident*. PhD thesis, Ohio State University, 2012.

[24] Chang H Oh and Eung S Kim. Air-ingress analysis: Part 1. Theoretical approach. *Nucl. Eng. Des.*, 241(1):203–212, 2011.

[25] Chang H Oh, Hyung S Kang, and Eung S Kim. Air-ingress analysis: Part 2—Computational fluid dynamic models. *Nuclear Engineering and Design*, 241(1):213–225, 2011.

[26] Chang H Oh, Cliff Davis, Larry Siefken, Richard Moore, Hee Cheon NO, Jong Kim, Goon C Park, John C Lee, and William R Martin. Development Of Safety Analysis Codes And Experimental Validation For A Very High Temperature Gas-Cooled Reactor. Technical Report INL/EXT-06-01362, Idaho National Labratory.

[27] David J. Arcilesi, Tae Kyu Ham, In Hun Kim, Xiaodong Sun, Richard N. Christensen, and Chang H. Oh. Scaling and design analyses of a scaled-down, high-temperature test facility for experimental investigation of the initial stages of a VHTR air-ingress accident. *Nuclear Engineering and Design*, 288:141–162, 2015.

[28] Tae K Ham, David J Arcilesi, In H Kim, Xiaodong Sun, Richard N Christensen, Chang H Oh, and Eung S Kim. Computational fluid dynamics analysis of the initial stages of a vhtr air-ingress accident using a scaled-down model. *Nuclear Engineering and Design*, 300:517–529, 2016.

[29] Hyung Gon Jin, Hee Cheon No, and Hyeon Il Kim. Stratified flow-induced air-ingress accident assessment of the gamma code in htgrs. *Nuclear Engineering and Design*, 241(8):3216–3223, 2011.

[30] Hyung Gon Jin, Hee Cheon No, and Byung Ha Park. Effects of the onset time of natural circulation on safety in an air ingress accident involving a htgr. *Nuclear Engineering and Design*, 250:626–632, 2012.

[31] Seungjin Kim, Mohan S Yadav, Justin D Talley, Andrew Ireland, and Stephen M Bajorek. Separate effects experiments for air-ingress in helium filled vessel. *Experimental Thermal and Fluid Science*, 49:1–13, 2013.

[32] Antonio Campo, Mohammad M Papari, and Eiyad Abu-Nada. Estimation of the minimum prandtl number for binary gas mixtures formed with light helium and certain heavier gases: Application to thermoacoustic refrigerators. *Applied Thermal Engineering*, 31(16):3142–3146, 2011.

[33] Jun Liu and Guenter Ahlers. Rayleigh-benard convection in binary-gas mixtures: Thermophysical properties and the onset of convection. *Physical Review E*, 55(6):6950, 1997.

[34] MF Taylor, KE Bauer, and DM McEligot. Internal forced convection to low-prandtl-number gas mixtures. *International journal of heat and mass transfer*, 31(1):13–25, 1988.

[35] Tetsuaki Takeda and Makoto Hishida. Studies on molecular diffusion and natural convection of two-component gases. 135:341–354, 1992.

[36] Tetsuaki Takeda and Makoto Hishida. Studies on molecular diffusion and natural convection of multi-component gases. volume 135, pages 1489–1497, 1993.

[37] Tetsuaki Takeda and Makoto Hishida. Studies on molecular diffusion and natural convection in a multicomponent gas system. 39(3):527–536.

[38] Chang H Oh, Eung S Kim, Hee C No, and Nam Z Cho. Final report on experimental validation of stratified flow phenomena, graphite oxidation, and mitigation strategies of air ingress accidents. Technical report, Idaho National Laboratory (INL), 2011.

[39] N Kodochigov, Yu Sukharev, E Marova, N Ponomarev-Stepnoy, E Glushkov, and P Fomichenko. Neutronic features of the gt-mhr reactor. *Nuclear Engineering and Design*, 222(2):161–171, 2003.

[40] Richard Edwin Nightingale. *Nuclear Graphite: Prepared under the Auspices of the Division of Technical Information United States Atomic Energy Commission*. Academic press.

[41] Donald G Schweitzer. Oxidation and Heat Transfer Studies in Graphite Channels I. The Effect of Air Flow Rate on the CO 2 and CO-O 2 Reactions. 12(1):49–45.

[42] Donald G Schweitzer. Oxidation and Heat Transfer Studies in Graphite Channels III. The Chemical Reactivity of BNL Graphite and Its Effect on the Length of Channel Cooled by Air. 12(1):51–58.

[43] D. G. Schweitzer. Experimental Results of Air Ingress in Heated Graphite Channels. In *Responce of fuel, fuel elements and gas cooled reator cores under accidental air or water ingress conditions*, number October, pages 50–55.

[44] Jo Jo Lee, Tushar K. Ghosh, and Sudarshan K. Loyalka. Comparison of NBG-18, NBG-17, IG-110 and IG-11 oxidation kinetics in air. 500:64–71.

[45] Se-Hwan Chi and Gen-Chan Kim. Comparison of the oxidation rate and degree of graphitization of selected IG and NBG nuclear graphite grades. 381(1-2):9–14.

[46] Mohamed S. El-Genk and Jean-Michel P. Tournier. Validation of gasification model for NBG-18 nuclear graphite. 250:142–155.

[47] Lance L. Snead, Christian I. Contescu, Thak Sang Byun, and W. Porter. Thermophysical property and pore structure evolution in stressed and non-stressed neutron irradiated ig-110 nuclear graphite. 476:102–109.

[48] Ram Krishna, James Wade, Abbie N. Jones, Michael Lasithiotakis, Paul M. Mummery, and Barry J. Marsden. An understanding of lattice strain, defects and disorder in nuclear graphite. 124:314–333.

[49] Daniel Gould, Daniel Franken, Hitesh Bindra, and Masahiro Kawaji. Transition from molecular diffusion to natural circulation mode air-ingress in high temperature helium loop. *Annals of Nuclear Energy*, 107:103–109, 2017.

[50] Jo Jo Lee, Tushar K. Ghosh, and Sudarshan K. Loyalka. Oxidation rate of nuclear-grade graphite NBG-18 in the kinetic regime for VHTR air ingress accident scenarios. 438(1-3):77–87.

[51] Jo Jo Lee, Tushar K. Ghosh, and Sudarshan K. Loyalka. Oxidation rate of nuclear-grade graphite IG-110 in the kinetic regime for VHTR air ingress accident scenarios. 446(1-3):38–48.

[52] Mohindar S. Seehra and Arthur S. Pavlovic. X-ray diffraction, thermal expansion, electrical conductivity, and optical microscopy studies of coal-based graphites. 31(4):557–564.

[53] Z. Zhou, W. G. Bouwman, H. Schut, and C. Pappas. Interpretation of x-ray diffraction patterns of (nuclear) graphite. 69:17–24.

[54] Guiqiu Zheng, Peng Xu, Kumar Sridharan, and Todd Allen. Characterization of structural defects in nuclear graphite IG-110 and NBG-18. 446(1-3):193–199.

[55] W. J. Parker, R. J. Jenkins, C. P. Butler, and G. L. Abbott. Flash method of determining thermal diffusivity, heat capacity, and thermal conductivity. 32(9):1679–1684.

[56] Klaudio Bari, Charles Osarinmwian, Eddie Lòpez-Honorato, and Timothy J. Abram. Characterization of the porosity in TRISO coated fuel particles and its effect on the relative thermal diffusivity. 265:668–674, 2013.

[57] Mohamed S. El-Genk and Jean-Michel P. Tournier. Development and validation of a model for the chemical kinetics of graphite oxidation. 411(1-3):193–207.

[58] Mohamed S. El-Genk and Jean-Michel P. Tournier. Comparison of oxidation model predictions with gasification data of ig-110, ig-430 and nbg-25 nuclear graphite. 420(1-3):141–158.

[59] 1 ASME B46. Surface texture (surface roughness, waviness, and lay): an american national standard.

[60] J D Plunkett and W D Kingery. The Spectral and Integrated Emissivity of Carbon and Graphite. In *Carbon*, volume 26, pages 457–472.

[61] Will Windes. NGNP Graphite R&D Technical Lead.

[62] Y S Touloukian and David P DeWitt. Thermal radiative properties: nonmetallic solids. In *Thermophysical Properties of Matter, Vol.8*.

[63] Jean-Remy Filtz, Ingrid Wetterlund, Bror Persson, Petra Andersson, Robert Jansson, Tony Lemaire, Maria Öhlin, Jukka Myllymäki, Jean-Remy Filtz, Ingrid Wetterlund, Bror Persson, Petra Andersson, Robert Jansson, Tony Lemaire, Maria Öhlin, and Jukka Myllymäki. Improving heat fluxmeter calibration for fire testing laboratories (HFCAL) Final report. Technical report.

[64] Julian Glasser and William Glasser. Directory of Graphite Availability. Technical report, Air Force Materials Laboratory.

CHAPTER 6. NUMERICAL SIMULATIONS OF FLOW LAMINARIZATION

This chapter focuses on a fundamental study of the phenomenon of turbulent flow laminarizing in a strongly heated gas in a vertical circular tube, as in a prismatic gas-cooled nuclear reactor. The Direct Numerical Simulation (DNS) study conducted at INL and recently published [Chu, Laurien and McEligot, IJHMT 2016; McEligot and Johnson, NERS 2017; McEligot et al., IJHMT 2018; McEligot et al., INL/JOU-19-54399] are presented in section 6.1 below. CCNY also conducted Nek5000 simulations of flow laminarization and the results are presented in section 6.2.

6.1 Direct Numerical Simulation of Flow Laminarization by INL (D.M. McEligot)

Well-resolved direct numerical simulation (DNS) was applied to investigate strongly heated air flow in a vertical pipe (L = 30D) at inlet Reynolds numbers of $Re_{D,in}$ = 4240 and 6020. The DNS is based on the experimental cases of Shehata and McEligot [IJHMT 1995] and showed excellent agreement with heat-transfer and flow statistical results. Flow relaminarization was observed in the strongly heated cases. We apply a new semi-local wall coordinate to replace the conventional one. With the semi-local wall coordinates, which consider the local property variation, both the velocity and temperature fields show the process of relaminarization. This relaminarization is also indicated by the significant decrease of turbulence intensity and Reynolds shear stress. In the quasi-laminar flow, the viscous sublayer becomes thicker. Turbulence in this layer shows a growing anisotropic character. And turbulence in the pipe center becomes approximately isotropic. This two-layer character was clearly displayed by flow visualization.

For internal vertical gas flow in tubes with *strong heating rates* at low *turbulent* Reynolds numbers, a typical experimental observation is that the local Nusselt number varies roughly as the square of the decreasing local Reynolds number. An aim of this study was to examine this situation. This examination leads to the hypothesis that the behavior results from the evolution of the thermal boundary layer developing within the primarily molecular transport layer which is also growing from the wall. Comparisons to direct numerical simulations demonstrate that reasonable predictions are provided by an extension of the Leveque similarity analysis for *laminar* thermal boundary layers. These observations modify and improve our fundamental understanding of the process called "relaminarization" in these flows.

Again for low "turbulent" Reynolds numbers in strongly-heated vertical gas flow, fundamental results of direct numerical simulations have been examined to deduce differences

between cases which revert to turbulent or remain turbulent and those that yield integral parameters which correspond to laminar flow (aka laminarizing). This DNS also modeled the experiments of Shehata [IJHMT 1998], all with significant air property variation.

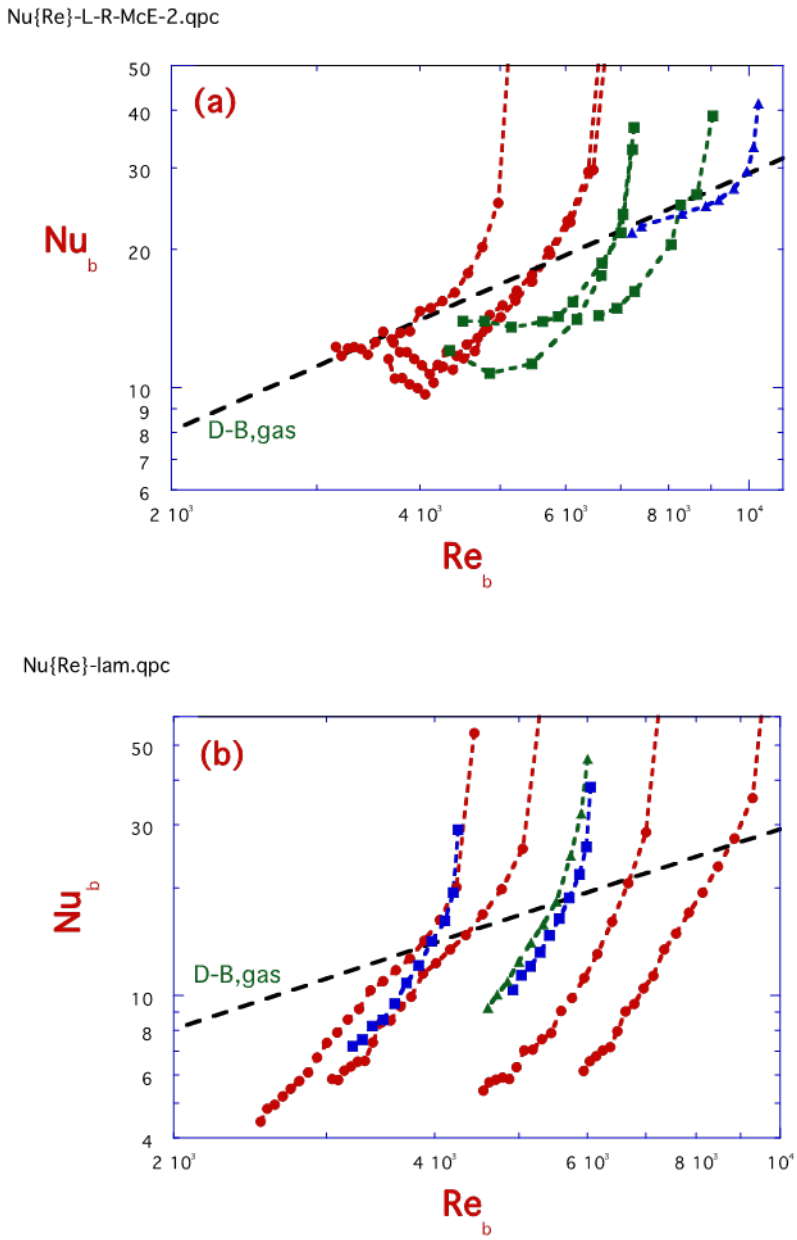

Fig. 6.1. Typical experimental results for internal convective heat transfer to gases at “low” Reynolds numbers with significant property variation. Dashed line = Dittus-Bölter correlation for gases [Drexel and McAdams, MIT TR 1945]. (a) Runs considered "turbulent," circles = Lee [MIT 2007], triangles = Reynolds [U. Arizona 1969], squares = McEligot [TID-19446], (b) runs considered "laminarizing," circles = Lee, triangles = Perkins [U. Arizona 1975] and squares = Shehata [U. Arizona 1984].

In terms of mean quantities, this so-called laminarization is a situation where the laminar entry thermal boundary layer remains within the molecular transport sublayer. So-called turbulent runs apparently revert to agreement with turbulent integral parameters when their thermal boundary layers grow beyond their molecular momentum transport sublayers to the region where there is turbulent transport. The evolution of near-wall fluid structures was studied via their instantaneous transverse cross-sections in the r-θ plane. We hazarded the idea that the observed prevalence of a ring of irregular quasi-streamwise vortices near the wall implies existence of a preferred mechanism. The transverse advection of this fundamental structure was hypothesized to provide a path of least resistance to the transport of streamwise momentum in the wall-normal direction for the turbulent cases. The qualitative ideas discussed were supported by the related quantitative literature reported. The apparent laminarization corresponds to the vortex aspect ratio changing so a larger proportion of the circulating flow would be in the wall shear layer, providing relatively more resistance to the circulation so that momentum advection is reduced. This effect was demonstrated quantitatively by the reduction of the circumferentially-averaged wall-normal transport of streamwise momentum transfer (aka Reynolds shear stress) in DNS results. The evolutions of several proposed laminarization parameters were evaluated to examine whether any could serve as a criterion for the apparent flow regime which resulted. Two possible criteria did discriminate: the non-dimensional radius ($y_{c,w}^{+} = Re_{\tau,w}$) and the modified wall Reynolds number. The latter would be easier to use operationally.

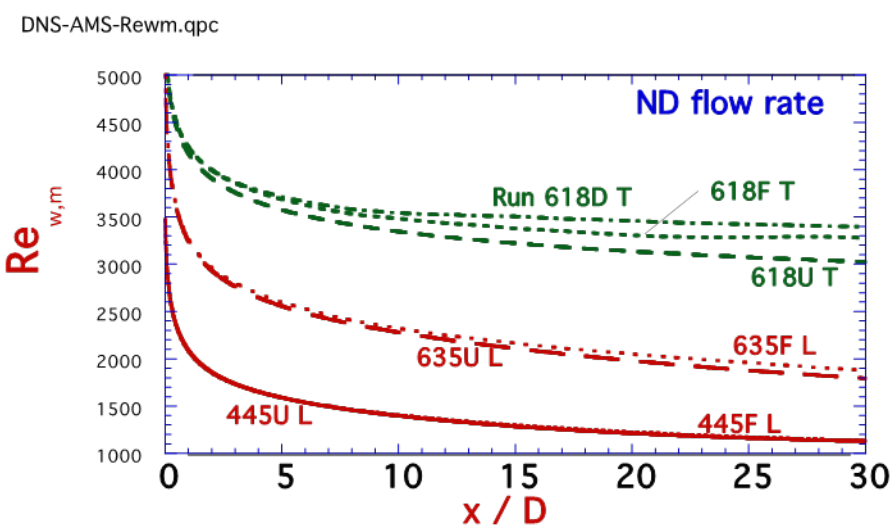

Fig. 6.2 Evolution of non-dimensional gas flow rate, $Re_{w.m} = (V_b D/\nu_w) = 4m/(\Pi\, D\rho_w\nu_w)$, for DNS cases considered, T = remains turbulent and L = laminarizes.

Acknowledgement for Chapter 6, Section 6.1

Foreign collaborators (not funded by DoE) aiding the study by INL and presented in section 6.1 included Prof. J. Y. Yoo of Seoul National University, Dr. J. H. Bae of Koren Air and Prof. E. Laurien and Dr. X. Chu, both of Universität Stuttgart. The participation of Prof. Yoo and Dr. Bae was an outgrowth of an earlier US/Korea I-NERI project.

6.2 Nek5000 Simulation of Flow Laminarization (CCNY)

6.2.1 Simulation problem

This section will discuss the simulation problem which has been worked on using the spectral element code, NEK5000. As mentioned in the previous section, the chief objective of the simulations is to better understand the heat-driven flow relaminarization phenomena in the graphite flow test section observed in our previous forced convection experiments (Valentin, F.I., Artoun, N. and Kawaji, M., 2018. Experimental Investigation of Flow Laminarization in a Graphite Flow Channel at High Pressure and High Temperature, J. Heat Transfer, 140 (11), 112004. doi:10.1115/1.4040786). Hence, for these turbulent flow simulations, we select a 3D pipe of similar dimensions and eventually apply experimental boundary conditions to study the heat-driven flow relaminarization phenomena at a more fundamental level. The simulation work incorporates a two-step process. Because we are dealing with turbulent flow, it is first imperative to make sure that turbulence is sustained throughout the pipe setup. Once that is achieved, we move on to the next part of the simulations that incorporates the experimental boundary conditions where the fluid properties are found to be changing with temperature. Table 6.1 shows the experimental conditions that will be applied to the simulation setup.

Table 6.1 Experimental Parameters incorporated in Simulations

PARAMETER	VALUE
Aspect Ratio (L/D)	~170
Max Inlet Re	5190

Hence, we can define our main objectives for the simulations as follows:

1. Sustain turbulence throughout in a 3D pipe of aspect ratio (L/D =170) under isothermal conditions. This value of aspect ratio comes from the experimental setup where the length

and the diameter of the graphite channel are 2.7 m and 0.016 m, respectively, thus giving us an aspect ratio (L./D) of ~170.

2. Once turbulence is found to be sustained, we apply the experimental conditions where the fluid properties are varying with temperature (Variable Material Property Simulations).

The next section gives a brief introduction to the code used for the simulations - NEK5000.

6.2.2 NEK5000 Code

Nek5000 is an open source, high-order, massively-parallel, spectral element CFD code that brings together the essential characteristics of speed and accuracy needed for solving the Navier-Stokes equations. Aside from the source code, Nek5000 uses three additional files in order to set up a problem, SIZE file, .rea file, and the .usr file. The files .usr and SIZE are compiled with the standard Nek5000 library using makenek which creates the executable file nek5000, they can be considered the surface and the core of the entire program. The .rea file contains case-specific information read during the initialization of the compiled program.

SIZE FILE

Most of the variables used to determine the memory usage are stated in SIZE. The size of the working arrays necessary to perform the calculations are mostly defined by the upper limits of elements, processors, scalars and of course the polynomial degree of the local Lagrange functions. The SIZE file can be considered as the necessary base of Nek5000.

.REA FILE

In the .rea file, all the problem specific parameters are given. While the content in SIZE is an absolute necessity to even compile the program, .rea contains variables that are not used until the initialization of the case. It gives us:

- job control parameters (viscosity, DT, Nsteps, integrator,etc.)
- geometry-element vertex and curvature information
- boundary condition types
- restart conditions

.USR FILE

This file contains a series of standard routines open for modification by the user. In addition, the user is free to specify new routines if needed. A description of these routines is given in the Nek5000 User manual. A list of those frequently used in this work is described below,

- initial and boundary conditions (useric & userbc)

- variable properties (uservp)
- forcing and volumetric heating (userf & userq)
- geometry morphing (usrdat*)
- data analysis routines: min/max/integrals, runtime average, rms, interpolation, etc.

NEK PARLANCE

In Nek parlance, the material properties are specified in the .rea file as:

DIMENSIONAL	NON-DIMENSIONAL
p1 = ρ	p1 = 1
p2 = μ	p2 = 1/Re (or -Re)
p7 = ρCp	p7 = 1
p8 = k	p8 = 1/Pe (or -Pe)

where p1, p2,...,p8 are the parameters in the .rea file.

6.2.3 Boundary Conditions

- **Fluid Boundary Conditions**

A few key boundary conditions that are incorporated are listed below.

BOUNDARY CONDITION	NAME	CONDITION
v	Velocity	specified in .usr
V	velocity	specified in .rea
W	wall	u = 0
O	outflow	$\partial_n u = 0$; p = 0

- **Thermal Boundary Conditions**

A few key thermal boundary conditions are listed below.

BOUNDARY CONDITION	NAME	CONDITION
t	temperature	specified in .usr
T	temperature	specified in .rea
I	Insulated	$\partial_n T = 0$
f	Flux	$k\partial_n T = f$

6.2.4 Governing Equations

- **Incompressible Navier-Stokes equations**

The governing equations of flow motion in dimensional form are

$$\rho\left(\frac{\partial u}{\partial t} + u \cdot \nabla \mathrm{u}\right) = -\nabla \mathrm{p} + \nabla \cdot \tau + \rho \mathrm{f} \qquad (Momentum) \tag{6.1}$$

where $\tau = \mu[\nabla u + \nabla u^T]$.

$$\nabla \cdot u = 0 \qquad (Continuity) \tag{6.2}$$

If the fluid viscosity is constant in the entire domain, the viscous stress tensor can be contracted to $\nabla \cdot \tau = \mu \nabla u$, therefore, one may solve the Navier–Stokes equations in either the stress formulation or no stress form.

- **Non-dimensional Navier Stokes equations**

Let us introduce the following non-dimensional variables

$$x^* = \frac{x}{L}, \qquad u^* = \frac{u}{U}, \qquad p^* = \frac{p}{\rho U^2}, \qquad t^* = \frac{tU}{L}, \qquad f^* = \frac{fL}{U^2} \tag{6.3}$$

For highly convective flows we obtain the non-dimensional Navier-Stokes:

$$\left(\frac{\partial u^*}{\partial t^*} + u^* \cdot \nabla u^*\right) = -\nabla \mathrm{p}^* + \frac{1}{\mathrm{Re}} \nabla \cdot \tau^* + \mathrm{f}^* \tag{6.4}$$

where $\tau^* = [\nabla u^* + \nabla u^{*T}]$ and f^* is a dimensionless user defined forcing function, e.g. gravity.

The non-dimensional number here is the Reynolds number, $Re = \frac{\rho \mathrm{UL}}{\mu}$.

- **Energy Equation**

In addition to the fluid flow, Nek5000 computes automatically the energy equation

$$\rho Cp\left(\frac{\partial T}{\partial t} + u \cdot \nabla T\right) = \nabla \cdot (k \nabla T) + q_{vol} \tag{6.5}$$

- **Non-dimensional energy/passive scalar equation**

A similar non-dimensionalization as for the flow equations using the non-dimensional variables.

$$x^* = \frac{x}{L}, \qquad u^* = \frac{u}{U}, \qquad t^* = \frac{tU}{L}, \qquad T = \frac{T^* - T^0}{\delta T} \tag{6.6}$$

$$\left(\frac{\partial T^*}{\partial t^*} + u^* \cdot \nabla T^*\right) = \frac{1}{\mathrm{Pe}} \nabla \cdot \nabla \mathrm{T}^* + q_{vol} \tag{6.7}$$

where $Pe = \frac{LU}{\alpha}$, with $\alpha = \frac{k}{\rho cp}$.

- **Low-Mach Navier Stokes**

The compressible Navier-Stokes differ mathematically from the incompressible ones mainly in the divergence constraint $\nabla \cdot u \neq 0$. In this case the system of equations is not closed and an additional equation of state (EOS) is required to connect the state variables, e.g. ρ = f(p,T). Nek5000 includes the ability to solve the low-Mach approximation of the compressible Navier-Stokes, ρ ≈ f(T). The low-Mach number approximation decouples the pressure from the velocity leading to a system of equations which can be solved numerically in a similar fashion as the incompressible Navier-Stokes equations.

The low-Mach number equations are

$$\rho\left(\frac{\partial u}{\partial t} + u \cdot \nabla \mathrm{u}\right) = -\nabla \mathrm{p} + \nabla \cdot \tau + \rho \mathrm{f} \tag{6.8}$$

$$\nabla \cdot u = -\frac{1}{\rho}\frac{d\rho}{dT}\left(\frac{\partial T}{\partial t} + u \cdot \nabla T\right) \tag{6.9}$$

$$\rho Cp\left(\frac{\partial T}{\partial t} + u \cdot \nabla T\right) = \nabla \cdot (k\nabla T) + q_{vol} \tag{6.10}$$

where $\tau = \mu[\nabla u + \nabla u^T - \frac{2}{3}\nabla \cdot \mathrm{uI}]$.

This allows for both variable density and variable viscosity calculations. The system is solved by substituting ρ ≈ f(T) into the continuity equation and obtaining a so-called thermal divergence.

6.2.5 Basics of the Solver

The Nek5000 code supports two distinct approaches:

- Option 1 (PN-PN-2):
  - Discretize in space using compatible approximation spaces.
  - Solve coupled system for pressure/velocity.
- Option 2 (PN-PN, or splitting):
  - Discretize in time first.
  - Take continuous divergence of momentum equation to arrive at a Poisson equation for pressure, with special boundary conditions.

6.2.6 Constant Property Simulations

A Conference paper presented at the International Topical Meeting on Advances in Thermal Hydraulics: ATH '18 Embedded Topical Meeting: 2018 Winter Meeting, November 11-15, 2018, Orlando, FL, describes the constant property simulations performed in order to sustain turbulence in a very long pipe. This paper is attached to this Final Report as **Appendix 2 -** Constant Property Simulations of Flow Laminarization using Nek5000.

6.2.7 Variable Property Simulations

This section presents the variable property simulations where the fluid properties change with temperature. The computational setup was the same as in the constant property simulations presented in Appendix 2. A temperature boundary condition was applied to the wall that was obtained from the experiments performed for helium at Re = 5,190. Once the simulations reached steady state, the effect on the axial variations of the fluid properties, velocity profiles and local Reynolds numbers are examined.

Axial Velocity and Temperature Profiles

Figure 6.3 shows the axial velocity and temperature profiles at steady state.

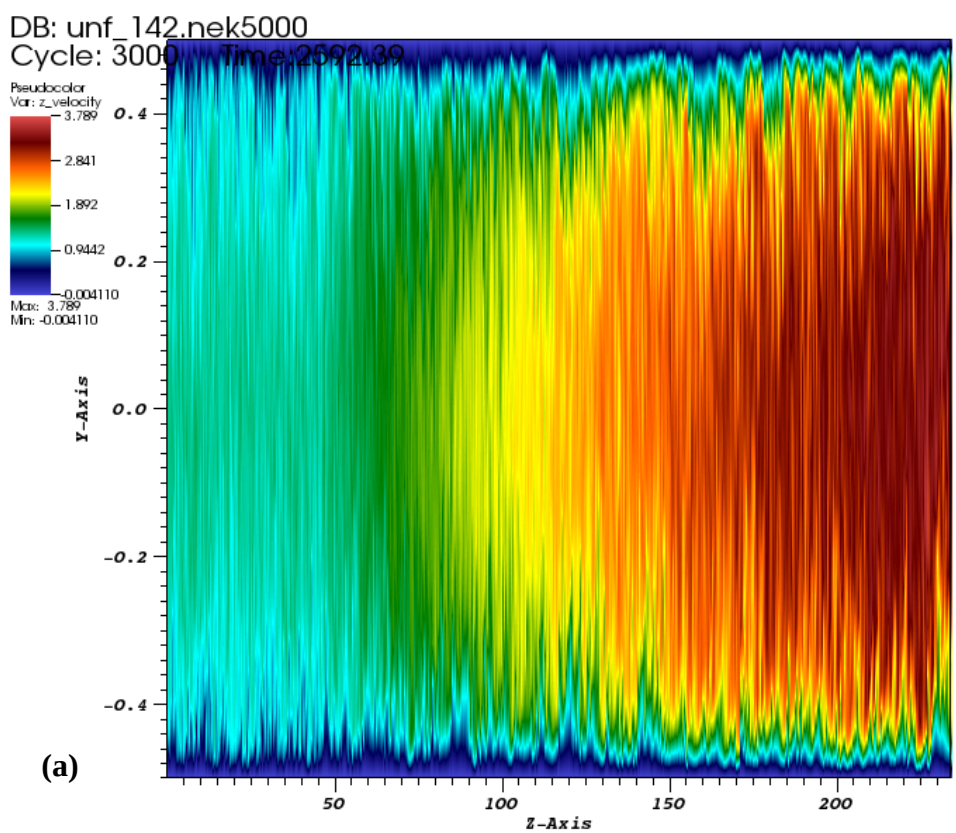

(a)

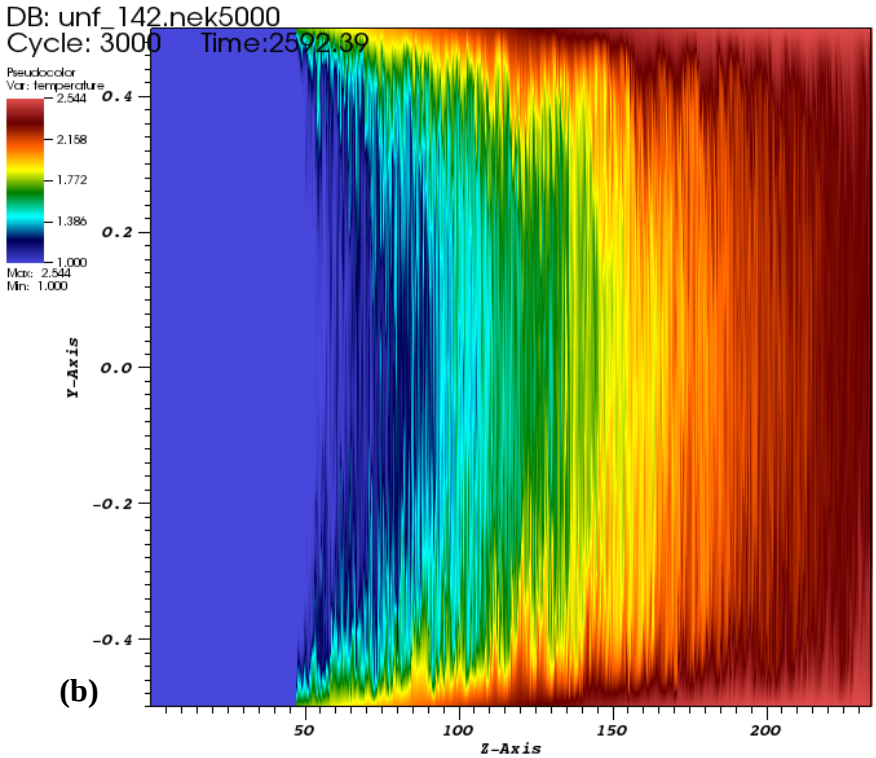

Figure 6.3 a) Axial velocity profile and b) Axial temperature profile at steady state.

Bulk Temperature Comparison

Figure 6.4 shows a comparison of the bulk temperatures obtained from the simulations and the measured values. As can be seen, there is a good match between the simulations and the experimental values.

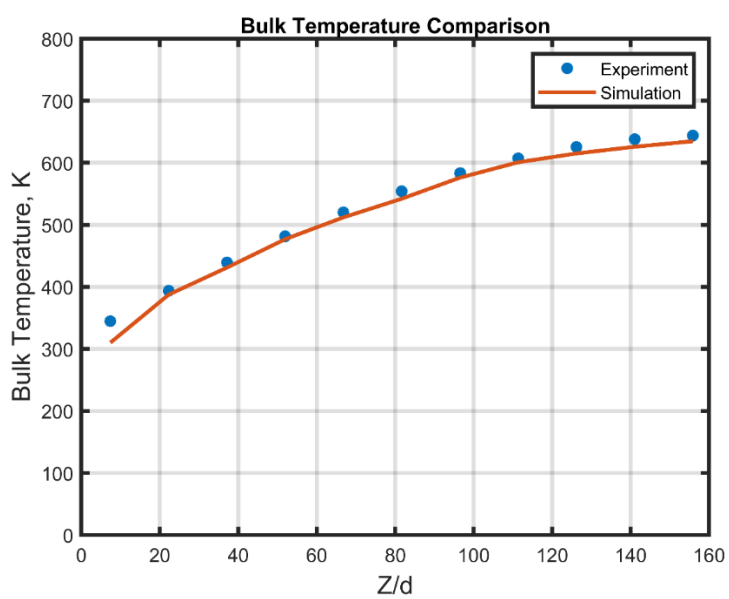

Figure 6.4 Comparison between experimental and predicted axial bulk temperatures.

Axial Velocity Profiles

Figure 6.5 shows the axial velocity profiles at different axial locations at steady state. It can clearly be seen that along the strongly heated channel, the gas becomes more heated and thus the velocity profile tends to laminarize owing to flow laminarization occurring. Figure 6.6 shows the radial cross sections of the velocities at corresponding axial locations shown in Figure 6.5. It can clearly be seen that the velocity is increasing due the gas heating as we move axially.

Several factors play crucial roles in flow laminarization. At steady state, as the fluid temperature increases, the gas viscosity (μ) and velocity (v) increase, while the gas density (ρ) decreases. Since the mass flux (ρv) remains constant, flow laminarization is a viscosity dominated phenomenon. This can lead to deterioration in the convection heat transfer which will be presented in the next section.

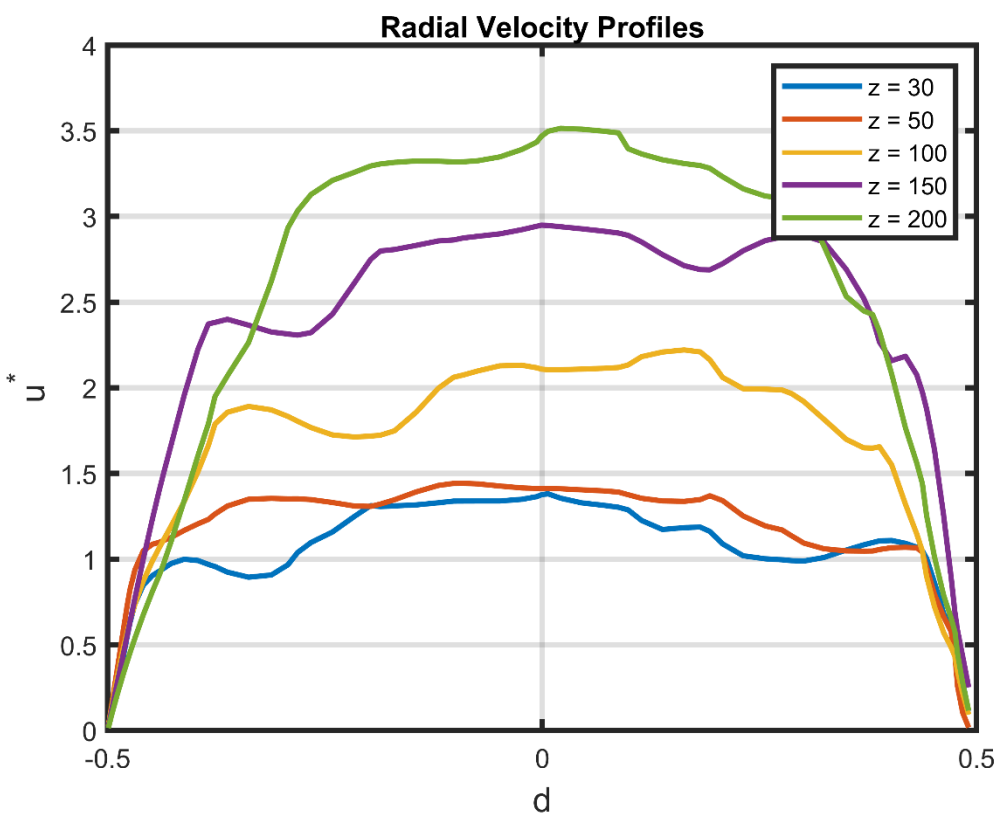

Figure 6.5 Axial velocity profiles at different axial locations: a) z =30, b) z =50, c) z =100, d) z =150, e) z =200.

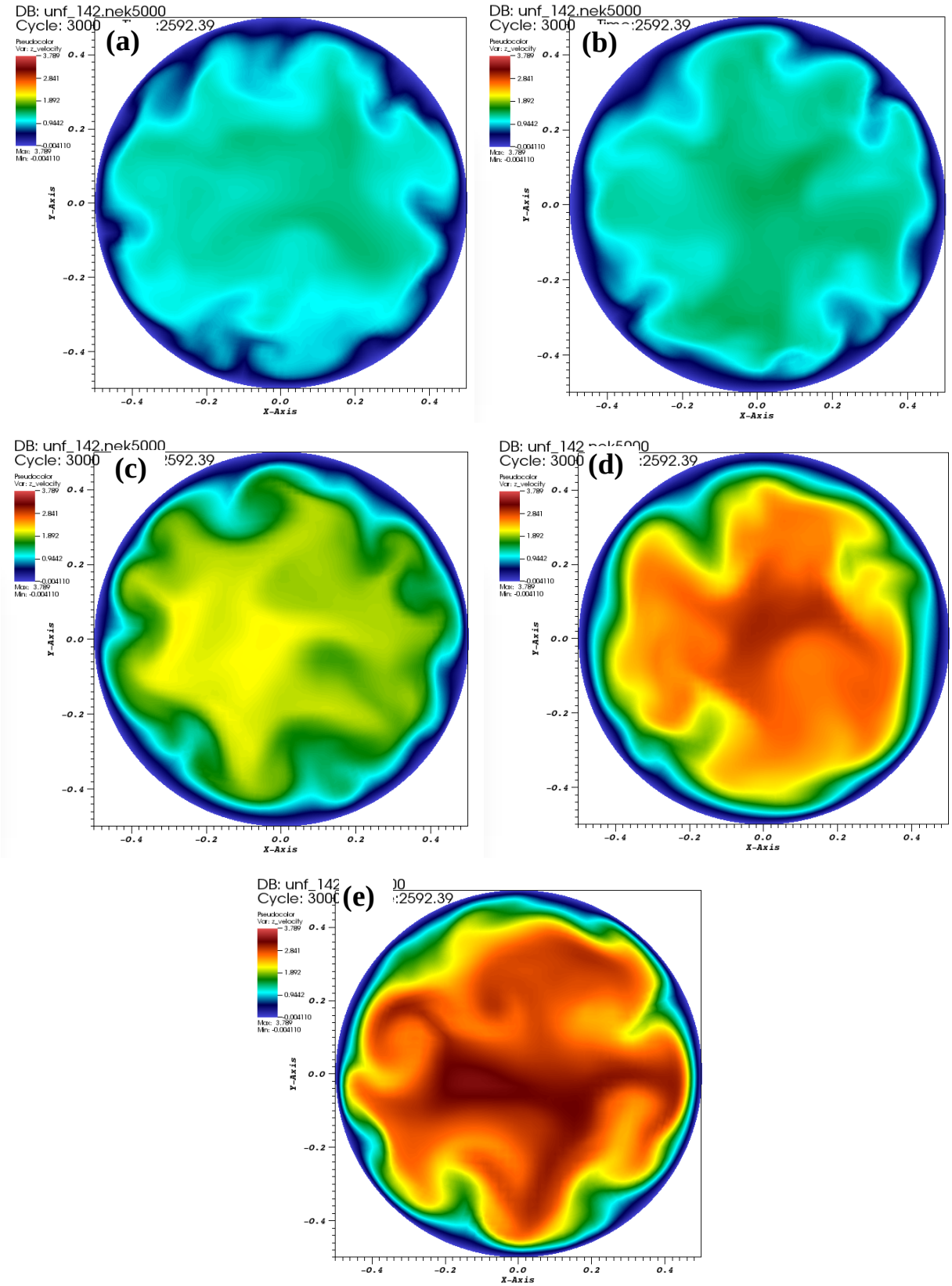

Figure 6.6 Axial velocity distributions at a) z =30, b) z =50, c) z =100, d) z =150, e) z =200.

Effect on Reynolds Number

This section discusses the impact of strong heating on local Reynolds numbers, due to gas property variations. Figure 6.7 displays significant reductions in the local Reynolds number as the gas flows through the strongly heated channel. The local Reynolds number is found to decrease by almost 35 percent thus showing the effect of strong heating on flow laminarization.

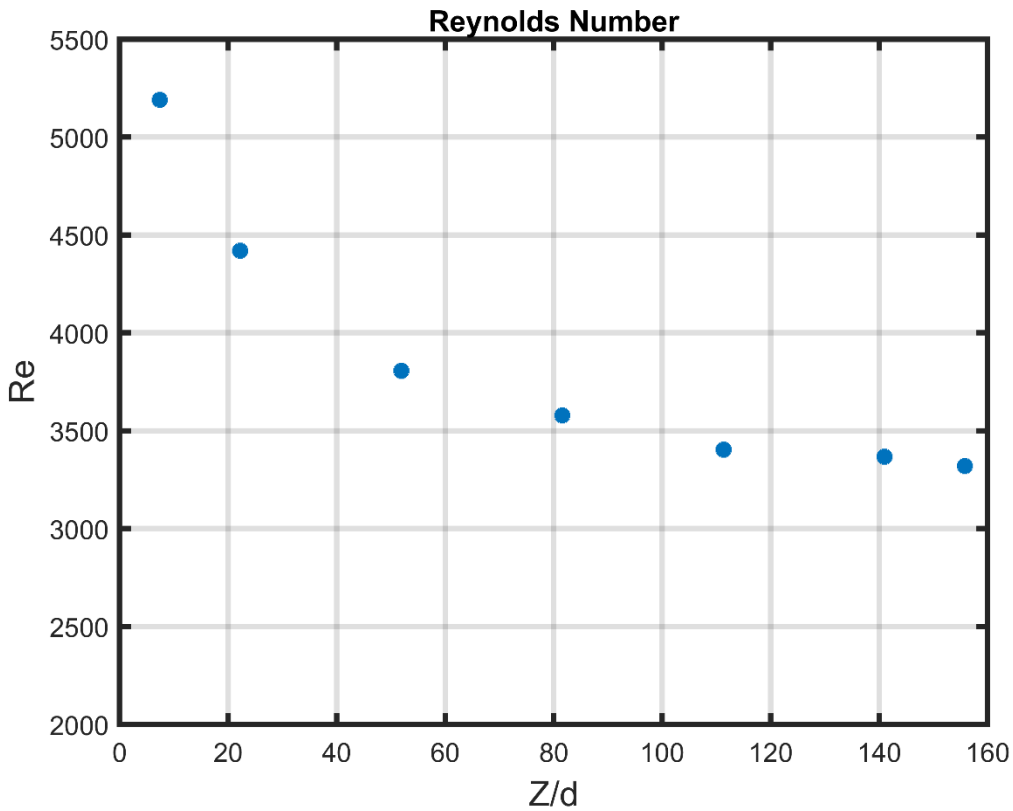

Figure 6.7 Axial variation of Reynolds number.

CHAPTER 7. VALIDATION AND VERIFICATION DATABASE

The experimental and numerical simulation data presented in this Final Report will be submitted to the Idaho National Laboratory's NGNP Data Management and Analysis System (NDMAS). They will also be made available to interested researchers upon request.

1. CCNY's Natural Circulation Experiment Data
2. CCNY's Bypass Flow Experiment Data
3. KSU's Radiation Heat Transfer and Air Ingress Experiment and Simulation Data
4. CCNY's Flow Laminarization Simulation Results

All the publications produced by the PI and Co-PIs of this NEUP project are listed below.

LIST OF PUBLICATIONS PRODUCED BY CCNY

Journal Papers

1. Valentín, F.I., Artoun, N., Anderson, R., Kawaji, M. and McEligot, D.M., 2016. Study of Convection Heat Transfer in a VHTR flow channel: Numerical and Experimental Results, Nuclear Technology, Volume 196, Number 3, pp. 661-673.

2. Valentín, F.I., Anderson, R. and Kawaji, M., 2017. Experimental Investigation of Convection Heat Transfer in High Pressure and High Temperature Gas Flows, ASME Journal of Heat Transfer, 139(9):091704-091704-12. DOI: 10.1115/1.4036524.

3. Swank, W.D., Valentin, F.I., Kawaji, M., and McEligot, D.M., 2017. Thermal conductivity of G-348 isostatic graphite, Nuclear Technology, 199(1), pp. 103-109. DOI.org/10.1080/00295450.2017.1317530

4. Gould, D., Franken, D., Bindra, H. and Kawaji, M., 2017. Transition from molecular diffusion to natural circulation mode air-ingress in high temperature helium loop, Annals of Nuclear Energy, 107, pp.103-109. DOI: 10.1016/j.anucene.2017.03.049

5. Valentin, F.I., Artoun, N., Kawaji, M. and McEligot, D.M., 2018. Forced and Mixed Convection Heat Transfer at High Pressure and High Temperature in a Graphite Flow Channel, J. Heat Transfer, 2018. doi:10.1115/1.4039585.

6. Valentin, F.I., Artoun, N. and Kawaji, M., 2018. Experimental Investigation of Flow Laminarization in a Graphite Flow Channel at High Pressure and High Temperature, J. Heat Transfer, 140 (11), 112004. doi:10.1115/1.4040786.

7. Rudra, A. Kalaga, D. and Kawaji, M., 2019. Experimental Investigation of Natural Circulation during Air Ingress Scenario in a Very High Temperature Reactor, Nuclear Science & Engineering, Vol. 193, pp. 1147–1159.

8. Rudra, A. Kalaga, D. and Kawaji, M., 2019, Quantitative Alanlysis of Mass Flow Rates during Natural Circulation in a High Temperature Gas Flow Loop, International Journal of Heat and Mass Transfer, under review.

Archival journal publications by INL

9. McEligot, D. M., X. Chu, R. S. Skifton and E. Laurien, 2018. Internal convective heat transfer to gases in the low-Reynolds-number "turbulent" range. *Int. J. Heat Mass Transfer*, 121, pp. 1118-1124.

10. Swank, W. D., F. I. Valentin, M. Kawaji and D. M. McEligot, 2017. Thermal conductivity of G-348 isostatic graphite. *Nuclear Technology*, 199, pp. 103-109.

11. McEligot, D. M., and R. W. Johnson, 2017. Bypass flow resistance in prismatic gas-cooled nuclear reactors. *J. Nuc. Eng. and Radiation Sci.*, 3, No. 1, pp. 011003-1 to 9. Available via nuclearengineering.asmedigitalcollection.asme.org/.

12. Ricco, P., E. J. Walsh, F. Brighenti and D. M. McEligot, 2016. Growth of boundary-layer streaks due to free-stream turbulence. *Int. J. Heat Fluid Flow*, 61, pp. 272-283. Available as http://dx.doi.org/10.1016/j.ijheatfluidflow.2016.05.003.

13. Chu, X., E. Laurien and D. M. McEligot, 2016. Direct numerical simulation of strongly heated air flow in a vertical pipe. *Int. J. Heat Mass Transfer*, 101, pp. 1163-1176.

Other information release

14. McEligot, D. M., J. H. Bae, X. Chu, J. Y. Yoo and E. Laurien, 2019. Some observations of proposed criteria for laminarization in heated vertical tubes. Draft journal manuscript, INL/JOU-19-54399.

15. McEligot, D. M., W. D. Swank, D. L. Cottle and F. I. Valentin, 2016. Thermal properties of G-348 graphite. Tech. report INL/EXT-16-38241, May.

Refereed Conference Papers

16. Valentín, F.I., Artoun, N., Kawaji, M., and McEligot, D.M., 2015. “Experimental study of forced convection heat transfer during upward and downward flow of helium at high pressure and high temperature,” Proc. of First Thermal and Fluids Engineering Summer Conference, New York, August 9-12, 2015.

17. Valentín, F.I., Artoun, N., Kawaji, M., and McEligot, D.M., 2015. “Investigation of helium flow laminarization at high temperatures and pressures in a graphite flow channel,” Proc. of the 1st Thermal and Fluids Engineering Summer Conference, New York, August 9-12, 2015.

18. Valentín, F.I., Artoun, N., Anderson, R. and Kawaji, M., 2015. "Study of Abnormal Heat transfer during forced and natural convection scenarios in a prismatic core of a VHTR: Numerical and Experimental Results," Proc. of 16th International Topical Meeting on Nuclear Reactor Thermal Hydraulics (Nureth-16), August 30-September 4, 2015, Chicago, IL.

19. Valentín, F.I. and Kawaji, M., 2015. "Role of radiation heat transfer in cooling of a scaled model of a prismatic graphite core in a VHTR," Proc. of International Topical Meeting on Nuclear Reactor Thermal Hydraulics (NURETH 16), Chicago, IL, August 30-September 4, 2015.

20. Kawaji, M., Rudra, A., Artoun, N., Schultz, R.R., Bindra, H. and McEligot, D.M., Experimental Investigation of Natural Circulation of a Gas Mixture during DCC in a VHTR, Proc. of ANS Winter Meeting, Las Vegas, November 6 – 10, 2016.

21. Valentin, F.I., Artoun, N. & Kawaji, M., 2017. Experimental investigation of flow laminarization in a graphite flow channel at high pressure and high temperature. Paper HT2017-4818 in Proc. of ASME 2017 Summer Heat Transfer Conference, July 9-14, 2017, Bellevue, Washington.

22. Rudra, A. V., D. V. Kalaga, N. Artoun and M. Kawaji, 2017. Experimental investigation of natural circulation during air ingress scenario in a VHTR. ANS Winter Meeting, Trans. ANS, 117, pp. 1623-1625.

23. Valentín, F.I., Artoun, N. and Kawaji, M. 2017. Study of Abnormal Heat Transfer during Natural Circulation Scenarios in a Prismatic Core of a VHTR: Numerical and Experimental Results, Proc. of the 17th International Topical Meeting on Nuclear Reactor Thermal Hydraulics (NURETH-17), Xi'an, China, September 3 - 8, 2017.

<u>Publications by Kansas State University</u>

Journal papers

24. Daniel Franken, Daniel Gould, Prashant Jain, Hitesh Bindra 'Transition from molecular diffusion to natural circulation mode air-ingress in high temperature helium loop', Annals of Nuclear Energy, 111, 2018.

25. Daniel Gould, Hitesh Bindra, Sanjoy Das 'Thermal response construction in randomly packed solids with graph theoretic Support Vector Regression', International Journal of Heat and Mass Transfer, 115, 2017.

26. Daniel Gould, Daniel Franken, Hitesh Bindra, Masahiro Kawaji 'Transition from molecular diffusion to natural circulation mode air-ingress in high temperature helium loop', Annals of Nuclear Energy, 107, 2017.

Peer Reviewed Conference Proceedings

27. Connor Medlen, Hitesh Bindra, Oxidation Effects of Air and Steam Ingress on Material Properties of Graphite in HTGRs, Transactions of American Nuclear Society, Washington D.C., (November 2019), Vol. 121.

28. Dan Gould, Molly Ross, Hitesh Bindra, Discrete element modeling of conduction cool down in pebble bed reactors under loss of forced convection, NURETH-18, Portland OR, August 2019.

29. Daniel Gould, Hitesh Bindra, Effect of Upper Head Leak on the Onset of Natural Convection in HTGRs, Transactions of American Nuclear Society, Washington D.C., USA (October 2017), Vol. 117.

30. Daniel Franken, Daniel Gould, Hitesh Bindra, Numerical Model of a High Temperature Helium Air-Ingress Experiment, Transactions of American Nuclear Society, Washington D.C., USA (October 2017), Vol. 117.

31. Daniel Gould, Hitesh Bindra, Mixed effects associated with air ingress in graphite channels, Transactions of American Nuclear Society, Las Vegas, NV, USA (November 2016), Vol. 115).

32. Daniel Gould, Eric Schlaikjier, Hanwen Liu, Hitesh Bindra, Air ingress experiments within high temperature graphite flow channels, Proceedings of International Conference in Nuclear Engineering, Charlotte, NC, USA (2016) V005T15A056. (Dan Gould also won an award for this presentation).

Conference Abstracts

33. Daniel Gould, Abhinav Gairola, Hitesh Bindra, Analyzing air-ingress currents in Gas-cooled nuclear reactors using Kramers Moyal expansion, Bulletin of the American Physical Society, Atlanta, GA, USA (2018).

APPENDIX 1

CCNY – High Pressure/High Temperature Test Facility

(Last updated on 16th August, 2019)

Prepared by

Dinesh V. Kalaga, Apoorva V. Rudra and Masahiro Kawaji

City College of New York

Table of Contents

1. Natural Circulation Flow Loop 157

1.1. Test facility 157

1.2. Experimental procedure 158

1.3. Internal volume of the flow loop 163

1.4. Mass flow measurement device 164

1.5. Pressure vessel 165

1.6. Graphite test section 166

1.7. Thermal insulation 167

2. Instrumentation for Natural Circulation Test Facility 168

2.1. Pressure measurement 168

2.2. Temperature measurement 170

2.2.1. Gas temperature 170

2.2.2. Graphite temperature 170

2.3. Helium analyzer 172

2.4. Heater rods and power control 174

2.5. Data acquisition system 176

3. Forced Circulation Bypass Flow Loop 176

3.1. Test facility 176

3.2. Experimental procedure 178

3.3. Internal volume of the bypass flow loop 186

3.4. Mass flow measurement device 186

3.5. Pressure vessel 187

3.6. Graphite test section 188

3.7. Thermal insulation 190

3.8. High pressure compressor 191

4. Instrumentation for Forced Circulation Bypass Flow Test Facility 193

4.1. Pressure measurement 193

4.2. Temperature measurement 195

4.2.1. Gas temperature 195

4.2.2. Graphite temperature 196

4.3 Heater rods and power control 197

4.4. Data acquisition system 199

1. Natural Circulation Flow Loop

Two different high pressure/high temperature test facilities have been constructed to obtain the fluid dynamic and heater transfer parameters pertinent to natural and forced gas circulation in a Very High Temperature Reactor (VHTR). For natural circulation experiments in VHTR, pure helium, pure nitrogen and mixtures of helium and nitrogen gases were used as a working fluid. For forced circulation experiments in VHTR with a by-pass flow channel, pure nitrogen gas was used as the working fluid.

1.1. Test facility

The photograph of the experimental set-up can be seen in Figure 1A. The schematics of the natural circulation test facilities can be found in Figure 1B and Figure 1C. The facility was mainly comprised of a stainless steel (SS-304) pressure vessel which simulates the hot fuel zone (riser or hot vessel (HV)), and a downcomer (cold vessel). The pressure vessel was rated at 70 bar/923 K and has ANSI Class 900 flanges welded at the top and bottom. The hot vessel housed a 2.7 m long graphite column with a 108mm outer diameter. The graphite column had four 2.3 kW heaters symmetrically placed around a central coolant channel of 16.8 mm diameter as shown in the cross-sectional view of the graphite column (Figure 2). The space between the graphite surface and the inner wall of the hot vessel was covered with a thick fiberglass thermal insulation layer to protect its wall from the high graphite temperatures and to reduce heat losses. A stainless-steel cylindrical chamber with a 7.0 cm diameter and 17.0 cm height was fabricated to simulate the lower plenum of a VHTR. A photograph of the lower plenum and the gas sampling system is shown in Figure 3. A stainless-steel tube of 14.5 mm inner diameter was used to connect the top of the riser and the lower plenum as a downcomer simulating the cooler reflector zone in the VHTR core. The temperatures in the graphite were measured using 40 thermocouples imbedded at ten axial locations 25 cm apart (please refer to Section 2.2). Each plane had four thermocouples at different radial and azimuthal locations. The flow channels in the riser and the downcomer were connected by stainless steel tubes at the bottom and top. A three-way valve connected a vacuum pump and nitrogen gas cylinder to the bottom of the downcomer. The vacuum pump was used to completely flush out the gases from the system before filling the system with helium initially. A pressure transducer was installed on the inlet piping connected to the pressure vessel for continuous monitoring of the system pressure. The thermocouples and pressure transducer were

connected to a National Instruments data acquisition system for continuous monitoring and data acquisition via a LabVIEW program.

1.2. Experimental procedure

Prior to the actual experiments, the test facility was vacuumed twice to near vacuum and filled with helium to an initial pressure of 103.4 kPa. Then, nitrogen was slowly injected into the lower plenum of the riser until the system pressure rose to required values. The gas mixture was allowed to settle for at least 10 minutes so heavier nitrogen would occupy the lowest part of the flow loop including the lower plenum. It should be noted that a certain amount of nitrogen occupied some parts of the riser volume in addition to the lower plenum consisting of a cylindrical section and the lower horizontal tube connecting the riser and downcomer (Figure 1) before each experiment was started. Since the lower plenum was not isolated from the riser and it took 1-2 hours before the graphite temperatures in the riser rose and reached steady state, some nitrogen gas slowly diffused up into the upper plenum. So, placing another valve between the lower plenum and riser inlet would have prevented this initial diffusion of nitrogen into the upper plenum, but there was limited space available for any valve installation. The valve (10) connecting the riser and downcomer at the bottom was then closed completely isolating the riser from the downcomer by not allowing any coolant circulation. The electric heater rods in the riser were turned on and the mean temperature of the riser was increased to a desired value. After the steady temperature profiles were reached in the heated riser test section, the valve (10) was opened to initiate natural circulation flow of a helium-nitrogen mixture through the riser and downcomer. Immediately after the opening of the valve (10), the helium-nitrogen mixture began flowing upward in the hot riser and downward in the cold downcomer due to the density difference arising from the temperature difference between the riser and downcomer. Since the downcomer was unheated, the coolant temperature in the downcomer decreased from the upper plenum to the lower plenum. Natural circulation experiments have been conducted in a helium filled flow loop after the injection of nitrogen into the lower plenum. Experiments have also been performed with single gases (pure helium and pure nitrogen) and binary gas mixtures (helium-nitrogen) to better understand the effect of nitrogen transport on natural circulation of helium during the air ingress scenario. An in-house mass flow measurement device was designed and used to measure the total gas circulation rates (mass flow rates) at steady state.

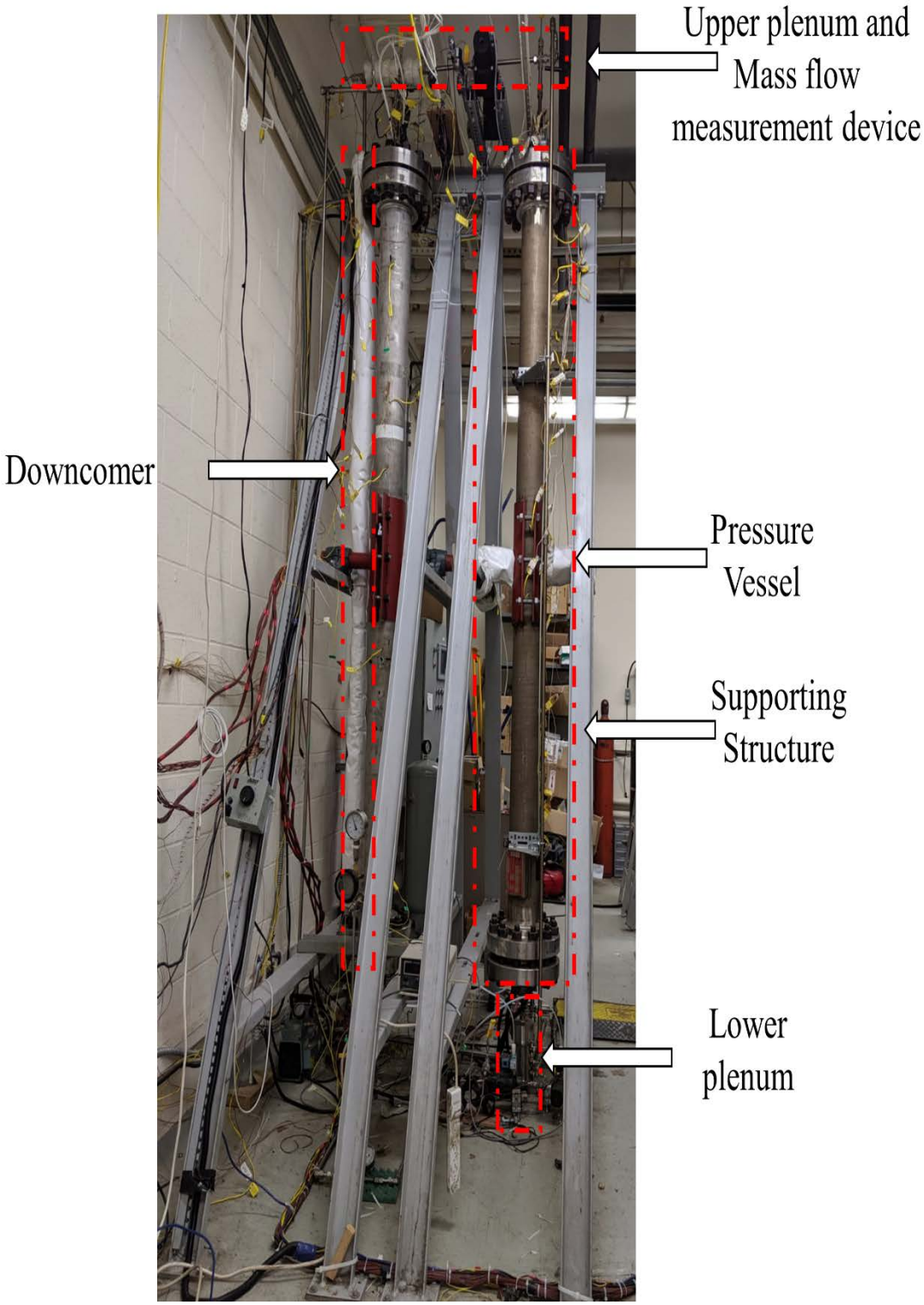

Figure 1A: Photograph of the Natural circulation test facility constructed at CCNY.

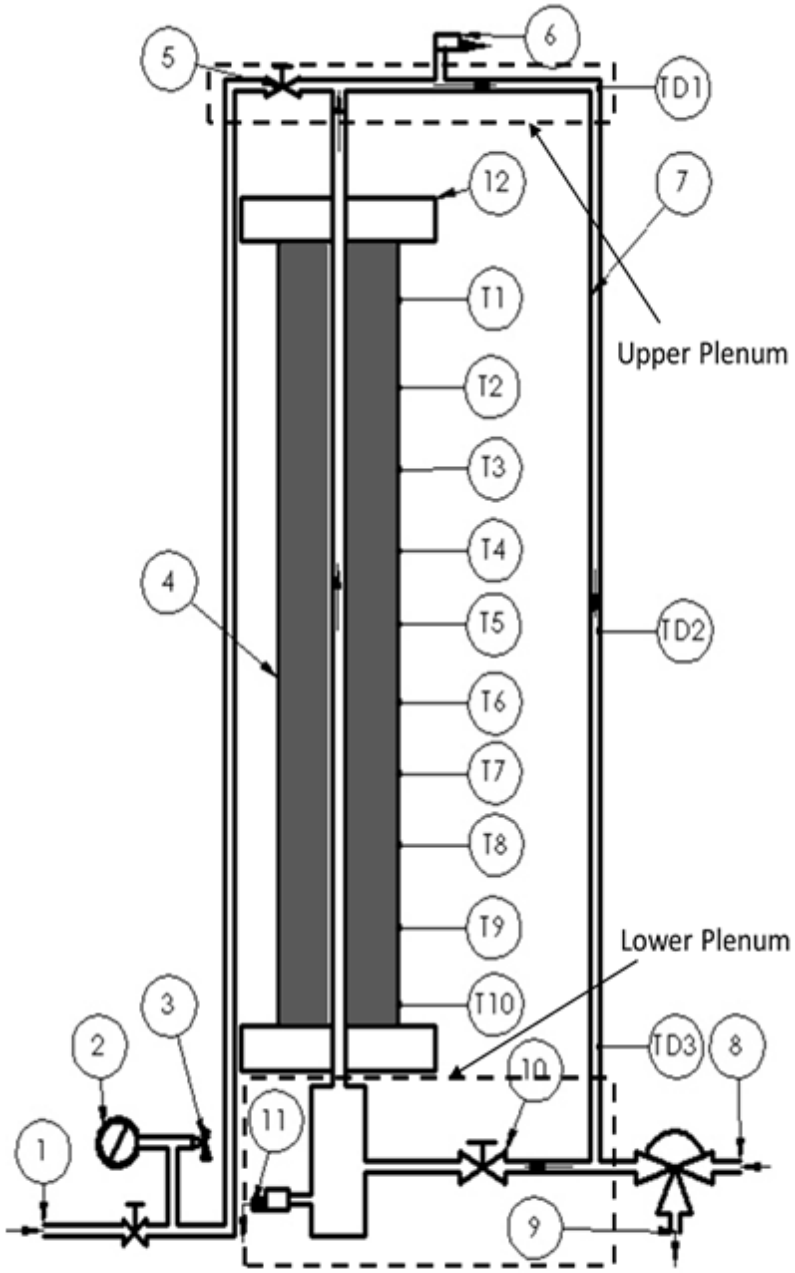

Figure 1B: Schematic of Natural Circulation Experimental Set-up. **Legend: (**1). Helium Injection, (2). Pressure gauge, (3). Pressure relief valve, (4). Hot Vessel (riser) containing a graphite column, (5). Helium injection line, (6). Upper plenum sampling port, (7). Cold Vessel Downcomer, (8). Nitrogen Injection, (9). vacuum pump line, (10). Needle valve, (11). Lower plenum sampling port, (12). Vessel flange, **T1-T10:** Thermocouples attached to the graphite column in the riser, **TD1-TD3:** Thermocouples attached to the downcomer tube inner wall.

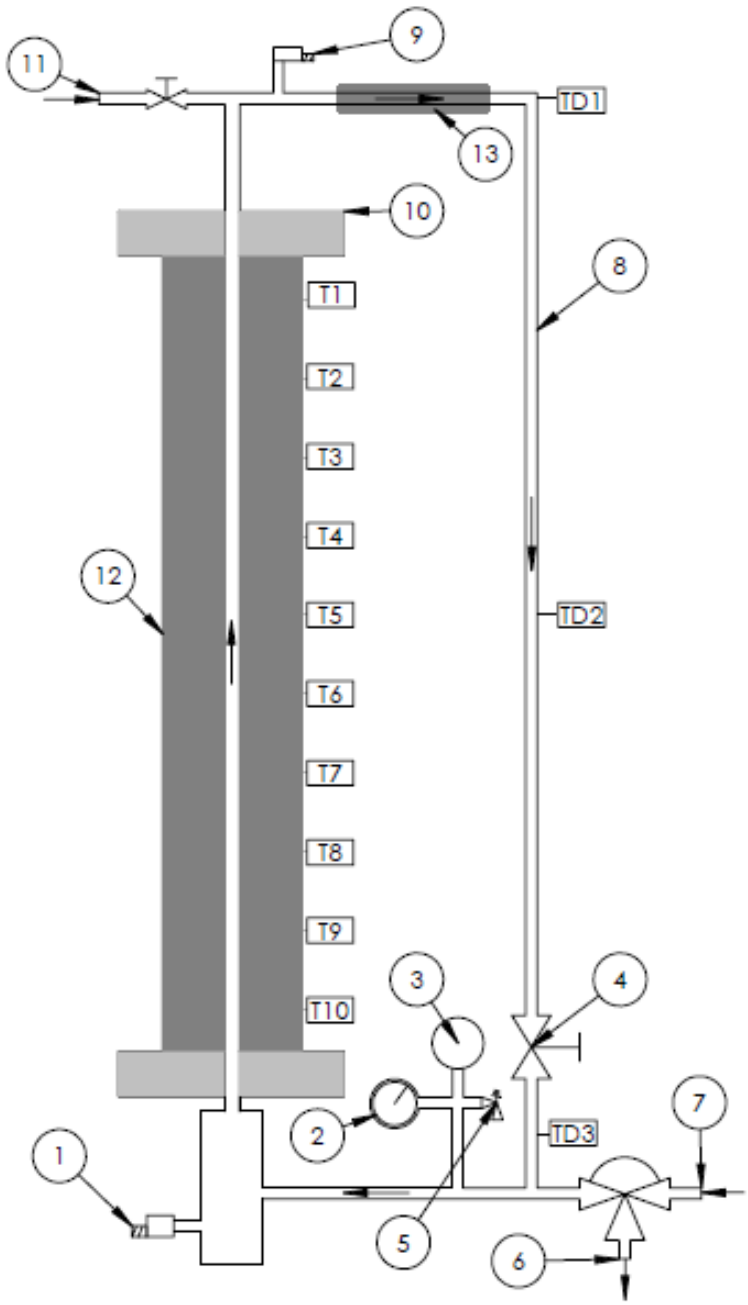

Figure 1C: Schematic of modified natural circulation experimental test facility. **LEGEND:** 1. Lower plenum sampling port, 2. Pressure gauge, 3. Pressure Transducer, 4. Needle valve, 5. Pressure relief valve 6. vacuum pump line, 7. Nitrogen Injection 8. Cold Vessel Downcomer, 9. Upper plenum sampling port, 10. Vessel flange, 11. Helium Injection, 12. Hot Vessel (riser) containing a graphite column, 13. Mass flow measurement device, T1-T10: Thermocouples attached to the graphite column in the riser, TD1-TD3: Thermocouples attached to the downcomer tube inner wall.

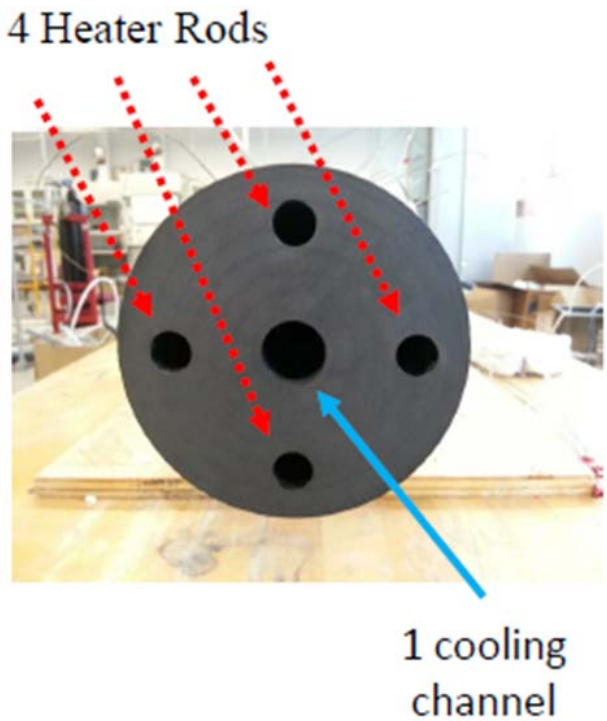

Figure 2. Photograph showing the circular flow channel and holes for four heater rods.

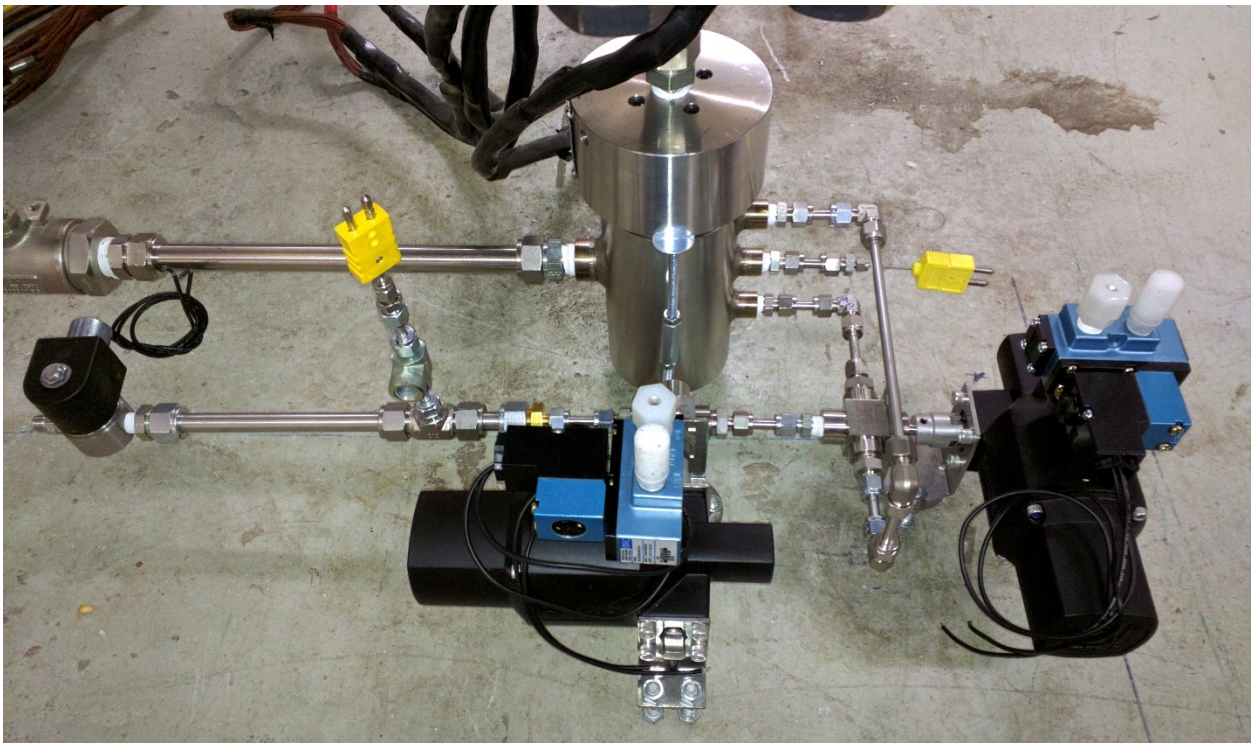

Figure 3. Photograph of the gas sampling system in the lower plenum

1.3. Internal volume of the flow loop

The detailed dimensions of the components such as graphite flow channel, downcomer pipe and the connecting pipes in the upper and lower plena of the test facility are tabulated in Table 1. The total internal volume of the flow loop is found to be 2.34 Liters. This information is useful for performing the scaling analysis and computational fluid dynamic modelling.

Table 1. Detailed dimensions of the Natural Circulation Test Facility

		Length (mm)	**Volume (mm^3)**
Hot riser	Graphite flow channel ID	16.8	6.08E+05
	Height of the graphite flow channel	2745	
UP	Vertical pipe above the Graphite ID	14.5	9.24E+04
	Height of vertical pipe above the Graphite	560	
UP	Horizantal pipe upper plenum ID	14.5	1.63E+05
	length of horizantal pipe upper plenum	990	
Downcomer	Dwoncomer ID	14.5	6.14E+05
	Downcomer Height	3720	
LP	Horizantal pipe lower plenum ID	14.5	1.58E+05
	Length horizantal pipe lower plenum	960	
LP	Lower plenum Chamber ID	70	6.54E+05
	Lower plenum Chamber Height	170	
LP	Vertical pipe below the Graphite	14.5	5.20E+04
	Ht vertical pipe below the Graphite	315	
		Total volume of the loop (mm^3)	**2.34E+06**
		Total volume of the loop (Lits.)	**2.34E+00**

1.4. Mass flow measurement device

A mass flow rate measurement device was designed, constructed and installed in the upper plenum in order to measure the gas circulation rate. The schematic view of this device is shown in Figure 4. This device consisted of two 50 W heating tapes [Chromalox, 121620] powered by a 24V DC source, that were connected in parallel and wrapped around the tube at the top (upper plenum). This tube connected the outlet of the hot riser and inlet of downcomer, and was also insulated on the outer surface to minimize heat losses. A thermocouple was also installed at the insulation surface to measure the temperature difference between the insulation surface and ambient temperature in order to further corroborate any heat loss values (see Figure 4). By adjusting the voltage and current on the power supply, the heater's power was adjusted in the mass flow measurement system to a desired value. Figure 5 shows the locations of the four thermocouples inserted into the tube to measure the gas temperatures before and after the heated section (see Figure 5). In order to determine the mass flow rate, a gas phase heat balance was performed across the mass flow measuring device.

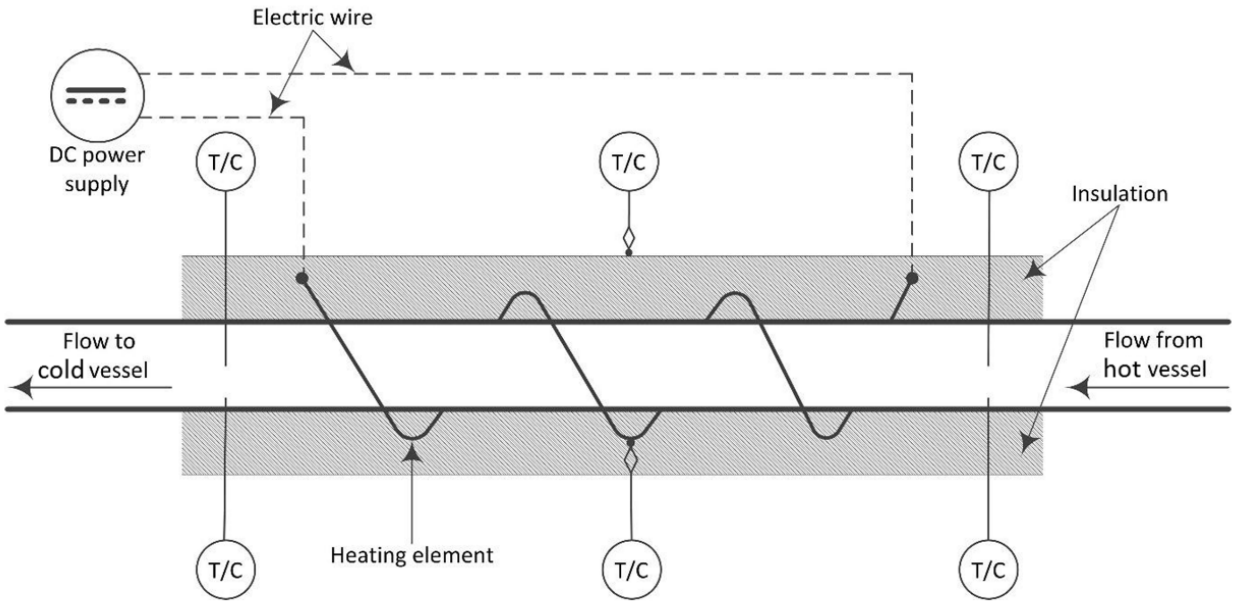

Figure 4. Schematic of the mass flow measurement device

Figure 5. Radially fixed thermocouples to measure the gas temperature near the wall and the center of tube inside the mass flow measurement device

Since an AC heating element may have fluctuations, a DC heating element was chosen for a constant output power. Specifications of the heating element is shown in Table 2.

Table 2. Specifications of the Heating Element

Manufacturer	Length	Max Voltage	Max Current	Max Output Power
Chromelox	10 in	24V DC	2.1 Amps	50 Watts

A DC power supply with an adjustable voltage and current was used to supply power to the heater. By adjusting the voltage and current on the DC power supply, the heater's output power was adjusted to a desired value. The heating tapes were insulated on the outer surface using soft insulation to minimize the heat loss to the ambient. To obtain the bulk gas temperatures with a higher precision, the gas temperatures were measured close to the tube wall in addition to the center of the pipe.

1.5. Pressure vessel

The graphite test section was housed in a stainless steel 304 pressure vessel (PV), which was ASME certified at 1,015 psi (69 bar) at a temperature of 350°C, and had ANSI Class 900

flanges welded at the top and bottom. A photograph of the PV installed inside a supporting frame is shown in Figure 1A and the detailed dimensions of the PV are listed in Table 3. Since the maximum gas and graphite temperatures could reach 600°C, a 19.2 mm (0.756”) thick layer of thermal insulation with low thermal conductivity was placed around the graphite test section surface to keep the PV inner wall temperature below 300 ^{o}C.

Table 3. Pressure Vessel Specifications

Material	Stainless Steel 304	
Length	2,826 mm	111.3”
Inner Diameter	146.3 mm	5.76”
Outer Diameter	168.3 mm	6-5/8”
Wall Thickness	11.0 mm	0.432”
Flanges	ANSI Class 900	
Flange thickness	55.6 mm	2.19”

1.6. Graphite test section

The graphite test section was a 108.0 mm (4.25”) diameter cylindrical column made of thermally isotropic graphite G348, and consisted of two 1,384.3 mm (54.5”) long sections joined in the middle with a 25.4 mm (1.0”) overlap, so the total test section length was 2,743 mm (108.0”). The dimensions and specifications of the graphite test section are summarized in Tables 4 and 5. The test section had a flow channel with a diameter of 16.8 mm along the central axis and four smaller holes in which 12.7 mm diameter heater rods were inserted (refer Figure 2). All four heater rods were 3,048 mm (120”) long and penetrated through the guide tubes welded on the top flange. The top 300 mm (12”) section of each heater rod was not generating heat, so that the part above the graphite test section as well as the guiding tubes on the top flange remained unheated.

Table 4. Dimensions of the graphite test section

Material	Graphite G348	
Length	2,743 mm	108.0” (2 x 54.5”)
Outer Diameter	108.0 mm	4.25”
Flow Channel Diameter	16.8 mm	0.66”
Heater Channel Diameter	12.7 mm	0.5”

Table 5. Specifications of the graphite material

Model	Composition	Density (g/cm^3)	Resistivity (μΩ-cm)	Young's Modulus (GPa)	Flexural strength (MPa)	Hardness (Shore)	Coefficient of thermal expansion ($10^{-6}/^oC$)	Thermal conductivity (W/mK)
G348	99.99% fixed carbon	1.92	1300	12.3	63.7	68	5.5	128

1.7. Thermal insulation

The graphite test section was covered with a layer of soft thermal insulation which was easy to install. Five stainless steel, ring shaped supports were used to keep the graphite fixed in the center of the pressure vessel. The physical properties of the insulation are shown in Table 6. A layer of thermal insulation was also placed at the top and bottom of the graphite test section to reduce heat conduction to the top and bottom flanges of the PV, in order to prevent the flanges from being heated up to above 350°C. Stainless steel support assemblies were provided to support the graphite test section above the bottom flange and below the top flange. A stainless-steel ring was also attached to the mid-section of the graphite test section to support the soft insulation.

Table 6. Properties of soft insulation material

Classification Temperature (ºC)		648
Service Temperature (ºC)		648
Density (kg/m^3)		160
Organic Content (Wt%)		0
Linear Shrinkage (24 hrs@ Temperature, "+" indicates growth)		4.8% @ 22ºC
Chemical Composition		Fiber glass
Thermal Conductivity (W/mK)	200ºC	0.05
	315ºC	0.07
	400ºC	0.08

2. Instrumentation for the Natural Circulation Test Facility

2.1. Pressure measurement

Three Omega pressure transducers and a digital pressure gauge (General Electric model DPI-104) were installed in the natural circulation test facility. One pressure transducer (PX303-100A5V) and digital pressure gauge were used to measure the reactor pressure. The calibrated digital pressure gauge is installed to get a quick pressure reading while filing and vacuuming the reactor. The digital pressure gauge was also used for verifying the calibration of the Omega pressure transducers. The other two pressure transducers (Omega: PX303-1KG5V) were installed in the gas sampling line, one in the upper plenum and the other in the lower plenum. Since the working temperature for the pressure transducers used were lower than 50ºC, a 2-foot-long stainless-steel tube was used between each pressure transducer and the inlet or outlet piping. This way, the stagnant gas in the 2-ft long tube was cooled enough that the pressure transducer was not exposed to a hot gas. The specifications of the pressure transducers and pressure gauges are given in Table 7.

Table 7. Specifications of the pressure transducers

General Electric	Model	Range (psi)	Type	Resolution (psi)	Max Working Pressure (psi)
	DruckDPI-104	$0-3000$	Sealed Gauge	0.1	3190
	Accuracy	0.05% FS including non-linearity, hysteresis, repeatability and temperature effects from $-10℃$ to $50℃$			
	Burst Pressure	Burst pressure is $2x$ working pressure			
	Selectable Pressure Units	$kPa, MPa, \frac{kg}{cm^2}, psi, mbar, bar, inHg, inH_2O, mH_2O, mmH_2O, mmH$			
Omega	Model	Range (psi)	Type	Resolution (psi)	Max Working Pressure (psi)
	PX303-100A5V	$0-100$	Sealed Gauge	2.5	200
	Accuracy	$0.25\%\ FS$ including non-linearity, hysteresis, repeatability and temperature effects.			
	Burst Pressure	Burst pressure is $2x$ working pressure.			
	Selectable Pressure Units	$kPa, MPa, \frac{kg}{cm^2}, psi, mbar, bar, inHg, inH_2O, mH_2O, mmH_2O, mmH$			
Omega	Model	Range (psi)	Type	Resolution (psi)	Max Working Pressure (psi)

	PX303-1KG5V	$0-1000$	Sealed Gauge	2.5	2000
	Accuracy	$0.25\%\ FS$ including non-linearity, hysteresis, repeatability and temperature effects.			
	Burst Pressure	Burst pressure is $2x$ working pressure.			
	Selectable Pressure Units	$kPa, MPa, \frac{kg}{cm^2}, psi, mbar, bar, inHg, inH_2O, mH_2O, mmH_2O, mmH$			

2.2. Temperature measurement

2.2.1. Gas temperature

The bulk gas temperatures inside the natural circulation flow loop were measured using type-K thermocouples. Two thermocouples were installed below and above the hot graphite channel to measure the gas temperature entering and exiting the hot vessel. The temperature data is very crucial to performing a heat balance along the graphite flow channel. Three thermocouples were installed at three different axial locations in the downcomer to measure the drop-in gas temperature. As mentioned before, two thermocouples were each installed one before and the other after the mass flow meter.

2.2.2. Graphite temperature

To measure the axial and radial temperatures in the graphite test section, a total of 48 type-K thermocouples were inserted into the pressure vessel. A total of 40 thermocouples were embedded in the graphite column at 10 axial locations. At each axial location, four thermocouples were installed at four azimuthal positions and at different radial locations as shown in Figure 6. The thermocouple A was inserted to a depth of 11 mm, B and D were inserted to a depth of 32.9 mm and closest to the flow channel, and C was at an intermediate depth (21.9 mm) as shown.

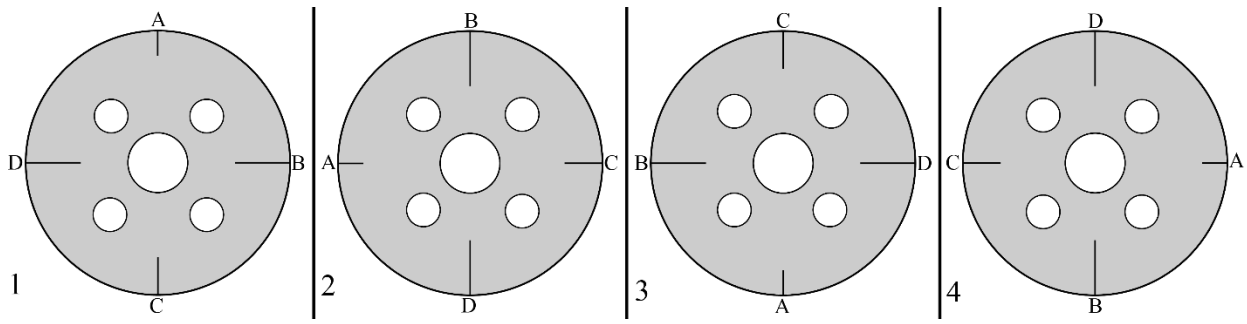

Thermocouple	A	B	C	D
Depth (mm)	11.0	32.9	21.9	32.9

Figure 6. Schematic of the thermocouple locations and their depths.

All 48 thermocouples were grouped into four bundles and each bundle had two spare thermocouples which could be used to replace any damaged thermocouples. The four thermocouple bundles were passed through a specially designed stainless-steel plate (shown in Figure 7) that also had the gas inlet pipe welded in the middle. This plate was rated to withstand a pressure of 1,015 psi at 650ºC, sealed with a gasket at the bottom flange. The thermocouple bundles and plate constituted the thermocouple assembly. As shown in Figure 1, 12 thermocouples were installed on the outer surface of the PV to measure the temperature of the hot vessel (riser) wall at six axial levels.

Figure 7. Thermocouple plate to pass four bundles of 12 sheathed thermocouple wires

2.3. Helium analyzer

The volumetric concentrations of helium and nitrogen were recorded with the help of helium analyzers (Divesoft-M12) which were connected to the upper and lower plena through gas sampling ports (6) and (11) shown in Figure 1B. A photograph of the helium analyzer is shown in the Figure 8 and the specifications can be found in table 8. A small volume of gas was sampled from each port for 30 seconds at certain time intervals and passed through a needle valve to reduce the pressure before flowing through the helium analyzer and being discharged to the atmosphere. The volumetric helium concentration in the gas sample was determined with the help of an electrochemical sensor in the helium analyzer which gave an output voltage proportional to the helium concentration in the gas mixture. For a greater accuracy of the measurement, a two-point calibration was performed with pure helium and nitrogen. The helium analyzer measured the speed of sound in the gas mixture which depends on the gas temperature and concentrations of helium and nitrogen, but little on the gas pressure. The speed of sound can be described in the mixture by a non-linear function of the helium and nitrogen concentrations as well as the temperature of the gas mixture.

Table: 8 Specifications of the Helium Analyzer

Dimensions of the analyzer	82 x 200 x 37 mm (3 1/4 x 7 7/8 x 1 1/2 inches)
Weight	720 g (1.6 lb)
Range of measuring the concentration of oxygen	0 to 100 %
Range of measuring the concentration of helium	0 to 100 %
Measuring temperature	0 to +40° C (32 – 104° F)
Mixture pressure	Consistent with ambient pressure, in the range of 700–1100 millibars (20–32 inches of Hg) which corresponds to the standard atmosphere at an elevation in the range of 0 to 3000 m (0–10000 feet) above sea level.

Rated gas throughput	0.2 L/min
Basis of measuring the speed of sound	800 mm
Measuring frequency	2 kHz
Oxygen sensor	Teledyne R-17D or compatible
Power source	9V alkaline battery, type 6F22 or 12V adapter DC.

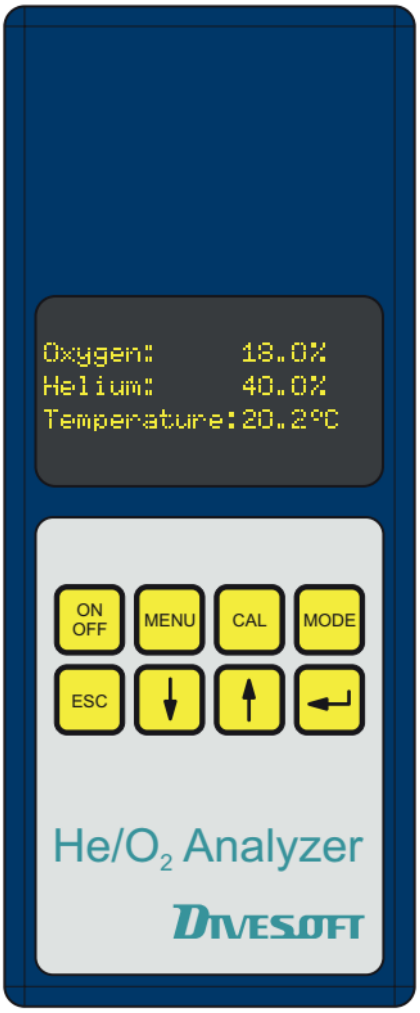

Figure 8. Photograph of the Helium analyzer.

2.4. Heater rods and power control

The graphite column in the riser of the natural circulation flow loop was heated by four 3 m (120”) long electric heater rods with an internal thermocouple to monitor the temperature of the heater rod and prevent overheating. This temperature data was used to calculate the power required to heat the graphite. Further details of the specifications are given in Table 9.

Table 9. Specifications of heater rods

Diameter (in)	Length (in)	AC Voltage (V)	Power (W)	Thermocouple
0.496 + /- 0.002	120 +/- 2.5	240	2,300	type K

Each heater rod was connected to an AC power source through a controller, a 0-240 V variac, and circuit breaker as shown in Figures 9-11, so that the heater power could be individually controlled and recorded by a data acquisition system. Each heater rod was equipped with a thermocouple to monitor the heater rod temperature which was displayed in a controller panel (Figure 10). The controller was set to shut off the AC heater power when the heater rod temperature exceeded a set point temperature. The four variacs and circuit breakers were located in the control room (Figure 10-11) which was separated from the gas flow loop by a concrete wall for safety. When the test section was pressurized and heated up, the operators could control the heater power without going into the lab where the gas flow loop was located.

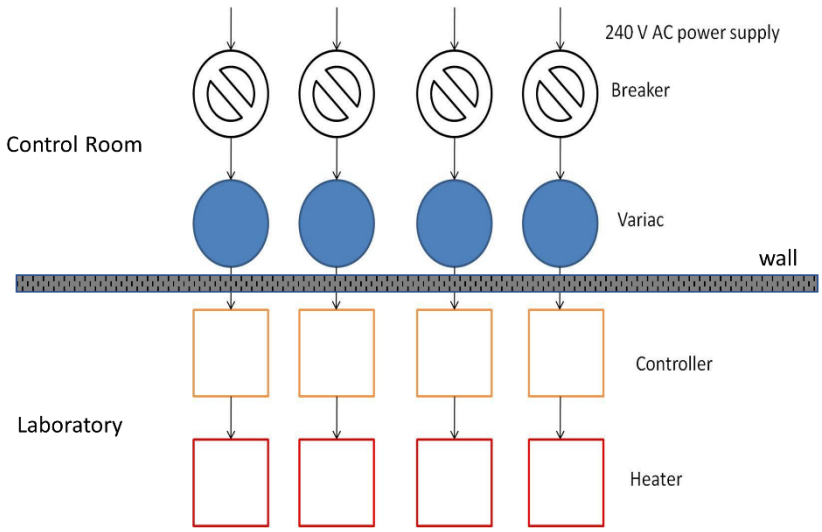

Figure 9. Schematic of electric heater power control

Figure 10. Heater rod power control panel on the left and thermocouple connector panel on the right.

Figure 11. Four variacs for individual heater power control and a 240 V AC circuit breaker panel.

2.5. Data acquisition system

A National Instruments Data Acquisition System (Model cDAQ-9188) was used with four 16 channel thermocouple modules (Model NI 9213) and one analog voltage input module (NI 9205). All the thermocouples, pressure transducer and flow meter cables were connected to the DAQ input modules in an electrical box as shown on the right-hand side in Figure 10. A PC-based DAQ system is shown in Figure 12. The data acquisition PC was a 64-bit system with an Intel Pentium CPU G2020 Windows 8 running at 2.90 GHz, and had an internal memory of 4 GB (3.88 GB usable).

Figure 12. A Data Acquisition System running LabVIEW software

3. Forced Circulation Bypass Flow Loop

3.1. Test facility

A high temperature and high pressure forced circulation bypass flow test facility has been constructed and it is rated for the maximum pressure and temperature of 68 bar (1000 psi) and 800^0C respectively. The components of the forced circulation test facility include a pressure vessel, graphite test section with a rectangular bypass flow channel, high pressure compressor, coil heat exchanger, and thermocouple assembly, as shown in Figures 13 and 14. Figure 13A shows the photograph of the bypass flow test section and the process flow diagram of the forced circulation bypass flow loop is given in Figure 13B. The cold gas line between feed tanks, low pressure tanks and the compressor inlet are connected using copper piping rated at 1800 psi with Parker fittings (material of construction: brass) rated at 1800. The copper piping was used for cold gas. The hot

gas lines between the compressor outlet, and pressure vessel inlet and the pressure vessel outlet and the coil heat exchanger are connected using stainless steel pipes with Swagelok compression fittings. The valves and fittings are made from 316 stainless steel. A graphite test section was designed and fabricated to accommodate a circular main flow channel, a rectangular bypass flow channel and three heater rods. The heater input power could be varied to maintain different mean graphite temperature in the graphite test section. The details of each component can be found in Figure 14B and Figure 14C and Table 10. A high-pressure compressor (Hydro-Pac Inc. Model No: C01.5-10-1300LX) was used to compress the low-pressure gas coming from the feed tanks for (initial filling of the flow loop) and low-pressure tanks (while operating in a closed loop). The gas temperature increased in the process of compression and hence the gas coming from the compressor was hot. The compressor is equipped with a shell and tube heat exchanger and chilled water (< 10^0C) is circulated through the shell side at a minimum volumetric flow rate of 2GPM. The high-pressure gas coming out of the compressor is filtered by a 10-micron filter (3Bfilters Inc. Model no: S8515C-V.3MA-BS6). A gas cylinder was (high pressure tank) installed, just before the pressure vessel inlet, to dampen the fluctuations in the gas flow rate. To ensure a uniform gas distribution before entering circular and rectangular by-pass flow channels, the high-pressure gas, which is at room temperature, flows through a stainless-steel tube into a component equipped with a porous disk to ensure uniform gas velocity distribution before entering the graphite test section. (refer Figure 15). The gas flowrate entering and leaving the test section is controlled by a gas regulator and needle valve (labels: 14, 28 in Figure 14). The hot gas coming out of the test section is being cooled down in a coil heat exchanger. A water trap is installed after the heat exchanger to separate the possible water condensed in the heat exchanger and prevent humidity from entering the flow meter. The gas circulation rate is measured using a mass flow meter (OMEGA MODEL: FMA-878A-V) installed downstream of the coil heat exchanger. A 7-micron filter is also installed before the flow meter to prevent particles from entering the flow meter. Eventually the high-pressure gases exiting the graphite test section is depressurized by a valve and flows into low pressure tanks consists of three gas cylinders (see Figure 13B). These low-pressure cylinders serve as feed tanks when the flow loop is in continuous operation. To avoid excessive pressure buildup and back flow, two check valves are installed in the compressor outlet line and in the pressure vessel outlet line after the coil heat exchanger. For safety reasons, the flow loop was also equipped with two pressure relief valves set at a relief pressure of 65 bar (950 psi). The thermocouples and

pressure transducer were connected to a National Instruments data acquisition system for continuous monitoring and data acquisition via a LabVIEW program.

3.2. Experimental procedure

Prior to the actual experiments, the test facility was thoroughly tested to check the gas leakage rate and the test facility was found to lose its pressure at a rate of 5psi per hour for nitrogen gas as working fluid. The pressure regulator installed near the high-pressure feed tank (~2500 psi) is slowly opened to fill the entire loop with ~ 20.4 bar or ~300 psi (this pressure varies proportionally with the operating pressure). The compressor was turned on after ensuring all the valves installed in the flow loop are fully opened. The compressor was ramped up to achieve the working pressure, by increasing the voltage signal of the compressor motor controller. The compressor was allowed to run for at least 15 mins to achieve the steady working pressure. The AC power for the three heaters was turned on and variacs were adjusted to maintain the prescribed mean graphite temperature. After ensuing both the thermal and dynamic stability, the velocity and temperature of the gas coming out of the hot circular graphite channel were measured, over a long time, using a hot wire probe and k-type thermocouple. Further, the gas circulation rate and the outlet temperature of the gas at the pressure vessel outlet were measured are being recorded simultaneously using OMEGA mass flow meter and thermocouple. Bypass flow experiments have been performed with pure nitrogen over a wide range of temperature and pressure.

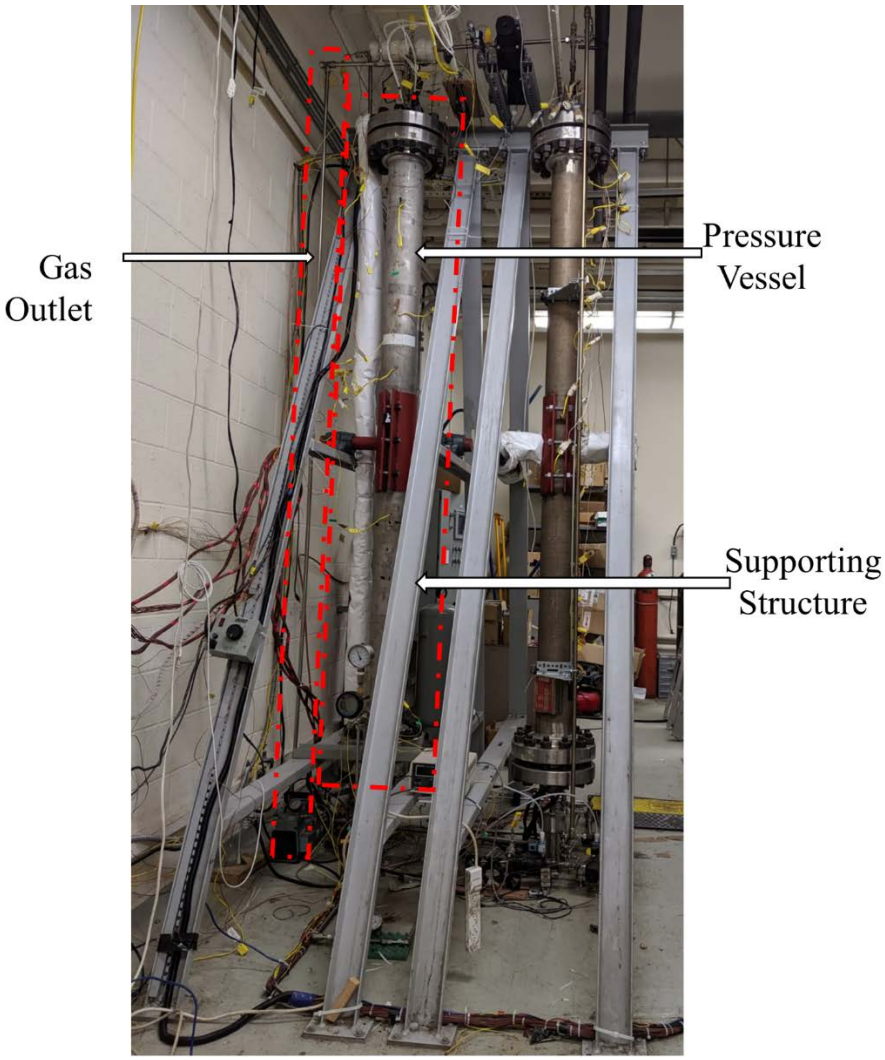

Figure 13A: Photograph of the forced circulation test facility at CCNY.

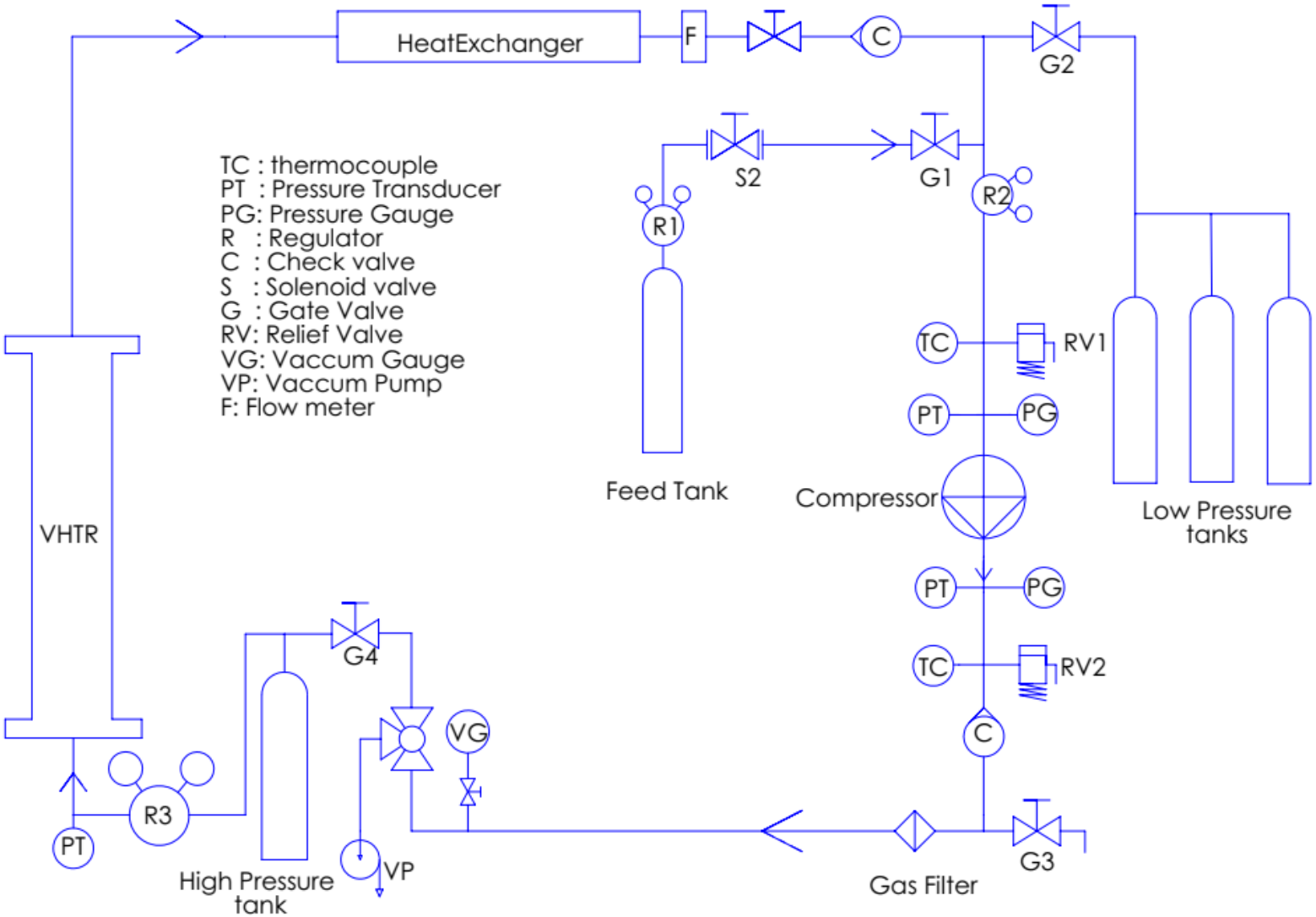

Figure 13B: Process Flow Diagram of the forced circulation test facility.

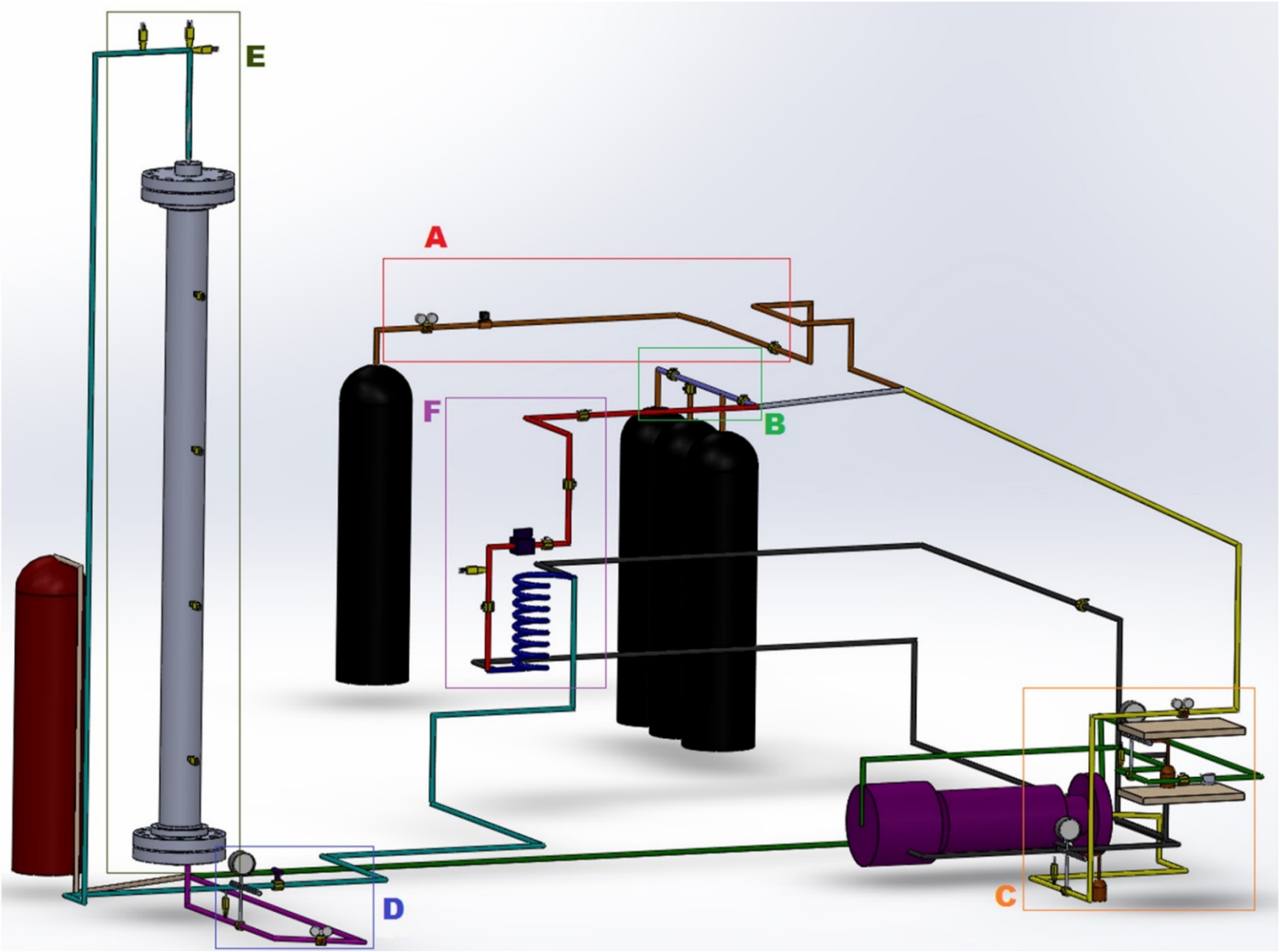

Figure 14A: 3D drawing of the forced circulation test facility.

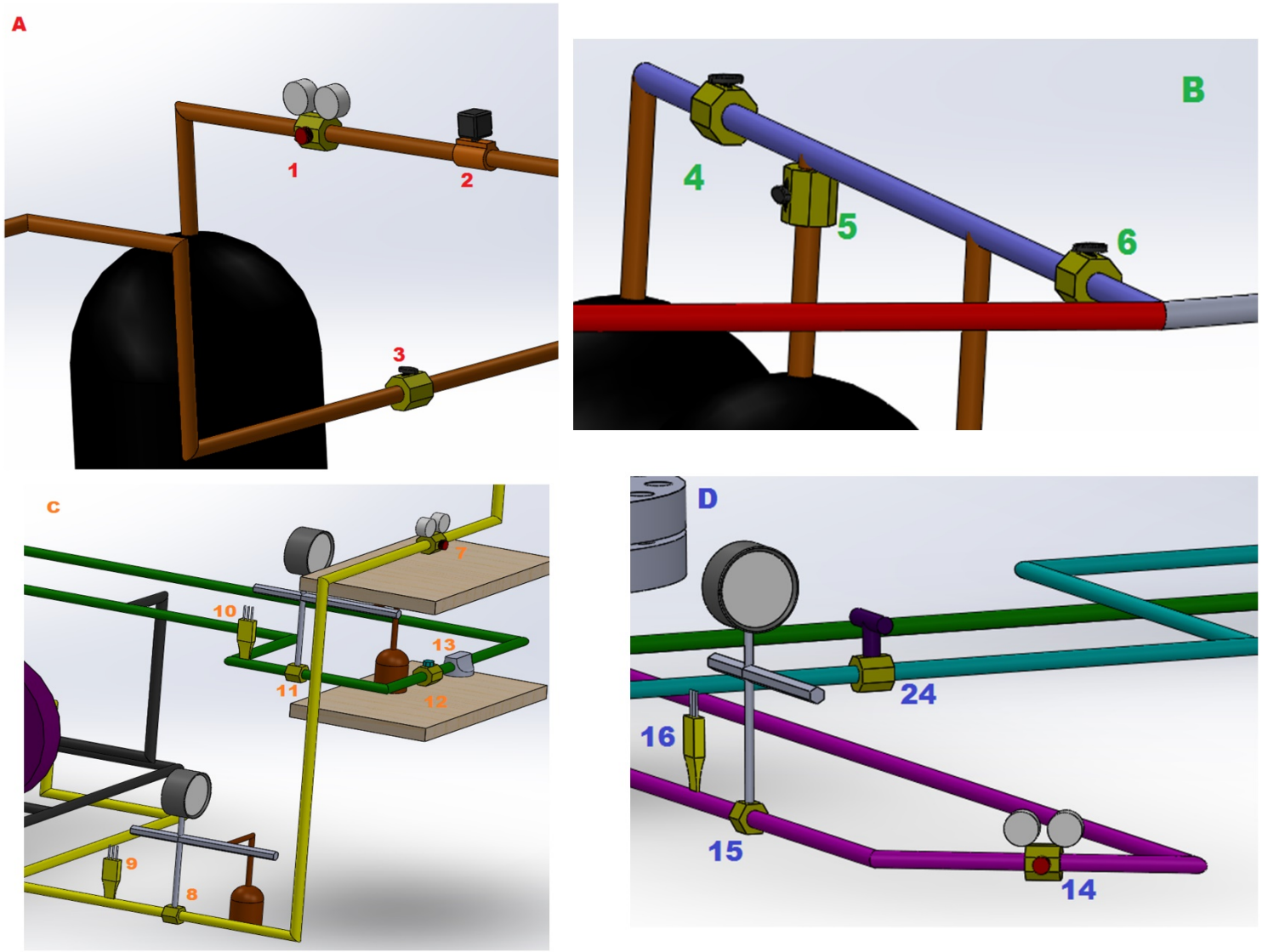

Figure 14B. Magnified view of the sub sections A to D of the flow diagram.

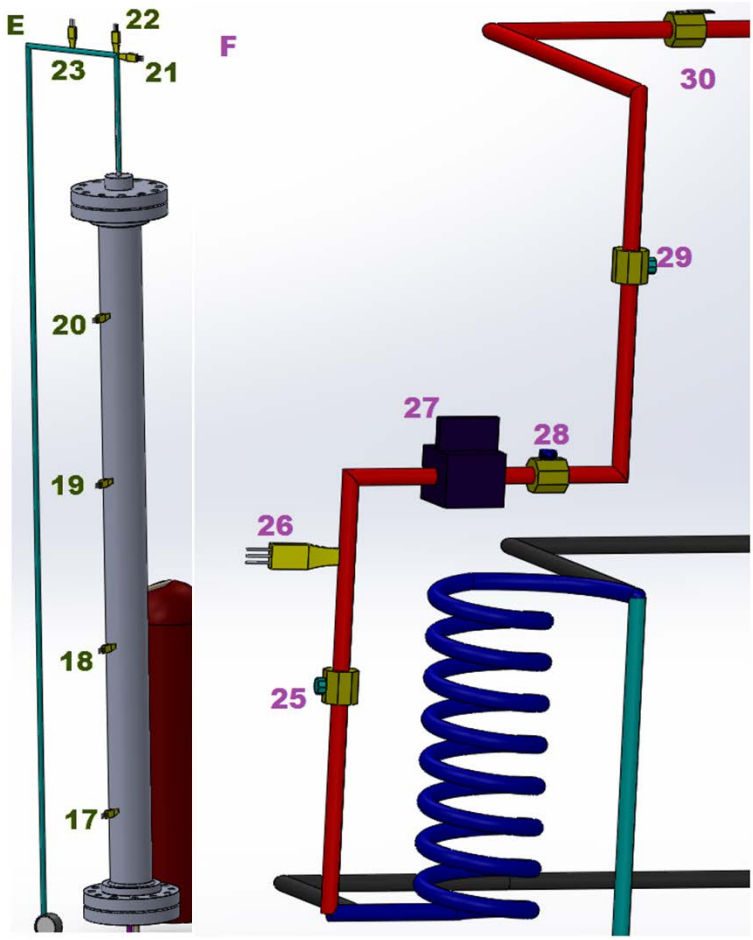

Figure 14C. Magnified view of the sub sections E and F of the flow diagram

Table 10: Legend of components in sections of Bypass flow test loop (Figs. 14B and 14C)

Label Number	Component Name	Section of Loop
1	Regulator	High Pressure Feed Tank
2	Solenoid Valve	
3	Ball Valve (ON/OFF)	
4	Ball Valve (ON/OFF)	Low Pressure Tanks
5	Ball Valve (ON/OFF)	
6	Ball Valve (ON/OFF)	
7	Gas Regulator	Compressor Inlet

8	T-joint (PT, RV, PG)	
9	Thermocouple	
10	Thermocouple	Compressor Outlet
11	T-joint (PT, RV, PG)	
12	Check Valve	
13	Gas Filter	
14	Gas Regulator	VHTR Inlet
15	T-Joint (PT, Vaccum Gauge, PG)	
16	Thermocouple	
17	Thermocouple	VHTR Surface
18	Thermocouple	
19	Thermocouple	
20	Thermocouple	
21	Thermocouple	VHTR Outlet
22	Hot Wire Probe	
23	Thermocouple	
24	Flow Control valve	
25	Check Valve	Coil Heat Exchanger
26	Thermocouple	
27	Mass Flow Meter	
28	Needle Valve	
29	Check Valve	
30	Ball valve (ON/OFF)	

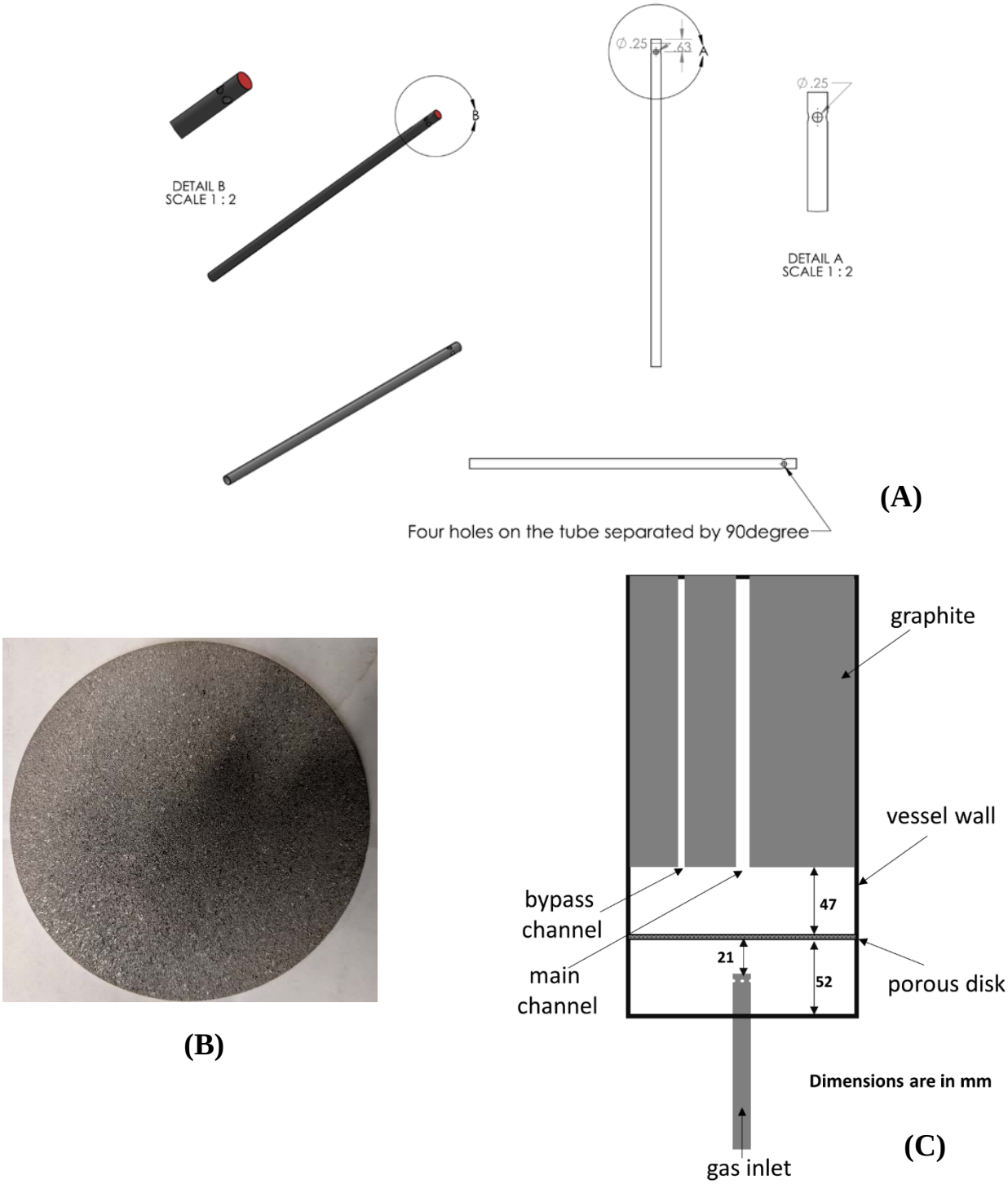

Figure 15: Gas injection system for the bypass flow test facility (A) SS pipe with four circular holes on the periphery, units are in inches (B) porous disk gas distributor, specifications are as follows: thickness: 2.3mm O.D: 92.2mm (3.63 Inch) , pore size 100µm (C) Schematic of the gas injection chamber.

3.3. Internal volume of the bypass flow loop

The piping dimensions (length and inner diameter) for the bypass flow test loop that includes a long piping for VHTR outlet, piping between compressor and VHTR inlet, the coil heat exchanger, and for the inlet stream after the gas supply and recycling system. The dimensions of the copper piping used to connect the gas supply cylinders to a three-way valve is given in the following table (Table 11). The total volume of the gas inside the forced circulation flow loop is 27738 liters.

Table 11. Detailed dimensions of the Natural Circulation Test Facility

	I.D. (cm)	Length (cm)	Volume (cm^3)	Colors in Forced Circulation 3D drawing
Hot graphite riser circualar channel	1.68	250	553.9	Inside VHTR
Hot graphite riser rectangular channel (3*40 mm)	1.2 (cm2)	250	300	
SS Tubing above the graphite	15.5	55.25	10419.9	
SS Tubing below the graphite	15.5	45.03	8492.5	
Hot gas outlet (SS piping VHTR outlet to coil inlet)	15.5	1233.5	232633.5	Teal
Coil heat exchanger	15.5	674	127113.9	Blue
Copper tubing (from coil to compressor inlet and upto ON/OFF brass valve near high pressure feed tank)	6.22	1088.5	33058.2	Red, light Blue,Gray, Orange
SS piping compressor Inlet	9.5	326	23095.9	Yellow
SS piping VHTR Inlet and Compressor Outlet	9.5	1658.3	117484.3	Green, Magenta, Tan
SS pipeing between coil and beginning of copper pipe	7	24	923.2	Green, Magenta, Tan
Volume of found gas cylinders			27184	
Total volume of the forced circulation bypass flow loop (liters)			27738.1	

3.4. Mass flow measurement device

A gas flow meter, Omega model FMA-878A-V, is used to measure the gas flow rate. It uses a heated bypass sensor tube that does not need pressure or temperature corrections, has a

digital display and is connected to a data acquisition system. The flow meter is installed on the outlet piping after the heat exchanger. The specifications of the flow meter are summarized in Table 12.

Table 12. Specifications of the gas flow meter

Accuracy	Maximum Pressure	Temperature Range	Pressure Coefficient	Temperature Coefficient
±2% full scale for 750 to 1,000 SLPM	1,000 psig	Gas and Ambient -10 to 70°C	0.1% typical	0.05% full scale/°C

3.5. Pressure vessel

The graphite test section is housed in a stainless steel 304 pressure vessel (PV), which is ASME certified at 69 bar (1,015 psi) at a temperature of 350°C, and has ANSI Class 900 flanges welded at the top and bottom. A photograph of the PV installed inside a supporting frame is shown in Figure 13A and the detailed dimensions of the PV are listed in Table 13. Since the maximum gas and graphite temperatures could reach 600°C, a 19.2 mm (0.756”) thick layer of thermal insulation with low thermal conductivity is placed between the graphite test section surface and inner wall of the PV to keep the PV wall temperature below 300^{0}C.

Table 13. Pressure Vessel Specifications

Material	Stainless Steel 304	
Length	2,826 mm	111.3”
Inner Diameter	146.3 mm	5.76”
Outer Diameter	168.3 mm	6-5/8”
Wall Thickness	11.0 mm	0.432”
Flanges	ANSI Class 900	
Flange thickness	55.6 mm	2.19”

3.6. Graphite test section

The graphite test section is a 108.0 mm (4.25”) diameter cylindrical column made of thermally isotropic graphite G348, and consists of two 1250 mm (49.52”) long sections that are joined in the middle using a rectangular slit (refer Figure 16). The total test section length is 2500 mm (98.4”). The dimensions and specifications of the graphite test section are summarized in Tables 4 and 5. The test section has a main flow channel with a diameter of 16.8 mm, rectangular bypass flow channel (40 mm × 3 mm cross section× 2500 mm) along with three smaller holes in which 12.7 mm diameter heater rods are inserted (refer to Figure 16). All three heater rods are 3,048 mm (120”) long and penetrate through the guide tubes welded on the top flange. The top 300 mm (12”) section of each heater rod is not generating heat, so that the part above the graphite test section as well as the guiding tubes on the top flange remain unheated. At the joint of the two halves of the graphite test section, thin-walled hollow circular and rectangular tubes were inserted into the main and bypass flow channels, respectively, to prevent any gas flow leaking out of those channels. Dimensions of the enlarged flow channels are shown in the Figure 16.

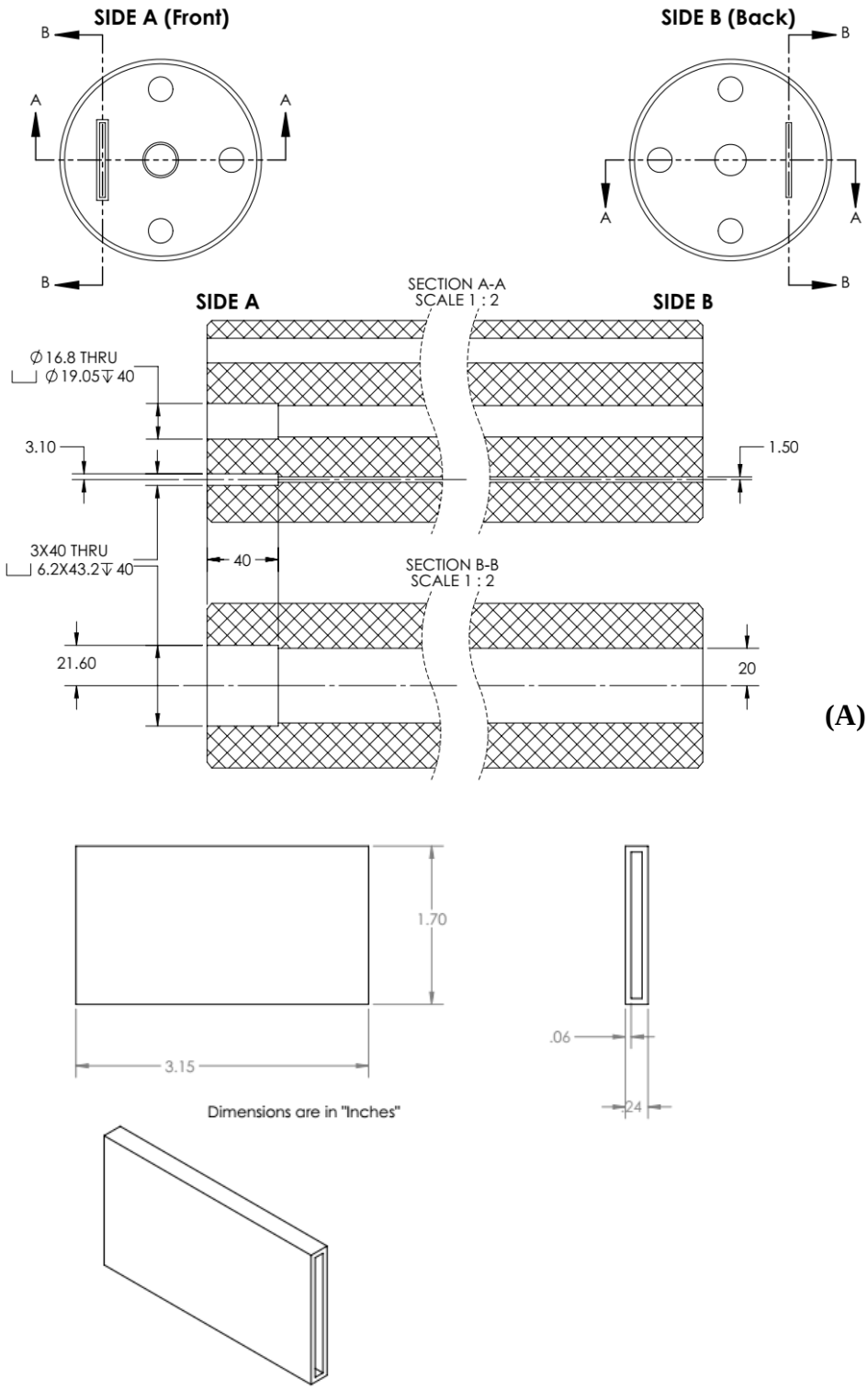

Figure 16: (A) Schematic of the graphite block (B) Hollow rectangular slit to align the two graphite blocks in-place

Table 14. Dimensions of the graphite test section

Material	Graphite G348	
Length	2,750 mm	108.0” (2 x 54.5”)
Outer Diameter	108.0 mm	4.25”
Flow Channel Diameter	16.8 mm	0.66”
Bypass flow Channel	40 × 3 mm	1.58” × 0.12”
Heater Channel Diameter	12.7 mm	0.5”

Table 15. Specifications of the graphite material

Model	Composition	Density (g/cm^3)	Resistivity (μΩ-cm)	Young's Modulus (GPa)	Flexural strength (MPa)	Hardness (shore)	Coefficient of thermal expansion ($10^{-6}/^oC$)	Thermal conductivity (W/mK)
G348	99.99 fixed carbon	1.92	1300	12.3	63.7	68	5.5	128

3.7. Thermal insulation

The graphite test section is covered with a layer of soft thermal insulation which is easy to install. Five stainless steel, ring shaped supports have been used to keep the graphite fixed in the center of the pressure vessel. The physical properties of the insulation are shown in Table 16. A layer of thermal insulation is also placed at the top and below the inlet gas chamber of the graphite test section to reduce heat conduction to the top and bottom flanges of the PV, in order to prevent the flanges from heating up above 350°C. Stainless steel support assemblies are provided to support the graphite test section above the bottom flange and below the top flange. A stainless-steel ring is also attached to the mid-section of the graphite test section to support the soft insulation.

Table 16. Properties of soft insulation material

Classification Temperature (°C)		648
Service Temperature (°C)		648
Density (kg/m^3)		160
Organic Content (Wt%)		0
Linear Shrinkage (24 hrs@ Temperature, "+" indicates growth)		4.8% @ 22°C
Chemical Composition		Fiber glass
Thermal Conductivity (W/mK)	200°C	0.05
	315°C	0.07
	400°C	0.08

3.8. High pressure compressor

A Hydro-Pac compressor is used to achieve high gas circulation rates through the bypass flow loop. The principle is to use a hydraulic power unit to supply a low-pressure hydraulic fluid to an intensifier. The low-pressure hydraulic fluid is delivered to the hydraulic drive cylinder of the intensifier. This cylinder contains a large area piston. The hydraulic pressure creates a force on the large area piston that results in a balanced force against a piston of a smaller area inside the high-pressure cylinder. The pressure of the fluid in the smaller high-pressure cylinder will be increased in proportion to the ratio of the two areas. The intensifier is made up of high-pressure cylinders and a hydraulic drive cylinder. Each cylinder contains a piston. Vented spacers attach the process fluid cylinders to the hydraulic cylinder and isolate the hydraulic fluid from the gas being compressed. During operation process fluid flows through the inlet check valve and fills the process fluid cylinder. Pressurized hydraulic fluid acting on the hydraulic piston strokes the piston assembly to the right. Process fluid in the right cylinder is forced through the discharge check valve. At the same time, fluid flows through the left inlet check valve and fills the left process fluid cylinder. At the end of this stroke, a directional control valve changes position and directs

pressurized hydraulic fluid to the right side of the hydraulic piston (Figure 17). The piston assembly moves to the left, discharging fluid from the left cylinder. The piston assembly reverses direction at the end of the stroke and the cycle repeats. The hydraulic cylinder is cycled by an internally piloted four-way valve. No external electrical signal is required (Table 17). The hydraulic drive is carefully matched to the gas intensifier section to provide efficient operation. Both the intensifier and hydraulic drive are water cooled to provide maximum reliability and efficiency.

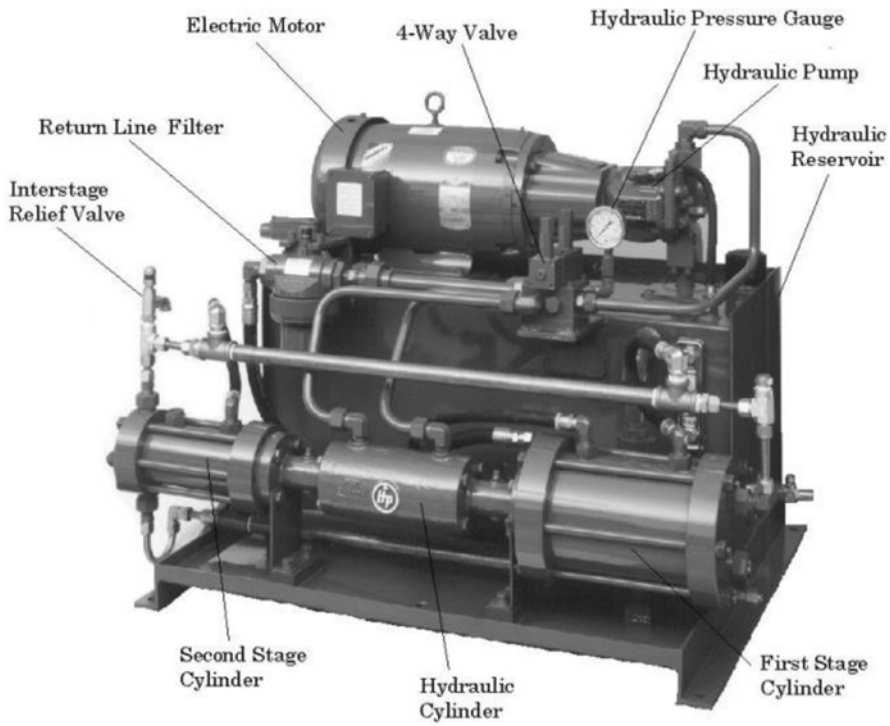

Figure 17: Schematic of the Hydro-Pac compressor used in this project

Table 17. Specifications of high-pressure compressor

Model Number	HydroPac: C01.5-10-1300LX
Gas	Helium/Nitrogen
Discharge Pressure	1,500 PSI (10 MPa)

Inlet Pressure	200 – 1,500 PSI (1.4 – 10 MPa)
Maximum Hydraulic Pressure	3,000 psi (20.69 MPa)
Capacity at 200 PSI (1.4 MPa), 80 °F (27 °C) Inlet	16.1 SCFM (29 NM_3/Hr)
Type	One Stage Hydraulically Driven Intensifier
Motor Power	10 hp (7.5 kW)
Motor Voltage	230/460 V, 3 PH, 60 Hz
Control Power	24 VDC
Flow Control Signal	4-20 mA
Cooling Water Temperature Range	60° - 80° F (16° - 27° C)
Cooling Water Flow Rate (Minimum)	1 gpm (4 lpm)
Intensifier Stroke Length	4 in (102 mm)
Actuation Type	Auto Shift Valve
Hydraulic Reservoir Capacity	30 US Gallons (114 liters)

4. Instrumentation for Forced Circulation Bypass Flow Test Facility

4.1. Pressure measurement

Three Omega pressure transducers, a digital pressure gauge (General Electric model DPI-104) and a vaccum gauge (-30 to 30 psi) are installed in the forced circulation bypass flow test facility. Two pressure transducers (PX303-2KG5V) and two analog pressure gauges (Range: 1-102 bar (1500 psi)) are installed in the discharge and suction lines of the compressor. The PTs are connected to the NI-DAQ to record and save the pressure data onto a computer, while, the analog gauges are used to check the system pressure while doing the actual experiment. A set of pressure transducers (PX303-1KG5V), a digital pressure gauge (General Electric model DPI-104), and a vaccum gauge (-30 to 30 psi) are installed at the pressure vessel inlet. The pressure reading at the inlet is used to maintain the required experimental pressure condition using a gas regulator

installed just before the pressure vessel inlet (Figure 13B and Figure 14A). The calibrated digital pressure gauge is installed to get a quick pressure reading while filling and vacuuming the flow loop. The digital pressure gauge is also used for verifying the calibration of the Omega pressure transducers. Since the working temperature for the pressure transducers used are lower than 50ºC, a 2-foot-long stainless-steel tube is used between each pressure transducer and the inlet or outlet piping. This way, the stagnant gas in the 2-ft tube is cooled enough that the pressure transducer is not directly exposed to a hot gas. The specifications of the pressure transducers and pressure gauges are given in Table 18.

Table 18. Specifications of the pressure transducers

	Model	Range (psi)	Type	Resolution (psi)	Max Working Pressure (psi)
General Electric	DruckDPI-104	$0-3000$	Sealed Gauge	0.1	3190
	Accuracy	0.05% FS including non-linearity, hysteresis, repeatability and temperature effects from $-10℃$ to $50℃$			
	Burst Pressure	Burst pressure is $2x$ working pressure			
	Selectable Pressure Units	$kPa, MPa, \frac{kg}{cm^2}, psi, mbar, bar, inHg, inH_2O, mH_2O, mmH_2O, mmH$			
Omega	Model	Range (psi)	Type	Resolution (psi)	Max Working Pressure (psi)
	PX303-1KG5V	$0-1000$	Sealed Gauge	2.5	2000
	Accuracy	0.25% FS including non-linearity, hysteresis, repeatability and temperature effects.			

	Burst Pressure	Burst pressure is $2x$ working pressure.			
	Selectable Pressure Units	$kPa, MPa, \frac{kg}{cm^2}, psi, mbar, bar, inHg, inH_2O, mH_2O, mmH_2O, mmH$			
Omega	Model	Range (psi)	Type	Resolution (psi)	Max Working Pressure (psi)
	PX303-2KG5V	$0 - 2000$	Sealed Gauge	2.5	4000
	Accuracy	0.25% FS including non-linearity, hysteresis, repeatability and temperature effects.			
	Burst Pressure	Burst pressure is $2x$ working pressure.			
	Selectable Pressure Units	$kPa, MPa, \frac{kg}{cm^2}, psi, mbar, bar, inHg, inH_2O, mH_2O, mmH_2O, mmH$			

4.2. Temperature measurement

4.2.1. Gas temperature

The gas temperatures inside the forced circulation bypass flow test facility have been measured using type-K thermocouples. A pair of two thermocouples were installed at upstream and downstream of the compressor to monitor the gas temperature. Two thermocouples were installed before and after the bypass flow channel to measure the gas temperatures entering and exiting the pressure vessel. One more thermocouple was installed upstream of the mass flowmeter to monitor the gas temperature entering the mass flow meter. Six thermocouples were installed on the pressure vessel outer surface (1 on the top flange, 1 on the bottom flange, and 4 equally distributed surface thermocouples between the upper and lower flanges). These temperature data

are very crucial for determining the heat loss from the graphite channel and pressure vessel body to the environment.

4.2.2. Graphite temperature

To measure the axial and radial temperature distributions in the graphite test section, a total of 48 type-K thermocouples are inserted into the pressure vessel. A total of 40 thermocouples are embedded into the graphite at 4 radial locations at each of 10 axial locations. At each axial location, four thermocouples are installed at four azimuthal positions and at different depths as shown in Figure 18. The thermocouple A is inserted to a depth of 16.0 mm from the graphite column surface, B and D are inserted to a depth of 32.0 mm and closest to the main circular flow channel, and C is at a depth of 9 mm close to the rectangular flow channel as shown in Figure 18.

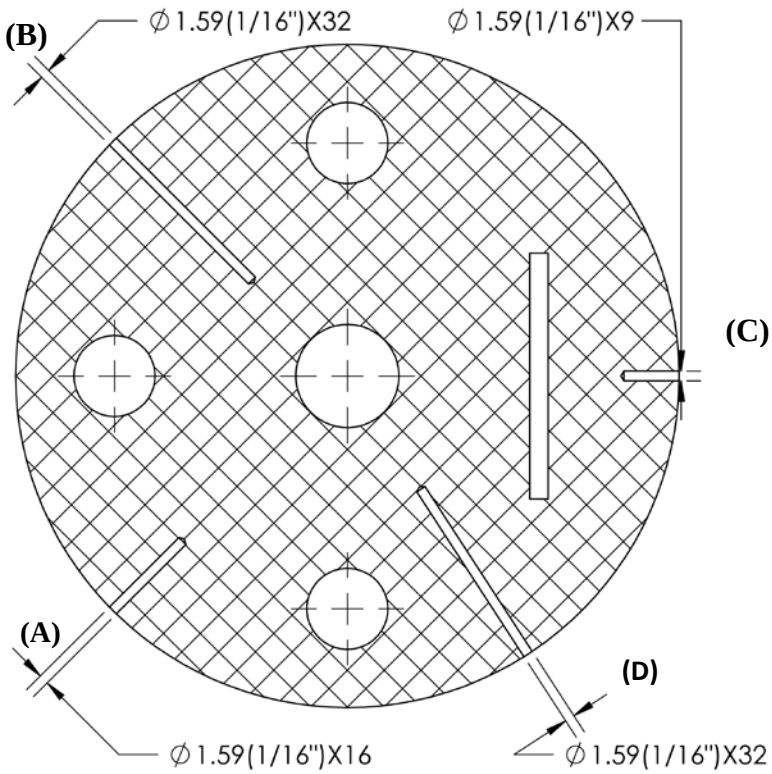

Thermocouple	A	B	C	D
Depth (mm)	16.0	32.0	9.0	32.0

Figure 18. Schematic of the thermocouple locations and their depths.

All 48 thermocouples are grouped into four bundles and each bundle has two spare thermocouples which can be used to replace any damaged thermocouples. The four thermocouple bundles pass through a specially designed stainless-steel plate (shown in Figure 19) that also has the gas inlet pipe welded in the middle. This plate is rated to withstand a pressure of 69 bar (1,015 psi) at 650ºC, sealed with a gasket at the bottom flange. The thermocouple bundles and plate constitute the thermocouple assembly.

Figure 19 Thermocouple plate to pass four bundles of 12 sheathed thermocouple wires

4.3 Heater rods and power control

The graphite test section in the bypass flow test facility is heated by three 3 m (120”) long electric heater rods with an internal thermocouple to monitor the temperature of the heater rod and prevent overheating. This temperature data is used to calculate the amount of power required to heat the graphite. Further details about the specifications are given in Table 19.

Table 19. Specifications of heater rods

Diameter (in)	Length (in)	Voltage (V)	Power (W)	Thermocouple
0.496 + /- 0.002	120 +/- 2.5	240	2,300	type K

Each heater rod is connected to an AC source through a controller, a 0-240 V variac, and circuit breaker as shown in Figure 20 and 21, so that the heater power can be individually

controlled and recorded by a data acquisition system. Each heater rod temperature is displayed in a controller panel. The controller is set to shut off the AC heater power when the heater rod temperature exceeds a set point temperature. The four variacs and circuit breakers are located in the control room (Figure 21) which are separated from the gas flow loop by a concrete wall for safety. When the test section is pressurized and heated up, the operators can control the heater power without going into the lab where the gas flow loop is located.

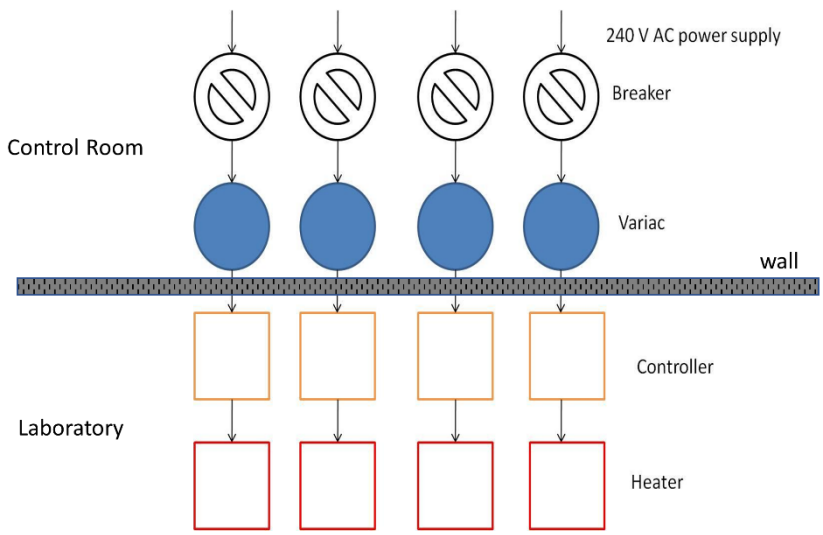

Figure 20. Schematic of electric heater power control

Figure 21. Four variacs for individual heater power control and a 240 V AC circuit breaker panel.

4.4. Data acquisition system

A National Instruments Data Acquisition System (Model cDAQ-9189) is used with a total of 8 input modules to record the experimental data. One analog voltage input module (NI 9205) for controlling the compressor outlet pressure, three NI-9213 modules, one NI-9211 and one NI-9263 module were used for recording the thermocouple data. Another module NI-9247 was used to record the pressure data coming from Pressure Transducers. Finally, one NI-9215 BNC module was used to record the Hot Wire Anemometer data. All the thermocouple, pressure transducer and flow meter cables are connected to the DAQ input modules in an electrical box and a PC-based DAQ system as shown in Figure 22. The data acquisition PC is a 64-bit system with an Intel Pentium CPU G2020 running on Windows 10 at 2.90 GHz speed, and has an internal memory of 32 GB.

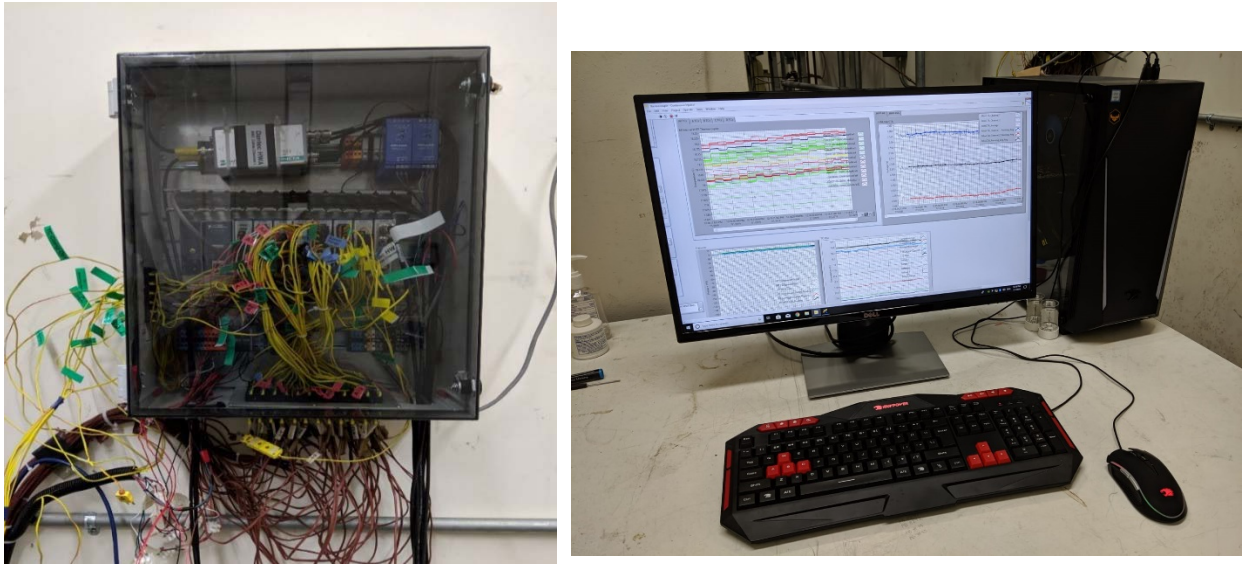

Figure 22. A Data Acquisition System and LabVIEW software

<u>The blue prints of the PV, Graphite test section etc. are available upon request.</u>

APPENDIX 2: Constant Property Simulations of Flow Laminarization using Nek5000

SUSTAINING TURBULENCE IN A VERY LONG PIPE TOWARDS STUDYING HEAT DRIVEN TURBULENT GAS RELAMINARIZATION

Apoorva Rudra, Masahiro Kawaji*
City College of New York
160 Convent Ave, New York, NY 10031, USA
arudra000@citymail.cuny.edu; banerjee@che.ccny.cuny.edu; mkawaji@ccny.cuny.edu

Aleksandr Obabko, Saumil Patel
Mathematics and Computer Science (MCS)
Argonne National Labs (ANL)
9700 Cass Ave, Lemont, IL 60439
obabko@mcs.anl.gov; spatel@anl.gov

ABSTRACT

Very High Temperature Reactors (VHTRs) have passive safety systems in comparison to the traditional current generation nuclear reactors that have active safety systems. In addition, they have gaseous coolants like helium proposed for them that allow them to operate at a temperature over 1000 ºC along with other applications. However, several substantial engineering challenges are expected in VHTRs and can lead to localized hot spots in the reactor core as a result of degraded heat transfer in coolant channels. Our work addresses one such scenario called flow relaminarization. The following work incorporates 3D simulations in a very long pipe wherein turbulence is sustained throughout for the largest aspect ratio (L/D ratio) known in literature (~235). This work is the first step of a two-step process towards the final objective of studying heat driven turbulent gas relaminarization. Simulations are performed using a high order, spectral element and massively parallel CFD code called NEK5000 that combines the geometric flexibility of finite elements with the high accuracy of spectral methods. A replication method along with recycled periodicity is incorporated to successfully sustain turbulence throughout the pipe. The maximum Reynolds number incorporated for these simulations is 5190 which is chosen keeping in mind the flow relaminarization (forced convection) experiments that were performed by the group in the past. A sensitivity study on the polynomial order was performed as well and based on that the polynomial order chosen for the simulations was 6.

KEYWORDS
VHTR, Turbulence, Relaminarization, Replication

1. INTRODUCTION

Gaseous coolants are proposed for Very High Temperature Reactors (VHTRs), which is one of six Generation IV reactors that have been proposed for DOEs Next Generation Nuclear Plant. Although these designs ensure passive cooling in case of loss of forced circulation or pressure [1], it is still not fully known how they will behave under all conceivable accident scenarios. Several Phenomena Identification and Ranking Tables (PIRT) for VHTRs show that under normal steady-state, transient, and accident scenarios,

* Corresponding Author: mkawaji@ccny.cuny.edu

the key phenomena leading to localized hot spots in the reactor core include flow laminarization, natural convection, air ingress, water or steam ingress, degraded heat transfer in coolant channels, effects of bypass flow, and non-uniform heat generation across the core. Due to the high temperatures of the coolant involved, material behavior in various components needs to be better understood. Some of these phenomena have been investigated in-depth in recent years. Our work addresses the issue of flow laminarization, in which a strongly heated turbulent gas flow, exhibits heat transfer characteristics of laminar flows in the downstream part. Under Forced convection conditions, deteriorated turbulent heat transfer (DTHT) can trigger flow laminarization even if the incoming flow in the heated flow channel is above the critical Reynolds number.

2. RELAMINARIZATION OF TURBULENT FLOW DURING FORCED CONVECTION

Relaminarization of turbulence is the phenomenon of reversion of flow from turbulent to laminar [2]. This transition or reversion is said to occur at high Reynolds numbers greater than the critical Reynolds number of ~ 2100. Laminarization is responsible for decrement in the heat transfer rates as a result of thickening of the thermal boundary layer [3]. The long run effect of the thermal boundary layer growth is that no truly fully established conditions are reached because the temperature increments lead to continuous axial and radial variations in thermophysical properties [4].

The criteria for the occurrence of laminarization and the heat transfer characteristics of this phenomenon have been the subject of study by several investigators. Most of the experiments in the early years that involved gas heating with significant property variations were conducted with circular tubes of small diameters and under forced convection conditions. The tubes were too small for probes to measure useful velocity and temperature profiles, so the experiments could only provide integral parameters. For dominant forced convection in low Mach number pipe flows with significant gas property variations, the only published mean profiles of temperature and velocity to guide the development of predictive turbulence models were given by Perkins [5] and Shehata and McEligot [6]. This was a huge limitation. Thus, more detailed thermal features of turbulent flow with strong heating may be predicted by turbulent models and numerical simulations. One issue with studying laminarization is that there exists a very limited numerical knowledge base. For example, many numerical studies are specific to the conditions used in the experiments of Shehata and McEligot [7]. This expresses the limited applications of even successful models, since their validation data was constrained to small tubes, low densities, and/or microgravity applications. These knowledge gaps are attempted to be addressed in this work.

In this study, we present the simulation results for the first step of a two-step process towards the final objective of studying heat driven turbulent gas relaminarization. We briefly describe the experimental setup that was incorporated to study forced convection experiments which is followed by the numerical method incorporated along with the governing equations. Finally, preliminary simulation results for a constant heat flux are presented in order to verify the correctness of the turbulence sustaining procedure.

2.1. Experiments

A high pressure and high temperature test facility has been constructed at City College of New York. This facility consists of a pressure vessel rated at 70 bar/923 K, and contains a 2.7 m long, 108 mm outer diameter graphite column with four 2.3 kW heaters symmetrically placed about a central coolant channel of 16.8 mm diameter (L/D ratio ~ 170) [8-11]. The temperature profiles in the graphite were measured by thermocouples imbedded at ten axial locations 25 cm apart. The experimental setup can be seen in Figure 1.

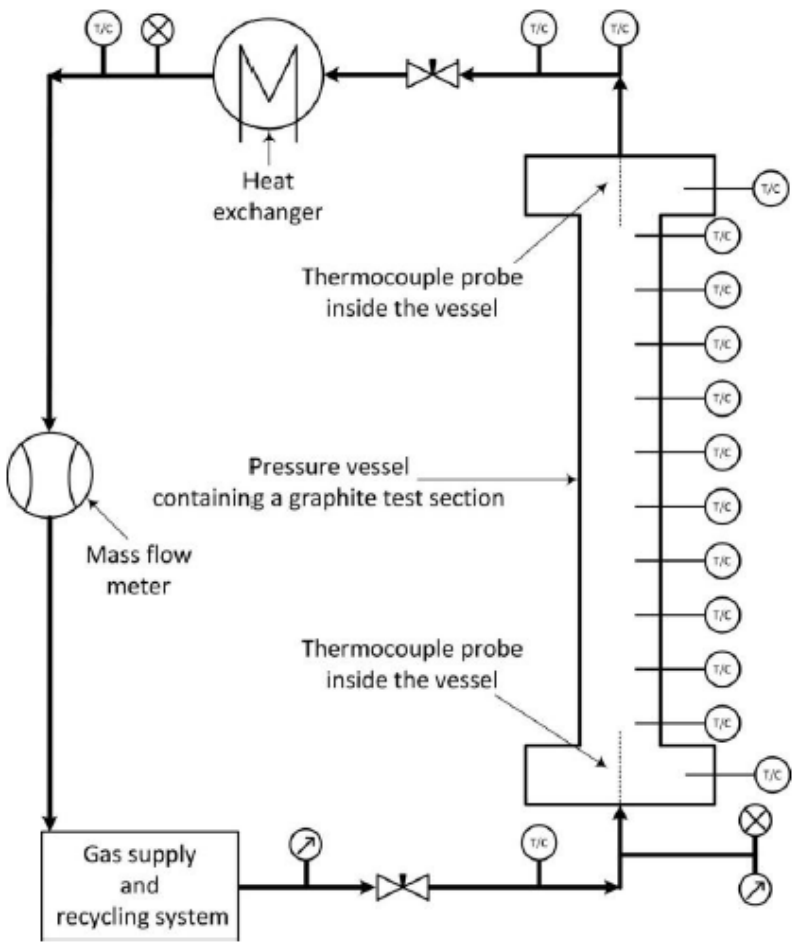

Figure 1. Experimental Setup [8-11]

Each forced convection experiment included the independent selection and control of three parameters: graphite mid-point temperature, system pressure and gas flow rate. Relaminarization of turbulent flow has been experimentally shown by Valentin et al. [8, 9] including hot wire anemometer measurements at high pressure and high temperature [11].

3. NUMERICAL METHOD AND GOVERNING EQUATIONS

We consider the incompressible flow of a viscous Newtonian fluid in a smooth circular pipe where the governing equations for fluid flow and energy are given by

$$\nabla \cdot \mathbf{u} = 0 \tag{1}$$

$$\rho\,(\partial_t \mathbf{u} + \mathbf{u} \cdot \nabla \mathbf{u}) = -\nabla p + \nabla \cdot \tau + \rho f \tag{2}$$

$$\rho C_p(\partial_t T + \mathbf{u} \cdot \nabla T) = \nabla \cdot (k \nabla T) + q_{vol} \tag{3}$$

The code used to numerically solve the above Eqs. is Nek5000 developed by Fischer et al. [12]. Nek5000 is a computational fluid dynamics solver based on the spectral element method (SEM) well known for its (spectral) accuracy, favorable dispersion properties, and efficient parallelization. In Nek5000,

incompressible Navier–Stokes equations are solved using a Legendre polynomial-based SEM. These equations are cast into weak form and discretized in space by the Galerkin approximation.

4. PROCEDURE TO SUSTAIN TURBULENCE

As mentioned earlier, the aspect ratio (L/D) in the experiments is ~ 170. Hence, it is important to assure that during the numerical simulations, turbulence is sustained throughout the entire circular pipe as the gas moves forward.

A replication method with recycling periodicity was incorporated in order to achieve this. Initially a small pipe of aspect ratio 13 was created with recycling periodic boundary conditions. After sustaining turbulence in this pipe (Fig. 2 (a)), replication was done for 3 times axial length (L/D = 39) and turbulence was again found to be sustained (Fig. 2 (b)). Finally, another replication was performed for 6 times the axial length (L/D = 234) wherein periodicity is recycled till L/D = 39. This recycled section behaves as the turbulence inflow generator while the remaining axial length (L/D = 195) accommodates the actual length of the experimental test section (required L/D ratio for experiments is ~170). Fig. 2 (c) and 2 (d) show the mesh generated for the simulations. The maximum number of elements that are incorporated in the simulations is ~1.5 M. Table 1 gives the important details of this procedure.

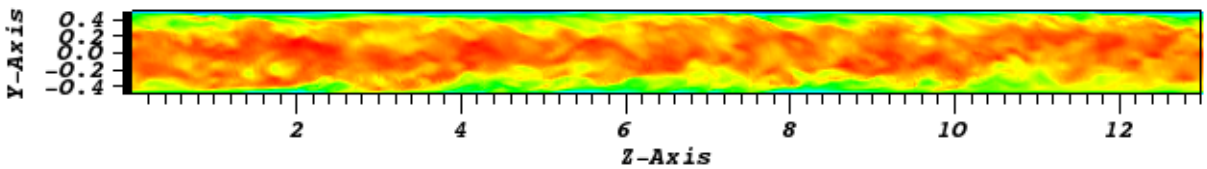

(a)

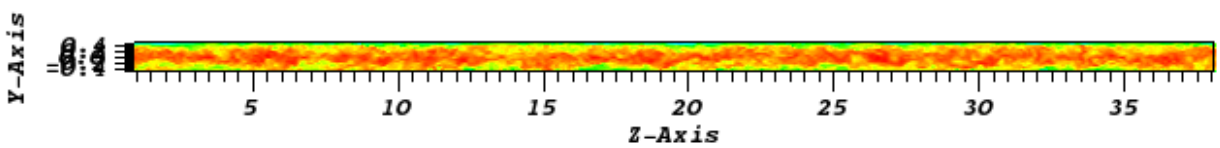

(b)

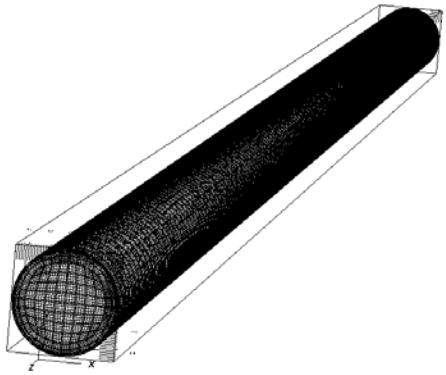

(c)

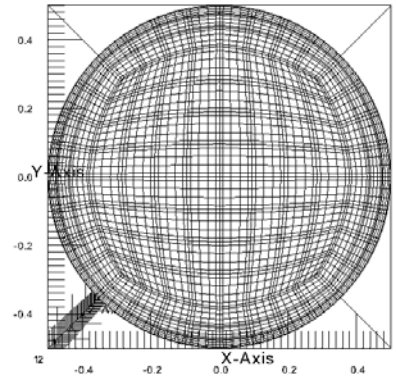

(d)

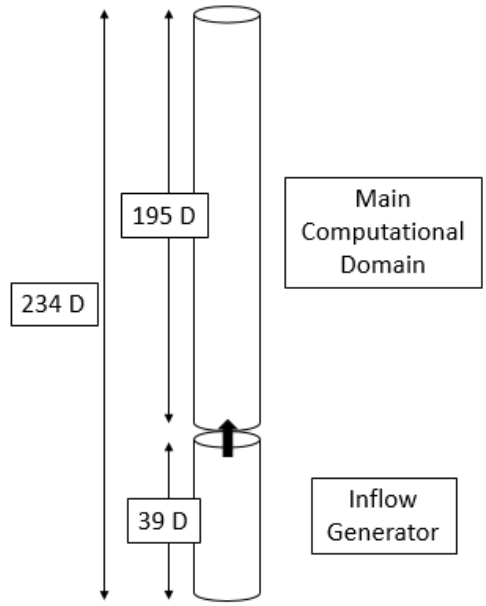

(e)

Figure 2. Sustaining turbulence for sectional view for a) L/D = 13, b) L/D = 39, c) mesh for L/D = 39, d) cross sectional view of final mesh and e) entire computational domain.

Table I. Details of Sustaining Turbulence Procedure

Section	Aspect Ratio (L/D)	Number of Elements
-	13	8,320
Inflow generator	39	24,960
Inflow generator + Main Computational Domain	39 + 195 = 234	149,760

5. RESULTS

Fig. 3 (a) shows the cross-sectional view of the velocity profile clearly showing turbulence. This can be further explained by Fig. 3 (b) where we have the sectional view of the velocity profile in the axial direction. The simulations are run till steady state or a statistically stable solution is reached. A sensitivity study was also performed on the polynomial order. Turbulence was found to be sustained for such a large aspect ratio at a minimum polynomial order of 6. Increasing the polynomial order further did not show any major differences in the velocity and temperature averages. Hence, the polynomial order of 6 was chosen keeping in mind the excessive computational time involved. Fig. 3 (c) shows the temperature profiles in the axial direction. Throughout the entire section of the pipe, turbulence is found to be sustained. As can be seen from Fig. 3 (c), the constant heat flux is applied only to the main computational domain. The inflow generator is unheated as it is used only to provide an initial sustained turbulence to the main computational domain.

6. CONCLUSIONS

Three-dimensional simulations have been performed using a spectral element code, Nek5000. These simulations were performed to complete the first step of a two-step process with the eventual objective of

studying heat driven turbulent gas relaminarization. During this first step, turbulence was sustained in a very long pipe with the largest aspect ratio known in literature. The turbulence was sustained with the help of a replication procedure with recycling periodicity. Finally, a constant heat flux is applied to the pipe to verify the correctness of the turbulence sustaining procedure. Future work will incorporate variable material properties as is the case with the experiments performed by the group in the past to study flow relaminarization.

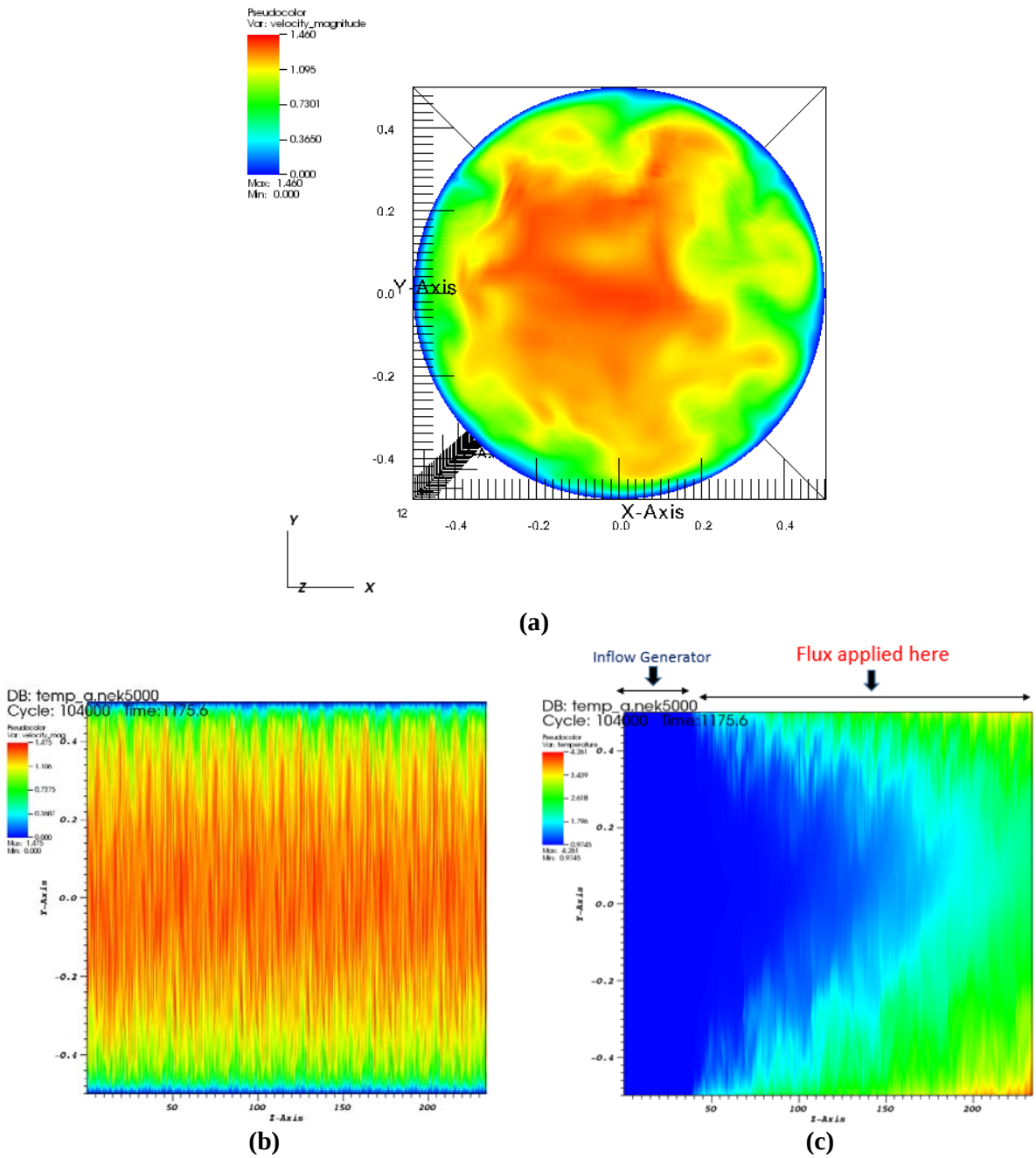

Figure. 3. Velocity profiles in the pipe a) cross section, b) along the pipe, and c) temperature profile in the axial direction

ACKNOWLEDGMENTS

This work has been supported by a grant from the U.S. Department of Energy's Nuclear Energy University Program under Contract No. DE-AC07-05ID14517. The authors would also like to thank Dr. Francisco Valentin of CREARE, Inc. for the past experimental work, and Prof. Sanjoy Banerjee for suggestions on turbulence sustenance.

REFERENCES

1. Vilim, R.B., Pointer, W.D., and Wei, T.Y.C., 2006, "Prioritization of VHTR System Modeling Needs Based on Phenomena Identification, Ranking and Sensitivity Studies," ANL-GenIV-071.
2. Narasimha, R. and Sreenivasan, K.R, 1979, "Relaminarization of fluid flows", Advances in Applied Mechanics, 19:221-309.
3. Keshmiri, A., Cotton, M.A., Addad, Y., and Laurence, D., 2012, "Turbulence models and large eddy simulations applied to ascending mixed convection flows", Flow, turbulence and combustion, 89(3):407-434.
4. Mikielewicz, D.P., Shehata, A.M., Jackson, J.D. and McEligot, D.M., "Temperature, velocity and mean turbulence structure in strongly heated internal gas flows: comparison of numerical predictions with data," 2002, International Journal of Heat and Mass Transfer, 45(21):4333-4352.
5. Perkins, K.R., 1975, "Turbulence Structure in Gas Flows Reliminarization by Heating," PhD thesis, University of Arizona, Tucson.
6. Shehata, A.M. and McEligot, D.M., 1995, "Turbulence structure in the viscous layer of strongly heated gas flows, Technical Report, Lockheed Idaho Technologies Co., Idaho Falls, ID.
7. Shehata, A.M. and McEligot. D.M., 1998, "Mean structure in the viscous layer of strongly-heated internal gas flows. Measurements". International journal of heat and mass transfer, 41(24):4297
8. Valentin, F.I., Artoun, N., Anderson, R., Kawaji, M., and McEligot, D.M., 2016, "Study of convection heat transfer in a very high temperature reactor flow channel: numerical and experimental results", Nuclear Technology, 196(3) 661-673.
9. Valentin, F.I., Anderson, R. and Kawaji, M., 2017, "Experimental Investigation of Convection Heat Transfer in High Pressure and High Temperature Gas Flows", J. Heat Transfer 139(9), 091704, doi: 10.1115/1.4036524.
10. Valentin, F.I., Artoun, N., Kawaji, M., and McEligot, D.M., 2018, "Forced and Mixed Convection Heat Transfer at High pressure and High Temperature in a Graphite Flow Channel," J. Heat Transfer, doi:10.1115/1.4039585
11. Valentin, F.I., Artoun, N., Kawaji, M., 2018, "Experimental Investigation of Flow Laminarization in a Graphite Flow Channel at High Pressure and High Temperature", Journal of Heat Transfer, in press.
12. Fischer, P.F., Lottes, J.W., Kerkemeier, S.G., 2008, nek5000 web page. http://nek5000.mcs.anl.gov